

Lecture Notes in Physics

688

M. Carmen Miguel
J.M. Rubi
(Eds.)

Jamming, Yielding,
and Irreversible
Deformation in
Condensed Matter



Springer

Editorial Board

R. Beig, Wien, Austria
W. Beiglböck, Heidelberg, Germany
W. Domcke, Garching, Germany
B.-G. Englert, Singapore
U. Frisch, Nice, France
P. Hänggi, Augsburg, Germany
G. Hasinger, Garching, Germany
K. Hepp, Zürich, Switzerland
W. Hillebrandt, Garching, Germany
D. Imboden, Zürich, Switzerland
R. L. Jaffe, Cambridge, MA, USA
R. Lipowsky, Golm, Germany
H. v. Löhneysen, Karlsruhe, Germany
I. Ojima, Kyoto, Japan
D. Sornette, Nice, France, and Los Angeles, CA, USA
S. Theisen, Golm, Germany
W. Weise, Garching, Germany
J. Wess, München, Germany
J. Zittartz, Köln, Germany

The Lecture Notes in Physics

The series Lecture Notes in Physics (LNP), founded in 1969, reports new developments in physics research and teaching – quickly and informally, but with a high quality and the explicit aim to summarize and communicate current knowledge in an accessible way. Books published in this series are conceived as bridging material between advanced graduate textbooks and the forefront of research to serve the following purposes:

- to be a compact and modern up-to-date source of reference on a well-defined topic;
- to serve as an accessible introduction to the field to postgraduate students and nonspecialist researchers from related areas;
- to be a source of advanced teaching material for specialized seminars, courses and schools.

Both monographs and multi-author volumes will be considered for publication. Edited volumes should, however, consist of a very limited number of contributions only. Proceedings will not be considered for LNP.

Volumes published in LNP are disseminated both in print and in electronic formats, the electronic archive is available at springerlink.com. The series content is indexed, abstracted and referenced by many abstracting and information services, bibliographic networks, subscription agencies, library networks, and consortia.

Proposals should be sent to a member of the Editorial Board, or directly to the managing editor at Springer:

Dr. Christian Caron
Springer Heidelberg
Physics Editorial Department I
Tiergartenstrasse 17
69121 Heidelberg/Germany
christian.caron@springer-sbm.com

M.C. Miguel M. Rubi (Eds.)

Jamming, Yielding, and Irreversible Deformation in Condensed Matter

Editors

M. Carmen Miguel
Miguel Rubi
Departament de Física Fonamental
Facultat de Física
Diagonal 647
08028 Barcelona
Spain
E-mail: carmen.miguel@ub.edu
mrubi@ub.edu

M.C. Miguel and M. Rubi, *Jamming, Yielding, and Irreversible Deformation*
in *Condensed Matter*, Lect. Notes Phys. 688 (Springer, Berlin Heidelberg 2006),
DOI 10.1007/b11581000

Library of Congress Control Number: 2005937150

ISSN 0075-8450

ISBN-10 3-540-30028-7 Springer Berlin Heidelberg New York

ISBN-13 978-3-540-30028-1 Springer Berlin Heidelberg New York

This work is subject to copyright. All rights are reserved, whether the whole or part of the material is concerned, specifically the rights of translation, reprinting, reuse of illustrations, recitation, broadcasting, reproduction on microfilm or in any other way, and storage in data banks. Duplication of this publication or parts thereof is permitted only under the provisions of the German Copyright Law of September 9, 1965, in its current version, and permission for use must always be obtained from Springer. Violations are liable for prosecution under the German Copyright Law.

Springer is a part of Springer Science+Business Media
springer.com

© Springer-Verlag Berlin Heidelberg 2006

Printed in The Netherlands

The use of general descriptive names, registered names, trademarks, etc. in this publication does not imply, even in the absence of a specific statement, that such names are exempt from the relevant protective laws and regulations and therefore free for general use.

Typesetting: by the authors and TechBooks using a Springer L^AT_EX macro package

Printed on acid-free paper SPIN: 11581000 54/TechBooks 5 4 3 2 1 0

Preface

This volume gathers a number of selected contributions from the XIX Sitges Conference on “Jamming, Yielding, and Irreversible Deformation in Condensed Matter”, held at Sitges (Barcelona, Spain) from 14–18 June, 2004. The contributions collected in this volume provide a general overview of the “state of the art”, and of the recent developments, in the fields of material yield and irreversible deformation in different physical systems, which are of great interest within the realm of Condensed Matter Physics.

The Conference was sponsored by several institutions that generously provided financial support: Ministerio de Educación y Ciencia of the Spanish Government, AGAUR of the Generalitat de Catalunya, Universitat de Barcelona, and the Centre Especial de Recerca (CER) *Física de Sistemes Complexos*. As in former editions of the Conference, the city of Sitges allowed us to use the beautiful Palau Maricel as the lecture hall. We thank them for their kind hospitality. We are also very grateful to all those who collaborated in organizing the event: M. Naspreda, A. Pérez-Madrid, R. Pastor-Satorras, and S. Zapperi.

Finally, we wish to express our gratitude to all the speakers and participants in the Conference, who contributed with high scientific level presentations, and created a very pleasant atmosphere.

Barcelona
April 2005

*M.-Carmen Miguel
Miguel Rubí*

Contents

Introduction	1
Yielding and Jamming of Dense Suspensions	
<i>M.E. Cates</i>	3
1 Introduction	3
2 Arrest in Colloidal Fluids	4
2.1 Mode Coupling Theory (MCT)	5
3 Yield and Flow of Glasses: Shear Thinning	6
3.1 A Microscopic Approach	6
3.2 Attractive Interactions	9
3.3 Schematic MCT Models	10
4 Shear Thickening and Jamming	11
4.1 Shear Thickening within MCT	11
4.2 Dilatancy and Granulation	13
4.3 Glassy versus Hydrodynamic Thickening	15
5 Static versus Dynamic Yield Stress	15
5.1 Viscosity Bifurcation	16
6 Rheological Instability and Chaos	17
7 Conclusion	18
References	19
Thermal Noise Properties of Two Aging Materials	
<i>L. Bellon, L. Buisson, M. Ciccotti, S. Ciliberto, F. Douarche</i>	23
1 Introduction	23
2 Dielectric Noise in a Polymer Glass	25
2.1 Experimental Setup	25
2.2 Response and Noise Measurements	27
2.3 Statistical Analysis of the Noise	31
2.4 Influence of the Quench Speed	33
2.5 T_{eff} after a Slow Quench	34
3 Mechanical Measurements on a Polycarbonate Cantilever	35
3.1 FDT in a Mechanical Oscillator	36
3.2 Experimental Apparatus	38
3.3 Experimental Results	39
4 Thermal Noise in a Colloidal Glass	40

VIII Contents

4.1	Experimental Setup	41
4.2	Electric Noise Measurements in Laponite	42
4.3	Influence of Concentration	45
4.4	Mechanical Noise on Laponite	45
5	Discussion and Conclusions	46
	References	50

Jamming in Dense Granular Media

<i>A. Coniglio, A. Fierro, A. de Candia, M. Nicodemi,</i>		
<i>M. Tarzia, M. Pica Ciamarra</i>		
		53
1	Introduction	53
2	Statistical Mechanics of Dense Granular Materials	55
3	Monodisperse Hard Sphere Model for Granular Materials	56
4	Stationary States and Time Averages	57
5	Ensemble Averages	59
6	Mean Field Solution in the Bethe-Peierls Approximation	60
7	Hard Spheres with an Internal Degree of Freedom	62
8	Conclusions	66
	References	67

**Rheological Aspects of the Solid-Liquid Transition
in Jammed Systems**

<i>P. Coussot</i>		
		69
1	Introduction	69
2	The Usual Concept of Yield Stress Fluids	70
	2.1 Yielding	70
	2.2 Thixotropy	72
	2.3 Flow Characteristics of Simple Yield Stress Fluids	73
3	Rheological Behavior of Jammed Systems from Local Rheometry	76
	3.1 Flow Characteristics at the Solid-liquid Transition and Shear-banding	76
	3.2 Consequences in Rheometry	79
	3.3 Extreme Shear Localization	80
4	The Solid-liquid Transition in Jammed Systems: A Dynamic Phenomenon	83
	4.1 Yielding and Thixotropy	83
	4.2 From Plasticity to Liquid Flow with Increase in Degree of Jamming	86
5	Conclusion	88
	References	88

Dynamics of Disordered Elastic Systems

<i>T. Giamarchi, A.B. Kolton, A. Rosso</i>		
		91
1	Introduction	91
2	Basic Concepts	93

3 Creep, Phenomenology 96
 4 Around Four Dimensions 98
 5 Low Dimensional Situation: Domain Walls 101
 6 Conclusions and Open Questions 106
 References 107

Edge Contamination Effects in the Dynamics of Vortex Matter in Superconductors: Memory Effects and Excess Flux-flow Noise

G. Jung, Y. Paltiel, E. Zeldov, Y. Myasoedov, M.L. Rappaport, M.J. Higgins, S. Bhattacharya 109

1 Introduction: Vortex Matter 110
 2 Edge Contamination 111
 2.1 Critical Current in the Edge Contamination Model 112
 2.2 Strip and Corbino Configuration 113
 3 Memory Effects, Dynamical Instabilities and Edge Contamination . 115
 4 Low Frequency Noise 118
 4.1 Simplified Model of the Noise 119
 4.2 Experimental Results 120
 4.3 Velocity vs. Density Fluctuations 123
 5 Conclusions 125
 References 126

Out-of-equilibrium Relaxation of a Time-dependent Effective Temperature

A. Lemaître 129

1 Assumptions and Constitutive Equations 129
 2 Out-of-equilibrium Relaxation 131
 3 Conclusion 135
 References 136

Depinning and Plasticity of Driven Disordered Lattices

M.C. Marchetti 137

1 Introduction 137
 2 Depinning of Noninteracting Particles 139
 3 Depinning of an Extended Medium 142
 3.1 Elastic Model 143
 3.2 Viscoelastic Model 144
 3.3 Viscoelastic Coupling as an Effective Description of Topological Defects 145
 4 Mean-field Solution 147
 4.1 Mean-field Theory for Viscous Model: $K = 0, \eta \neq 0$ 148
 4.2 Mean-field Theory for VE Model: $K \neq 0$ and $\eta \neq 0$ 150
 5 Relationship to Other Models and to Experiments 152
 References 155

**Mixing, Ergodicity and the Fluctuation-Dissipation Theorem
in Complex Systems**

M.H. Vainstein, I.V.L. Costa, F.A. Oliveira 159

1 Introduction 159

2 Diffusion 161

3 Reaction Rates 164

4 Complex Systems have Memory 166

5 Random Walk 168

6 Noise 170

7 Reversibility and Correlation Functions 171

8 Mixing, Ergodicity, and the Fluctuation-Dissipation Theorem 174

9 Ballistic Motion 176

10 Shape of Things to Come 178

11 Spatio-temporal Conjecture for Disordered System 179

12 Conclusion 179

References 181

**Jamming and Yielding of Dislocations: from Crystal
Plasticity to Superconducting Vortex Flow**

S. Zapperi, M.C. Miguel, P. Moretti, M. Zaiser 189

1 Introduction 189

2 Dislocations 191

 2.1 Crystal Dislocations 191

 2.2 Vortex Lattice 191

3 Experimental Background 192

 3.1 Acoustic Emission and Dislocation Avalanches 192

 3.2 Andrade Creep 193

 3.3 Solid Solution Hardening 193

 3.4 Plasticity in Vortex Matter 194

4 Jamming and Yielding in Crystal Plasticity 194

 4.1 Two Dimensional Model of Interacting Dislocations 194

 4.2 Dislocation Jamming and Andrade Creep 195

 4.3 Dislocation Avalanches 196

5 Plastic Yielding in the Vortex Lattice 197

6 Depinning of Dislocation Systems 199

 6.1 Isolated Dislocations 199

 6.2 Pileup and Low Angle Grain Boundaries 200

 6.3 Zener Pinning in Grain Growth 201

7 Conclusions 203

References 203

Index 207

List of Contributors

S. Bhattacharya

NEC Research Institute
Princeton, New Jersey 08540, USA
and
Tata Institute of Fundamental
Research
Mumbai-400005, India

L. Bellon

Ecole Normale Supérieure de Lyon
Laboratoire de Physique, C.N.R.S.
UMR5672
46, Allée d'Italie
69364 Lyon Cedex 07, France

L. Buisson

Ecole Normale Supérieure de Lyon
Laboratoire de Physique, C.N.R.S.
UMR5672
46, Allée d'Italie
69364 Lyon Cedex 07, France

M. E. Cates

University of Edinburgh
School of Physics, JCMB King's
Buildings
Mayfield Road
Edinburgh EH9 3JZ, Scotland

M. Ciccotti

Ecole Normale Supérieure de Lyon
Laboratoire de Physique, C.N.R.S.
UMR5672
46, Allée d'Italie
69364 Lyon Cedex 07, France

S. Ciliberto

Ecole Normale Supérieure de Lyon
Laboratoire de Physique, C.N.R.S.
UMR5672
46, Allée d'Italie
69364 Lyon Cedex 07, France

A. Coniglio

Università di Napoli "Federico II"
Dipartimento di Fisica
INFN
Coherentia and Unità di Napoli
Via Cinthia
Napoli, I-80126, Italy

I.V.L. Costa

University of Brasília, Institute of
Physics and International Center of
Condensed Matter Physics
CP 04513, 70919-970, Brasília-DF
Brazil

P. Coussot

Institut Navier
LMSGC
Champs sur Marne, France

A. de Candia

Università di Napoli "Federico II"
Dipartimento di Fisica
INFN Coherentia and Unità di
Napoli
Via Cinthia
Napoli, I-80126, Italy

F. Douarche

Ecole Normale Supérieure de Lyon
Laboratoire de Physique, C.N.R.S.
UMR5672
46, Allée d'Italie
69364 Lyon Cedex 07, France

A. Fierro

Università di Napoli "Federico II"
Dipartimento di Fisica
INFN
Coherencia and Unità di Napoli
Via Cinthia
Napoli, I-80126, Italy

T. Giamarchi

University of Geneva
DPMC
24 Quai Ernest Ansermet
1211 Geneva, Switzerland

M. J. Higgins

NEC Research Institute
Princeton
New Jersey 08540, USA

G. Jung

Ben Gurion University of the Negev
Department of Physics
Beer-Sheva 84105, Israel
and
Weizmann Institute of Science
Department of
Condensed Matter Physics
Rehovot 76100, Israel

A.B. Kolton

University of Geneva, DPMC
24 Quai Ernest Ansermet
1211 Geneva, Switzerland

A. Lemaître

University of California
Department of Physics
Santa Barbara, California 93106
USA

M.C. Marchetti

Syracuse University
Physics Department
Syracuse, NY 13244, USA

M.C. Miguel

Universitat de Barcelona
Departament de Física Fonamental
Diagonal 647
E-08028, Barcelona, Spain

P. Moretti

University of Edinburgh
Center for Materials Science and
Engineering
King's Buildings
Sanderson Building
Edinburgh EH93JL, UK

Y. Myasoedov

Weizmann Institute of Science
Department of Condensed Matter
Physics
Rehovot 76100, Israel

M. Nicodemi

Università di Napoli "Federico II"
Dipartimento di Fisica
INFN
Coherencia and Unità di Napoli
Via Cinthia
Napoli, I-80126, Italy

F.A. Oliveira

University of Brasília
Institute of Physics
and
International Center of Condensed
Matter Physics
CP 04513, 70919-970, Brasília-DF
Brazil

Y. Paltiel

Weizmann Institute of Science
Department of
Condensed Matter Physics
Rehovot 76100, Israel
and
Electro-Optics Division
Soreq NRC
Yavne 81800, Israel

M. Pica Ciamarra

Università di Napoli “Federico II”
Dipartimento di Fisica
INFN
Coherencia and Unità di Napoli
Via Cinthia
Napoli, I-80126, Italy

M. L. Rappaport

Weizmann Institute of Science
Department of
Condensed Matter Physics
Rehovot 76100, Israel

A. Rosso

Université Paris-Sud
Laboratoire de Physique
Théorique
et Modèles Statistiques Bât. 100
91405 Orsay Cedex, France

M. Tarzia

Università di Napoli “Federico II”
Dipartimento di Fisica
INFN
Coherencia and Unità di Napoli
Via Cinthia
Napoli, I-80126, Italy

M. H. Vainstein

University of Brasília
Institute of Physics
and
International
Center of Condensed Matter Physics
CP 04513, 70919-970, Brasília-DF
Brazil

M. Zaiser

University of Edinburgh
Center for Materials
Science and Engineering
King’s Buildings
Sanderson Building
Edinburgh EH93JL
UK

S. Zapperi

Università “La Sapienza”
Dipartimento di Fisica
INFN UdR Roma 1 and SMC
P.le A. Moro 2
00185 Roma, Italy

E. Zeldov

Weizmann Institute of Science
Department of
Condensed Matter Physics
Rehovot 76100, Israel

Introduction

A general jamming scenario has been recently proposed to understand the nonequilibrium behavior of a broad class of amorphous materials as diverse as colloidal suspensions, emulsions, foams, gels, polymeric melts, supercooled liquids, biological tissues, or granular matter which share common features near the so-called jamming transition. The dynamics of this wide class of physical systems is governed by the presence of kinematical constraints, induced by both interactions and geometry, which may be able to suppress their temporal relaxation and thus their ability to explore the space of configurations. On the other hand, they flow like a viscous fluid above the so-called yield stress value. Shear yielding is thus another feature they have in common, together with other characteristics of their intriguing rheology.

Under stress conditions, not only amorphous materials but also crystalline solids are able to display jamming and shear yielding, due to the interactions and spatial arrangement of their linear topological defects. The collective dynamics of these defects, known as dislocations, is responsible for the irreversible or plastic deformation of most crystals, including ordered self-assembled structures formed by various materials like synthetic nanocrystals, magnetic colloids, charged particles in Coulomb crystals, proteins, or vortices in type II superconductors. Dislocations are at the origin of important phenomena in crystalline materials such as strain hardening or fatigue. Moreover, the slow and heterogeneous dynamics, the time laws of creep, and the stress-strain relations observed in some plastically deforming crystals also resemble the time-dependent rheology and flow curves reported for soft amorphous materials.

More generally, elastic manifolds driven by an external force can also undergo a dynamic phase transition from a blocked to a moving phase due to the presence of quenched disorder. This general process is usually referred to as depinning transition. If pinning forces are sufficiently strong, topological defects proliferate disrupting the topological order of the manifold and giving rise to plastic flow. The current theoretical understanding of plastic depinning and plastic flow under these circumstances is by no means complete. Nevertheless, some of the characteristic features of this nonequilibrium transition, for instance, scaling properties, slow time relaxation, and non-trivial steady-state force-velocity curves, resemble those observed in the creep dynamics

around the jamming threshold, despite the absence of quenched disorder in the latter case.

Motivated by the previous considerations, in the XIX Sitges Conference we gathered several leading experts in the fields of jamming, irreversible deformation, and flow in Condensed Matter Physics. This book contains a number of selected contributions that will give the reader a general overview of the most recent developments in the field. These contributions emphasize the similarities and differences of these kinetic processes in a diversity of physical systems, which allows to explore the jamming scenario in a much broader context to favor the interchange and cross-fertilization of ideas. We hope that this book will represent a comprehensive introduction to this emerging field and a useful tool towards the final aim of deepen the understanding of its open questions.

Yielding and Jamming of Dense Suspensions

M.E. Cates

School of Physics, University of Edinburgh, JCMB King's Buildings,
Mayfield Road, Edinburgh EH9 3JZ, Scotland

Recent progress in the understanding of yielding and jamming of colloids, based on extensions of the mode coupling theory (MCT) of glasses, is reviewed. This includes schematic extensions to shear-thickening fluids based on the ad-hoc introduction of a stress-dependent vertex in MCT. The possible distinction between dynamic and static yield stress, and its implications for shear-banding and other instabilities, is considered. Finally, what we know about systems where steady stress leads to unsteady flow or vice versa (“rheochaos”) is briefly summarised.

1 Introduction

The flow behaviour of very dense suspensions can, if the flow is steady, be characterized by the so-called flow curve, $\sigma(\dot{\gamma})$ which plots the shear stress σ as a function of shear rate $\dot{\gamma}$. (We assume a simple shearing flow with fluid velocity $\mathbf{u}(\mathbf{r}) = \dot{\gamma}y\hat{\mathbf{x}}$ in a cartesian coordinate system (x, y, z) ; z is the neutral or “vorticity” direction, and σ denotes the shear stress $\sigma_{xy} = \sigma_{yx}$.) Note that normal stresses can also be present [1, 2]; we do not discuss these here. Nor do we discuss the fluid response at finite frequency. But at the end of the paper (Sect. 6) we do consider materials where steady shear stress leads to unsteady shear rate or vice versa.

A Newtonian fluid has the linear flow curve $\sigma = \eta\dot{\gamma}$ with η its viscosity. More generally η is defined as the limiting value of the ratio $\sigma/\dot{\gamma}$ as $\dot{\gamma} \rightarrow 0$. Upward curvature of the flow curve is called shear thickening, downward curvature, shear thinning. If a yield stress σ_Y is present, the stress σ tends to a finite limit σ_Y as $\dot{\gamma} \rightarrow 0$; the viscosity η is then divergent. However, divergent viscosity does not imply a yield stress; counter-examples are “power-law fluids” with $\sigma \sim \dot{\gamma}^p$ with $0 < p < 1$. Below we will encounter flow curves that are nonmonotonic; these require special consideration (Sect. 4).

If a fluid is nonergodic, its properties can be age-dependent. However, there are good reasons to believe, in dense suspensions with relatively simple interactions at least, that nonergodicity is possible only for $\dot{\gamma} = 0$. Explicit consideration of aging effects has been given, for a simple model of “soft glassy materials” (foams, dense emulsions etc.) which confirms this statement [3, 4] (as does related work on spin-glass models, [5]). That model shows a range of

interesting flow behaviour, some of which might be useful in describing dense colloidal suspensions; however, we review here a different, complementary, approach [6–10]. This is based on mode coupling theory (MCT) and is limited in scope to address the steady state flow curve: it cannot, as yet, address either ageing or time-dependent flows. Care must be taken in such an approach when defining the yield stress σ_Y . We return to this in Sect. 5.

2 Arrest in Colloidal Fluids

Colloidal fluids can be studied by light scattering [11,12]. A key observable is the dynamic structure factor $S(q, t_1 - t_2) = \langle \rho(\mathbf{q}, t_1) \rho(-\mathbf{q}, t_2) \rangle / N$ which includes the static one, $S(q) = S(q, 0)$. Here $\rho(\mathbf{r}, t) = \sum_i \delta(\mathbf{r}_i(t) - \mathbf{r}) - N/V$; this is the real space particle density (with the mean value subtracted), and $\rho(\mathbf{q}, t)$ is its Fourier transform. For particles of radius a with short-range repulsions, $S(q)$ exhibits a peak at a value q^* with $q^*a = \mathcal{O}(1)$. The dynamic structure factor $S(q, t)$, at any q , decays monotonically from $S(q)$ as t increases. In an ergodic colloidal fluid, $S(q, t)$ decays to zero eventually: all particles can move, and the density fluctuations have a finite correlation time. In an arrested state, which is nonergodic, this is not true. Instead the limit $S(q, \infty)/S(q) = f(q)$ defines the *nonergodicity parameter*. The presence of nonzero $f(q)$ signifies frozen-in density fluctuations. Although $f(q)$ is strongly wavevector-dependent, it is common to quote only $f(q^*)$ [13].

The above formulas assume time-translation invariance; nonergodic systems can violate this, in which case $S(q, t_1 - t_2)$ as defined above must be written $S(q, t_1, t_2)$ with two time arguments. Also note that, in the real world, the idea that $S(q, t)$ remains finite forever could be an idealisation. However, it is close enough to reality, on the experimental timescales relevant for dense colloids, to be useful: the idealisation of a glass transition is one we accept in this paper. The same applies to (closely related) concepts such as the yield stress [14]; it is possible that in real fluids this represents a sharp kink rather than an actual discontinuity in the flow curve. Note that the conceptual validity of these idealisations is less secure for colloids with strong short range attractions than for purely hard-sphere colloids [15].

In many colloidal materials the effective interparticle interaction $u(r)$ comprises a hard sphere repulsion, operative at separation $2a$, perhaps combined with an attraction at larger distance. (For simplicity one can imagine a square well potential of depth ϵ and range $a\delta$, with $\delta < 1$ typically.) Colloidal fluids of this type are found to undergo nonergodicity transitions into two different broad classes of arrested nonequilibrium states. One is the colloidal glass, in which arrest is caused by the imprisonment of each particle in a cage of neighbours. This occurs even for $\epsilon = 0$ (i.e. hard spheres) at volume fractions above about $\phi \equiv 4\pi a^3 N/3V \simeq 0.58$. The nonergodicity parameter for the colloidal glass obeys $f(q^*) \simeq 0.8$. The second arrested state is called the colloidal gel. Unlike the repulsive glass, the arrest here is driven by attractive

interactions, resulting in a bonded, network-type structure. Such gels can be unambiguously found, for short range attractions, whenever $\beta\epsilon \gtrsim 5 - 10$. (Here $\beta \equiv 1/k_B T$.) Hence it is not necessary that the local bonds are individually irreversible (this happens, effectively, at $\beta\epsilon \gtrsim 15 - 20$); and when they are not, the arrest is a collective, not just a local, phenomenon. It is found experimentally that for colloidal gels, $f(q^*) \gtrsim 0.9$, which is distinctly different from the colloidal glass.

2.1 Mode Coupling Theory (MCT)

One widely used form of the theory [16] is based on projection methods. These have technical advantages and are used in our own work on MCT under shear [6, 8]. However, to many physicists these methods are somewhat unfamiliar. Fortunately, at least for the static case and in a stripped-down version (see e.g. [17, 18]) the resulting equations can alternatively be viewed as a fairly standard one-loop selfconsistent approximation to a dynamical theory for the particle density field. We present this approach briefly here.

We take $\beta = 1$, bare particle diffusivities $D_0 = 1$, and start from the overdamped Langevin equations $\dot{\mathbf{r}}_i = \mathbf{F}_i + \mathbf{f}_i$ for independent particles subject to external forces \mathbf{F}_i and random forces \mathbf{f}_i . One proceeds by a standard route to a Smoluchowski equation $\dot{\Psi} = \Omega\Psi$ for the N -particle distribution function Ψ , with evolution operator $\Omega = \sum_i \nabla_i \cdot (\nabla_i - \mathbf{F}_i)$. Now take the forces \mathbf{F}_i to originate (via $\mathbf{F}_i = -\nabla_i H$) from an interaction Hamiltonian

$$H = -\frac{1}{2} \int d^3\mathbf{r} d^3\mathbf{r}' \rho(\mathbf{r}) \rho(\mathbf{r}') c(|\mathbf{r} - \mathbf{r}'|) \quad (1)$$

where $Nc(q) = V[1 - S(q)^{-1}]$. This is a harmonic expansion in density fluctuations; $c(q)$ is the direct correlation function, and this form ensures that $S(q)$ is recovered in equilibrium. We neglect solvent-mediated dynamic forces (hydrodynamic couplings). In principle these couplings mean that the noise in the Langevin equation should be correlated between particles, in contrast to the independent white noise assumed here. In addition we neglect anharmonic terms in H ; to regain the correct higher order density correlators (beyond the two point correlator $S(q)$) in equilibrium, these terms would have to be put back. (Our ad-hoc introduction of a stress-dependent vertex in Sect. 4 below can be viewed as a poor man's way of dealing with such omitted terms, in their effect on arrest.)

From the Smoluchowski equation (or the corresponding nonlinear Langevin equation for the density $\rho(\mathbf{r})$ [7, 17]), one can derive a hierarchy of equations of motion for correlators such as $S(q, t)$, more conveniently expressed via $\Phi(q, t) \equiv S(q, t)/S(q)$. Factoring arbitrarily the four-point correlators that arise in this hierarchy into products of two Φ 's, one obtains a closed equation of motion for the two point correlator

$$\dot{\Phi}(q, t) + \Gamma(q) \left[\Phi(q, t) + \int_0^t m(q, t - t') \dot{\Phi}(q, t') dt' \right] = 0 \quad (2)$$

where $\Gamma(q) = q^2/S(q)$ is an initial decay rate, and the memory function obeys

$$m(\mathbf{q}, t) = \sum_{\mathbf{k}} V_{\mathbf{q},\mathbf{k}} \Phi(\mathbf{k}, t) \Phi(\mathbf{k} - \mathbf{q}, t) \quad (3)$$

with the vertex

$$V_{\mathbf{q},\mathbf{k}} = \frac{N}{2V^2 q^4} S(q) S(k) S(|\mathbf{k} - \mathbf{q}|) [\mathbf{q} \cdot \mathbf{k} c(k) + \mathbf{q} \cdot (\mathbf{k} - \mathbf{q}) c(|\mathbf{k} - \mathbf{q}|)]^2 \quad (4)$$

Equations 2–4 are slightly simpler than the ones used in molecular glasses because of the justified neglect of inertial terms. They fully specify MCT as it is usually applied in colloidal systems [16].

The MCT equations exhibit a bifurcation that corresponds to a sudden arrest transition, upon smooth variation of either the density ϕ or any interaction parameters that control $c(q)$ (equivalently, $S(q)$). Here the nonergodicity parameters $f(q)$, suddenly jump (for all q at once) from zero to nonzero values. Near this (on the ergodic side, which is always the direction MCT approaches from), $\Phi(q, t)$ develops interesting behaviour. Viewed as a function of time, it decays onto a plateau of height $f(q)$, stays there for a long time, and then finally decays again at very late times. The two decays are called β and α respectively. Upon crossing the bifurcation, their relaxation times diverge smoothly with the parameters; hence $f(q) \equiv S(q, \infty)/S(q)$ jumps discontinuously from zero to a finite value.

3 Yield and Flow of Glasses: Shear Thinning

3.1 A Microscopic Approach

In [6], a theory is given, along MCT lines, of colloidal suspensions under flow. The work studies the effect of imposed shear flow either on a glass, or on a fluid phase very near the glass transition. Although intended initially for repulsive glasses, it also offers interesting predictions for attraction-driven ones [19]; see Sect. 3.2 below. Note also that a closely related theory has been offered by Miyazaki and Reichman [20]. However, unlike the work of [6], which uses a projection operator methodology, [20] assumes that a fluctuation-dissipation relation between correlators and response functions, valid in equilibrium and used en-route to deriving (2), continues to hold under shear. The results have qualitative similarities to [6] but differ in many important details.

Close to a glass transition, the bare diffusion time $\tau_0 = a^2/D_0$ is small compared to the “renormalized” one $\tau = a^2/D$, which in fact diverges (enslaved to the α relaxation time) at the transition. For $\dot{\gamma}\tau_0 \ll 1 \leq \dot{\gamma}\tau$, the details of the local dynamics should be inessential and universal features related to glass formation should dominate. Note, however, that by continuing

to use a quadratic H (1), we will assume that, even under shear, the system remains “close to equilibrium” in the sense that the density fluctuations that build up remain small enough for a harmonic approximation to be useful. This may well be inadequate for hard spheres, and its breakdown could be linked to the physics of jamming (Sect. 4).

We again take $\beta = 1$, $D_0 = 1$, and start from the Langevin equations $\dot{\mathbf{r}}_i = \mathbf{u} + \mathbf{F}_i + \mathbf{f}_i$, where an imposed flow velocity $\mathbf{u}(\mathbf{r}) = \dot{\gamma}y\hat{\mathbf{x}}$ has been added. The Smoluchowski equation $\dot{\Psi} = \Omega\Psi$ is unchanged but the evolution operator is now $\Omega = \sum_i \nabla_i \cdot (\nabla_i - \mathbf{F}_i - \mathbf{u}(\mathbf{r}_i))$. (For related earlier work see [21, 22].) So far, the adaption to deal with shearing is fairly trivial. The next stages are not. We assume an initial equilibrium state with $\Psi(t = 0) \propto \exp[-H]$, and switch on shearing at $t = 0+$. We define an *advected correlator*

$$\Phi(\mathbf{q}, t) = \langle \rho(\mathbf{q}, 0) \rho(-\mathbf{q}(t), t) \rangle / S(q)N \quad (5)$$

where $\mathbf{q}(t) = (q_x, q_y + q_x \dot{\gamma}t, q_z)$. This definition subtracts out the trivial part of the advection, which merely transports density fluctuations from place to place. The nontrivial part comes from the effect of this transport on their time evolution; the main effect (see e.g. [22]) is to kill off fluctuations by moving their wavenumbers away from q^* where restoring forces are weakest. Hence the fluctuations feel a stronger restoring force coming from H , and decay away more strongly. This feeds back, through the nonlinear term, onto the other fluctuations, including ones with \mathbf{q} along the neutral direction, z , for which the trivial advection is absent.

There follow a series of MCT-like manipulations which differ from those of the standard approach because they explicitly deal with the switching on of the flow at $t = 0+$. We integrate through the transient response to obtain the steady state correlators, under shear, as $t \rightarrow \infty$. (There is no integration through transients in standard MCT; one works directly with steady-state quantities.) Despite all this, the structure of the resulting equations is remarkably similar to (2, 3) [6]:

$$\dot{\Phi}(\mathbf{q}, t) + \Gamma(\mathbf{q}, t) \left[\Phi(\mathbf{q}, t) + \int_0^t m(\mathbf{q}, t, t') \dot{\Phi}(\mathbf{q}, t') dt' \right] = 0. \quad (6)$$

(6) involves a time dependent, anisotropic “initial decay rate”:

$$\Gamma(\mathbf{q}, t)S(q) = q^2 + q_x q_y \dot{\gamma}t + (q_x q_y \dot{\gamma}t + q_x^2 \dot{\gamma}^2 t^2)S(q) - q_x q_y \dot{\gamma}S'(q)/q. \quad (7)$$

The memory kernel is no longer a function of the time interval $t - t'$ but depends on both arguments separately

$$m(\mathbf{q}, t, t') = \sum_{\mathbf{k}} V(\mathbf{q}, \mathbf{k}, t, t') \Phi(\mathbf{k}, t - t') \Phi(\mathbf{k} - \mathbf{q}, t - t') \quad (8)$$

through a time-dependent vertex V which was published in [9] and whose detailed derivation will be given in [23]. Using a nonequilibrium Kubo-type

relationship [6] one can also obtain an expression for the steady state viscosity $\eta = \sigma(\dot{\gamma})/\dot{\gamma}$ where $\sigma(\dot{\gamma})$ is the shear stress as a function of shear rate. The viscosity is expressed as an integral

$$\eta = \int_0^\infty dt \sum_{\mathbf{k}} V_\eta(\mathbf{k}, t) \Phi^2(\mathbf{k}, t) \quad (9)$$

where the function V_η may be found in [6].

The calculations reviewed above give some useful insights. First, as promised earlier, even an infinitesimal steady shear rate $\dot{\gamma}$ restores ergodicity for all wavevectors (including ones that do not undergo direct advection). It is the absence of ergodicity that normally prevents MCT-like theories being used inside the glass phase, at $T < T_g$ or $\phi > \phi_g$. Here we may use the theory in that region, so long as the shear rate is finite. This gives a new approach to the static glass in which a small shear rate is used as a regularising parameter. However, it also means we have to be careful in interpreting flow curves. In particular, in this approach, the yield stress $\sigma_Y = \sigma(\dot{\gamma} \rightarrow 0+)$ is defined dynamically: it is the limiting stress found in a series of measurements at successively smaller flow rate $\dot{\gamma}$, where each of these measurements has been allowed to achieve steady state after decay of all transients. The latter requirement may not be practically achievable since the equilibration time could diverge at small $\dot{\gamma}$: certainly one would expect to have to wait at least for times t such that $\dot{\gamma}t \gtrsim 1$. But unless the flow curve has unexpected structure at small shear rates, the required extrapolation can presumably be made. Note that even if all this is true, alternative definitions of the yield stress are possible; we return to this issue in Sect. 5.

In the liquid phase ($\phi < \phi_g$) the flow curve $\sigma(\dot{\gamma})$ that results from these calculations shows shear thinning at $\dot{\gamma}\tau \gtrsim 1$, which is when the shearing becomes significant on the timescale of the slow relaxations. This is basically as expected. Less obviously, throughout the glass, one finds that σ_Y is nonzero, whereas the viscosity is finite throughout the liquid phase. There is no intermediate power law fluid regime, in contrast to trap-based models of soft glasses [3]. At the glass transition $\phi = \phi_g$, the yield stress jumps discontinuously from zero to a nonzero value, σ_Y^c . The existence of a yield stress seems to be in line with most experimental data on the flow of colloidal glasses [24].

To calculate actual values for quantities like σ_Y^c , one must invoke further technical approximations to the sheared MCT calculation, beyond those already enumerated above. The best current estimates come from the ISHSM or “isotropically sheared hard sphere model” [8] in which the effect of shear advection on density fluctuations is isotropised (whereas in reality it should depend strongly on the direction in q space). This gives, for example, $\sigma_Y^c = 0.75k_B T/a^3$ for hard spheres of radius a . The experimental data [24] suggests a value perhaps twice as high as this; however, the theory predicts a very rapid rise in σ_Y beyond the transition so this could be the result of the experiments lying just a percent or so, in volume fraction, beyond the true

glass point. ISHSM predicts a power law exponent 0.152 for the growth of $\sigma - \sigma_Y$ at small $\dot{\gamma}$, and a square root growth of σ_Y within the glass phase [8]. These two predictions are also closely mimicked by an even simpler schematic model called $F_{12}^{\dot{\gamma}}$, as outlined in Sect. 3.3. Note the shape of the flow curve in these models: in the fluid, the curve always has downward curvature (shear thinning), at least for small and intermediate $\dot{\gamma}$. In the glass, the curve is similar, but offset vertically by σ_Y . This still corresponds to shear thinning. In neither case is the curve nonmonotonic.

3.2 Attractive Interactions

The ISHSM refers to hard-sphere colloids only. However, since the interaction between colloids enters only via the static structure factor $S(q)$, the same methods can be used for attracting colloids also. It is simplest to combine these with a virial-type analysis of the adhesive hard sphere system (AHSS) [25]; the results have been presented in [19] and are reviewed briefly here.

The scaling of the critical yield stress σ_Y^c with the attraction range δ can, for small δ , be estimated from a virial expansion of S_q for the AHSS: one finds $1 - S_q^{-1} \rightarrow 6A\phi\delta \sin(2qa)/(qa)$, where $A = \exp \epsilon - 1$. Inserting this expression into the ISHSM formulae [6, 19], one can take the low density limit $\phi \rightarrow 0$ and $A \rightarrow \infty$ with $\Gamma_v = 6\phi A^2 \delta / \pi^2$ held fixed. This leads to the asymptotic memory kernel [19]:

$$m_{\tilde{q}}(t) \rightarrow \frac{\Gamma_v}{2\tilde{q}^2} \int^{\tilde{k}_>} d^3 \tilde{k} \left(\frac{\tilde{\mathbf{q}} \cdot \tilde{\mathbf{k}}}{\tilde{q}\tilde{k}} \right)^2 \cos \left(\frac{\tilde{k}(t) - \tilde{k}}{\delta/2} \right) \Phi_{\tilde{k}}(t) \Phi_{|\tilde{\mathbf{q}} - \tilde{\mathbf{k}}|}. \quad (10)$$

The corresponding expression for the steady state shear stress becomes [19]:

$$\sigma \rightarrow \dot{\gamma} \frac{k_B T}{a^3} \frac{\phi \Gamma_v}{5\delta^2} \int_0^\infty dt \int_0^{\tilde{k}_>} d\tilde{k} \tilde{k}^2 \cos \left(\frac{\tilde{k}(t) - \tilde{k}}{\delta/2} \right) \Phi_{\tilde{k}}^2(t). \quad (11)$$

Here, the limit $\delta \rightarrow 0$ applies, and the rescaled wavenumbers $\tilde{q} = qa\delta$ and a cutoff $\tilde{k}_>$ were introduced; choosing $\tilde{k}_> \approx 3.68$ maps the AHSS virial results onto those of an attractive square well system with range δ [25].

These equations can be closed via (6) [6] for the normalized density correlation functions $\Phi_{\tilde{q}}(t)$ to find the nonlinear rheology close to the arrest transition (at $\Gamma_v^c = 1.42$) of attracting colloids. Although the low- ϕ approximation appears drastic, if shear is switched off in (10), the results for the arrest line at small δ agree qualitatively with those of [26] up to rather large ϕ [25, 27]. With shear present, the $\Phi_{\tilde{q}}(t)$ asymptotically obey a ‘‘yielding scaling law’’, $\Phi_{\tilde{q}}(t) \rightarrow \Phi_{\tilde{q}}^+(\hat{t})$ with $\hat{t} = t/\tau(\dot{\gamma})$ and $\tau(\dot{\gamma})$ a shear-rate dependent characteristic time. Making use also of a limiting closure relation [19], the yield stress σ_Y^c then follows from inserting $\Phi_{\tilde{q}}^+(\hat{t})$ into (11).

The expressions for the memory kernel and stress, (10, 11), contain a rapidly oscillating term $\cos(2(\tilde{k}(t) - \tilde{k})/\delta)$, from interference of the particle

density fluctuations within the narrow region of attraction. Without shear, constructive interference holds, and this factor is unity; the memory kernels describe bond-formation, and the correlator stays arrested at its glass value. Under shear, the advection of wavevectors produces rapid oscillations in this factor when δ is small. The interference is destroyed, causing a fast decay of the memory functions. The time scale $\tau(\dot{\gamma})$ needs to be found self-consistently [19]; it scales as $\tau(\dot{\gamma}) = c_a \delta / |\dot{\gamma}|$ where c_a is of order unity. In contrast, for repulsive interactions one has [6, 8] $\tau(\dot{\gamma}) = c_r / |\dot{\gamma}|$ with c_r of order unity.

Integrating (11), one obtains (with further constants $c'_{a,r}$) the scaling expressions $\sigma_Y^c = c'_a G_a \delta$ for AHSS, which differs by one power of the range parameter δ from the result, $\sigma_Y^c = c'_r G_r$, for hard spheres without attraction. Here $G_{a,r}$ are the corresponding shear moduli which, within MCT, have finite values on arrest, and whose scalings have been discussed elsewhere [25–29]. (For AHSS one has $G_a \sim kTa^{-3}\delta^{-2}$ whereas $G_r \simeq kTa^{-3}$ holds for hard spheres.)

The final scaling result for AHSS is thus $\sigma_Y^c \simeq G_a \delta \simeq kTa^{-3}\delta^{-1}$. This dependence of the yield stress on the attraction range leads to interesting scenarios in systems where both attraction and repulsion-driven arrest can be observed [30, 31]. Interpreting the ratio of yield stress to the elastic modulus as a yield strain $u_y = \sigma_Y^c / G$, the scaling dependence of yield stress on δ can easily be understood. The yield strain of an attraction-driven glass of order the relative range of the attraction δ : the solid is shear-melted as soon as particle bonds are broken. Because the yield strain is much smaller for a bonded glass than for a caged one, the nonlinear rheology should vary strongly between these two cases.

3.3 Schematic MCT Models

It has long been known that the key mathematical structure behind (2–4) can be captured by low-dimensional schematic models in which the full \mathbf{q} dependence is suppressed [16, 32]. In other words, one chooses a single mode, with a representative wavevector around the peak of the static structure factor, and writes mode coupling equations for this mode treated by itself. At a phenomenological level, one can capture the physics similarly even with shearing present (despite the more complicated vectorial structure that in reality this implies). Specifically one can define [6] the $F_{12}^{\dot{\gamma}}$ model – the sheared extension of a well known static model, F_{12} – via

$$\dot{\Phi}(t) + \Gamma \left[\Phi(t) + \int_0^t m(t-t') \dot{\Phi}(t') dt' \right] = 0 \quad (12)$$

with memory function (schematically incorporating shear)

$$m(t) = [v_1 \Phi(t) + v_2 \Phi^2(t)] / (1 + \dot{\gamma}^2 t^2). \quad (13)$$

The vertex parameters $v_{1,2}$ are smooth functions of the volume fraction ϕ (and any interactions). To calculate flow curves, etc., one also needs a schematic

form of (9); here we take the first moment of the correlator to fix the time scale for stress relaxation (which is, in suitable units, simply the viscosity):

$$\eta = \int_0^\infty \Phi(t) dt \quad (14)$$

Note that a different choice, e.g. with $\Phi(t)^2$ in this equation to closer resemble (9), would yield quite similar results. This simplest of schematic models gives very similar results to the ISHSM [8, 9].

4 Shear Thickening and Jamming

The calculations described above predict, generically, shear thinning behaviour: advection kills fluctuations, reducing the α relaxation time, which causes the system to flow more easily at higher stresses. However, in some colloidal systems, the reverse occurs. This is shear thickening, and gives a flow curve $\sigma(\dot{\gamma})$ with upward curvature. In extreme cases, an essentially vertical portion of the curve is reported [2, 33]. One interpretation of the latter scenario (called “discontinuous shear thickening”) is that the underlying flow curve is actually S-shaped. Since any part of the curve with negative slope is mechanically unstable (a small increase in the local shear rate would cause an acceleration with positive feedback). This allows a hysteresis cycle in which, at least according to the simplest models, discontinuous vertical jumps on the curve bypass the unstable section (see Fig. 1).

These jumps are analogous to first order phase transitions in thermodynamics and the corresponding phase-separation is called “shear banding”: slabs of material, with equal $\dot{\gamma}$ but unequal σ are stacked with layer normals along the neutral (z) direction [34]. (This orientation is called “transverse” shear banding.) Note that for shear thinning materials shear banding can also occur, but now with the “normal” orientation, which has slabs of equal σ and unequal $\dot{\gamma}$ stacked along y .

If this viewpoint of discontinuous shear thickening is adopted, there seems to be nothing to prevent the upper, re-entrant part of the curve from extending right back to the vertical axis (see Fig. 1) in which case there is zero steady-state flow within a certain interval of stress. The system has both an upper and a lower yield stress delimiting this region. (If it is nonergodic at rest, it could also have a regular yield stress on the lower part of the curve near the origin – we ignore this here.) This case has been called “full jamming” [4]. Although mostly a theoretical speculation, at least one experimental report of this kind of behaviour has appeared in the literature recently [35].

4.1 Shear Thickening within MCT

The above discussion suggests that shear thickening and full jamming might be viewed as a stress-induced glass transition of some sort [1]. If so, it is

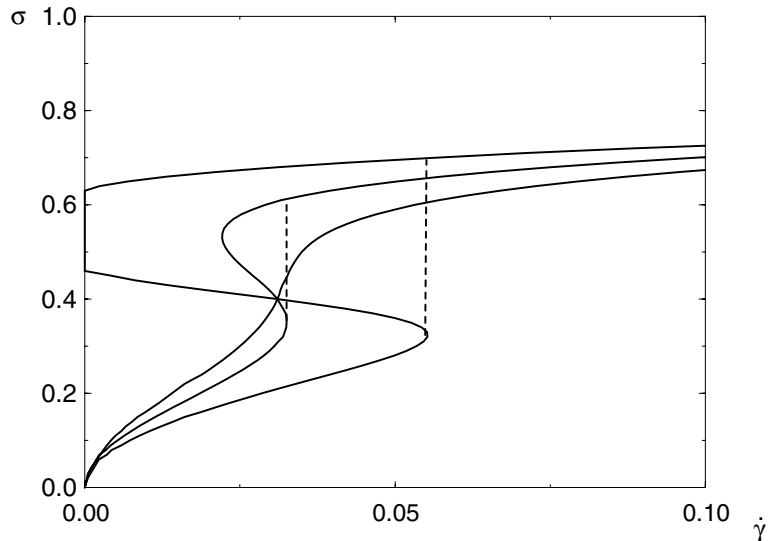


Fig. 1. Three possible flow curves for a shear thickening material. The monotonic curve corresponds to continuous shear thickening. The remaining two curves are S-shaped; one expects, on increasing the shear rate, the stress to jump from the lower to upper branch at (or before) the *vertical dashed* line shown in each case. One *curve* shows the full jamming scenario: the existence of an interval of stress, here between 0.45 and 0.63, within which the flow rate is zero, even in a system ergodic at rest (Stress and strain rate units are arbitrary)

natural to ask whether this idea can be accommodated within an MCT-like approach. Since the analysis of [6] gives only shear thinning, this is far from obvious. In particular, a stress-induced glass transition would require the vertex V to “see” the stress; this might require one to go beyond harmonic order in the density, that is, it might require improvement to (1). Indeed, since it is thought that jamming arises by the growth of chainlike arrangements of strong local compressive contacts [1], it is very reasonable to assume that correlators beyond second order in density should enter.

In [10] we develop a schematic model along the lines of (12–14) to address shear thickening (with, for simplicity, $v_2 = 0$). This is the $F_1^{\dot{\gamma}, \sigma}$ model

$$\dot{\Phi}(t) + \Gamma \left[\Phi(t) + \int_0^t m(t-t') \dot{\Phi}(t') dt' \right] = 0 \quad (15)$$

with memory function

$$m(t) = [v_0 + \alpha\sigma] \exp[-\dot{\gamma}t] \Phi(t) \quad (16)$$

and viscosity $\eta = \sigma/\dot{\gamma}$ obeying

$$\eta = \int_0^\infty \Phi(t) dt. \quad (17)$$

The memory function now schematically incorporates both the loss of memory by shearing and a stress-induced shift of the glass transition. (Without stress or shear, the latter occurs at $v_0 = 4$.) The choice of an exponential strain rate dependence is purely for algebraic convenience, whereas the form in (13) is closer to the one found in the full \mathbf{q} -dependent vertex under shear (see above and [6]). The choice of a linear dependence of the vertex on stress (rather than the quadratic one that would arise in a Taylor expansion about the quiescent state) can be viewed as a linearization about a finite stress chosen to lie close to the full jamming region: this, rather than the behaviour at very small stresses, is the interesting region of the model. In any case, the qualitative scenarios that emerge from (15–17) are relatively robust to the precise details of the model [10, 36].

This model results in a “full jamming” scenario as part of a wider range of rheological behaviour. Figure 2 shows three kinds of thickening behaviour, dependent on model parameters; v_0 is varied close to the quiescent glass transition, and for the chosen α there is a progression from a monotonic, continuously shear-thickening curve, via a nonmonotonic S-shaped curve, to a curve that extends right back to the vertical axis. For the largest values of the parameter v_o , in Fig. 2, there is therefore a range of stress for which the shear rate returns to zero: there is then no ergodic solution, and the jammed state is stable. This represents full jamming. Note that if, as seems likely, α depends on the details of interparticle interactions, then the evolution between these scenarios does too. This makes sense since one would certainly expect hard particles to be more “jammable” than soft ones.

The lower and upper endpoints σ_{c1} and σ_{c2} of the stable jammed state represent distinct jamming transitions. Their critical stresses obey

$$f_c [(v_o + \alpha\sigma_c) f_c - 2] = \sigma_c, \quad (18)$$

where f_c is given by the largest solution of $\frac{f_c}{1-f_c} = (v_o + \alpha\sigma_c) f_c^2$. Such transitions exist provided that both v_o and α are sufficiently large. Bertrand et al. [35] found that, for concentrations below a certain value, their samples showed ordinary thickening, whilst above this value the shear-induced solid was seen. The behaviour illustrated in Fig. 2 is reminiscent of this. Note that the re-fluidisation under increasing stress depends on α : if this is too large (for a given v_o) this refluidisation is not present.

4.2 Dilatancy and Granulation

Several variants of this model, all involving an ad-hoc stress dependence of the vertex, are possible [36]; the results are broadly similar to those outlined above.

The absence of refluidisation at large values of the “jammability” parameter α has interesting consequences. It is reminiscent of the dilatancy of dry powders: above a certain packing density (which seems to lie quite close

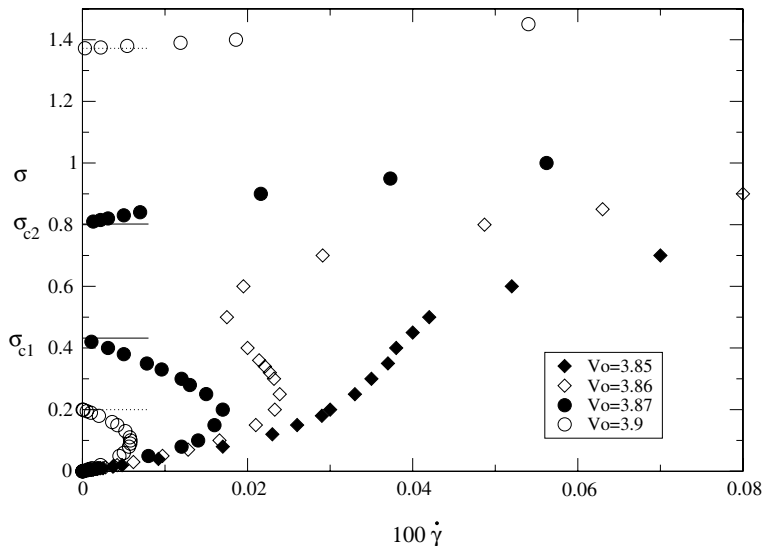


Fig. 2. Flow curves for $\alpha = 0.95$. For the two largest values of v_o , for a window in σ , the relaxation time has diverged. Analytic calculations of the limits of this window are indicated as horizontal lines near the stress axis. These values of the stress are σ_{c1} and σ_{c2} , as shown here for one of the parameter sets

to 0.58 for spherical particles [37]) these cannot flow without expansion of the sample. In dense suspensions, expansion is effectively prohibited by the presence of a fixed volume of solvent; therefore a suspension dense enough that it cannot flow without dilating will never refluidise, whatever the stress. (Brownian motion of course complicates the picture but this is included in the MCT approach.) In practice, we can expect such a suspension to undergo brittle fracture, in which the material cracks and air ingresses to create new interfaces with the solvent. (Such effects are clearly not handled within our schematic model.) The stress required to create large amounts of new surface is large but not off-scale for colloidal suspensions, and indeed a phenomenon very like this arises in the industrial process of “granulation”. In this process, a very dense suspension is converted by shear into discrete granular lumps which rest on each other under gravity but are essentially surrounded by air. It is possible that these lumps are themselves examples of full jamming, in which capillary forces are responsible for supplying the required stress.

It seems reasonable to assume that the jammability parameter α and the “glassiness” parameter v_o are both monotonically increasing functions of volume fraction ϕ . However, depending on the exact ϕ -dependence of each, various sequences of flow curve can emerge as ϕ is increased. An appealing one, which seems in tune with experimental data [35, 38, 39] is as follows:

Newtonian \rightarrow *continuous shear thickening* \rightarrow *discontinuous shear thickening* \rightarrow *full jamming* \rightarrow *yielding glass* \rightarrow *brittle glass*

where a brittle glass will “flow”, at high enough stresses, but only by fracture or granulation. This avenue will be explored further elsewhere [40].

4.3 Glassy versus Hydrodynamic Thickening

Shear thickening is widely reported (e.g. [2, 33, 41, 42]) and usually attributed to a buildup of hydrodynamic forces between clusters of particles [43, 44]. Our work suggests that, at least in some systems, this may not be the only mechanism at work. In particular, Fig. 2 admits shear thickening at Peclet numbers $\dot{\gamma}\tau_0 \sim 10^{-4}$, rather than values of order unity predicted by most theories of hydrodynamic clustering. Such theories do not so far appear to offer any natural explanation of the S shaped flow curve that appears to underly *discontinuous* shear thickening (see e.g. [45], and references therein). On the other hand, simulations of dense colloids do predict, for hard spheres in the absence of Brownian motion, a catastrophic jamming transition. In this transition, a network of close contacts propagates to infinity at *finite strain*, creating a solid [46]. To whatever extent full jamming is actually observed [35, 38], hydrodynamic theories cannot explain it. This is because hydrodynamic forces are dynamical in origin and therefore cannot be responsible for maintaining a purely static state of arrest. It is conceivable that a limit exists in which interparticle velocities and separations both vanish at late times in such a fashion that the resulting forces approach constant values. However, we do not find this particularly plausible.

Most existing hydrodynamic theories (rather than simulations [46]) of colloid rheology, by taking no account of the glass transition, predict that the zero shear viscosity diverges only at random close packing (volume fraction $\phi = 0.63$) [47]. This appears inconsistent with experimental observations where the viscosity divergence occurs instead at the colloidal glass transition ($\phi = \phi_g = 0.58$) [48]. Accordingly it is necessary to develop a new theory, as outlined in Sect. 3, to describe flow curves at $\phi > \phi_g$. The hypothesis of the work on colloidal jamming reported here is that the proximity of this transition also affects flow properties in a window of densities *below* ϕ_g , to the extent that one should treat hydrodynamic forces as a perturbation (which we neglect) to the dynamics of collective arrest, rather than vice versa.

5 Static versus Dynamic Yield Stress

Let us now return to an issue raised earlier, which is the definition adopted above for the yield stress σ_Y . It was emphasised that, within MCT or any other theory where one approaches the arrest transition from the fluid side,

the natural definition of σ_Y comes from considering a sequence of steady-state flows. Each flow has a smaller flow rate $\dot{\gamma}$ than the last, and if in the limit of the sequence, as $\dot{\gamma} \rightarrow 0+$, the steady-state stress remains finite, then the limiting stress is the yield stress. It is crucial to note that *every state in the sequence considered is flowing and hence ergodic*.

A quite different, static, definition of the yield stress (call this σ_y) is as follows. Consider a sample at rest. Allow it to reach thermal equilibrium as best it can (if it is aging, it may never quite make it). Now switch on a steady stress σ and see if, after relaxing to a steady state, the material has finite shear rate $\dot{\gamma}$ or not. If not, repeat the whole experiment at a slightly larger stress and find the largest such value for which there is no steady flow. This largest value is σ_y .

The distinction between static and dynamic yield stresses, and the relevance of this to systems undergoing a glass transition, is emphasised by Berthier [49]. At a qualitative level, the relation between σ_y and σ_Y is analogous to that between static and dynamic friction for a solid block on an inclined plane. Clearly, $\sigma_y \geq \sigma_Y$. Interestingly also, although σ_Y is found from ergodic states and hence not subject to aging, σ_y could be age-dependent and might generally be expected to increase with age, assuming that the material at rest tends to consolidate rather than fall apart.

5.1 Viscosity Bifurcation

If, as the above discussion allows, $\sigma_y > \sigma_Y$ with strict inequality [49, 50] then some interesting new flow scenarios are permitted. In particular, recall the flow curve of a yielding glass, as predicted by [6, 8] without any ad-hoc stress dependence in the vertex, is monotonically increasing. Accordingly, for a yielding glass one does not expect any form of shear banding to arise. However, if we allow for a static yield stress σ_y there is a new branch to the flow curve, which is a vertical line segment on the $\dot{\gamma} = 0$ axis, between σ_Y and σ_y . Exactly this scenario is reported by Varnik et al. in recent simulations [50]. The resulting composite flow curve is no longer strictly monotonic; it is possible in principle to have a shear banded state involving coexistence of a completely static phase (undergoing aging) and a fluidized phase which is ergodic. To achieve this state in the laboratory one might have to start from an aged sample and shear, rather than create a system at uniformly high shear rate and then back off the stress – the latter would, according to the MCT model for a yielding glass, remain in an ergodic state so long as it was uniform, and vice versa. Accordingly one might expect extreme bistability of banded and unbanded flows, in systems where $\sigma_y > \sigma_Y$.

This could help explain the phenomenon of “viscosity bifurcation”, which we interpret here as shear-banding in which one band is not flowing ($\dot{\gamma} = 0$). This phenomenon has been reported in a very wide range of systems [51], including some for which our glass models, and perhaps those of [3], should offer a reasonable theoretical description. If one does not allow $\sigma_y > \sigma_Y$,

then the simplest way to explain viscosity bifurcation is to have a flow curve with a dynamic yield stress σ_y and a negative slope at $\dot{\gamma} \rightarrow 0+$, with an upturn at higher shear rates [52]. However, our MCT-based models for colloidal suspensions at high density show no such tendencies. (The scenario is more plausible for weak, low density gels where a fluffy bonded structure is created at rest and destroyed progressively under shear.) Therefore, if viscosity bifurcation is seen in a dense colloidal suspension, this offers strong evidence for $\sigma_y > \sigma_Y$.

6 Rheological Instability and Chaos

Throughout the above discussion we have emphasised the role of the flow curve $\sigma(\dot{\gamma})$ in describing steady states. However, this curve contains no information about transient phenomena. Nor, indeed, does our ability to calculate such a curve prove that the steady states that it describes are stable. The commonest form of instability (negative slope) can be resolved by partitioning into steady shear bands as described previously. However, in some cases these bands can be unstable with the interface between them constantly in motion [53–55]. Moreover, this type of instability, can lead not only to oscillation but to chaos. In complex fluids at effectively zero Reynolds number, this is sometimes called “rheochaos” to distinguish it from the well studied hydrodynamic instabilities of Newtonian flows. (The latter are generally caused by inertial nonlinearity, rather than the constitutive nonlinearity (stress/strain) that matters here.) Rheochaos is reported experimentally in several systems [56], including some that are shear-thickening; but so far there are no quantitative reports in dense colloids. However there are several reports of highly erratic $\dot{\gamma}(t)$ at fixed σ or vice versa, e.g. [2, 57].

Recently, rheological instability, leading to rheochaos, has been studied in a very simple model of a shear-thickening material [54, 58]. This model is not based on MCT; indeed, we as yet have no machinery for addressing unsteady flow within that framework. Remarkably the steady-state flow curve in this model is monotonic (continuous shear thickening) and yet unstable [59]. This can be traced to the presence, in the model, of a relaxation time for a structural parameter that exceeds the relaxation time for stress. (The slowly relaxing structure could be local colloid concentration, or a textural property such as chaininess of the bonding network in an attractive system.) If this slow relaxation is quenched, the flow curve ceases to be monotonic: a material of fixed internal structure would show discontinuous thickening and shear banding [58]. Yet the two bands arising would have different history; their coexistence requires equality of the structural parameter between bands, and this cannot be maintained at timescales beyond the structural relaxation. Hence steady unbanded and steady banded flow are both ruled out. Figure 3 shows the time evolution of the unsteady banded state and the resulting flow rate at fixed imposed stress for model parameter settings

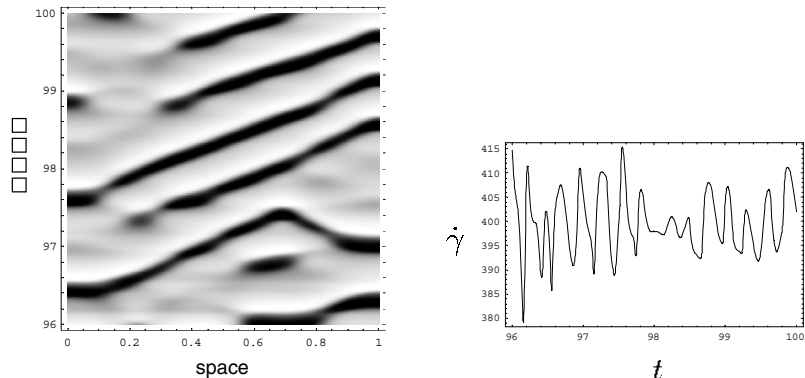


Fig. 3. Chaotic shear bands and the resulting erratic strain rate for the shear thickening model of [58] (see also [54]). In the spacetime plot (*left*) time is vertical and space axis (z) is horizontal; the gray scale denotes local stress. (In transverse shear banding, the constant externally imposed stress on the rheometer plate does not fix the local stress, only the global mean value.) Figure courtesy of A. Aradian

in the chaotic regime. In other parameter ranges simpler, but nonetheless quite exotic oscillatory behaviours are found [58]. The relevance of rheochaos to dense colloids largely remains to be explored; however, there is probably some connection with the observation of aperiodic “stick-slip” type dynamics around the jamming transition where discontinuous shear thickening sets in (e.g., [2, 57]).

7 Conclusion

Theoretical developments directly inspired by MCT now offer a promising framework for calculating the nonlinear flow behaviour of colloidal glasses and glassy liquids [6]. (Other work on the rheology of glasses [3, 5] does not, as yet, offer quantitative prediction of experimental quantities.) While promising, many things are missing so far from the approach initiated in [6]: velocity fluctuations, hydrodynamic forces, anharmonicity in H etc., are all ignored. The fact that only shear thinning is predicted in this case is excusable.

The schematic work of [10] (see also [36]) on shear thickening suggests how new physics (beyond two-point correlations) may need to be added to MCT before the full range of observed colloidal flow behaviour is properly described. Hydrodynamic interactions, and perhaps velocity fluctuations, are certainly also important in some aspects of shear thickening though we might hope that these do not dominate very close to the glass transition where the longest relaxation time is structural rather than hydrodynamic.

Of course, even for systems at rest, some important physics is missing from MCT, in particular, activated dynamics (see [9] for a discussion). These allow

the system to move exponentially slowly despite being in a region of phase space where, according to MCT, it cannot move at all (see e.g. [18]). Qualitatively, stress-induced jamming seems a quite different phenomenon from this; we can suspect that there are more things missing from MCT than just activated processes. In particular a more general treatment of anharmonic terms (or equivalently, a treatment of three-point and higher order correlations) may be required before one has a fully workable theory of sheared colloidal glasses.

Inserting an ad-hoc stress dependence of the MCT vertex within a schematic model, we were able to rationalise a number of jamming phenomena including, in principle, the existence at high enough colloid densities of brittle rather than yielding glasses. Brittle behaviour is implicated in the industrial process of granulation and could be intimately linked to the phenomenon of dilatancy in dry powders.

Because our version of MCT approaches the glass transition from the ergodic side, it cannot address the important distinction between static and dynamic yield stresses. Some other MCT-like schematic models can do this [49], as can simulation [50], and both suggest a finite difference between the two yield stress values. This opens the door to a “viscosity bifurcation” [51] involving the shear-banded coexistence, at a common stress value, of an arrested, aging phase and an ergodic flowing one. This bypasses the need for a negative slope on any part of the ergodic flow curve at nonzero shear rates.

Finally, our MCT-based theories are yet to evolve to the point where unsteady flow can meaningfully be discussed. This is a major deficiency since unsteady and even chaotic flow might be expected in various dense colloidal systems, especially in connection with jamming and the transition to discontinuous shear banding. Fortunately, some of these effects can be captured within very simple models [53, 58] although it remains a challenge to connect these with a more microscopic picture or, indeed, with the glass transition.

Acknowledgements

I thank Matthias Fuchs, Colin Holmes, and Achod Aradian for their enthusiastic and stimulating collaboration in the various areas addressed by this review.

References

1. M. E. Cates, J. P. Wittmer, J.-P. Bouchaud, P. Claudin: *Phys. Rev. Lett.* **81**, 1841 (1998); A. J. Liu, S. R. Nagel: *Nature* **396**, 21 (1998).
2. H. M. Laun: *J. Non-Newtonian Fluid Mec.* **54**, 87 (1994).
3. S. M. Fielding, P. Sollich, M. E. Cates: *J. Rheol.* **44**, 323 (2000); P. Sollich, F. Lequeux, P. Hebraud, M. E. Cates: *Phys. Rev. Lett.* **78**, 2020 (1997); P. Sollich: *Phys. Rev. E* **58**, 738 (1998).

4. D. A. Head, A. Ajdari, M. E. Cates: Phys. Rev. E **64**, 061509 (2001).
5. L. Berthier, J.-L. Barrat, J. Kurchan: Phys. Rev. E **61**, 5464 (2000).
6. M. Fuchs, M. E. Cates: Phys. Rev. Lett. **89**, 248303 (2002); Faraday Discussion **123**, 267 (2002).
7. M. E. Cates: Ann. Henri Poincaré **4**, S647 (2003) (cond-mat/0211066).
8. M. Fuchs, M. E. Cates: J. Phys. Cond. Mat. **15**, S401 (2003).
9. M. E. Cates, C. B. Holmes, M. Fuchs, O. Henrich: in “Unifying Concepts in Granular Media and Glasses”, Eds. A. Coniglio, A. Fierro, H. J. Herrmann and M. Nicodemi, pp. 203–216, (Elsevier, Amsterdam, 2004) (cond-mat/0310579).
10. C. B. Holmes, M. Fuchs, M. E. Cates: Europhys. Lett. **63**, 240 (2003).
11. M. E. Cates, M. R. Evans (eds): *Soft and Fragile Matter: Nonequilibrium Dynamics, Metastability and Flow* (IOP Publishing, Bristol, 2000).
12. D. J. Pine: Light Scattering and Rheology of Complex Fluids Driven far from Equilibrium. In: [11], pp 9–47.
13. W. Kob: Supercooled Liquids and Glasses. In: [11], pp 259–284.
14. H. A. Barnes, J. F. Hutton, K. Walters: *An Introduction to Rheology* (Elsevier, Amsterdam 1989).
15. K. Kroy, M. E. Cates, W. C. K. Poon, Phys. Rev. Lett. **92**, 148302 (2004).
16. W. Götze, L. Sjögren: Rep. Prog. Phys. **55**, 241 (1992).
17. S. Ramaswamy: Self-Diffusion of Colloids at Freezing. In: *Theoretical Challenges in the Dynamics of Complex Fluids*, ed by T. C. B. McLeish (Kluwer, Dordrecht 1987), pp 7–20.
18. K. Kawasaki, B. Kim: J. Phys. Cond. Mat. **14**, 2265 (2002) 2265.
19. M. E. Cates, M. Fuchs, K. Kroy, W. C. K. Poon, A. M. Puertas: J. Phys. Cond. Mat. **16**, S4861-S4875 (2004) (cond-mat/0403684).
20. K. Miyazaki, D. R. Reichman: Phys. Rev. E **66**, 050501 (2002); see also, K. Miyazaki, D. R. Reichman, R. Yamamoto: Phys. Rev. E **70**, 011501 (2004).
21. A. V. Indrani, S. Ramaswamy: Phys. Rev. E **52**, 6492 (1995).
22. M. E. Cates, S. T. Milner: Phys. Rev. Lett. **62**, 1856 (1989).
23. M. Fuchs, M. E. Cates: J. Phys. Cond. Mat. **17**, S1681-S1696 (2005).
24. G. Petekidis, D. Vlassopoulos, P. N. Pusey: Faraday Discussions **123**, 287 (2003); G. Petekidis, D. Vlassopoulos, P. N. Pusey: *submitted*.
25. J. Bergenholtz, M. Fuchs, T. Voigtmann: J. Phys. Cond. Mat. **12**, 6575 (2000).
26. K. Dawson, G. Foffi, M. Fuchs, W. Götze, F. Sciortino, M. Sperl, P. Tartaglia, T. Voigtmann, E. Zaccarelli: Phys. Rev. E **63**, 011401 (2001); L. Fabbian, W. Götze, F. Sciortino, P. Tartaglia, F. Thiery: Phys. Rev. E **59**, R1347 (1999).
27. J. Bergenholtz, W. C. K. Poon and M. Fuchs: Langmuir **19**, 4493 (2003).
28. J. Bergenholtz, M. Fuchs: Phys. Rev. E **59**, 5706 (1999).
29. S.A. Shah, Y.-L. Chen, K. S. Schweizer, C. F. Zukoski: J. Chem. Phys. **117**, 8747 (2003).
30. K. N. Pham, A. M. Puertas, J. Bergenholtz, S. U. Egelhaaf, A. Moussaid, P. N. Pusey, A. B. Schofield, M. E. Cates, M. Fuchs, W. C. K. Poon: Science **296**, 104 (2002); W. C. K. Poon, K. N. Pham, S. U. Egelhaaf, P. N. Pusey: J. Phys. Cond. Mat. **15**, S269 (2003).
31. T. Eckert, E. Bartsch: Phys. Rev. Lett. **89**, 125701 (2002).
32. W. Götze: Z. Phys. B **60**, 95 (1985).
33. J. Bender, N. J. Wagner: J. Rheol. **40**, 889 (1996).
34. P. D. Olmsted: Curr. Opin. Colloid Interface Sci. **4**, 95 (1999); O. Radelescu, P. D. Olmsted: J. Non-Newtonian Fluid Mech. **91**, 143 (2000); C. Y. D. Lu, P. D. Olmsted, R. C. Ball: Phys. Rev. Lett. **84**, 642 (2000); N. A. Spenley, M. E. Cates, T. C. B. McLeish: Phys. Rev. Lett. **71**, 939 (1993).

35. E. Bertrand, J. Bibette, V. Schmitt: Phys. Rev. E **66**, 06040 (2002).
36. C. B. Holmes, M. E. Cates, M. Fuchs, P. Sollich: *submitted* (cond-mat/0406422).
37. G. Y. Onoda, E. G. Liniger: Phys. Rev. Lett. **64**, 2727 (1990).
38. M. D. Haw: Phys. Rev. Lett. **92**, 185506 (2004); M. D. Haw: *private communication*.
39. P. B. Warren: *private communication*.
40. M. E. Cates, M. D. Haw, C. B. Holmes: J. Phys. Cond. Mat. **17**, S2517-S2531 (2005).
41. W. J. Frith, P. d'Haene, R. C. Buscall, J. Mewis: J. Rheol. **40**, 531 (1996).
42. V. T. O'Brien, M. E. Mackay: Langmuir **16**, 7931 (2000).
43. J. F. Brady: Curr. Opin. Colloid Interface Sci. **1**, 472 (1996) and references therein.
44. R. S. Farr, J. R. Melrose, R. C. Ball: Phys. Rev. E **55**, 7203 (1997).
45. J. Bergenholtz, J. F. Brady, M. Vucic: J. Fluid Mech. **456** 239 (2002).
46. R. C. Ball, J. R. Melrose: Adv. Colloid Interface Sci. **59**, 19 (1995).
47. J. F. Brady: J. Chem. Phys. **91**, 3335 (1993).
48. P. N. Segre, S. P. Meeker, P. N. Pusey, W. C. K. Poon: Phys. Rev. Lett. **75**, 958 (1995); Z. Cheng, J. Zhu, P. M. Chaikin, S.-E. Phan, W. B. Russel: Phys. Rev. E **65**, 041405 (2002).
49. L. Berthier: J. Phys. Cond. Mat. **15**, S933 (2003).
50. F. Varnik, L. Bocquet, J.-L. Barrat, L. Berthier: Phys. Rev. Lett. **90**, 095702 (2003); see also L. Berthier, J.-L. Barrat: J. Chem. Phys. **116** 6228 (2002).
51. F. Da Cruz, F. Chevoir, D. Bonn, P. Coussot: Phys. Rev. E **66**, 051305 (2002).
52. P. Coussot, Q. D. Nguyen, H. T. Huynh, D. Bonn: Phys. Rev. Lett. **88**, 175501 (2002).
53. S. M. Fielding, P. D. Olmsted: Phys. Rev. Lett. **92**, 084502 (2004).
54. A. Aradian, M. E. Cates: Proc. 3rd Int. Symp. on Slow Dynamics in Complex Systems, AIP Proceedings **708**, 84 (2004) (cond-mat/0310660).
55. B. Chakrabarti, M. Das, C. Dasgupta, S. Ramaswamy, A. K. Sood: Phys. Rev. Lett. **92**, 055501 (2004).
56. R. Bandyopadhyay, A. K. Sood: Europhys. Lett. **56**, 447 (2003); R. Bandyopadhyay, G. Basappa, A. K. Sood: Phys. Rev. Lett. **84**, 2022 (2000); A. S. Wunenberger, A. Colin, J. Leng, A. Arneodo, D. Roux: Phys. Rev. Lett. **86**, 1374 (2001); J. B. Salmon, A. Colin, D. Roux: Phys. Rev. E **66**, 031505 (2002); J. B. Salmon, S. Manneville, A. Colin: Phys. Rev. E **68**, 051503 (2003).
57. D. Lootens, H. Van Damme, P. Hebraud: Phys. Rev. Lett. **90**, 178301 (2003).
58. A. Aradian, M. E. Cates: Europhys. Lett. **70**, 397-403 (2005).
59. M. E. Cates, D. A. Head, A. Ajdari: Phys. Rev. E. **66**, 025202 (2002).

Thermal Noise Properties of Two Aging Materials

L. Bellon, L. Buisson, M. Ciccotti, S. Ciliberto[◇], F. Douarche

Ecole Normale Supérieure de Lyon, Laboratoire de Physique,
C.N.R.S. UMR5672, 46, Allée d'Italie, 69364 Lyon Cedex 07, France
[◇] *correspondence to: Sergio.Ciliberto@ens-lyon.fr*

In this lecture we review several aspects of the thermal noise properties in two aging materials: a polymer and a colloidal glass. The measurements have been performed after a quench for the polymer and during the transition from a fluid-like to a solid-like state for the gel. Two kind of noise has been measured: the electrical noise and the mechanical noise. For both materials we have observed that the electric noise is characterized by a strong intermittency, which induces a large violation of the Fluctuation Dissipation Theorem (FDT) during the aging time, and may persist for several hours at low frequency. The statistics of these intermittent signals and their dependence on the quench speed for the polymer or on sample concentration for the gel are studied. The results are in a qualitative agreement with recent models of aging, that predict an intermittent dynamics. For the mechanical noise the results are unclear. In the polymer the mechanical thermal noise is still intermittent whereas for the gel the violation of FDT, if it exists, is extremely small.

1 Introduction

When a glassy system is quenched from above to below the glass transition temperature T_g , any response function of the material depends on the time t_w elapsed from the quench [1]. For example, the dielectric and elastic constants of polymers continue to evolve several years after the quench [1]. Similarly, the magnetic susceptibility of spin-glasses depends on the time spent at low temperature [2]. Another example of aging is given by colloidal-glasses, whose properties evolve during the sol-gel transition which may last a few days [3]. For obvious reasons related to applications, aging has been mainly characterized by the study of the slow time evolution of response functions, such as the dielectric and elastic properties of these materials. It has been observed that these systems may present very complex effects, such as memory and rejuvenation [1, 4–6], in other words their physical properties depend on the whole thermal history of the sample. Many models and theories have been constructed in order to explain the observed phenomenology, which is not yet completely understood. These models either predict or assume very different dynamical behaviours of the systems during aging. This dynamical behaviour

can be directly related to the thermal noise features of these aging systems and the study of response functions alone is unable to give definitive answers on the approaches that are the most adapted to explain the aging of a specific material. Thus it is important to associate the measure of thermal noise to that of response functions. The measurement of fluctuations is also related to another important aspect of aging dynamics. Indeed glasses are out of equilibrium systems and usual thermodynamics does not necessarily apply. However, as the time evolution is slow, some concepts of the classical approach may be useful for understanding the glass aging properties. A widely studied question is the definition of an effective temperature in these systems which are weakly, but durably, out of equilibrium. Recent theories [7] based on the description of spin glasses by a mean field approach proposed to extend the concept of temperature using a Fluctuation Dissipation Relation (FDR) which generalizes the Fluctuation Dissipation Theorem (FDT) for a weakly out of equilibrium system (for a review see [8–10]). However the validity of this temperature is still an open and widely studied question.

For all of these reasons, in recent years, the study of the thermal noise of aging materials has received a growing interest. However in spite of the large amount of theoretical studies there are only a few experiments dedicated to this problem [11,22]. The available experimental results are in some way in contradiction and they are unable to give definitive answers. For example the thermal noise may present a strong intermittency which slowly disappears during aging. Although several theoretical models predict this intermittency [23–26] the experimental conditions which produce such a kind of behaviour are unclear. Therefore new experiments are necessary to increase our knowledge on the thermal noise properties of the aging materials.

In this lecture we will review several experimental results on the electrical and mechanical thermal fluctuations of a polymer and a colloidal glass. We will mainly focus on the measurements of the dielectric susceptibility and of the polarization noise in the polymer material, in the range 20 mHz–100 Hz, because the results of these measurements demonstrate the appearance of a strong intermittency of the noise when this material is quickly quenched from the molten state to below its glass-transition temperature. This intermittency produces a strong violation of the FDT at very low frequency. The violation is a decreasing function of the time t_w elapsed from the quench, and of the frequency of measurement $f = \omega/2\pi$. Nevertheless, this violation is observed at $\omega t_w \gg 1$ and may last for more than 3 h for $f > 1$ Hz. We have also observed that the intermittency is a function of the cooling rate of the sample and it almost disappears after a slow quench. In this case the violation of FDT remains but it is very small. Preliminary mechanical measurements done on a polycarbonate beam confirm the presence of an intermittent behaviour after a fast quench. We also review some equivalent measurements in a different material: a colloidal glass of Laponite. As for the polymer, a strong intermittency, sensible to initial conditions, is observed with electrical

measurements. It is interesting to note however that no such effect can be detected on the mechanical behaviour.

The paper is organized in three main sections, the first one on the electrical measurements in polycarbonate, a second one on the mechanical measurements and a third one on the fluctuations in Laponite preparations. In the first section we describe the experimental set up and the measurement procedure, the results of the noise and response measurements and the statistical analysis of the noise. We then discuss the dependence on the quench speed of the FDT violation and the temporal behaviour of the effective temperature after a slow quench. In Sect. 3 we describe the experimental set-up for mechanical measurements and the preliminary results on the mechanical noise. In Sect. 4 the electrical noise in the colloidal gel is analyzed. We briefly discuss the case of the mechanical properties for the gel. Finally in Sect. 5 we first compare the experimental results on polycarbonate with those of colloidal glasses and other materials. We then discuss the relevance of these results in the context of the recent theoretical models before concluding.

2 Dielectric Noise in a Polymer Glass

We present in this section measurements of the dielectric susceptibility and of the polarization noise, in the range 20 mHz–100 Hz, of a polymer glass: polycarbonate. These results demonstrate the appearance of a strong intermittency of the noise when this material is quickly quenched from the molten state to below its glass-transition temperature. This intermittency produces a strong violation of the FDT at very low frequency. The violation is a decreasing function of time and frequency and it is still observed for $\omega t_w \gg 1$: it may last for more than 3 h for $f > 1$ Hz. We have also observed that the intermittency is a function of the cooling rate of the sample and almost disappears after a slow quench. In this case the violation of FDT remains, but it is very small.

2.1 Experimental Setup

The polymer used in this investigation is Makrofol DE 1-1 C, a bisphenol A polycarbonate, with $T_g \simeq 419$ K, produced by Bayer in form of foils. We have chosen this material because it has a wide temperature range of strong aging [1]. This polymer is totally amorphous: there is no evidence of crystallinity [28]. Nevertheless, the internal structure of polycarbonate changes and relaxes as a result of a change in the chain conformation by molecular motions [1, 29, 30]. Many studies of the dielectric susceptibility of this material exist, but none had an interest on the problem of noise measurements.

In our experiment polycarbonate is used as the dielectric of a capacitor. The capacitor is composed by 14 cylindrical capacitors in parallel in order to reduce the resistance of the sample and to increase its capacity [20]. Each

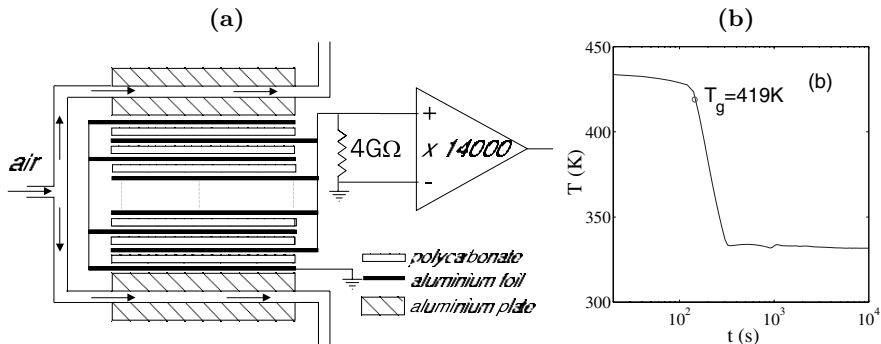


Fig. 1. Polycarbonate experimental set-up (a) Design of polycarbonate capacitance cell. (b) Typical temperature quench: from $T_i = 453$ K to $T_f = 333$ K, the origin of t_w is set at $T = T_g$

capacitor is made of two aluminum electrodes, $12\mu\text{m}$ thick, and by a disk of polycarbonate of diameter 12 cm and thickness $125\mu\text{m}$. The experimental set-up is shown in Fig. 1(a). The 14 capacitors are sandwiched together and put inside two thick aluminum plates which contain an air circulation used to regulate the sample temperature. This mechanical design of the capacitor is very stable and gives very reproducible results even after many temperature quenches. The capacitor is inside 4 Faraday screens to insulate it from external noise. The temperature of the sample is controlled within a few percent. Fast quenches of about 1 K/s are obtained by injecting Nitrogen vapor in the air circulation of the aluminum plates. The electrical impedance of the capacitor is $Z(\omega, t_w) = R/(1 + i\omega R C)$, where C is the capacitance and R is a parallel resistance which accounts for the complex dielectric susceptibility. This is measured by a lock-in amplifier associated with an impedance adapter [20]. The noise spectrum $S_Z(\omega, t_w)$ of the impedance $Z(\omega, t_w)$ is:

$$S_Z(f, t_w) = 4 k_B T_{eff}(f, t_w) \text{Re}[Z(\omega, t_w)] = \frac{4 k_B T_{eff}(f, t_w) R}{1 + (\omega R C)^2} \quad (1)$$

where k_B is the Boltzmann constant and T_{eff} is the effective temperature of the sample. This effective temperature takes into account the fact that FDT (Nyquist relation for electric noise) can be violated because the polymer is out of equilibrium during aging, and in general $T_{eff} > T$, with T the temperature of the thermal bath. Of course when FDT is satisfied then $T_{eff} = T$. In order to measure $S_Z(f, t_w)$, we have made a differential amplifier based on selected low noise JFET(2N6453 InterFET Corporation), whose input has been polarized by a resistance $R_i = 4G\Omega$. Above 2 Hz , the input voltage noise of this amplifier is $5\text{ nV}/\sqrt{\text{Hz}}$ and the input current noise is about $1\text{ fA}/\sqrt{\text{Hz}}$. The output signal of the amplifier is directly acquired by a NI4462 card. It is easy to show that the measured spectrum at the amplifier input is:

$$S_V(f, t_w) = \frac{4 k_B R R_i (T_{eff}(f, t_w) R_i + T_R R + S_\xi(f) R R_i)}{(R + R_i)^2 + (\omega R R_i C)^2} + S_\eta(f) \quad (2)$$

where T_R is the temperature of R_i and S_η and S_ξ are respectively the voltage and the current noise spectrum of the amplifier. In order to reach the desired statistical accuracy of $S_V(f, t_w)$, we averaged the results of many experiments. In each of these experiments the sample is first heated to $T_i = 1.08T_g$. It is maintained at this temperature for several hours in order to reinitialize its thermal history. Then it is quenched from T_i to the working final temperature T_f where the aging properties are studied. The maximum quenching rate from T_i to T_f is 1 K/s. A typical thermal history of a fast quench is shown in Fig. 1(b). The reproducibility of the capacitor impedance, during this thermal cycle is always better than 1%. The origin of aging time t_w is the instant when the capacitor temperature is at $T_g \simeq 419$ K, which of course may depend on the cooling rate. However adjustment of T_g of a few degrees will shift the time axis by at most 30 s, without affecting our results.

2.2 Response and Noise Measurements

Before discussing the time evolution of the dielectric properties and of the thermal noise at T_f we show in Fig. 2 the dependence of R and C measured at 1 Hz as a function of temperature, which is ramped as a function of time as indicated in the inset of Fig. 2(a). We notice a strong hysteresis between cooling and heating. In the figure T_α is the temperature of the α relaxation at 1 Hz. The other circles on the curve indicate the T_f where the aging has been studied. We have performed measurements at $T_f = 0.79T_g, 0.93T_g, 0.98T_g$ using fast and slow quenches. The cooling rate is 1 K/s and 0.06 K/s for the fast and slow quenches respectively. As at $T_f = 0.98T_g$ the dielectric constant strongly depends on temperature (see Fig. 2), the temperature stability has to be much better at $T_f = 0.98T_g$ than at the two other smaller T_f . Because of this good temperature stability needed at $T_f = 0.98T_g$ it is impossible to reach this temperature too fast. Therefore at $0.98T_g$ we have performed only measurements after a slow quench.

We first describe the results after a fast quench at the smallest temperature, that is $T_f = 0.79T_g$. In Fig. 3(a) and (b), we plot the measured values of R and C as a function of f at $T_i = 1.08T_g$ and at T_f for $t_w \geq 200$ s. The dependence of R , at 1 Hz, as a function of time is shown in Fig. 3(c). We see that the time evolution of R is logarithmic in time for $t > 300$ s and that the aging is not very large at $T_f = 0.79T_g$, it is only 10% in 3 hours. At higher temperature close to T_g aging is much larger.

Looking at Fig. 3(a) and (b), we see that lowering temperature R increases and C decreases. As at $0.79T_g$ aging is small and extremely slow for $t_w > 200$ s the impedance can be considered constant without affecting our results. From the data plotted in Fig. 3 (a) and (b) one finds that $R =$

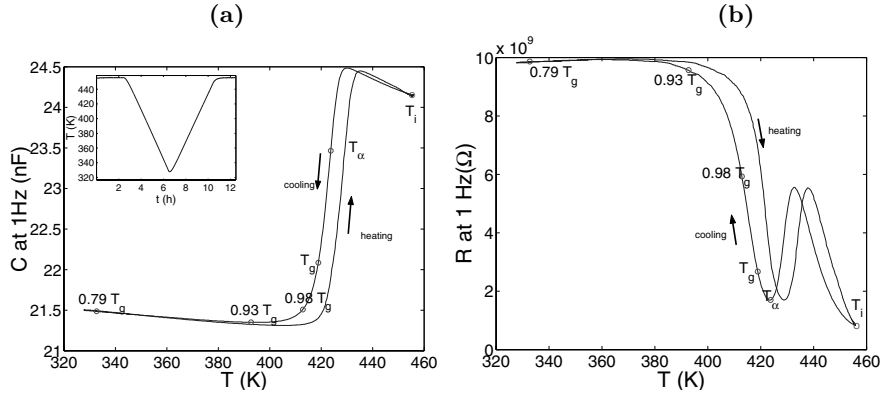


Fig. 2. Polycarbonate response function at 1 Hz (a) Dependence of C , measured at 1 Hz, on temperature, when T is changed as function of time as indicated in the inset. (b) Dependence of R , measured at 1 Hz, on T . T_α is the temperature of the α relaxation at 1 Hz, T_g is the glass transition temperature. The other circles on the curve indicate the T_f where aging has been studied

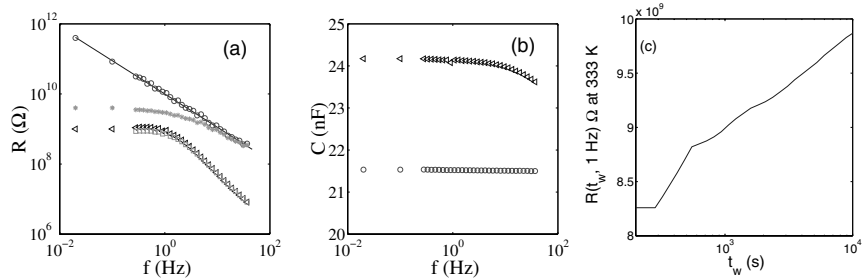


Fig. 3. Polycarbonate response function (a) Polycarbonate resistance R as a function of frequency measured at $T_i = 1.08T_g$ (\triangleleft) and at $T_f = 0.79T_g$ (\circ) (after a fast quench). The effect of the $4G\Omega$ input resistance in parallel with the polycarbonate impedance is also shown at $T = 433\text{ K}$ (\square) and at $T = 333\text{ K}$ ($*$). (b) Polycarbonate capacitance versus frequency measured at $T_i = 433\text{ K}$ (\triangleleft) and at $T_f = 333\text{ K}$ (\circ). (c) Typical aging of R measured at 1 Hz as a function of t_w

$10^{10}(1 \pm 0.05) f^{-1.05 \pm 0.01} \Omega$ and $C = (21.5 \pm 0.05)nF$. In Fig. 3(a) we also plot the total resistance at the amplifier input which is the parallel of the capacitor impedance with R_i . We see that at T_f the input impedance of the amplifier is negligible for $f > 10\text{ Hz}$, whereas it has to be taken into account at slower frequencies.

Figure 4(a) represents the evolution of $S_V(f, t_w)$ after the fast quench. Each spectrum is obtained as an average in a time window starting at t_w . The time window increases with t_w so to reduce error for large t_w . The results of 7 quenches have been averaged. At the longest time ($t_w = 1\text{ day}$)

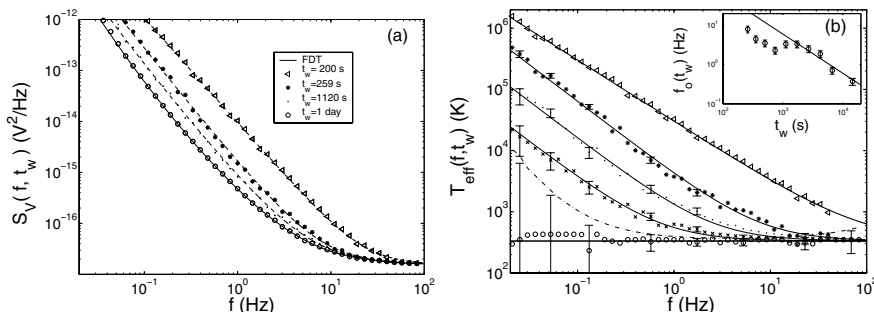


Fig. 4. Voltage noise and effective temperature in polycarbonate after a fast quench (a) Noise power spectral density $S_V(f, t_w)$ measured at $T_f = 333$ K and different t_w . The spectra are the average over seven quenches. The continuous line is the FDT prediction. Dashed lines are the fit obtained using (2) and (3) (see text for details). (b) Effective temperature vs frequency at $T_f = 333$ K for different aging times: (\triangleleft) $t_w = 200$ s, ($*$) $t_w = 260$ s, (\bullet) $t_w = 2580$ s, (\times) $t_w = 6542$ s, (\circ) $t_w = 1$ day. The continuous lines are the fits obtained using (3). The *horizontal straight* line is the FDT prediction. The *dot dashed* line corresponds to the limit where the FDT violation can be detected. In the inset the frequency $f_o(t_w)$, defined in (3), is plotted as a function of t_w . The continuous line is not a fit, but it corresponds to $f_o(t_w) \propto 1/t_w$

the equilibrium FDT prediction (continuous line) is quite well satisfied. We clearly see that FDT is strongly violated for all frequencies at short times. Then high frequencies relax on the FDT, but there is a persistence of the violation for lower frequencies. The amount of the violation can be estimated by the best fit of $T_{eff}(f, t_w)$ in (2) where all other parameters are known. We started at very large t_w when the system is relaxed and $T_{eff} = T$ for all frequencies. Inserting the values in (2) and using the S_V measured at $t_w = 1$ day we find $T_{eff} \simeq 333$ K, within error bars for all frequencies (see Fig. 4b). At short t_w data show that $T_{eff}(f, t_w) \simeq T_f$ for f larger than a cutoff frequency $f_o(t_w)$ which is a function of t_w . In contrast, for $f < f_o(t_w)$ we find that T_{eff} is: $T_{eff}(f, t_w) \propto f^{-A(t_w)}$, with $A(t_w) \simeq 1$. This frequency dependence of $T_{eff}(f, t_w)$ is quite well approximated by

$$T_{eff}(f, t_w) = T_f \left[1 + \left(\frac{f}{f_o(t_w)} \right)^{-A(t_w)} \right] \quad (3)$$

where $A(t_w)$ and $f_o(t_w)$ are the fitting parameters. We find that $1 < A(t_w) < 1.2$ for all the data set. Furthermore for $t_w \geq 250$, it is enough to keep $A(t_w) = 1.2$ to fit the data within error bars. For $t_w < 250$ s we fixed $A(t_w) = 1$. Thus the only free parameter in (3) is $f_o(t_w)$. The continuous lines in Fig. 4(a) are the best fits of S_V found inserting (3) in (2).

In Fig. 4(b) we plot the estimated $T_{eff}(f, t_w)$ as a function of frequency at different t_w . We see that just after the quench $T_{eff}(f, t_w)$ is much larger than T_f in all the frequency interval. High frequencies rapidly decay towards the FDT prediction whereas at the smallest frequencies $T_{eff} \simeq 10^5$ K. Moreover we notice that low frequencies decay more slowly than high frequencies and that the evolution of $T_{eff}(f, t_w)$ towards the equilibrium value is very slow. From the data of Fig. 4(b) and (3), it is easy to see that $T_{eff}(f, t_w)$ can be superposed onto a master curve by plotting them as a function of $f/f_o(t_w)$. The function $f_o(t_w)$ is a decreasing function of t_w , but the dependence is not a simple one, as it can be seen in the inset of Fig. 4(b). The continuous straight line is not fit, it represents $f_o(t_w) \propto 1/t_w$ which seems a reasonable approximation for these data for $t > 1000$ s. For $t_w > 10^4$ s we find the $f_o < 1$ Hz. Thus we cannot follow the evolution of T_{eff} anymore because the contribution of the experimental noise on S_V is too big, as it is shown in Fig. 4(b) by the increasing of the error bars for $t_w = 1$ day and $f < 0.1$ Hz.

We do not show the same data analysis for the other working temperature after a fast quench, because the same scenario appears in the range $0.79T_g < T < 0.93T_g$, where the low frequency dielectric properties are almost temperature independent (see Fig. 2(b)). The only important difference to mention here is that aging becomes faster and more pronounced as the temperature increases. At $T_f = 0.93T_g$, the losses of the capacitor change of about 50% in about 3 h, but all the spectral analysis performed after a fast quench gives the same evolution. We can just notice that T_{eff} for $T = 0.93T_g$ is higher than that at $T = 0.79T_g$. At $T = 0.93T_g$, T_{eff} is well fitted by (3). It is enough to keep $A(t_w) = 1$ for all t_w and $f_o(t_w) \sim 1/t_w^{1.5}$, (see Fig. 5a). We notice that at $0.93T_g$ the power law behaviour is well established, whereas it was more doubtful at $0.73T_g$. The dependence of T_{eff} as a function of t_w is

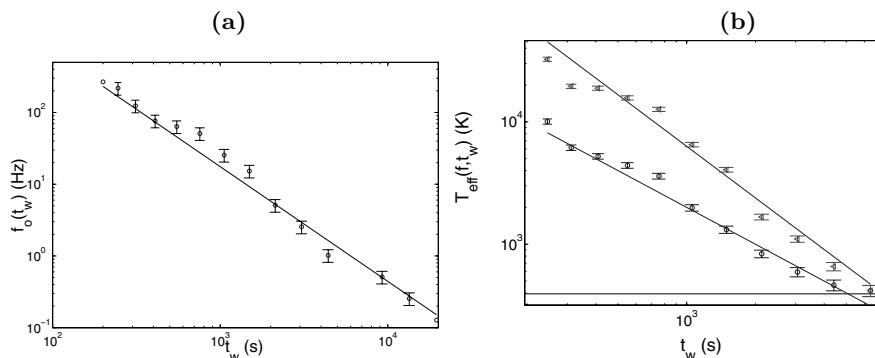


Fig. 5. f_o and T_{eff} as a function of t_w at $T_f = 0.93T_g$ after a fast quench. (a) f_o defined in (3) as a function of t_w (b) Evolution of T_{eff} at two different frequencies (o) 7 Hz and (◄) 2 Hz

plotted in Fig. 5 for two values of f and has also a power law dependence on t_w .

For $T > 0.93T_g$ fast quenches cannot be performed for the technical reasons mentioned at the beginning of Sect. 3. The results are indeed quite different. Thus we will not consider, for the moment, the measurement at $T_f = 0.98T_g$ and we will mainly focus on the measurements done in the range $0.79T_g < T < 0.93T_g$ with fast quenches. For these measurements the spectral analysis on the noise signal indicates that Nyquist relation (FDT) is strongly violated for a long time after the quench. The question is now to understand the reasons of this violation.

2.3 Statistical Analysis of the Noise

In order to understand the origin of such large deviations in our experiment we have analyzed the noise signal. We find that the signal is characterized by large intermittent events which produce low frequency spectra proportional to $f^{-\alpha}$ with $\alpha \simeq 2$. Two typical signals recorded at $T_f = 0.79T_g$ for $1500 \text{ s} < t_w < 1900 \text{ s}$ and $t_w > 75000 \text{ s}$ are plotted in Fig. 6. We clearly see that in the signal recorded for $1500 \text{ s} < t_w < 1900 \text{ s}$ there are very large bursts which are on the origin of the frequency spectra discussed in the previous section. In contrast in the signal which was recorded at $t_w > 75000 \text{ s}$, when FDT is not violated, the bursts totally disappear (Fig. 6b).

The probability density function (PDF) of these signals is shown in Fig. 7 (a). We clearly see that the PDF, measured at small t_w , has very high tails which becomes smaller and smaller at large t_w . Finally the Gaussian profile is recovered after 24 h. The PDF are very symmetric in their gaussian parts, i.e. 3 standard deviations. The tails of the PDF are exponential and are decreasing functions of t_w .

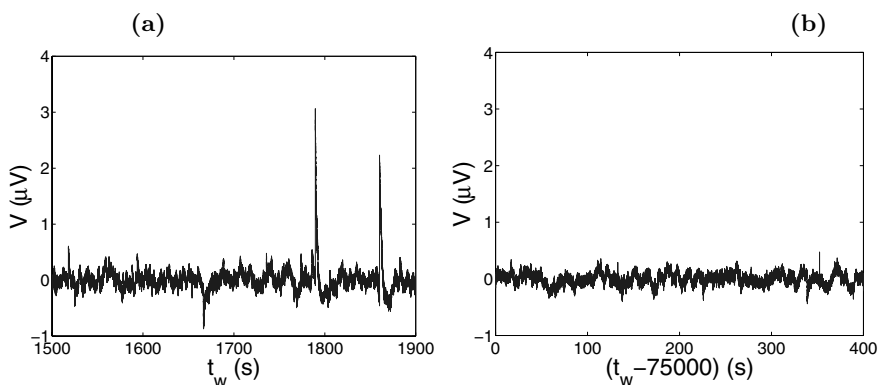


Fig. 6. Voltage noise signal in polycarbonate after a fast quench Typical noise signal of polycarbonate measured at $T_f = 333 \text{ K}$ for $1500 \text{ s} < t_w < 1900 \text{ s}$ (a) and $t_w > 75000 \text{ s}$ (b)

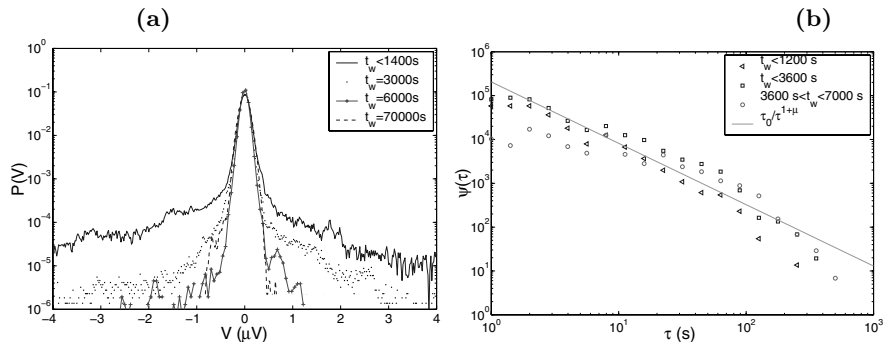


Fig. 7. PDF of voltage noise in polycarbonate after a fast quench at $T_f = 0.79T_g$. (a) The large tails of the PDF at early t_w are a signature of strong intermittency. (b) Histogram of time interval τ between two successive pulses: $\Psi(\tau, t_w)$. At early t_w , $\Psi(\tau, t_w)$ is power law distributed

The time interval τ between two successive pulses is power law distributed. In order to study this distribution $\Psi(\tau, t_w)$ of τ , we have first selected the signal fluctuations with amplitude larger than a fixed threshold, which has been chosen between 3 and 4 standard deviations of the equilibrium noise, i.e. the noise predicted by the FDT. We have then measured the time intervals τ between two successive large fluctuations. The histogram $\Psi(\tau, t_w)$ computed for $t_w < 20$ min and for $20 \text{ min} < t_w < 3h$ is plotted in Fig. 7(b). We clearly see that $\Psi(\tau, t_w)$ is a power law, specifically $\Psi(\tau) \propto \frac{1}{\tau^{1+\mu}}$ with $\mu \simeq 0.4 \pm 0.1$. This result agrees with one of the hypothesis of the trap model [31,32], which presents non-trivial violation of FDT associated to an intermittent dynamics. In the trap model τ is a power-law-distributed quantity with an exponent $1+\mu$ that, in the glass phase, is smaller than 2. However, there are important differences between the dynamics of our system and that of the trap model. Indeed in this model one finds short and large τ for any t_w which is in contrast with our system because the probability of finding short τ seems to decrease as a function of t_w . But this effect could be a consequence of the imposed threshold. It seems that there is no correlation between the τ and the amplitude of the associated bursts. Finally, the maximum distance τ_{max} between two successive pulses grows as a function of t_w logarithmically, that is $\tau_{\text{max}} = [10 + 152 \log(t_w/300)]\text{s}$ for $t_w > 300\text{s}$. This slow relaxation of the number of events per unit of time shows that the intermittency is related to aging.

The same behaviour is observed at $T_f = 0.93T_g$ after a fast quench. The PDF of the signals measured at $T_f = 0.93T_g$ are shown in Fig. 8(a). The behaviour is the same except for the relaxation rate towards the Gaussian distribution which is faster in this case, because the aging effects are larger at this temperature. From these measurements one concludes that after a fast quench the electrical thermal noise is strongly intermittent and

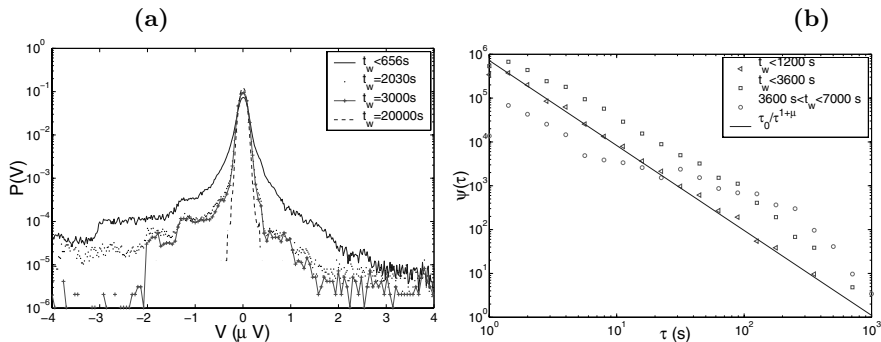


Fig. 8. PDF of voltage noise in polycarbonate after a fast quench at $0.93T_g$
 (a) PDF of the noise signal of polycarbonate measured at various t_w . (b) Histograms $\Psi(\tau, t_w)$, following at early t_w a $1/\tau^{1+\mu}$ law with $\mu = 0.9 \pm 0.1$

non-Gaussian. The number of intermittent events increases with the temperature : for $T_f = 0.93T_g$, T_{eff} is higher than for $T_f = 0.79T_g$ and PDF tails are more important. The histograms $\Psi(\tau, t_w)$ are shown Fig. 8 (b). The behaviour is the same with $\mu = 0.9 \pm 0.1$. By comparing $\Psi(\tau, t_w)$ for short τ and short t_w there are more events at $0.93T_g$ (Fig. 8 (b)) than at $0.79T_g$ (Fig. 7 (b)). This is consistent with activation processes for the aging dynamics. Indeed the probability of jumping from a potential well to another increases with temperature. Thus one expects to find more events at high temperature than at low temperature.

2.4 Influence of the Quench Speed

The intermittent behaviour described in the previous sections depends on the quench speed. In Fig. 9(a) we plot the PDF of the signals measured after a slow quench (3.6 K/min) at $T_f = 0.93T_g$. We clearly see that the PDF are very different: intermittency has almost disappeared. The comparison between the fast quench and the slow quench merits a special comment. During the fast quench $T_f = 0.93T_g$ is reached in about 100 s after the passage of T at T_g . For the slow quench this time is about 1000 s. Therefore one may wonder whether after 1000 s of the fast quench one recovers the same dynamics of the slow quench. By comparing the PDF of Fig. 8(a) with those of Fig. 9(a) we clearly see that this is not the case. Furthermore, by comparing the histograms of Fig. 8(b) with those of Fig. 9(b), we clearly see that there are less events separated by short τ for the slow quench. Therefore one deduces that the polymer is actually following a completely different dynamics after a fast or a slow quench [33, 34]. This is a very important observation that can be related to well known effects of response function aging. The famous Kovacs effect is an example [4] where depending on the cooling rate the isothermal compressibility presents a completely different time evolution.

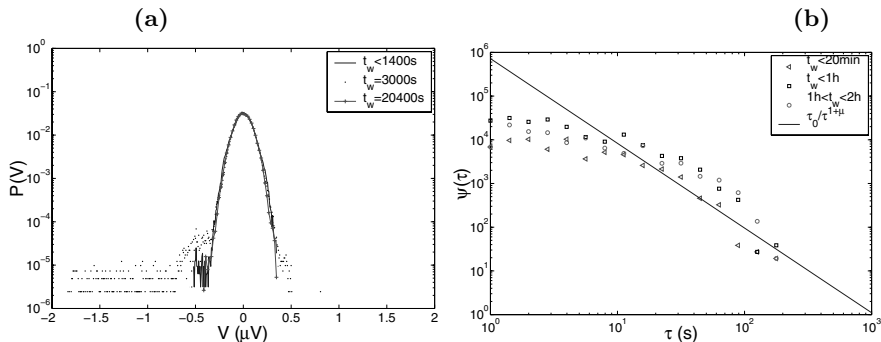


Fig. 9. PDF of voltage noise in polycarbonate after a slow quench at $T_f = 0.93T_g$. (a) No intermittency is visible after a slow quench at 3.6 K/min. (b) Histograms $\Psi(\tau, t_w)$ after a slow quench. The line corresponds to the $\tau_0/\tau^{1+\mu}$ fit of Fig. 8(b), where $\mu = 0.93$

2.5 T_{eff} after a Slow Quench

In the previous section we have shown that the intermittent aging dynamics is strongly influenced by the cooling rate. We discuss in this section the behaviour of the effective temperature after a slow quench. We use for this purpose the measurement at $T_f = 0.98T_g$. The time evolution of the response function is much larger at this temperature than at $T_f = 0.79T_g$ as it can be seen in Fig. 10. It is about 50% at the small frequencies, therefore it has to be kept into account in the evaluation of FDT. The spectrum of the capacitance noise measured at $0.98T_g$ is plotted for two different times in Fig. 11. The continuous lines represent the FDT predictions computed using the measured response function reported in Fig. 10. We clearly see that the experimental points are very close to the FDT predictions, thus the violation of FDT, if it exists, is very small. To check this point, we have computed T_{eff} in the range [1 Hz – 10 Hz], which is plotted as a function of time in Fig. 12. Although the error bars are rather large, we clearly see that T_{eff} decreases logarithmically as a function of time. We also notice that the maximum violation at short times is about 25% which is much smaller than that measured at smaller T_f after a fast quench. The PDF of the noise signal at $0.98T_g$ are plotted in Fig. 13(a) and they do not show very large tails as in the case of the intermittent dynamics. The statistics of the time intervals τ between two large events does not present any power law either (see Fig. 13(b)). Thus the signal statistics look much more similar to those measured at $0.93T_g$ after a slow quench than to the intermittent ones. This comparison shows that independently of the final temperature the intermittent behaviour is induced by the fast quench and that the FDT violation is cooling rate dependent.

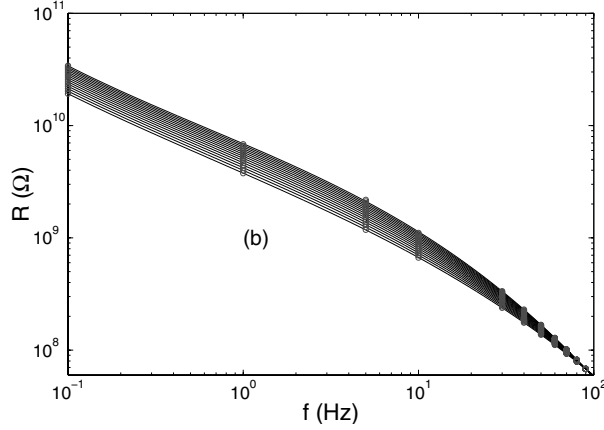


Fig. 10. Capacitance losses at $T_f = 0.98T_g$ after a slow quench. Resistance as a function of frequency for different t_w from $t = 100$ s (lower curve) to $t_w = 14400$ s

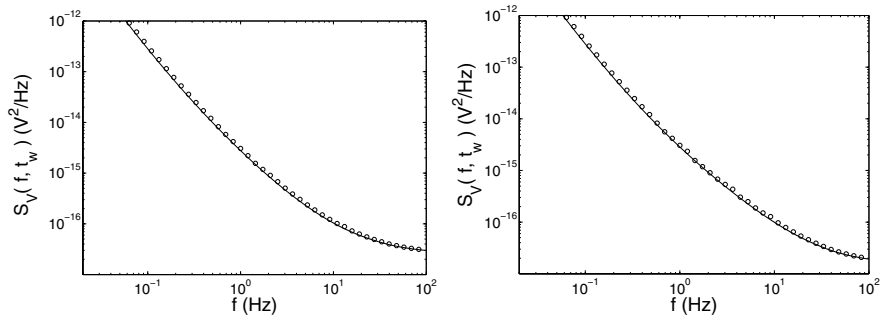


Fig. 11. Power spectral density of the capacitance noise at $T_f = 0.98T_g$ after a slow quench. $S_V(f, t_w)$ as a function of f for two different time: (a) $t_w = 200$ s, (b) $t_w = 7200$ s. Circles stand for measurement points, whereas the continuous line is the FDT prediction

3 Mechanical Measurements on a Polycarbonate Cantilever

In the previous section we have studied the properties of dielectrical thermal noise during the aging of polycarbonate. In this section we want to check if the thermal noise features are independent of the observable. As a second observable, we have chosen to measure the thermally excited vibrations of a cantilever made of polycarbonate.

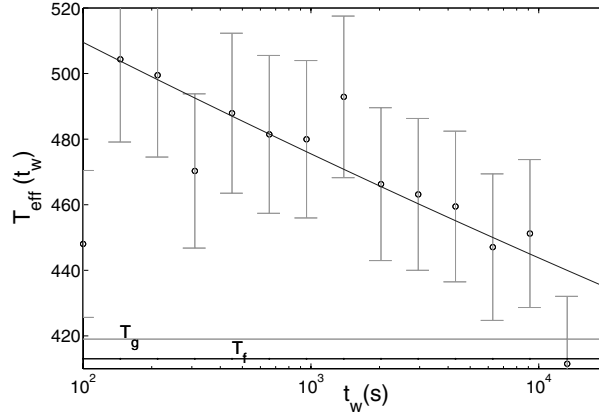


Fig. 12. T_{eff} as a function of time at $T_f = 0.98T_g$ after a slow quench. T_{eff} averaged in the frequency band [1 Hz – 10 Hz]. It has been computed from the spectra $S_V(f, t_w)$ and the measured (R, C) using (2)

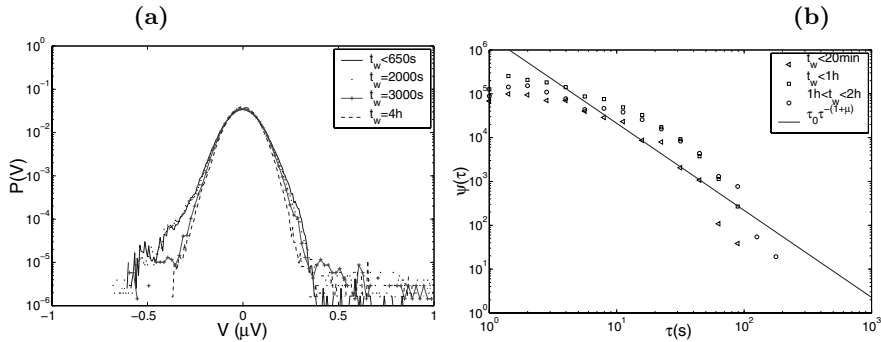


Fig. 13. PDF of the signal at $T_f = 0.98T_g$ after a slow quench. (a) PDF of the signal. No intermittency is visible. (b) Histograms $\Psi(\tau, t_w)$ after a slow quench. The continuous line represent the $1/\tau^{1+\mu}$ law where we chose $\mu = T_f/T_g$ to compare with the theoretical estimation of the trap model

3.1 FDT in a Mechanical Oscillator

The physical object of our interest is a small plate with one end clamped and the other free, i.e. a cantilever. The plate is of length l , width a , thickness b , mass m_{Polyc} . On the free end of the cantilever a small golden mirror of mass m_{mirror} is glued. As described in the next section, this mirror is used to detect the amplitude x_c of the transverse vibrations of the cantilever free end. The motion of the cantilever free end can be assimilated to that of a driven harmonic oscillator, which is damped only by the viscoelasticity of the polymer. Consequently, the equation of motion of the cantilever free end takes a simple form in Fourier space:

$$[-m\omega^2 + K(\omega)]\hat{x}_c = \hat{F}_{\text{ext}} \quad (4)$$

where \hat{x}_c is the Fourier transform of x_c , m is the total effective mass of the plate plus the mirror, $K = K' + iK''$ is the complex elastic stiffness of the plate free end, and \hat{F}_{ext} is the Fourier transform of the external driving force. The complex $K(\omega)$ takes into account the viscoelastic nature of the cantilever. From the theory of elasticity [35] one obtains that, for low frequencies, an excellent approximations for m and K are:

$$m = \frac{3}{(3.52)^2} m_{\text{Polyc}} + m_{\text{mirror}} , \quad (5)$$

$$\text{and } K = \frac{Eab^3}{4l^3} , \quad (6)$$

where $E = E' + iE''$ is the plate Young modulus. Notice that if $m_{\text{mirror}} = 0$, then one recovers the smallest resonant frequency of the cantilever [35]. For Polycarbonate at room temperature, E is such that $E' = 2.2 \times 10^9$ Pa and $E'' = 2 \times 10^7$ Pa, and its frequency dependence may be neglected in the range of frequency of our interest, that is from 0.1 to 100 Hz [36]. Thus we neglect the frequency dependence of K in this specific example.

When $F_{\text{ext}} = 0$, the amplitude of the thermal vibrations of the cantilever free end x_T is linked to its response function χ via the FDT [37]:

$$\langle |\hat{x}_T|^2 \rangle = \frac{2k_B T}{\omega} \text{Im } \hat{\chi} , \quad (7)$$

where $\langle |\hat{x}_T|^2 \rangle$ is the thermal fluctuations spectral density of x_c , k_B the Boltzmann constant and T the temperature. From (4) one obtains that the response function of the harmonic oscillator is

$$\hat{\chi} = \frac{\hat{x}_c}{\hat{F}_{\text{ext}}} = \frac{1}{m[\omega_0^2 - \omega^2 - i(\text{sign } \omega) \gamma \omega^2]} , \quad (8)$$

where $\omega_0^2 = K'/m$ and $\gamma = K''/K'$.

Inserting (8) into (7), one can compute the thermal fluctuations spectral density of the Polycarbonate cantilever for positive frequencies:

$$\langle |\hat{x}_T|^2 \rangle = \frac{2k_B T}{\omega} \frac{\gamma \omega_0^2}{m[(\omega_0^2 - \omega^2)^2 + (\gamma \omega_0^2)^2]} . \quad (9)$$

Notice that $\langle |\hat{x}_T|^2 \rangle \sim \omega^{-1}$ for $\omega \ll \omega_0$, because the viscoelastic damping K'' is constant in our frequency range. In the case of a viscous damping (for example, a cantilever immersed in a viscous fluid) $K'' = \alpha \omega$, where α is proportional to the fluid viscosity and to a geometry dependent factor. Then the thermal fluctuations spectral density of the cantilever free end, in the case of viscous damping, is

$$\langle |\hat{x}_T|^2 \rangle = \frac{2k_B T \alpha}{m^2 [(\omega_0^2 - \omega^2)^2 + (\frac{\alpha}{m}\omega)^2]}, \quad (10)$$

which is constant for $\omega \ll \omega_0$. Therefore, the thermal fluctuations spectral density shape depends on $K''(\omega)$. In the case of a viscoelastic damping (9), the thermal noise increases when ω goes to 0, and with a suitable choice of the parameters the low frequency spectral density of an aging polymer can be measured using this method.

However, the cantilever is also sensitive to the mechanical noise, and the total displacement x_c of the cantilever free end actually reads $x_c = x_T + x_{acc}$, where x_{acc} is the displacement induced by the external mechanical noise. Thus, it is important to compute the signal-to-noise ratio (SNR) of our apparatus, which we define as the ratio between the thermal fluctuations and the mechanical noise spectral densities. All the details on the optimization of the SNR can be found in [38].

3.2 Experimental Apparatus

Let us estimate the amplitude of $\sqrt{\langle |\hat{x}_T|^2 \rangle}$ at $\nu = \omega/2\pi = 1$ Hz for the following choice of the parameters: $\gamma \simeq 10^{-2}$, $l \simeq 10$ mm, $a \simeq 1$ mm, $b = 125$ μm and $m_{\text{mirror}} \lesssim 10^{-3}$ g. We find $\nu_0 \simeq 100$ Hz and $\sqrt{\langle |\hat{x}_T(1 \text{ Hz})|^2 \rangle} \simeq 10^{-11}$ m/ $\sqrt{\text{Hz}}$, which is a very small signal. As a consequence, extremely small vibrations of the environment may greatly perturb the measurement. Therefore, to increase the signal-to-noise ratio of the measurement, one has to reduce the coupling of the cantilever to the environmental noise (acoustic and seismic) using vibration isolation systems. This may be not enough in this specific case because of the smallness of the thermal fluctuations. Therefore we have applied an original noise subtraction technique described in [38] in order to recover x_T from the measurement of x_c .

The measurement of x_c is done using a Nomarski interferometer (for detailed reviews, see [39–41]) which uses the mirror glued on the Polycarbonate cantilever in one of the two optical paths. The interferometer noise is about 5×10^{-14} m/ $\sqrt{\text{Hz}}$, which is two orders of magnitude smaller than the cantilever thermal fluctuations. The cantilever is inside an oven under vacuum. A window allows the laser beam to go inside (cf Fig. 14). The size of the Polycarbonate cantilever are, $l \simeq 13.5$ mm, $a \simeq 1$ mm and $b = 125$ μm , and the mirror mass is $m_{\text{mirror}} \lesssim 10^{-3}$ g such that $\nu_0 \simeq 100$ Hz. As already mentioned, the cantilever is sensitive to unavoidable mechanical vibrations which are the main source of error and strongly reduce the signal to noise ratio. To improve the signal-to-noise ratio we have applied the reduction technique described in [38]. This technique is based on a mechanical noise detection system whose scheme is shown in Fig. 14: A second cantilever, the parameter of which are tuned to be only sensitive to external vibration (and not to its own thermal fluctuations), is used to subtract the mechanical noise component

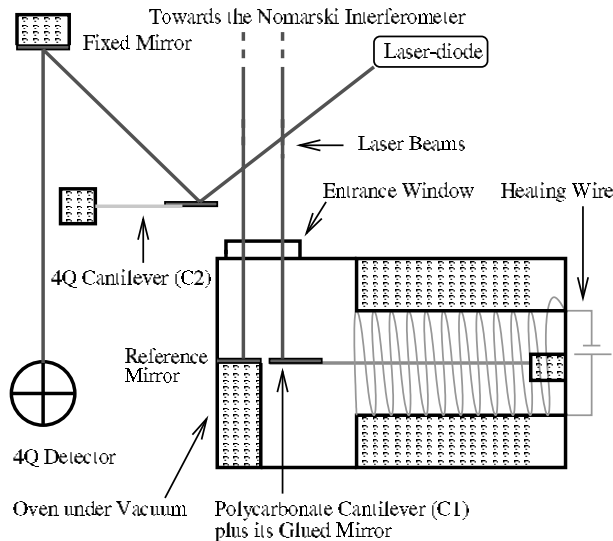


Fig. 14. Experimental setup for measuring the mechanical noise in polycarbonate The polycarbonate cantilever (C1) is inside an oven to control the temperature. Its displacement is measured by a very sensitive Nomarski Interferometer. The cantilever (C2) the laser diode, and the 4Q detector, are use for the noise reduction technique (see text)

from the signal of the polycarbonate cantilever. More details can be found in [38].

3.3 Experimental Results

We first check whether the polycarbonate cantilever verifies the FDT at room temperature. The results are shown in Fig. 15a), where the square root of the spectral density is plotted as a function of f . The dashed line is the FDT prediction obtained from a direct measurement of the cantilever response function. The agreement is good. For comparison the square root of the spectral density of the interferometer noise is plotted too. We see that the SNR is quite good. The extra picks on the spectrum of x_c come from residual mechanical vibrations. This figure shows that the experimental system is well suited to study fluctuation relations in an aging material. To study the polycarbonate cantilever noise after a quench we used a protocol that is different from that described in Sect. 1) for dielectric measurement. As polycarbonate is almost liquid above T_g it is impossible to keep it in the above described measurement cell. Thus we put the cantilever inside a box which has in the bottom a groove where the cantilever fits perfectly inside. Then this box is first heated at $T_i = 460$ K and then rapidly cooled by putting it into a cool water. Thus in a few seconds the cantilever is quenched from 460 K to about

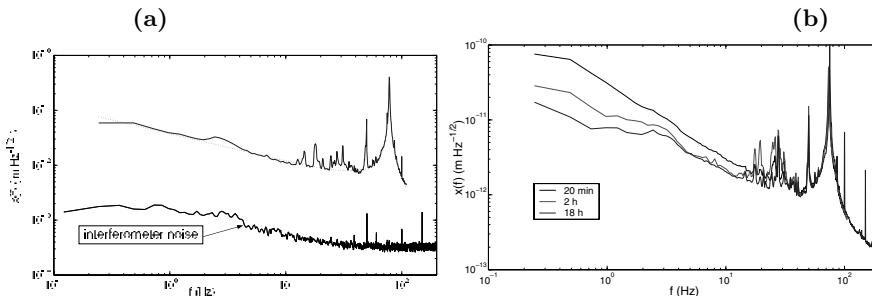


Fig. 15. Spectra of the thermal noise of the polycarbonate cantilever
(a) Equilibrium spectrum at 293K of the cantilever tip thermal fluctuations. The dashed line is the FDT prediction. the noise of the detection system (spectrum in the bottom of the figure) is shown for comparison. **(b)** Time evolution of the cantilever noise spectrum recorded at three different times $t_w = 20$ min, 2 h, 18 h after that the temperature $T_f = 393$ K has been reached from below (see text)

280 K. Then the cantilever is installed inside the measurement cell that is heated to the working temperature T_f which is now reached from low temperature. The polycarbonate ages anyway: it is well known that in aging systems the time spent at low temperature does not affect the aging at high temperature. We report here a measurement of the time evolution of the noise spectrum performed at $T_f = 0.93T_g$. A typical evolution of the polycarbonate cantilever fluctuation spectrum is plotted in Fig. 15. The spectra recorded at $t_w = 20$ min, 2 h, 18 h are shown. We see that at very short time the spectrum present a very large power law behaviour at low frequencies. This component relaxes towards equilibrium in several hours. As the response function of the cantilever evolves of just a few percent during the same amount of time it is clear that the violation of FDT is very large also in the case of this mechanical measurement. The reason is the presence of a strong intermittency as in the case of the dielectric measurements described in Sect. 2.

4 Thermal Noise in a Colloidal Glass

We review in this section results on electrical noise measurements in Laponite during the transition from a fluid like solution to a solid like colloidal glass. The main control parameter of this transition is the concentration of Laponite [42], which is a synthetic clay consisting of discoid charged particles. It disperses rapidly in water to give gels even for very low mass fraction. Physical properties of this preparation evolves for a long time, even after the sol-gel transition, and have shown many similarities with standard glass aging [3]. Recent experiments have even proved that the structure function of Laponite at low concentration (less than 3% mass fraction) is close to that of a glass, suggesting the *colloidal glass* appellation [43].

In previous studies, we showed that the early stage of this transition was associated with a small aging of its bulk electrical conductivity, in contrast with a large variation in the noise spectrum at low frequency. As a consequence, the FDT in this material appeared to be strongly violated at low frequency in young samples, and it is only fulfilled for high frequencies and long times [14, 15, 18, 19]. As in polycarbonate, this effect was shown to arise from a strong intermittency in the electrical noise of the samples, characterized by a strong deviation to a standard gaussian noise [19]. We summarize these results in the first part of this section, before presenting preliminary results on the role of concentration in the noise behavior.

4.1 Experimental Setup

The experimental setup is similar to that of previous experiments [14, 15, 19]. The Laponite [42] dispersion is used as a conductive material between the two golden coated electrodes of a cell. It is prepared in a clean N_2 atmosphere to avoid CO_2 and O_2 contamination, which perturbs the aging of the preparation and the electrical measurements. Laponite particles are dispersed at a concentration of 2.5% to 3% mass fraction in pure water under vigorous stirring for 300 s. To avoid the existence of any initial structure in the sol, we pass the solution through a $1\ \mu m$ filter when filling the cell. This instant defines the origin of the aging time t_w (the filling of the cell takes roughly two minutes, which can be considered the maximum inaccuracy of t_w). The sample is then sealed so that no pollution or evaporation of the solvent can occur. At these concentrations, light scattering experiments show that Laponite [42] structure functions are still evolving several hundreds hours after the preparation, and that solid like structures are only visible after 100 h [3]. We only study the beginning of this glass formation process.

The two electrodes of the cell are connected to our measurement system, which records either the impedance value or the voltage noise across it. The electrical impedance of the sample is the sum of two effects: the bulk is purely conductive, the ions of the solution following the forcing field, whereas the interfaces between the solution and the electrodes give mainly a capacitive effect due to the presence of the Debye layers [44]. This behavior has been validated using a four-electrode potentiostatic technique [45] to make sure that the capacitive effect is only due to the surface. In order to probe mainly bulk properties, the geometry of the cell is tuned to push the surface contribution to low frequencies: the cell consists in two large reservoirs where the fluid is in contact with the electrodes (area of $25\ cm^2$), connected through a small rigid tube – see Fig. 16(b). The main contribution to the electrical resistance of the cell is given by the Laponite sol contained in this tube connecting the two tanks. Thus by changing the length and the section of this tube the total bulk resistance of the sample can be tuned around $R_{opt} = 100\ k\Omega$, which optimizes the signal to noise ratio of voltage fluctuations measurements with our amplifier. The cut-off frequency of the equivalent R-C circuit (composed

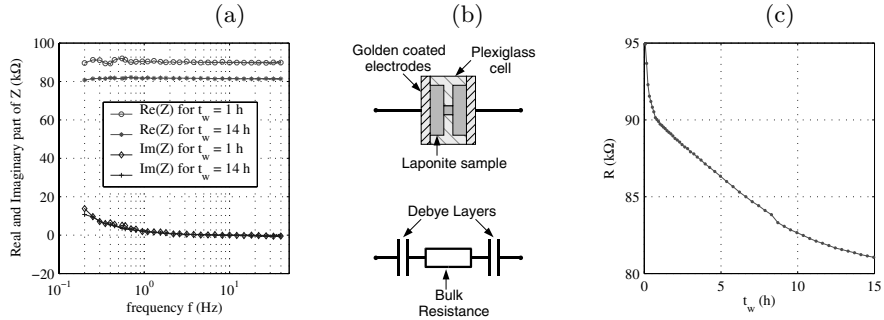


Fig. 16. Impedance of a 2.5 wt% Laponite cell. (a) Frequency dependence of a sample impedance for 2 different aging times ($t_w = 1$ h and $t_w = 14$ h). (b) Cell design and equivalent electrical model (c) Time evolution of the bulk resistance: this long time evolution is the signature of the aging of the colloidal suspension. In spite of the decreasing mobility of Laponite particles in solution during the formation of the gel, the electrical conductivity increases

by the series of the Debye layers plus the bulk resistance) is about 20 mHz. In other words above this frequency the imaginary part of the cell impedance is about zero, as shown in Fig. 16(a). The time evolution of the resistance of one of our sample is plotted in Fig. 16(c): it is still decaying in a non trivial way after 24 h, showing that the sample has not reached any equilibrium yet. This aging is consistent with that observed in light scattering experiments [3].

4.2 Electric Noise Measurements in Laponite

In order to study the voltage fluctuations across the Laponite cell, we use a custom ultra low noise amplifier to raise the signal level before acquisition. To bypass any offset problems during this strong amplification process, passive high pass filtering above 30 mHz is applied. The power spectrum density of the voltage noise of a 2.5 wt% Laponite preparation is shown in Fig. 17. As the dissipative part of the impedance $Re(Z)$ is weakly time and frequency dependent, one would expect from the Nyquist formula [46] that so does the voltage noise density S_Z . But as shown in Fig. 17, we have a large deviation from this prediction for the lowest frequencies and earliest times of our experiment: S_Z changes by several orders of magnitude between highest values and the high frequency tail. For long times and high frequencies, the FDT holds and the voltage noise density is that predicted from the Nyquist formula for a pure resistance at room temperature (300 K). In order to be sure that the observed excess noise is not due to an artifact of the experimental procedure, we filled the cell with an electrolyte solution with a pH close to that of the Laponite preparation such that the electrical impedance of the cell was the same (specifically: $NaOH$ solution in water at a concentration

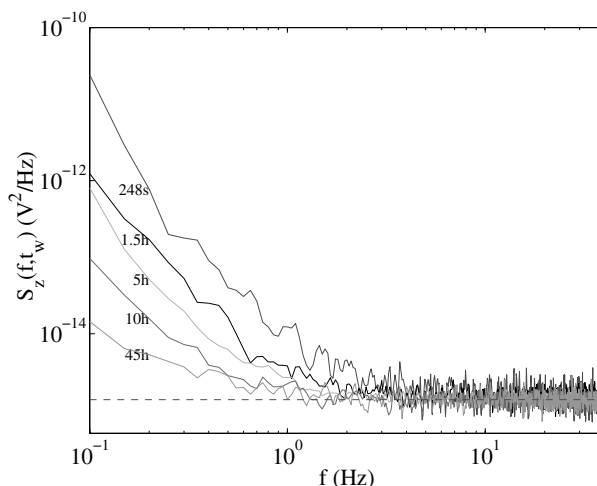


Fig. 17. Voltage noise density for a 2.5 wt% Laponite sample. The power spectrum density of voltage fluctuations across the impedance of a 2.5 wt% Laponite cell exhibit strong aging, and match the Nyquist formula prediction (*horizontal dashed line*) only for long times or large frequencies

of $10^{-3} \text{ mol} \cdot \text{l}^{-1}$). In this case, the noise spectrum was flat and in perfect agreement with the Nyquist formula [14].

Aiming at a better understanding of the physics underlying such a behavior, we have directly analyzed the voltage noise across the Laponite cell. This test can be safely done in our experimental configuration as the amplifier noise is negligible with respect to the voltage fluctuations across cell, even for the lowest levels of the signal, that is when the FDT is satisfied. In Fig. 18(a) we plot a typical signal measured 2 h after the gel preparation, when the FDT is strongly violated. The signal plotted in Fig. 18(b) has been measured when the system has relaxed and FDT is satisfied in all the frequency range. By comparing the two signals we immediately realize that there are important differences. The signal in Fig. 18(a) is interrupted by bursts of large amplitude which are responsible for the increasing of the noise in the low frequency spectra (see Fig. 17). The relaxation time of the bursts has no particular meaning, because it corresponds just to the characteristic time of the filter used to eliminate the very low frequency trends. As time goes on, the amplitude of the bursts reduces and the time between two consecutive bursts becomes longer and longer. Finally they disappear as can be seen in the signal of Fig. 18(b) recorded for a 50 h old preparation, when the system satisfies FDT.

As in polycarbonate, the intermittent properties of the noise can be characterized by the PDF of the voltage fluctuations. To compute these distributions, the time series are divided in several time windows and the PDF

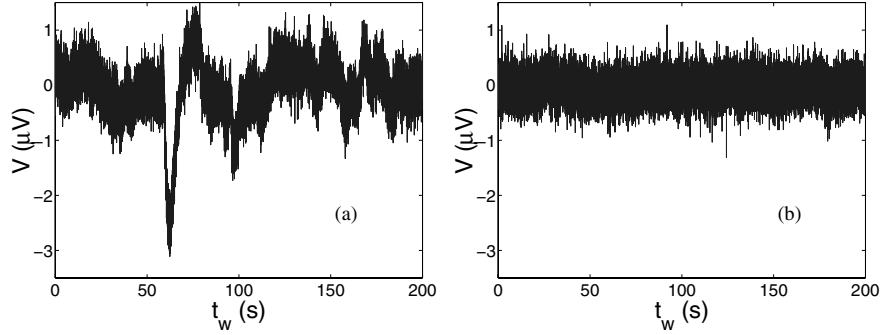


Fig. 18. Voltage noise signal in a 2.5 wt% Laponite sample. (a) Noise signal, 2 hours after the Laponite preparation, when FDT is violated. (b) Typical noise signal when FDT is not violated ($t_w = 50$ h)

are computed in each of these window. Afterwards the result of several experiments are averaged. The distributions computed at different times are plotted in Fig. 19. We see that at short t_w the PDF presents heavy tails which slowly disappear at longer t_w . Finally a Gaussian shape is recovered after $t_w = 16$ h. This kind of evolution of the PDF clearly indicate that the signal is very intermittent for a young sample and it relaxes to the Gaussian noise at long times.

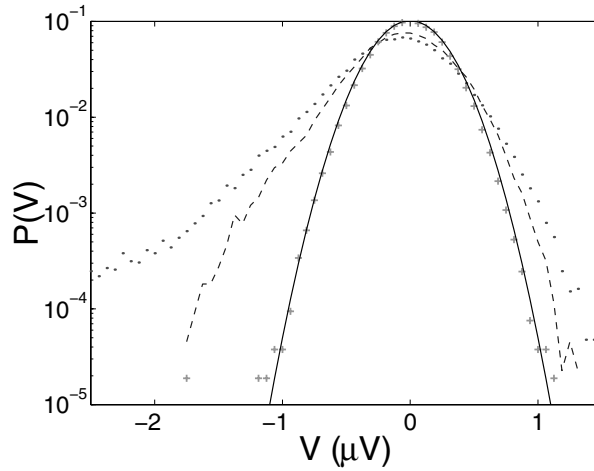


Fig. 19. PDF of the voltage noise in a 2.5 wt% Laponite sample. Typical PDF of the noise signal at different times after preparation, with from top to bottom: (...) $t_w = 1$ h, (--) $t_w = 2$ h, (+) $t_w = 50$ h. The continuous line is obtained from the FDT prediction

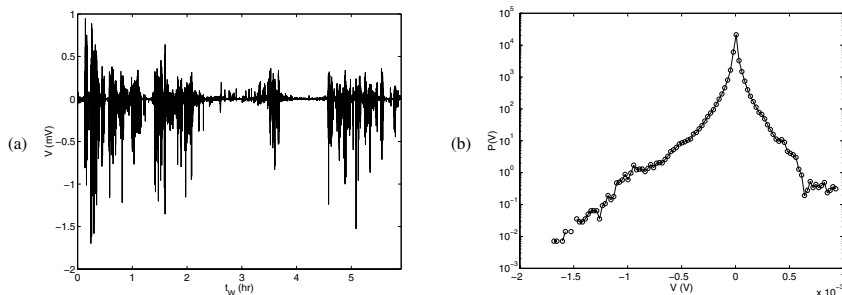


Fig. 20. Voltage noise in a 3 wt% Laponite sample. (a) During the first hours, the voltage noise is dominated by huge intermittent fluctuations: bursts over 1 mV are detected, when thermal noise should present a typical $1 \mu\text{V}$ rms. amplitude. (b) The PDF of this intermittent signal departs clearly from a gaussian distribution

4.3 Influence of Concentration

To check for the influence of concentration on these results, we recently started new series of measurements with 3 wt% Laponite preparations. In Fig. 20(a) we plot a typical signal measured during the first 6 hours of such a sample. Again, this signal is interrupted by bursts of very large amplitude. As time goes on, the amplitude of the bursts reduces and the time between two consecutive bursts becomes longer and longer. Finally they disappear after a few days, and we only observe classic thermal noise. The main difference with less concentrated samples is in the amplitude and density of this intermittency: now bursts over 1 mV are detected, when thermal noise should present a typical $1 \mu\text{V}$ rms. amplitude, and they are much more frequent. This difference is also clear on the PDF of the signal, plotted in Fig. 20(b). The non gaussian shape is much more pronounced, and the presence of heavy tails clearly indicate that the signal is very intermittent at the beginning of the experiment. In fact, the dynamic is so important that we don't even have enough precision to resolve the classic thermal fluctuations predicted by the Nyquist formula in this measurement. The influence of increasing the concentration of Laponite preparation thus appears to be somehow similar to the effect of increasing the cooling rate during the quench of the polymer glass: the resulting dynamics is more intermittent in both cases.

4.4 Mechanical Noise on Laponite

We have studied the mechanical noise of Laponite in very sensitive thermal rheometer [15] which is based on a principle very similar to the one described for the polycarbonate cantilever in Sect. 3 (see also [47]). We have found that in this case no intermittency is present and the violation of FDT, if it exists, is

certainly very small [15]. Recent measurements done on the Brownian motion of a particle inside a Laponite preparation seems to confirm these observations [48].

5 Discussion and Conclusions

In the previous sections we have presented several measurements of the electric and mechanical thermal noise in two very different materials: a polymer and a colloidal glass. We first compare the main results on the electric noise measurements which are certainly the most complete. These results are:

- (1) At the very beginning of aging the noise amplitude for both materials is much larger than what predicted by Nyquist relations. In other words Nyquist relations, or more generally FDT, are violated because the materials are out of equilibrium: they are aging. In agreement with theoretical prediction the amplitude and the persistence time of the FDT violation is a decreasing function of frequency and time. The violation is observed even at $\omega t_w \gg 1$ and it may last for more than 3 h for $f > 1$ Hz.
- (2) The noise slowly relaxes to the usual value after a very long time.
- (3) For the polymer there is a large difference between fast and slow quenches. In the first case the thermal signal is strongly intermittent, in the second case this feature almost disappears. The features of fast and slow quenches in polycarbonate are:
 - (3.1) **After a fast quench** the T_{eff} estimated using FDR is huge. This huge T_{eff} is produced by very large intermittent bursts which are at the origin of the low frequency power law decay of noise spectra. The statistic of these events is strongly non Gaussian when FDT is violated and slowly relaxes to a Gaussian one at very long t_w . The time intervals τ between two intermittent events are power law distributed with an exponent which depends on T_f .
 - (3.2) **After a slow quench** the T_{eff} estimated using FDR is about 20% larger than T_f . The intermittency disappears, the noise signal PDF are much closer to a Gaussian and the time between two large fluctuations is not power law distributed.
- (4) The colloidal suspension signal is strongly intermittent, all the more as concentration is increased. The noise signal PDF at small t_w is strongly non-Gaussian. The asymmetry of the noise may be linked to the spontaneous polarization of the cell.

We want first to discuss the intermittence of the signal, which has been observed in other aging systems. Our observations are reminiscent of the intermittence observed in the local measurements of polymer dielectric properties [13] and in the slow relaxation dynamics of another colloidal gel [21,22]. Indeed several theoretical models predict an intermittent dynamics for an aging system. For example the trap model [32] which is based on a phase space

description of the aging dynamics. Its basic ingredient is an activation process and aging is associated to the fact that deeper and deeper valleys are reached as the system evolves [23–27]. The dynamics in this model has to be intermittent because either nothing moves or there is a jump between two traps [23]. This contrasts, for example, with mean field dynamics which is continuous in time [7]. Furthermore two very recent theoretical models predict skewed PDF both for local [51] and global variable [27]. This is a very important observation, because it is worth noticing that one could expect to find intermittency in local variables but not in global. Indeed in macroscopic measurements, fluctuations could be smoothed by the volume average and therefore the PDF would be Gaussian. This is not the case both for our experiments and for the numerical simulations of aging models [27]. In order to push the comparisons with these models of intermittency on a more quantitative level one should analyze more carefully the PDF of the time between events, which is very different in the various models [26, 27, 32]. Our statistics is not yet enough accurate to give clear answers on this point, thus more measurements are necessary to improve the comparisons between theory and experiment. But the time statistics of the trap model [32] seems to fit the data better than that of [26]. The large T_{eff} produced by the intermittent dynamics merits a special comment too. Indeed such a huge T_{eff} is not specific to this class of systems, it has also been observed in domain growth models [10, 49]. The behaviour of these models is however not consistent with that of our system, because in the case of domain growth the huge temperature is given by a weak response, not by an increase of the noise signal.

Going back to the analysis of our experimental data there is another observation, which merits to be discussed. This concerns the difference between fast and slow quenches in polycarbonate. In order to discuss the problem related to this difference it is important to recall that the zero of t_w is defined as the instant in which the temperature crosses T_g . The first question that one may ask, already discussed in Sect. 2.4, is whether the behaviour of the system at the same t_w after a slow and a fast quenches is the same. This is certainly not the case because the system takes about 20 min during a slow quench to reach T_f and we have seen that after a fast quench the signal remains intermittent for many hours, whereas after a slow quench intermittency is never observed. Thus one concludes that it is not just a matter of time delay between fast and slow quenches, the dynamics is indeed very different in the two cases. This result can be understood considering that during the fast quench the material is frozen in a state which is highly out of equilibrium at the new temperature. This is not the case for a slow quench. More precisely one may assume that when an aging system is quenched very fast, it explores regions of its phase space that are completely different than those explored in the quasi-equilibrium states of a slow quench. This assumption is actually supported by two recent theoretical results [33, 34], which were obtained in order to give a satisfactory explanation, in the framework of the more recent

models, of the old Kovacs effect on the volume expansion [4]. Our results based on the noise measurements can be interpreted in the same way.

Finally, we want to discuss the analogy between the electrical thermal noise in the fast quench experiment of the polymer and that of the gel during the sol-gel transition. In spite of the physical mechanisms that are certainly very different, the statistical properties of the signals are very similar. Thus one may wonder, what is the relationship between the fast quench in the polymer and the gel formation. As already mentioned, during the fast quench the polymer is strongly out of equilibrium, which is the same situation for the liquid-like state at the very beginning of the gel transition. The speed of this transition is controlled by the initial Laponite/water concentration and therefore intermittency should be a function of this parameter. Preliminary measurements seem to confirm this guess: the higher the concentration, the stronger the intermittency.

The main consequence of these observations in the electric measurements is that the definition of T_{eff} based on FDR depends on the cooling rate (on the concentration for the colloid) and probably on T_f . In Fig. 21 we have summarized the T_{eff} obtained by electric measurements performed on glycerol [11] and on polycarbonate (Sect. 2) and by magnetic measurements performed on a spin glass [16]. Specifically we plot T_{eff}/T_g versus T_f/T_g . The straight line is the FDT prediction for T_{eff} . Looking at this figure we see that the situation is rather confused. However it becomes more clear if one takes into account the cooling rate. As the T_g is quite different in the various materials we define a relative cooling rate $Q = \frac{\partial T}{\partial t} \frac{1}{T_g}$, which takes the following values: 0.5 min^{-1} for the spin glass, 0.12 min^{-1} for the polycarbonate fast quenches ($T_f/T_g = 0.93$ and 0.79), 0.009 min^{-1} for the polycarbonate slow quenches ($T_f/T_g = 0.98$) and 0.012 min^{-1} for the glycerol experiment. Thus by considering the relative cooling rate it is clear that in the fast quenches T_{eff} is very large and in the slow quenches it is small independently of the material. However a dependence on T_f seems to be present too. Many more measurements are certainly necessary to confirm this dependence of T_{eff} on T_f and on the cooling rate.

Let us now briefly discuss the results on the mechanical thermal noise. To the best of our knowledge there are only three measurements done on this kind of noise in aging systems, one in polycarbonate (Sect. 3) and two in Laponite [15,48]. The two measurements done in Laponite show that for short t_w there is no intermittency and the violation of FDT is very small. Thus in the case of this colloidal glass different observables give different T_{eff} . However this result contrasts with the one described in Sect. 3 where we have shown that the measurements of the mechanical thermal noise agree with the electric ones because after a fast quench both measurements confirm the presence of a strong intermittency in the aging dynamics of polycarbonate. This comparison between the mechanical and electric measurements in polycarbonate is at the moment rather qualitative due to the difficulty of the

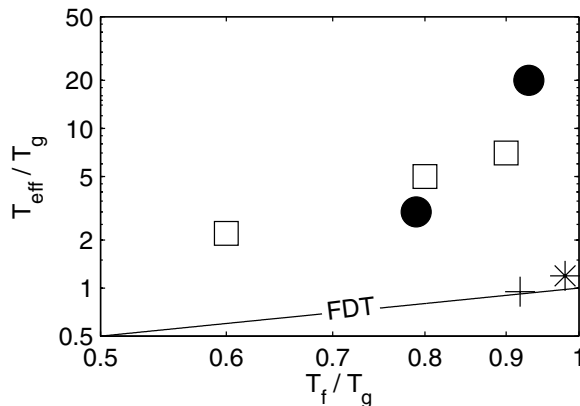


Fig. 21. T_{eff} as a function of T_f . T_{eff} measured in several experiments on different types of glasses at the beginning of the aging regime. (+) glycerol ($f = 7$ Hz) [11], (\square) spin glass ($q = q_{min}$) [16], (\bullet) polycarbonate ($f = 7$ Hz, fast quench), ($*$) polycarbonate ($f = 7$ Hz, slow quench)

mechanical measurements. Much more precise data are certainly necessary to give a clear answer. The difference between the mechanical noise in polycarbonate and in Laponite is still unexplained. It is certainly related with the fact the intermittency in the electrical measurements in Laponite is related to the important role played by the ions in the gel formation.

We want to conclude by a few important and general questions which remain opens. The first concerns the quench rate. Indeed, is it the speed in which T_g is crossed that determines the dynamics or the time in which T_f is approached? This question has been already studied in the context of response functions but it will be important to analyze it in terms of noise. The second important open question is why in realistic simulations of Lenard-Jones glasses intermittency has not been observed [52,53]. Several hypothesis can be done: (i) The simulations are done for a time which is too short to observe intermittency which is a very slow phenomenon. (ii) In the simulation the quench are performed at imposed volume, this is a big difference with respect to the experiments which are done at imposed pressure. A third open question concerns the different dynamics of the thermal noise measured on different observables. Indeed even from a theoretical point view the effective temperature of different observables is the same in certain models [54] and different in others [23]. This is certainly a useful information that can give new insight to the problem of the mechanisms of aging dynamics in different materials.

This lecture clearly shows the importance of associating thermal noise and response measurements. As we have already pointed out in the introduction the standard techniques, based on response measurements and on the

application of thermal perturbations to the sample, are certainly important to fix several constraints for the phase space of the system. However they do not give information on the dynamics of the sample, which can be obtained by the study of FDR and of the fluctuation PDF.

Acknowledgments

We acknowledge useful discussions with J.L. Barrat, J. P. Bouchaud, S. Franz and J. Kurchan. We thank P. Metz, F. Vittoz and D. Le Tourneau for technical assistance. This work has been partially supported by the DYGLAGE-MEM contract of EEC, and by the contract "Vieillessement des matériaux amorphes" of Région Rhône-Alpes.

References

1. L.C. Struick, *Physical aging in amorphous polymers and other materials* (Elsevier, Amsterdam, 1978).
2. *Spin Glasses and Random Fields*, edited by A. P. Young, Series on Directions in Condensed Matter Physics Vol.12 (World Scientific, Singapore 1998).
3. M. Kroon, G. H. Wegdam, and R. Sprik, "Dynamic light scattering studies on the sol-gel transition of a suspension of anisotropic colloidal particles", *Phys. Rev. E* **54**, p. 1, 1996.
4. A.J. Kovacs, *La contraction isotherme du volume des polymères amorphes*, *Journal of polymer science*, **30**, p. 131–147, (1958).
5. K. Jonason, E. Vincent, J. Hamman, J. P. Bouchaud, *Memory and chaos effects in spin glasses*, *Phys. Rev. Lett.*, **81**, 3243 (1998).
6. L. Bellon, S. Ciliberto, C. Laroche, *Advanced Memory effects in the aging of a polymer glass*, *Eur. Phys. J. B.*, **25**, 223, (2002).
7. L. Cugliandolo, J. Kurchan, *Analytical Solution of the Off Equilibrium Dynamics of a Long Range Spin Glass Model*, *Phys. Rev. Lett.*, **71**, p. 173, (1993).
8. J.P. Bouchaud, L. F. Cugliandolo, J. Kurchan, M. Mézard, *Out of equilibrium dynamics in Spin Glasses and other glassy systems*, in *Spin Glasses and Random Fields*, ed A.P. Young (World Scientific, Singapore 1998). (also in cond-mat/9702070)
9. L. Cugliandolo, *Effective temperatures out of equilibrium*, to appear in *Trends in Theoretical Physics II*, eds. H Falomir et al, Am. Inst. Phys. Conf. Proc. of the 1998 Buenos Aires meeting, cond-mat/9903250
10. L. Cugliandolo, J. Kurchan, L. Peliti, *Energy flow, partial equilibration and effective temperatures in systems with slow dynamics*, *Phys. Rev. E*, **55**, p. 3898 (1997).
11. T. S. Grigera, N. Israeloff, *Observation of Fluctuation-Dissipation-Theorem Violations in a Structural Glass*, *Phys. Rev. Lett.*, **83**, p. 5038 (1999).
12. W.K. Kegel, A. van Blaaderen *Direct observation of dynamical heterogeneities in colloidal hard-sphere suspensions*, *Science*, **287**, p. 290, (2000).
13. E. Vidal Russel, N. E. Israeloff, *Direct observation of molecular cooperativity near the glass transition*, *Nature*, **408**, 695 (2000).

14. L. Bellon, S. Ciliberto, C. Laroche, *Violation of fluctuation dissipation relation during the formation of a colloidal glass*, *Europhys. Lett.*, **53**, 511 (2001).
15. L. Bellon, S. Ciliberto, *Experimental study of fluctuation dissipation relation during the aging process*, *Physica D*, **168**, 325 (2002).
16. D. Herrisson, M. Ocio, *Fluctuation-dissipation ratio of a spin glass in the aging regime*, *Phys. Rev. Lett.*, **88**, 257702 (2002).
17. E.R. Weeks, D.A. Weitz *Properties of cage rearrangements observed near the colloidal glass transition*, *Phys. Rev. Lett.*, **89**, p. 95704, (2002).
18. L. Buisson, A. Garcimartin, S. Ciliberto, *Intermittent origin of the large fluctuation-dissipation relations in an aging polymer glass*, *Europhys. Lett.*, **63**, p. 603, (2003).
19. L. Buisson, L. Bellon and S. Ciliberto, *Intermittency in aging*, *J. Phys.: Condens. Matter* **15**, pp. S1163-S1179, 2003.
20. L. Buisson, S. Ciliberto, "Off equilibrium fluctuations in a polymer glass", *Physica D*, **204**, p. 1 (2005).
21. L. Cipelletti, H. Bissig, V. Trappe, P. Ballestat, S. Mazoyer, *Direct observation of dynamical heterogeneities in colloidal hard-sphere suspensions*, *J. Phys: Condens. Matter*, **15**, p. S257, (2003).
22. H. Bissig, V. Trappe, S. Romer, Luca Cipelletti, *Intermittency and non-Gaussian fluctuations in the dynamics of aging colloidal gels*, submitted *Phys.Rev.Lett.*
23. S. Fielding, P. Sollich, *Observable dependence of Fluctuation dissipation relation and effective temperature*, *Phys. ReV Lett.*, **88**, 50603-1, (2002).
24. A. Perez-Madrid, D. Reguera, J.M. Rubi, *Physica A*, **329**, 357 (2003).
25. M. Naspreda, D. Reguera, A. Perez-Madrid, J.M. Rubi, *Glassy dynamics: effective temperatures and intermittencies from a two-state model*, *cond-mat/0411063*
26. P. Sibani, and J. Dell, *Europhys. Lett.* **64**, p. 8, 2003.
27. P. Sibani, H. J. Jensen, *Intermittency, aging and record fluctuations*, *cond-mat/0403212*
28. C.G. Robertson, G. L. Wilkes, *Long term volume relaxation of bisphenol A polycarbonate and atactic polystyrene*, *Macromolecules* **33**, 3954 (2000).
29. L. Saviot, E. Duval, J.F. Jal, A.J. Dianoux, *Very fast relaxation in polycarbonate glass* *Eur. Phys. J. B.*, **17** (4), 661, (2000).
30. R. Quinson, *Caractérisation et modélisation de la déformation non élastique des polymères amorphes à l'état solide*, *Ph.D. thesis, (INSA), (1998)*.
31. J.P.Bouchaud, *Weak ergodicity breaking and aging in disordered systems*, *J.Phys. I France*, **2**, p. 1705, (1992).
32. J.P. Bouchaud, D. S. Dean, *Aging on Parisi's tree*, *J. Phys. I France*, **5**, 265 (1995).
33. E.M.Bertin, J.P.Bouchaud, J. M. Drouffe, C. Godreche, *The Kovacs effect in model glasses*, *J. Phys. A: Math. Gen* **36**, 10701 (2003).
34. S. Mossa, F. Sciortino, *Kovacs effects in aging molecular liquid*, *Phys. Rev. Lett.* **92**, 045504 (2004).
35. L.D. Landau, E.M. Lifshitz, *Theory of Elasticity*, 3rd edition, Butterworth-Heinemann (1986)
36. N.G. McGrum, B.E. Read, G. Williams, *Anelastic and Dielectric Effects in Polymeric Solids*, Wiley (1967)
37. L.D. Landau, E.M. Lifshitz, *Statistical Physics*, Part 1, 3rd edition, Butterworth-Heinemann (1980)

38. F. Douarche, L. Buisson, S. Ciliberto, A. Petrosyan, *A Simple Noise Subtraction Technique*, Rev. Sci. Inst., 75,12, 5084 (2004).
39. G. Nomarski, *Microinterféromètre à ondes polarisées*, J. Phys. Radium **16**, 9S-16S (1954).
40. M. Françon, S. Mallick, *Polarization Interferometers*, Wiley (1971).
41. L. Bellon, S. Ciliberto, H. Boubaker, L. Guyon, *Differential interferometry with a complex contrast*, Optics Communications **207**, 49–56 (2002).
42. Laponite RD is a registered trademark of Laporte Absorbents, P.O Box 2, Cheshire, UK.
43. D. Bonn, H. Tanaka, G. Wegdam, H. Kellay, and J. Meunier, “Aging of a colloidal “Wigner” glass,” *Europhysics Letters*, **45**, p. 52, 1999; D. Bonn, H. Kellay, H. Tanaka, G. Wegdam, and J. Meunier, *Langmuir*, **15**, p. 7534, 1999.
44. R. Hunter, *The foundation of colloid science*, Oxford Science Publications, 1989.
45. J. Koryta, L. Dvorak and L. Kavan, *Principles of Electrochemistry - 2nd Ed.*, Wiley, 1993.
46. H. Nyquist, “Thermal agitation of electrical charge in conductors,” *Phys. Rev.* **32**, pp. 110–113, 1928.
47. L. Bellon, L. Buisson, S. Ciliberto, F. Vittoz, *Zero applied stress rheometer*, Rev. Sci. Instrum. 73, 9, 3286–3290 (2002).
48. B. Abou, F. Gallet, *Probing an nonequilibrium Einstein relation in an aging colloidal glass*, Phys. Rev. Lett., **93**, 160603 (2004).
49. A. Barrat, *Monte-Carlo simulations of the violation of the fluctuation-dissipation theorem in domain growth processes*, Phys. Rev., **E57**, p. 3629 (1998).
50. L. Buisson, M. Ciccotti, L. Bellon, S. Ciliberto, *Electrical noise properties in aging materials.*, In: Fluctuations and Noise in Materials, edited by D. Popovic, M.B. Weissman and Z.A. Racz. Proceedings of SPIE Vol. 5469 (SPIE, Bellingham, WA, 2004). Invited paper. pp. 150–163.
51. A. Crisanti, and F. Ritort, *Intermittency of Glassy relaxation and the emergence of non-equilibrium spontaneous measure in the aging regime*, Europhys. Lett. **66** (2): 253(2004).
52. W. Kob, J. L. Barrat, *Aging effects in a Lennard Jones Glass*, Phys. Rev. Lett., **78**, p. 4581 (1997).
53. J. L. Barrat, W. Kob, *Fluctuation dissipation ratio in an aging Lennard-Jones* Europhys. Lett., **46**, p. 637 (1999).
54. L. Berthier, J.L. Barrat, *Shearing a glassy material: Numerical tests of non-equilibrium mode-coupling approaches and experimental proposals*, Phys. Rev. Lett., **89**, 095702 (2002).

Jamming in Dense Granular Media

A. Coniglio, A. Fierro, A. de Candia, M. Nicodemi,
M. Tarzia, and M. Pica Ciamarra

Dipartimento di Fisica, Università di Napoli “Federico II”, INFN, Coherentia and Unità di Napoli, Complesso Universitario Monte Sant’Angelo, Via Cinthia, 80126, Napoli, Italy

We review some recent results on Statistical Mechanics approach to dense granular media. In particular, by analytical mean field investigation we derive the phase diagram of a monodisperse system. We show that “jamming” corresponds to a phase transition from a “fluid” to a “glassy” phase. The nature of such a “glassy” phase turns out to be the same found in mean field models for glass formers. This gives quantitative evidence to the idea of a unified description of the “jamming” transition in granular media and thermal systems, such as glasses.

1 Introduction

A deep connection between the glass transition in molecular glass formers, structural arrest in colloidal systems, and jamming transition in granular media [1–6] has often been stressed in the past few years. In spite of the fact that these systems are very different one from each other, varying suitably the control parameters, a slowdown and a subsequent structural arrest in a solid-like disordered state are found in each of them. In [2, 6] a possible phase diagram for jamming is suggested, which takes into account the fact that jamming is obtained either raising the volume fraction or lowering the temperature or lowering the applied stress. Colloidal suspensions and molecular glass formers are both thermal systems, and it is commonly accepted that both colloidal glass transition and molecular glass transition are of the same type despite of the fact that different control parameters may drive the transition. The case of granular materials is instead very different: They are athermal systems, since the thermal fluctuations are significantly less than the gravitational energy and the system cannot explore the phase space without any external driving. Nevertheless an exceedingly slowing down is observed when a granular material is shaken at low shaking amplitude, or flows under a low shear stress, with strong analogies with the slowing down observed in glass formers. Experimental and numerical studies [4–7] have confirmed this connection, however its precise nature is still unclear [3, 6].

In the present paper in order to study this connection we apply a statistical mechanics approach to granular media. This approach, which has been extensively developed in previous works [8, 9], is based on an elaboration of

the original ideas suggested by Edwards [10]. The basic assumption is that for a granular system subject to an external drive (e.g. tapping), after having reached stationarity, time averages coincide with suitable ensemble averages over the “mechanically stable” states. We have shown [9] that this assumption works for different lattice models namely that a generalized Gibbs distribution of the stable states describes with good approximation the stationary state attained by the system under tapping dynamics. Here each tap consists in raising the bath temperature to a finite value (called tap amplitude) and, after a lapse of time (called tap duration) quenching the bath temperature back to zero. By cyclically repeating the process the system explores the space of the mechanically stable states.

We thus consider one of the above lattice model for which the statistical mechanics approach works. The model is made up of hard spheres under gravity. Then we apply standard statistical mechanics methods in order to investigate analytically the existence and the nature of a possible jamming transition. More precisely we consider the Bethe-Peierls approximation using the cavity method [11, 12]: By changing the control parameter a phase transition from a fluid to a crystal is found, and, when crystallization is avoided, a glassy phase appears. The nature of this glassy phase is analogous to that found in mean field models for glass formers [12–14]: In particular we observe a dynamical transition, where an exponentially high number of metastable states appears, and at a lower temperature a thermodynamic discontinuous phase transition to a glassy state. A brief account of these calculations can be found in [15].

However, $3d$ numerical simulations of the model described above show a strong tendency to crystallize. For this reason we also consider here a variant of the model [13] which has the virtue of avoiding crystallization. We find that the system under gravity evolved by Monte Carlo taps presents features characteristic of real granular media [16, 17], and at low tap amplitudes a dynamical transition with properties recalling those of usual glass formers. In particular we observe a dynamical non linear susceptibility with a maximum at increasing time: This behavior, typical of glass formers, is usually interpreted as the sign of dynamic heterogeneities in the system.

In conclusions the results confirm early speculations about the deep connection between the jamming transition in granular media and the glass transition in usual glass formers, giving moreover a precise interpretation to its nature.

In Sects. 2, 3, 4, and 5 we review the statistical mechanics approach to granular materials. In Sect. 6 based on this approach we use standard method of statistical mechanics in order to study the jamming transition in granular materials. Finally in Sect. 7 the $3d$ model is presented and the numerical results are shown.

2 Statistical Mechanics of Dense Granular Materials

In this section we summarize the essential ideas in the statistical mechanics of dense granular media. These are strongly dissipative systems not affected by temperature, because thermal fluctuations are usually negligible. Therefore, the usual temperature of the external bath can be considered zero and these media called *non-thermal*. As the system cannot explore its phase space (unless perturbed by external forces, such as shaking or tapping) it is frozen, at rest, in its mechanically stable microstates, also called inherent states in analogy with the glass terminology.

In the statistical mechanics of powders introduced by Edwards [10] it is postulated that the system at rest (i.e., not in the “fluidized” regime) can be described by suitable ensemble averages over its “mechanically stable” states.

The simplest assumption about the ensemble distribution at stationarity is that the probability, P_r , to find the system in one of its mechanically stable state r is given by [9] the maximization of the system entropy,

$$S = - \sum_r P_r \ln P_r \quad (1)$$

with the macroscopic constraint, in the case of the canonical ensemble, that the system average energy, $E = \sum_r P_r E_r$, is given. This assumption leads to the Gibbs result:

$$P_r \propto e^{-\beta_{conf} E_r} \quad (2)$$

where β_{conf} is a *Lagrange multiplier*, called *inverse configurational temperature*, enforcing the above constraint on the energy:

$$\beta_{conf} = \frac{\partial S_{conf}}{\partial E} \quad S_{conf} = \ln \Omega(E) \quad (3)$$

Here, $\Omega(E)$ is the number of mechanically stable states with energy E . Thus, summarizing, the system at rest has $T_{bath} = 0$ and $T_{conf} = \beta_{conf}^{-1} \neq 0$.

These basic considerations, to be validated by experiments or simulations, settle a theoretical Statistical Mechanics framework to describe granular media. Consider, for definiteness, a system of monodisperse hard spheres of mass m . In the system whole configuration space Ω_{Tot} , we can write Edwards’ generalized partition function as:

$$Z = \sum_{r \in \Omega_{Tot}} \exp(-\mathcal{H}_{HC} - \beta_{conf} mgH) \cdot \Pi_r \quad (4)$$

where \mathcal{H}_{HC} is the hard core interaction between grains, mgH is the gravity contribution to the energy (H is particles height), and the factor Π_r is a projector on the space of “mechanically stable” states.

As well as in usual equilibrium “thermal” Statistical Mechanics, it is straightforward to verify that in the present approach a “standard” (i.e., not

“out-of-equilibrium”) Fluctuation Dissipation (FD) Theorem holds linking at stationarity, for instance, the system average energy, E , to its fluctuations, ΔE^2 :

$$-\frac{\partial E}{\partial \beta_{conf}} = \Delta E^2 . \quad (5)$$

Usefully, the integration of such *equilibrium* FD relation may provide direct access to β_{conf} from energy (or density, etc.) data measured at stationarity [9]:

$$\beta_{conf}(E) = \beta_{conf}^0 - \int_{E_0}^E (\Delta E^2)^{-1} dE . \quad (6)$$

Summarizing, such an “equilibrium” statistical mechanics approach is based on the hypothesis that at stationarity the system properties do not depend on the details of the dynamical history. This has to be checked by computer simulations and experiments. The next step is to verify that a few macroscopic parameters (such as energy or density, etc.) are completely characterizing the status of the system, i.e., that a “thermodynamic” description is indeed possible. In such a case, β_{conf} can be derived, for example, from (6). Finally, one must check that time averages obtained using such a dynamics compare well with ensemble averages over the distribution (2).

In the following sections we discuss some recent results [9] about schematic models validating and generalizing Edwards’ Statistical Mechanics approach. In particular, we show by mean field analytical calculations that granular media undergo a phase transition from a (supercooled) “fluid” phase to a “glassy” phase, when their crystallization transition is avoided. The nature of such a “glassy” phase results to be the same found in mean field models for glass formers: a discontinuous one step Replica Symmetry Breaking phase preceded by a dynamical freezing point. These results are supported by Monte Carlo (MC) “tap dynamics” simulations which, in the region of low MC shaking amplitudes, show a pronounced jamming similar to the one found in experiments on granular media.

3 Monodisperse Hard Sphere Model for Granular Materials

The simplest model for granular media we considered [9] is a system of hard-spheres of equal diameter $a_0 = \sqrt{2}$, subjected to gravity. We have studied this model on a lattice, constraining the centers of mass of the spheres on the sites of a cubic lattice (see inset in Fig. 3). The Hamiltonian of the system is:

$$\mathcal{H} = \mathcal{H}_{HC}(\{n_i\}) + gm \sum_i n_i z_i , \quad (7)$$

where the height of site i is z_i , $g = 1$ is gravity acceleration, $m = 1$ the grains mass, $n_i = 0, 1$ the usual occupancy variable (i.e., $n_i = 0$ or 1 if site i

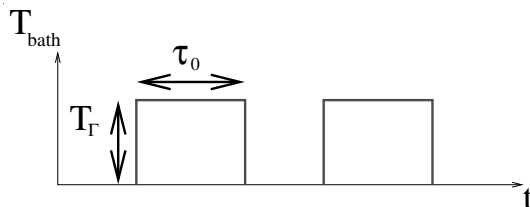


Fig. 1. Our lattice models for granular media are subject to a Monte Carlo dynamics made of “taps” sequences. A “tap” is a period of time, of length τ_0 (the tap duration), during which the system evolves at a finite bath temperature T_T (the tap amplitude); after each “tap” the system evolves at $T_T = 0$ and reaches a mechanically stable state

is empty or filled by a grain) and $\mathcal{H}_{HC}(\{n_i\})$ an hard-core interaction term that prevents the overlapping of nearest neighbor grains (this term can be written as $\mathcal{H}_{HC}(\{n_i\}) = J \sum_{\langle ij \rangle} n_i n_j$, where the limit $J \rightarrow \infty$ is taken).

We perform a standard Metropolis algorithm on the system. The particles, initially prepared in a random configuration, are subject to taps (see Fig. 1), each one followed by a relaxation process. During a tap, for a time τ_0 (called tap duration), the temperature is set to the value T_T (called tap amplitude), so that particles have a finite probability, $p_{up} \sim e^{-mg/T_T}$, to move upwards. During the relaxation the temperature is set to zero, so that particles can only reduce the energy, and therefore can move only downwards. The relaxation stops when the system has reached a blocked state, where no grain can move downwards. Our measurements are performed at this stage when the shake is off and the system is at rest. The time, t , is the number of taps applied to the system.

Under such a tap dynamics the systems reaches a stationary state where the Statistical Mechanics approach to granular media can be tested, and particularly Edwards hypothesis can be verified by comparing time averages to ensemble averages of (2).

4 Stationary States and Time Averages

During the tap dynamics, in the stationary state, the time average of the energy, \bar{E} , and its fluctuations, $\overline{\Delta E^2}$, are calculated. Figure 2 shows \bar{E} (main frame) and $\overline{\Delta E^2}$ (inset) as function the tap amplitude, T_T , (for several values of the tap duration, τ_0). Since sequences of taps, with same T_T and different τ_0 , give different values of \bar{E} and $\overline{\Delta E^2}$, it is apparent that T_T is not the right thermodynamic parameter. On the other hand, if the stationary states are indeed characterized by a *single* thermodynamic parameter the curves corresponding to different tap sequences (i.e. different T_T and τ_0) should collapse onto a single master function, when $\overline{\Delta E^2}$ is parametrically plotted

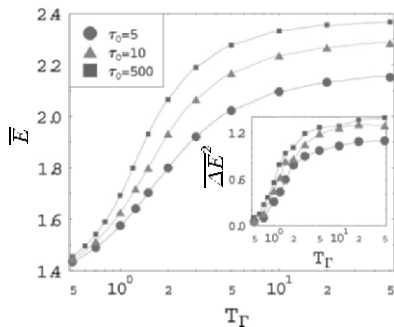


Fig. 2. The time average of the energy, \bar{E} , and (inset) its fluctuations, $\overline{\Delta E^2}$, recorded at stationarity during a tap dynamics, as a function of the tap amplitude, T_Γ , in the 3D lattice monodisperse hard sphere model. Different curves correspond to sequences of tap with different values of the duration of each single tap, τ_0

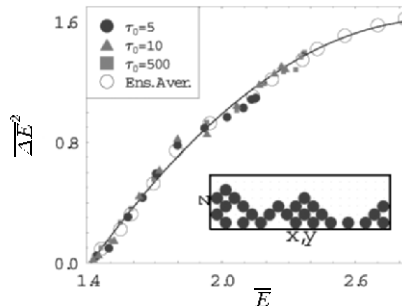


Fig. 3. Time averages of energy fluctuations $\overline{\Delta E^2}$ plotted as function of the time average of energy \bar{E} . Filled circles, triangles and squares are time averages obtained with different tap dynamics. Empty circles are independently calculated ensemble. The collapse of the data obtained with different dynamics shows that the system stationary states are characterized by a *single* thermodynamic parameter. The agreement with the ensemble averages show the success of Edwards' approach to describe the system macroscopic properties

as function of \bar{E} . This is the case in the present model, where the data collapse is in fact found and shown in Fig. 3. This is a prediction that could be easily checked in real granular materials.

A technique to derive from raw data the thermodynamic parameter β_{fd} conjugated to E (apart from an integration constant, β_0), is through the usual *equilibrium* Fluctuation-Dissipation relation of (5). By integrating (5), (6) is obtained and $\beta_{fd} - \beta_0$ can be expressed as function of \bar{E} or (for a fixed value of τ_0) as function of $\beta_\Gamma = 1/T_\Gamma$: $\beta_{fd} - \beta_0 \equiv g(\beta_\Gamma)$ (the constant β_0 can be determined as explained in [9]). By now, we use the name β_{fd} for the thermodynamic parameter conjugated to E because we can conclude that $\beta_{fd} = \beta_{conf}$ only when the average over the tap dynamics and the ensemble average with (2) coincide. Thus, even though we have just shown that a “thermodynamic”, i.e., a Statistical Mechanics description is indeed possible, we have still to show that specifically the distribution of (2) holds. This is accomplished in the next section.

5 Ensemble Averages

Summarizing, in Sect. 4 we have found that the fluctuations of the energy in the stationary state depend only on the energy, E , and not on the past history. More generally, we found [9] that all the macroscopic quantities we observed depend only on the energy, E , or on its conjugate thermodynamic parameter, β_{fd} , thus the stationary state can be genuinely considered a “thermodynamic state”.

We now show that ensemble averages based on the theoretical distribution of (2) coincide with time averages over the tap dynamics. We compare, for instance, the time average of the energy, $\overline{E}(\beta_{fd})$, recorded during the taps sequences, with the ensemble average, $\langle E \rangle(\beta_{conf})$, over the distribution (2). To this aim we have independently calculated the ensemble average $\langle E \rangle$, as function of β_{conf} . Fig. 4 (see also Fig. 3) shows a very good agreement between $\langle E \rangle(\beta_{conf})$ and $\overline{E}(\beta_{fd})$ (notice that there are no adjustable parameters). Such an agreement was found for all the observables we considered [9]. In Fig. 4 (inset) we also show the dependence of the configurational temperature T_{conf} on the parameters of the tap dynamics T_Γ and τ_0 . Finally, we mention that we have also successfully tested Edwards scenario in an other model, the “frustrated lattice gas” [9], a system in the category of spin glasses.

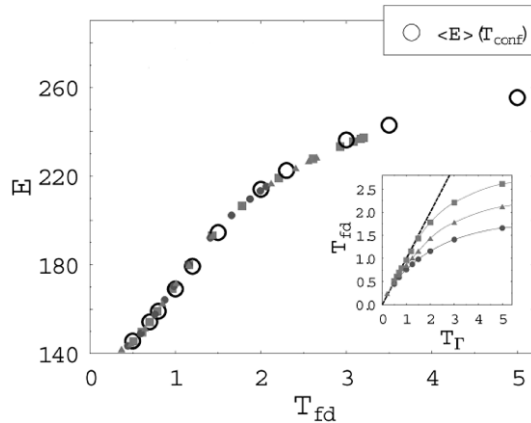


Fig. 4. Main frame The time average \overline{E} and the ensemble average over the distribution (2) $\langle E \rangle$, plotted respectively as a function of T_{fd} and T_{conf} (in units $mg a_0$), in the 3D monodisperse hard-sphere system under gravity described in the text. Symbols are as in Fig. 3. Time averages over the tap dynamics and Edwards’ ensemble averages coincide. **Lower Inset** The temperature $T_{fd} \equiv \beta_{fd}^{-1}$ defined by (5) as function of T_Γ (in units $mg a_0$) for $\tau_0 = 500, 10, 5$ MCS (from top to bottom). The straight line is the function $T_{fd} = T_\Gamma$

6 Mean Field Solution in the Bethe-Peierls Approximation

Having shown in previous sections that in the model (7) the partition function is given by (4), in the present section we show the phase diagram of the model, (7), obtained using a mean field theory in the Bethe-Peierls approximation (see [11,12] and refs therein), based on a random graph (plotted in Fig. 5) which keeps into account that the gravity breaks up the symmetry along the z axis. This lattice is made up by H horizontal layers (i.e., $z \in \{1, \dots, H\}$). Each layer is a random graph of connectivity, $k - 1 = 3$. Each site in layer z is also connected to its homologous site in $z - 1$ and $z + 1$ (the total connectivity is thus $k + 1$). Locally the graph has a tree-like structure but there are loops whose length is of order $\ln N$, insuring geometric frustration. In the thermodynamic limit only very long loops are present. The details of calculations are given in [27] (see also [15, 18] where this mean field theory was first introduced).

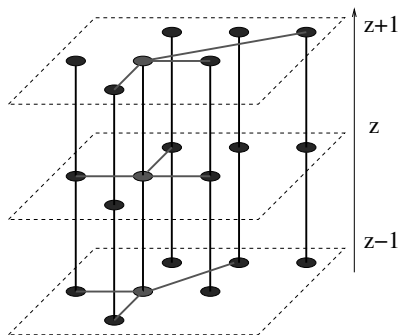


Fig. 5. In the mean field approximation, the grains are located on a Bethe lattice, sketched in the figure, where each horizontal layer is a random graph of given connectivity. Homologous sites on neighboring layers are also linked and the overall connectivity, c , of the vertices is $c \equiv k + 1 = 5$

We solve the recurrence equations found in the Bethe-Peierls approximation in three cases: 1) A fluid-like homogeneous phase; 2) a crystalline-like phase characterized by the breakdown of the horizontal translational invariance; 3) a glassy phase described by a 1-step Replica Symmetry Breaking (1RSB).

The results of the calculations are summarized in Fig. 6, where the bulk density at equilibrium, $\Phi \equiv N_s / (2\langle z \rangle - 1)$ [19] (where $\langle z \rangle$ is the average height) is plotted as a function of the configurational temperature, T_{conf} , for a given value of the number of grains per unit surface, N_s . We found that at high T_{conf} a homogeneous solution corresponding to the fluid-like phase is found. By lowering T_{conf} at T_m a phase transition to a crystal phase

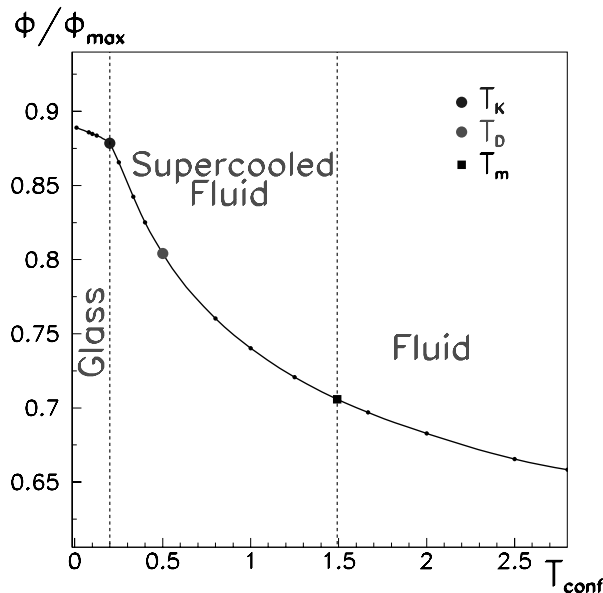


Fig. 6. The density, $\Phi \equiv N_s/(2\langle z \rangle - 1)$, for $N_s = 0.6$ as a function of T_{conf} . Φ_{max} is the maximum density reached by the system in the crystal phase

(an anti-ferromagnetic solution with a breakdown of the translation invariance) occurs. The fluid phase still exist below T_m as a metastable phase corresponding to a supercooled fluid when crystallization is avoided. Finally a 1RSB solution (found with the cavity method [11]), characterized by the presence of a large number of local minima in the free energy [11], appears at T_D , and becomes stable at a lower point T_K , where a thermodynamic transition from the supercooled fluid to a 1RSB glassy phase takes place. The temperature T_D , which is interpreted in mean field as the location of a dynamical transition where the relaxation time diverges, in real systems might instead correspond to a crossover in the dynamics (see [12, 14, 20] and Refs. therein). $\Phi(T_{conf})$ has a shape very similar to that observed in the “reversible regime” of tap experiments [16, 21]. The location of the glass transition, T_K , corresponds to a cusp in the function $\Phi(T_{conf})$. The dynamical crossover point T_D might correspond to the position of a characteristic shaking amplitude Γ^* found in experiments and simulations where the “irreversible” and “reversible” regimes approximately meet.

The model, (7), simulated in $3d$ by means of Monte Carlo tap dynamics [15] presents a transition from a fluid to a crystal as predicted by the mean field approximation, density profiles in good agreement with the mean field ones, and in the fluid phase a large increase of the relaxation time as a function of the inverse tap amplitude. In the following section we study a

more complex model for hard spheres, where an internal degree of freedom allows to avoid crystallization [13].

7 Hard Spheres with an Internal Degree of Freedom

The Hamiltonian of the model is

$$\mathcal{H} = \sum_{\langle ij \rangle} n_i n_j \phi_{ij}(\sigma_i, \sigma_j) + mg \sum_i n_i z_i, \quad (8)$$

where z_i is the height of site i , $g = 1$ is the gravity acceleration, $m = 1$ the grain mass, $n_i \in \{0, 1\}$ is the occupancy variable (absence or presence of a grain on site i), $\sigma_i \in \{1, \dots, q\}$ represents the internal degree of freedom (which we call spin), and $\phi_{ij}(\sigma_i, \sigma_j)$ is the interaction energy between spins. Different values of the spin correspond to different positions of the particle inside the cell. It is reasonable that a few number of internal states might be enough to catch the main features of real systems.

As in [13] we study a simple realization of the model described by (8). Interpreting the spin as position of the particle in the cell, our choice can be easily visualized in $2d$, as shown in Fig. 7. We partition the space in square cells, and subdivide each cell into four internal positions (namely $q = 4$). When a cell is occupied by a particle in any given position, a hard-core repulsion excludes the presence of particles in some of the internal states of the neighboring cells (namely the interaction $\phi_{ij}(\sigma_i, \sigma_j)$ is chosen zero if the positions σ_i and σ_j are “compatible”, and infinite otherwise). This choice can be interpreted as a coarse grained version of a hard sphere system in the continuum. In $3d$ we subdivide the space into cubic cells, and considers six internal positions instead of four.

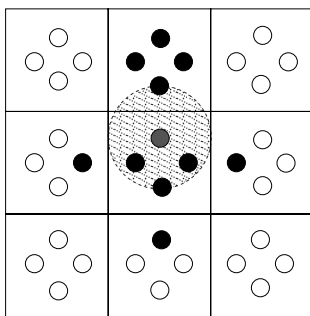


Fig. 7. The model in two dimensions: the space is partitioned in square cells, and each cell can be occupied by at most one particle in any one of the four shown positions (*little circles*). A particle in any given position (*large shaded circle*) excludes the presence of particles in any of the black colored positions

In the Monte Carlo simulations, $N = 433$ grains are confined in a $3d$ box of linear size $L = 12$ (i.e. $N_s = 3$), between hard walls in the vertical direction and with periodic boundary conditions in the horizontal directions. The system is again subjected to a Monte Carlo tap dynamics as described in Sect. 3.

In the following the tap duration is fixed, $\tau_0 = 10MCsteps/particle$, and different tap amplitudes, T_T , are considered. In Fig. 8 the bulk density, $\Phi \equiv N/L^2(2\langle z \rangle - 1)$, is plotted as a function of T_T : $\Phi(T_T)$ has a shape resembling that found in the “reversible regime” of tap experiments [16,21], and moreover very similar to that obtained in the mean field calculations and shown in Fig. 6. At low shaking amplitudes (corresponding to high bulk densities) a strong growth of the equilibration time (i.e. the time necessary to reach stationarity) is observed, and for the lowest values here considered (the black stars in Fig. 8) the system remains out of stationarity. In conclusions the system here studied presents a jamming transition at low tap amplitudes as found in real granular media.

In order to test the predictions of the mean field calculations, in the following we measure quantities usually important in the study of glass transition: The relaxation functions, the relaxation time and the dynamical susceptibility, connected to the presence a dynamical correlation length.

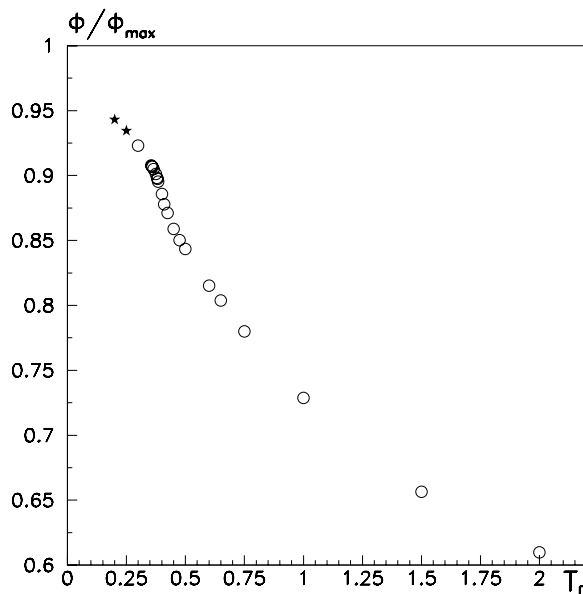


Fig. 8. The bulk density, $\Phi \equiv N/L^2(2\langle z \rangle - 1)$, is plotted as function of T_T for $\tau_0 = 10 MCsteps/particle$. The empty circles correspond to stationary states, and the black stars to out of stationarity ones. Φ_{max} is the maximum density reached by the system in the crystal phase, $\Phi_{max} = 6/7$

In particular we calculate the two-time autocorrelation functions:

$$C(t, t_w) = \frac{1}{N} \sum_i \overline{n_i(t) n_i(t_w) \boldsymbol{\sigma}_i(t) \cdot \boldsymbol{\sigma}_i(t_w)}, \quad (9)$$

where $\boldsymbol{\sigma}_i$ are unit length vectors, pointing in one of the six coordinate directions, representing the position of the particles inside the cell; the average $\overline{(\dots)}$ is done over 16 – 32 different realizations of the model obtained varying the random number generator in the simulations, and the errors are calculated as the fluctuations over this statistical ensemble. For values of t_w long enough, the system reaches a stationary state, where the time translation invariance is recovered, i.e., $C(t, t_w) = C(t - t_w)$. In this time region, by averaging $C(t', t_w)$ over t' and t_w such that $t = t' - t_w$ is fixed, we calculate the “equilibrium” autocorrelation functions

$$\langle q(t) \rangle = \langle C(t' - t_w) \rangle, \quad (10)$$

and the dynamical non linear susceptibility

$$\chi(t) = \langle q(t)^2 \rangle - \langle q(t) \rangle^2. \quad (11)$$

As shown in Fig. 9, at low values of the tap amplitudes, T_T , two-step decays appear, well fitted in the intermediate time region, by the β -correlator

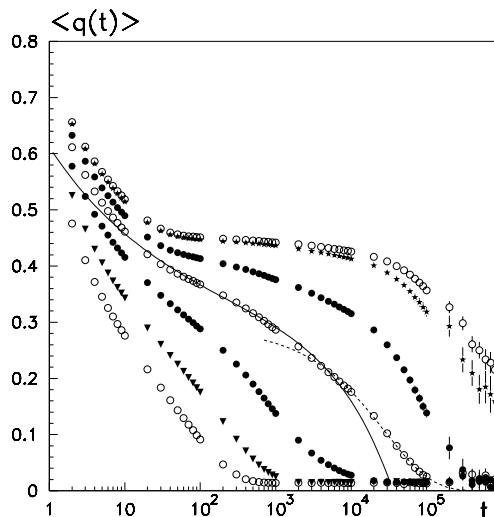


Fig. 9. The “equilibrium” autocorrelation function, $\langle q(t) \rangle$, plotted as function of t , for tap amplitudes $T_T = 0.60, 0.50, 0.425, 0.40, 0.385, 0.365, 0.36$ (from bottom to top). The continuous line in figure is the β -correlator of the mode coupling theory with exponent parameters $a = 0.30$ and $b = 0.52$. The dashed line is a stretched exponential $\propto \exp[-(t/\tau)^\beta]$ with $\beta = 0.70$

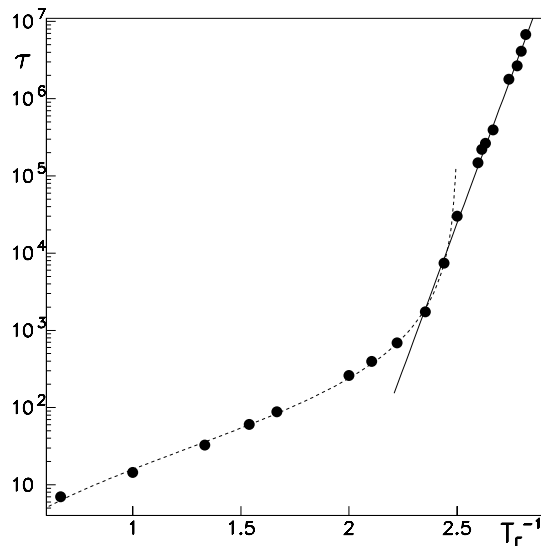


Fig. 10. The relaxation time, τ , as function of the tap amplitude inverse, T_T^{-1} . The *dashed line* is a power law, $(T_T - T_D)^{-\gamma_2}$, with $T_D = 0.40 \pm 0.01$ and $\gamma_2 = 1.52 \pm 0.10$. The *continuous line* is an Arrhenius fit, e^{A/T_T} , with $A = 17.4 \pm 0.5$ (the data in this region are also well fitted by both a super-Arrhenius and Vogel-Fulcher laws)

predicted by the mode coupling theory for supercooled liquids [22, 23] (the continuous curve in Fig. 9), and at long time by stretched exponentials (the dashed curve in figure). The relaxation time, τ , is defined as $\langle q(\tau) \rangle \sim 0.1$.

In Fig. 10 the relaxation time, τ , is plotted as a function of the tap amplitude, T_T : A clear crossover from a power law to a different regime is observed around a tap amplitude T_D . The power law divergence can be interpreted as a mean field behavior, followed by a hopping regime.

The divergence of the relaxation time at vanishing tap amplitude is consistent with the experimental data of Philippe and Bideau [16] and D'Anna et al. [4]. Their findings are in fact consistent with an Arrhenius behavior as function of the experimental tap amplitude intensity. However a direct comparison with our data is not possible since we do not know the relation between the experimental tap amplitude and the tap amplitude in our simulations.

The dynamical non linear susceptibility, $\chi(t)$, plotted in Fig. 11 at different T_T , exhibits a maximum at a time, $t^*(T_T)$. The presence of a maximum in the dynamical non linear susceptibility is typical of glassy systems [24, 25]. In particular the value of the maximum, $\chi(t^*)$, diverges in the p -spin model [24] as the dynamical transition is approached from above, signaling the presence of a diverging dynamical correlation length. In the present case the value of the maximum increases as T_T decreases (except at very low T_T where the

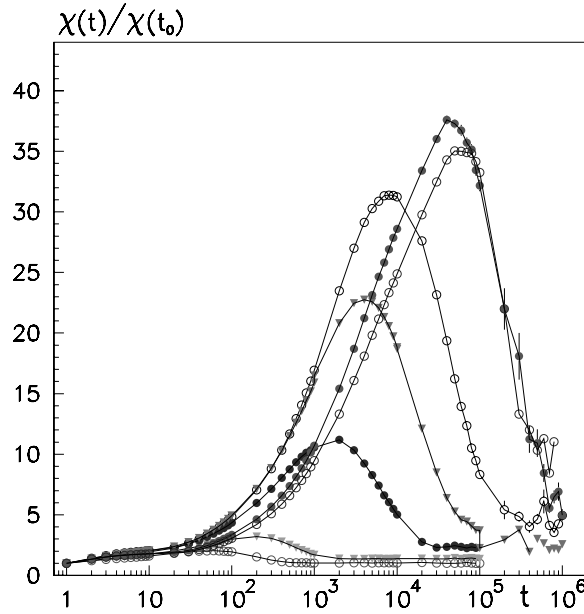


Fig. 11. The dynamical non linear susceptibility, $\chi(t)$, (normalized by $\chi(t_0)$, the value at $t_0 = 1$) as a function of t , for tap amplitudes $T_T = 0.60, 0.50, 0.425, 0.41, 0.40, 0.385, 0.3825$ (from left to right)

maximum seems to decrease [26]). The growth of $\chi(t^*)$ in our model suggests the presence of a growing dynamical length also in granular media.

8 Conclusions

In conclusions using standard methods of statistical mechanics we have investigated the jamming transition in a model for granular media. We have shown a deep connection between the jamming transition in granular media and the glass transition in usual glass formers. As in usual glass formers the mean field calculations obtained using a statistical mechanics approach to granular media predict a dynamical transition at a finite temperature, T_D , and, at a lower temperature, T_K , a thermodynamics discontinuous phase transition to a glass phase. In finite dimensions 1) the dynamical transition becomes only a dynamical crossover as also found in usual glass formers [12, 14, 20] (here the relaxation time, τ , as a function of both the density and the tap amplitude, presents a crossover from a power law to a different regime); and 2) the thermodynamics transition temperature, T_K , seems to go to zero (the relaxation time, τ , seems to diverge only at $T_T \simeq 0$, even if a very low value of the transition temperature is consistent with the data).

References

1. A. Coniglio and H.J. Herrmann, *Physica A* **225**, 1 (1996); M. Nicodemi, A. Coniglio and H.J. Herrmann, *Phys. Rev. E* **55**, 3962 (1997).
2. A.J. Liu and S.R. Nagel, *Nature* **396**, 21 (1998).
3. C.S. O’Hern, S.A. Langer, A.J. Liu, S.R. Nagel, *Phys. Rev. Lett.* **86**, 111 (2001).
4. G. D’Anna and G. Gremaud, *Nature* **413**, 407 (2001); G. D’Anna, P. Mayor, A. Barrat, V. Loreto, and F. Nori, *Nature* **424**, 909 (2003).
5. A. Mehta and J. Berg, *Europhys. Lett.* **56**, 784 (2001).
6. C.S. O’Hern, L.E. Silbert, A.J. Liu, S.R. Nagel, *Phys. Rev. E* **68**, 011306 (2003).
7. M. Nicodemi and A. Coniglio, *Phys. Rev. Lett.* **82**, 916 (1999).
8. M. Nicodemi, *Phys. Rev. Lett.* **82**, 3734 (1999). A. Barrat, J. Kurchan, V. Loreto, and M. Sellitto, *Phys. Rev. Lett.* **85**, 5034 (2000). J.J. Brey, A. Prados, B. Sánchez-Rey, *Physica A* **275**, 310 (2000). D. S. Dean and A. Lefèvre, *Phys. Rev. Lett.* **86**, 5639 (2001). H. A. Makse and J. Kurchan, *Nature* **415**, 614 (2002). J. Berg, S. Franz and M. Sellitto, *Eur. Phys. J. B* **26**, 349 (2002). G. De Smedt, C. Godreche, J.M. Luck, *Eur. Phys. J. B* **32**, 215-225 (2003). G. Tarjus and P. Viot, *Phys. Rev. E* **69**, 011307 (2004).
9. A. Coniglio and M. Nicodemi, *Physica A* **296**, 451 (2001). A. Fierro, M. Nicodemi and A. Coniglio, *Europhys. Lett.* **59**, 642 (2002); *Europhys. Lett.* **60**, 684 (2002); *Phys. Rev. E* **66**, 061301 (2002).
10. S.F. Edwards and R.B.S. Oakeshott, *Physica A* **157**, 1080 (1989). A. Mehta and S.F. Edwards, *Physica A* **157**, 1091 (1989). S.F. Edwards, in *Current Trends in the physics of Materials*, (Italian Phys. Soc., North Holland, Amsterdam, 1990).
11. M. Mézard and G. Parisi, *Eur. Phys. J. B* **20**, 217 (2001).
12. G. Biroli and M. Mézard, *Phys. Rev. Lett.* **88**, 025501 (2002).
13. M. PicaCiamarra, M. Tarzia, A. de Candia, and A. Coniglio, *Phys. Rev. E* **67**, 057105 (2003); *Phys. Rev. E* **68**, 066111 (2003).
14. L.F. Cugliandolo and J. Kurchan, *Phys. Rev. Lett.* **71**, 173 (1993). J. Kurchan, *cond-mat/9812347*; and in “Jamming and Rheology”, A.J. Liu and S.R. Nagel Eds., Taylor and Francis, London (2001).
15. M. Tarzia, A. de Candia, A. Fierro, M. Nicodemi and A. Coniglio, *Europhys. Lett.* **66**, 531 (2004).
16. P. Philippe and D. Bideau, *Europhys. Lett.* **60**, 677 (2002).
17. E. Clement and J. Rajchenbach, *Europhys. Lett.* **16**, 133 (1991).
18. M. Tarzia, A. Fierro, M. Nicodemi and A. Coniglio, *Phys. Rev. Lett.* **93**, 198002 (2004).
19. In the case of uniform density profile, i.e. $\sigma(z) = const.$, we have $\sigma(z) = \Phi$ (where $\Phi \equiv N/L^2(2\langle z \rangle - 1)$) below the maximum height and zero above.
20. C. Toninelli, G. Biroli, D. S. Fisher, *Phys. Rev. Lett.* **92**, 185504 (2004).
21. J.B. Knight, C. G. Fandrich, C. N. Lau, H. M. Jaeger, and S. R. Nagel, *Phys. Rev. E* **51**, 3957 (1995). E. R. Nowak, J. B. Knight, E. Ben-Naim, H. M. Jaeger, and S.R. Nagel, *Phys. Rev. E* **57**, 1971 (1998).
22. W. Gotze, in *Liquids, Freezing and Glass Transition*, eds. J.P. Hansen, D. Levesque, and Zinn-Justin, Elsevier (1991). T. Franosch, M. Fuchs, W. Gotze, M.R. Mayr and A.P. Singh, *Phys. Rev. E* **55**, 7153 (1997). M. Fuchs, W. Gotze and M. R. Mayr, *Phys. Rev. E* **58**, 3384 (1998).

23. The β -correlator predicted by the MCT is given by $\Phi(t) = f_c + g(t/t_\sigma)$, where $g(t/t_\sigma) \propto (t/t_\sigma)^{-a}$ for $t_0 \ll t \ll t_\sigma$, and $g(t/t_\sigma) \propto -(t/t_\sigma)^b$ for $t_\sigma \ll t \ll \tau_\alpha$.
24. S. Franz, C. Donati, G. Parisi and S. C. Glotzer, *Philos. Mag. B* **79**, 1827 (1999). C. Donati, S. Franz, S. C. Glotzer and G. Parisi, *J. Non-cryst. Solids*, **307**, 215 (2002)
25. S. C. Glotzer, V. N. Novikov, and T. B. Schröder, *J. Chem. Phys.* **112**, 509 (2000).
26. Interestingly this anomalous behavior seems to occur around the crossover temperature T_D previously calculated. The origin of this behavior, also observed in molecular dynamics simulations of a usual glass former [25], is still unclear.
27. A. Fierro, M. Nicodemi, M. Tarzia, A. de Candia and A. Coniglio, *cond-mat/0412120*.

Rheological Aspects of the Solid-Liquid Transition in Jammed Systems

P. Coussot

LMSGC, Institut Navier, Champs sur Marne, France

A common property of jammed systems is a yield stress they have to overcome in order to start to flow. In rheology it is generally assumed that the corresponding solid-liquid transition is continuous, the steady state viscosity progressively decreasing from infinity to a finite value as the applied shear stress is increased beyond the yield stress. Recent experiments with various materials such as colloidal suspensions, foams, emulsions, or polymer gels, show that this transition is in fact abrupt: in steady state, at a critical stress the material viscosity abruptly turns from infinity to a finite value. This phenomenon corresponds to another effect observed from MRI-rheometry tests: in steady state such pasty materials either flow at a shear rate larger than a critical, finite value, associated to a critical stress, or do not flow at all. This phenomenon has also a dynamic character, which is in particular illustrated by the “viscosity bifurcation” in time under controlled stress: below the critical stress value the shear rate progressively decreases until reaching stoppage; beyond this critical stress the shear rate increases and reaches a finite value. Moreover for a material initially at rest the interface between the sheared and unsheared regions, i.e. the slope break, progressively reaches its asymptotic position in time. From these results we deduce that usual macroscopic observations basically reflect complex space and time evolutions of flow and material characteristics in the rheometer gap, rather than local time-dependent properties.

1 Introduction

From a physical point of view concentrated emulsions, foams, colloidal suspensions or polymeric gels can be considered as jammed systems [1] since they are made of a great number of elements (droplets, bubbles, particles, polymer chains) in strong (direct or at distance) interaction in a liquid. From a mechanical point of view these are pasty materials or, equivalently, yield stress fluids, in the sense that they cannot flow in steady state unless the stress applied to them overcomes a critical, finite value. This property results from the existence of a continuous network of interactions between elements, which has to be broken for flow to occur. The strength of this network is related to the current distribution of positions and states of the elements

within the liquid. Since we are dealing with out-of-equilibrium systems we can expect that the strength of this network will continuously evolve in time. Nevertheless, in practice, the mechanical behavior of such materials has been generally considered within the frame of simple yield stress fluids which neglects possible time-dependent effects and assumes a continuous transition from a solid to a liquid regime as the stress increases beyond a critical value. Since the “jammed character” of these systems mainly relies on their mechanical characteristics, and more precisely on their ability to become “liquid” beyond some critical stress, here we intend to clarify the characteristics of the solid-liquid transition from a rheological point of view, and in particular the interplay of yielding and time-effects.

In the following we start by reviewing the usual yield stress fluid concept and its implications (Sect. 2). Then, in particular taking advantage of MRI-rheometry coupled observations, we show that the steady state rheological behavior of pasty materials differs from the usual assumption (Sect. 3): there is a discontinuity in shear rate at the transition between the solid and the liquid regime. The practical consequences of this phenomenon in rheometry are reviewed. Some aspects of the rheological behavior of pastes in transient regime are then described in Sect. 4. We show that before a critical deformation the material can be considered as a viscoelastic solid. Beyond this critical deformation the material falls in its liquid regime and exhibits thixotropic properties which mainly result in the displacement of the sheared region in time.

2 The Usual Concept of Yield Stress Fluids

2.1 Yielding

Yield stress fluids are materials which can flow only when the applied stress overcomes a critical value, namely their yield stress τ_c . At first sight they resemble ideal plastic materials but they are in fact viscoplastic, since the resulting flow rate increases with the difference between the applied stress and the yield stress. In this context usual models describing such a behavior in simple shear steady state express as follows:

$$\tau < \tau_c \rightarrow \dot{\gamma} = 0 \quad (1)$$

$$\tau > \tau_c \rightarrow \tau = \tau_c + f(\dot{\gamma}), \quad (2)$$

in which τ and $\dot{\gamma}$ are the shear stress and shear rate amplitudes [2]. A “solid” and a “liquid” regimes thus respectively correspond to (1) and (2). A fundamental assumption of usual yield stress models is that f is an increasing function tending to zero when $\dot{\gamma}$ tends to zero. This means that there is a continuous transition from the solid to the liquid regime in terms of shear rate: as the shear stress decreases to the yield stress, the shear rate progressively

tends to its value in the solid regime, i.e. zero. In other terms the apparent viscosity ($\eta = \tau/\dot{\gamma}$) of the material is finite in the liquid regime and progressively tends to infinity (its value in the solid regime) as the applied stress tends to the yield stress. In practice the Herschel-Bulkley model, for which $f(\dot{\gamma}) = K\dot{\gamma}^n$, in which K and n are two material parameters, and the Casson model, for which $f(\dot{\gamma}) = K\dot{\gamma} + 2\sqrt{K\tau_c\dot{\gamma}}$, are the most often used models. Note that the Bingham model is recovered from the Herschel-Bulkley model with $n = 1$. The Herschel-Bulkley model appeared to be capable to very well represent usual shear stress vs. shear rate data over a wide range of shear rates (several decades) [3, 4]. Note however that in general such data were obtained either in steady state under controlled velocity or in pseudo steady state under controlled, but more or less slowly increasing or decreasing, stress (see 3). A typical example of corresponding data and model fitting is shown in Fig. 1.

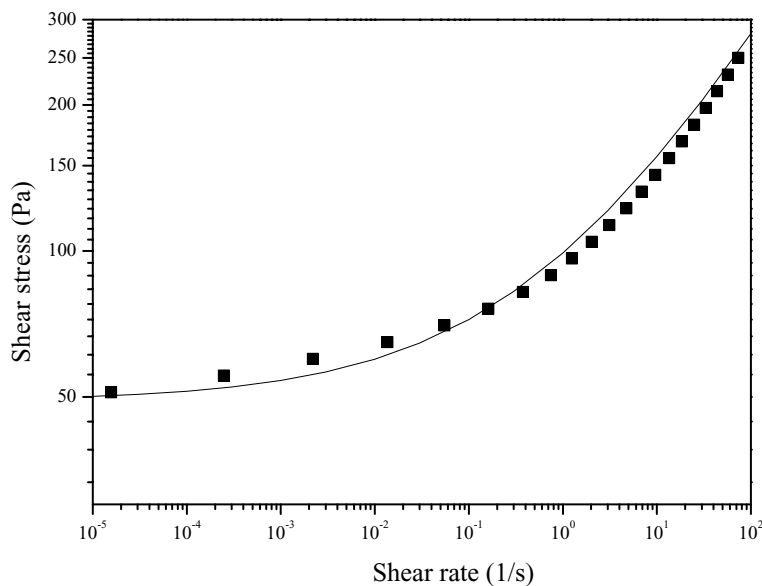


Fig. 1. Pseudo steady state shear stress vs shear rate data for a model emulsion (see characteristics in [35]), and fit of a Herschel-Bulkley model

More sophisticated models were also proposed to take into account a possible viscoelastic solid regime for stresses below the yield stress or, more precisely, before a critical deformation from the rest state [5–7]. For example a basic approach consists to replace equation (1) by a viscoelastic solid model such as the Kelvin-Voigt model for $\dot{\gamma} < \dot{\gamma}_c$, i.e. $\tau = G\gamma + \mu\dot{\gamma}$, in which G and μ are two material parameters and γ is the deformation from the initial (rest) state. Note that in this frame the solid-liquid transition is expected for the

critical deformation γ_c , and the minimum stress value making it possible to reach this value is $\tau_c = G\gamma_c$.

Twenty years ago it was suggested that the concept of yielding was inappropriate [8, 9] because all materials tend to flow, possibly at extremely low shear rates, for shear stresses below the yield stress. In this frame the solid regime would in fact be a *pseudo solid* regime and the behavior of the material would be represented by equation (2) along with a modified version of equation (1): $\tau < \tau_c \rightarrow \dot{\gamma} = \tau/\eta_\infty$, in which η_∞ is the Newtonian viscosity of the material under low shear stresses. This question was the subject of strong conceptual debates in rheology [10–14] and the main conclusion was that since the shear rate values possibly reached in this pseudo-solid regime are extremely small (say of the order of 10^{-6}s^{-1}) the corresponding flows could hardly play a role in practice. Moreover it was remarked that in several cases, although such materials apparently flowed under low shear stresses in rheometers, they did not flow under other conditions (the material kept its own shape in a container or a denser ball did not settle through it over several years). This suggests that some experimental problems may affect rheometrical data under low shear rates, a point that will be enlightened by recent results presented below.

2.2 Thixotropy

In the solid and the liquid regime, pasty materials can exhibit thixotropic properties: under given boundary conditions (stress or velocity) their apparent viscosity varies in time. Note that this phenomenon is a reversible aging of the material. In order to deal with the rheology of such systems a basic though often used approach consists to consider that this phenomenon adds a time-dependence in the above, simple, yield stress model for the liquid regime: τ_c and f are now functions of the flow history. A practical way for expressing this relies on the assumption that thixotropy in fact reflects the evolution of the internal organization in time of fluid elements such as bubbles, droplets or colloidal particles, which may be described by a single parameter, λ , the structure state parameter [15–18]. Under these conditions τ_c and f are now considered as functions of the parameter λ which, as for it, depends on flow history. A simple way to express this dependence consists to write a kinetic equation for [19, 20]:

$$\frac{d\lambda}{dt} = g(\lambda) - \alpha\dot{\gamma}h(\lambda) \quad (3)$$

The form of (3) relies on some physical assumptions: it is assumed that the rate of change of λ is equal to the difference between a rate of “restructuring” of the system, which solely depends on the current state of structure, and a rate of “destruction” due to flow, which is proportional to the shear rate because it is natural to expect it to be proportional to the amplitude of

deformation undergone by the fluid per unit time, namely $d\gamma/dt = \dot{\gamma}$. Unfortunately the exact physical meaning of λ is generally ignored so that no clear technique has been identified for measuring it directly. Although it was suggested that it could for example be related to the number of links between particles, the average size of flocs in a flocculating system or the average depth of the potential wells of particles in a non-flocculating suspension, this fundamentally remains a phenomenological parameter of rheological models. For the same reason the exact form of (3) cannot take advantage of a clearer physical approach.

2.3 Flow Characteristics of Simple Yield Stress Fluids

Due to their strongly non-linear rheological behavior the flow characteristics of yield stress fluids can be very sensitive to heterogeneous shear stress distributions. Here we focus on these effects by reviewing their basic flow characteristics in the case of conduit and Couette flows.

Capillary Flow

Let us consider a yield stress fluid the behavior of which may well be represented by a Herschel-Bulkley model and flowing in steady state through a cylindrical conduit of radius r_o . For reasons of symmetry it may be shown that the flow occurs in the form of concentric fluid layers gliding relatively to each other along the conduit axis. From the momentum equation applied on a virtual rod of length L we deduce the following relationship between the shear stress and the pressure drop: $2\tau/r = \Delta p/L$. Since the first term only depends on r while the second term only depends on z they are both constant. It follows from (1-2) that there exists a critical radius at which the yield stress is reached:

$$r_c = \frac{2\tau_c}{\Delta p/L} \quad (4)$$

and the complete velocity profile writes:

$$r \leq r_c \rightarrow v_z(r) = A(r_o - r_c)^{(n+1)/n} \quad (5)$$

$$r > r_c \rightarrow v_z(r) = A \left((r_o - r_c)^{(n+1)/n} - (r - r_c)^{(n+1)/n} \right) \quad (6)$$

in which $A = (n/n + 1)(\Delta p/2kL)^{1/n}$. This velocity profile is composed of a rigid (“plug”) region around the central axis (equation (5)) and a sheared region (equation (6)) between the plug and the wall. The flow of a yield stress fluid in an open channel of rectangular shape is more complex but the shear stress also increases towards the wall so that we again expect a plug region around the central axis. This is effectively what we could observe at the free surface of a channelized mudflow (cf. Fig. 2).

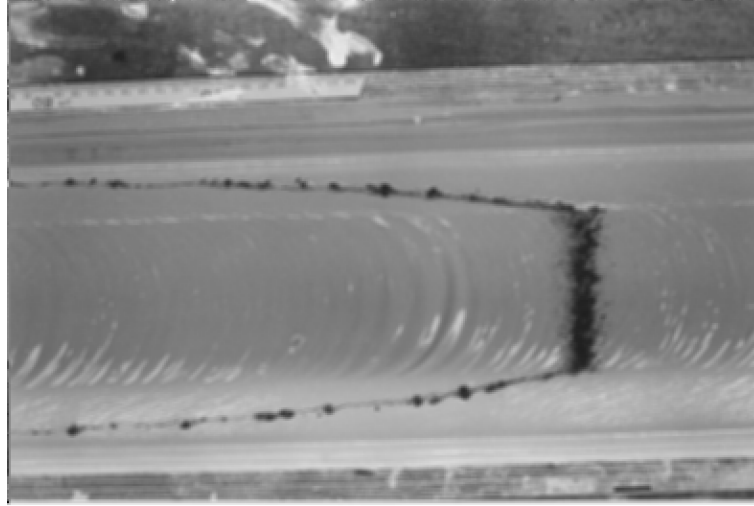


Fig. 2. View from upper of a channelized flow of a mud suspension: the deformation of the line of pepper dropped upstream transversally reflects the velocity profile (from [38])

Couette Flow

In a Couette flow between two coaxial cylinders of radii r_1 and r_2 (outer radius), when the flow is stable and with negligible edge effects and inertia it may be shown that the flow consists in the relative motion of concentric fluid layers so that the local shear rate is defined as:

$$\dot{\gamma}(r) = r \frac{\delta(v_\theta/r)}{\delta r} \quad (7)$$

in which $v_\theta(r)$ is the tangential velocity of the fluid at the distance r . Moreover, from the momentum equation we obtain the shear stress distribution:

$$\tau = \frac{M}{2\pi h r^2} \quad (8)$$

in which M is the torque applied onto the inner cylinder and r the distance from the axis.

For a yield stress fluid there again exists a critical distance at which the yield stress is reached:

$$r_c = \sqrt{\frac{M}{2\pi h \tau_c}}. \quad (9)$$

If $r_c > r_2$ the fluid in the gap is completely sheared. More interesting is the case for which $r_c < r_2$ since there is an unsheared region between the two cylinders:

$$r_c < r \leq r_2 \rightarrow v_\theta(r) = 0 ; \quad (10)$$

$$r_1 \leq r \leq r_c \rightarrow v_\theta(r) = \left(\frac{M}{2\pi hk} \right)^{1/n} r \left(\int_r^{r_c} \frac{1}{r'} \left(\frac{1}{r'^2} - \frac{1}{r_c^2} \right)^{1/n} dr' \right). \quad (11)$$

There is no analytical solution of the integral in (11) except for entire values of $1/n$.

For both capillary and Couette flows it may be shown from (6) and (11) that the variations of the velocity at the approach of the unsheared region as a function of the distance r are proportional to $|r - r_c|^{1+1/n}$. We deduce that $v_\theta(r) \rightarrow 0$ when $r \rightarrow r_c$ and that the shear rate is continuous:

$$\dot{\gamma}(r) \rightarrow 0 \quad \text{when} \quad r \rightarrow r_c. \quad (12)$$

This result is in fact a straightforward consequence of the rheological behavior of the fluid. The same result would be obtained for any yield stress model of the type (2) such that $f \rightarrow 0$ when $\dot{\gamma} \rightarrow 0$. Typical resulting velocity profiles are shown in Fig. 3. Since the shear stress decreases with the distance from the inner cylinder the slope of the velocity profile, which is related to the shear rate via (7), decreases with the distance r . At the approach of the plug region this slope tends to zero. Moreover, in the limit of small $(r - r_c)/r_c$, it may be shown that the velocity profiles are self-similar, i.e. they have exactly the same shape at different scales.

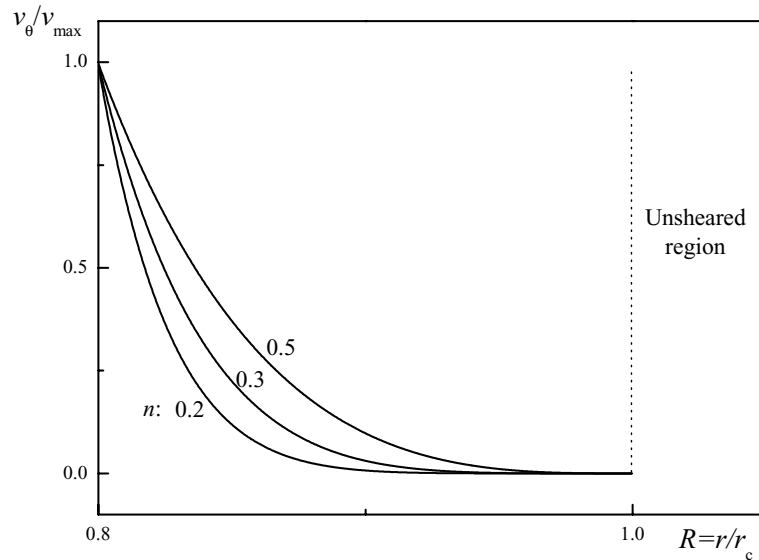


Fig. 3. Herschel-Bulkley velocity profiles in a Couette flow geometry for different values of n

3 Rheological Behavior of Jammed Systems from Local Rheometry

The exact value of the yield stress of a given material appears to be hard to determine in practice, as proved by the fact that different techniques usually provide different values for the same material. It is also worth noting that, for a fluid following a yield stress model, at low shear rates, the shear stress vs shear rate curve is almost horizontal at the approach of the yield stress, so that a small uncertainty on stress may lead to a very large error on the effective shear rate, say of the order of one or two decades. This implies that the shear rate effectively reached for some stress value close to the yield stress can significantly depend on the exact stress distribution in the fluid. In this context it recently became clear that direct observations of the flow field should make it possible to clarify the exact behavior of the fluid at the solid-liquid transition.

When the stress distribution is known, direct observations of the flow field may be used for a “local rheometry”. For example, for a Couette flow, as soon as we have measured the velocity profile we know the local shear rate from (7), and since we a priori know the shear stress distribution from (8), we have the shear stress and the shear rate at any point r in the gap. By eliminating r between these two expressions we deduce the shear stress vs shear rate relation at any time. Different ways exist for measuring the velocity profiles in a flowing fluid: Particle Imaging Velocimetry (PIV), Dynamic Light Diffusion, Laser Doppler Anemometry, X or Gamma ray, ultrasounds. These techniques are based on the analysis of signal attenuation or scattering, often with the help of autocorrelation functions. On the contrary MRI is based on the direct, local excitation of material particles within the sample under study. Although some of the above techniques have been used marginally for studying complex fluids this is mainly MRI which has been developed with rheological objectives [21–33].

3.1 Flow Characteristics at the Solid-liquid Transition and Shear-banding

Typical tangential velocity profiles obtained for a pasty material in steady state flows within a Couette geometry are presented in Fig. 4. At first sight they look as expected for a yield stress fluid. However it appears impossible to fit a Herschel-Bulkley model over such a velocity profile over the complete range of velocities [34, 35]. This is because the velocity profiles for such materials are not self-similar at the approach of the solid-liquid interface (cf. Fig. 5). In fact at a sufficiently small scale the slope of the velocity profile remains almost constant over several millimeters until the velocity reaches zero (cf. Figs. 4–6). Thus, along the solid-liquid interface, in contrast with one fundamental prediction of simple yield stress models (cf. §2.3), the shear

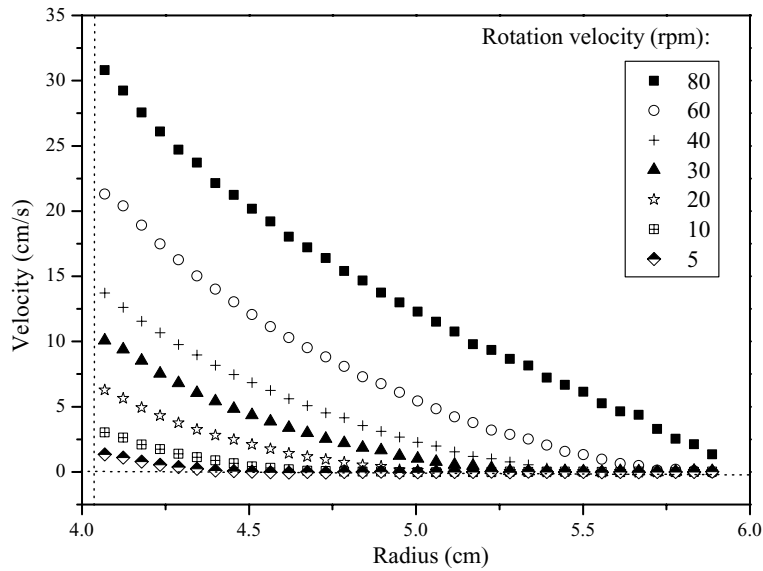


Fig. 4. Tangential velocity profiles under different rotation velocities of the inner cylinder for a bentonite suspension obtained from MRI-rheometry (from [36])

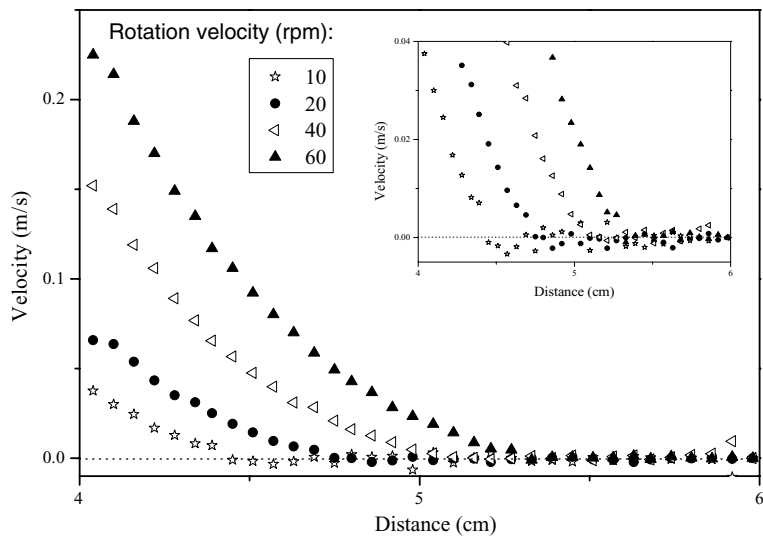


Fig. 5. Tangential velocity profiles under different rotation velocities of the inner cylinder for a foam obtained from MRI-rheometry (from [41]). The insert shows the aspect of the profiles at a smaller scale

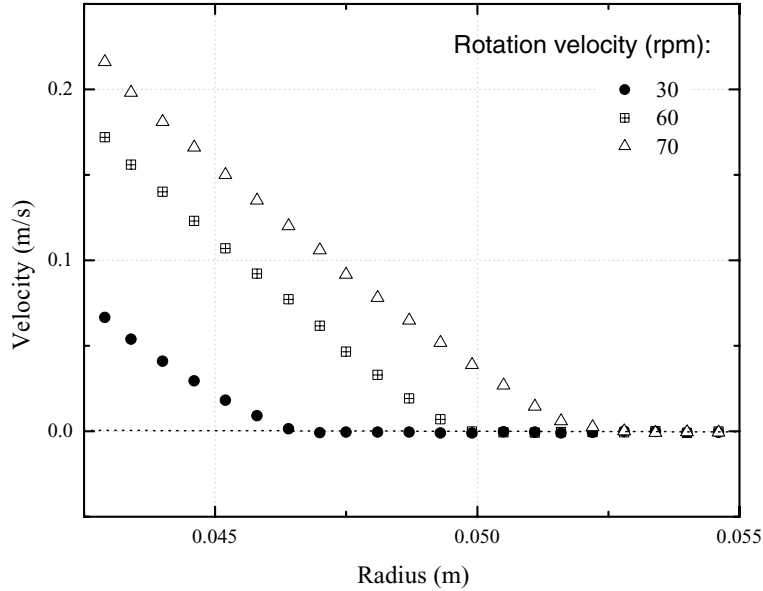


Fig. 6. Tangential velocity profiles under different rotation velocities of the inner cylinder for a cement paste obtained from MRI-rheometry (from [40])

rate in the liquid differs from zero. This result was obtained with various pasty materials: chocolate, clay suspensions (bentonite [36], laponite [37]), mayonnaise, silica suspensions [38], carbopol gel [39], cement paste [40], concentrated emulsion [35], foam [41], sewage sludges [42], and was also obtained from molecular dynamics simulations [43].

In most cases the critical shear rate ($\dot{\gamma}_c$), that is the slope of the velocity profile in the liquid region along the solid-liquid interface, does not change significantly when the boundary conditions of the flow, such as the rotation velocity of the inner cylinder, change, although the position of the interface changes. Moreover it appears that the shear stress associated to the position of this interface $M(\Omega)/2\pi hr_{c2} = \tau_c$ remains constant¹. The critical shear rate ($\dot{\gamma}_c$) may thus be considered as a rheological parameter of the fluid, associated to a critical shear stress (τ_c). Finally the typical form of the effective constitutive equation of a yield stress fluid in steady state is given by equation (1) for the solid regime and a modified version of equation (2) for the liquid regime:

$$\tau > \tau_c \rightarrow \tau = f(\dot{\gamma}) \quad (13)$$

¹Nevertheless note that for some materials exhibiting strong thixotropic properties (such as bentonite or laponite suspensions) this is strictly true only if the material has undergone analogous previous flow histories.

in which f is now an increasing function such that $f(\dot{\gamma}_c) = \tau_c$. For example existing data could be well represented [38] by a power-law function of the form:

$$f(\dot{\gamma}) = \tau_c \left(\frac{\dot{\gamma}}{\dot{\gamma}_c} \right)^n . \quad (14)$$

However it is worth noting that the range of shear rates studied from MRI-rheometry is in general rather narrow (typically one decade).

These results imply that at low apparent shear the thickness of the sheared region should tend towards zero. Such a behavior is reminiscent of shear-banding in plastic materials and it suggests that the local flow properties of a paste turn continuously from those of a pure plastic material to those of a yield stress fluid as the apparent shear rate increases. However our insight in the local behavior of these materials show that for pastes in steady state, whatever the size of the sheared band, the fluid is rapidly sheared (at a rate larger than $\dot{\gamma}_c$) in some region while the rest of the fluid remains rigid. This phenomenon is critical when the power n is of the order of 1 because in that case the shear rate slowly varies with the shear stress. For example, for a cement paste, a (Newtonian) region in which the fluid is sheared at an almost constant rate coexists with a (solid) region in which it does not flow (cf. Fig. 6), but the apparent behavior is that of a simple yield stress fluid.

3.2 Consequences in Rheometry

From these observations it results that a pasty material submitted to an increasing stress should suddenly turn from a solid to a liquid at a certain stress value, with a shear rate abruptly growing from zero to $\dot{\gamma}_c$. In fact usual observations of yield stress fluids show that the apparent shear rate grows from zero as the stress increases beyond the yield stress (cf. §2). This is so because in practice there always subsists some slight stress heterogeneities in viscometric flows. For example in a cone and plate geometry the stress is strictly homogeneous only if the cone angle is infinitely small and if the peripheral free surface is spherical. As a consequence, during an increasing stress ramp the regions in which the stress is the largest should first fall in the liquid regime and flow at a shear rate approximately equal to $\dot{\gamma}_c$ while the rest of the fluid remains in the solid regime. Then, as the stress increases, the thickness (h) of the liquid region increases, and the apparent shear rate, equal to $h\dot{\gamma}_c/H$ in which H is the gap between rheometer tools, progressively increases from zero. This scheme is consistent with the direct observations of Pignon et al. [44], Coussot et al. [38] (cf. Fig. 7) and the simulations of Varnik et al. [43]. The corresponding, apparent, flow curve, may be computed as soon as one assumes (or knows) the exact stress distribution in the gap. It appears to be very close to the typical Herschel-Bulkley flow curves observed in practice (cf. Fig. 8).

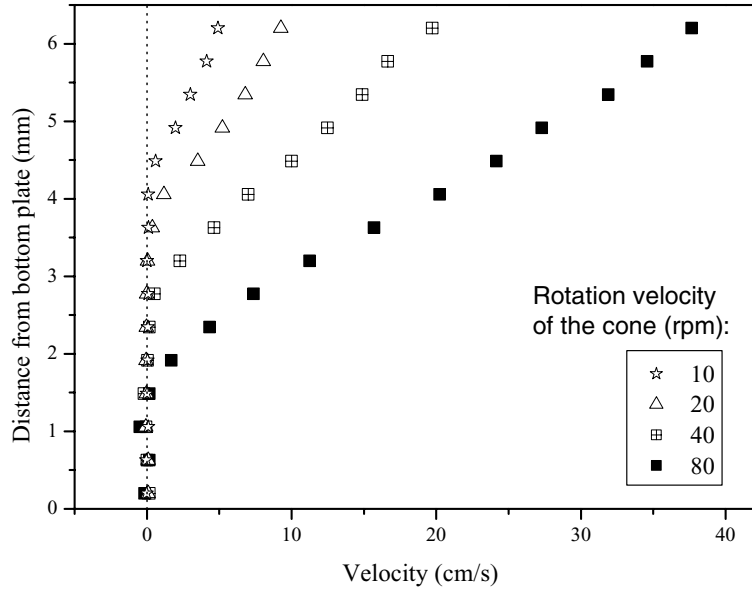


Fig. 7. Tangential velocity profiles under different rotation velocities of the upper cone for a bentonite suspension obtained from MRI-rheometry (from [36])

General consequences for rheometry of jammed systems follow:

- 1) Rheometrical tests with such materials are systematically affected by shear-banding at apparent shear rates below $\dot{\gamma}_c$.
- 2) Usual yielding flow curves do not only reflect the intrinsic rheological behavior of the materials; in particular the apparent shear rate under a given stress value strongly depends on the exact stress distribution in the fluid, which conditions the way the shear localizes.

3.3 Extreme Shear Localization

The above results also imply that under (apparent) shear rates sufficiently smaller than the thickness of the sheared region may be of the order of few times the size of the elements of the fluid. In that case the continuum assumption is no longer valid and the flow of the corresponding band does not correspond to a flow of the homogeneous paste (at a larger scale). For example the apparent behavior of a single layer of droplets sheared between two plates a priori differs from the behavior of a much larger volume of an emulsion made of such droplets. Depending on material this effect takes different forms. For example, for a foam (cf. Fig. 9) or a laponite suspension [44], under controlled velocity, the shear stress tends to increase towards low shear rates. Such a situation cannot reflect the effective rheological behavior of a unique, homogeneous material since it would lead to flow instability. Under

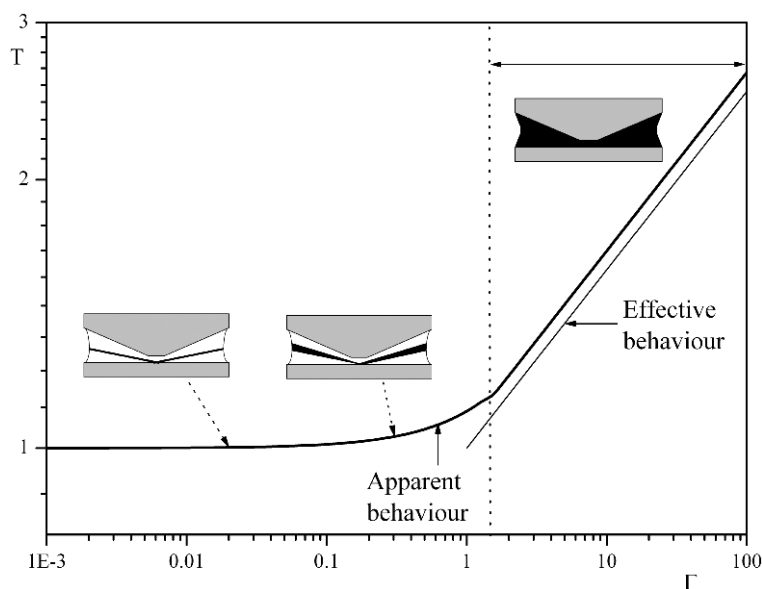


Fig. 8. Effective flow curve (in terms of $T = \tau_{app}/\tau_c$ vs. $\Gamma = \dot{\gamma}_{app}/\dot{\gamma}_c$) of a pasty material following the constitutive equation (1) and (14) with $n = 0.2$, and corresponding apparent flow curve as deduced from conventional rheometry with a cone and plate geometry, assuming a homogeneous stress distribution with a slight power-law perturbation. Note that a qualitatively similar result is obtained with a Couette geometry in which the stress variations are well controlled. The distribution of shear in the gap in different situations is represented by successive schemes in which the sheared region is in dark while the white region corresponds to unsheared material

controlled stress, for such materials, no steady state data can be obtained in the range of shear rates for which such a decreasing flow curve is obtained under controlled velocity. This effect is reminiscent of the decrease of the friction coefficient for solids at low velocities, and it is likely that for pastes it indeed corresponds to some kind of “frictional” effects in a thin layer of such particulate materials.

An opposite effect is obtained with other materials (cf. Fig. 10): below some shear rate value the stress tends to abruptly decrease towards low shear rates. This effect is reminiscent of wall slip [35] but here rough surfaces were used (as in all the experiments reported in this paper). This likely reflects some specific arrangements of the fluid elements along parallel layers. At last, for many other materials, one obtains the usual, apparent, simple yielding behavior well represented by a Herschel-Bulkley model [3, 45]. This might result from some kind of mixing of the material occurring under any flow rate and leading to an energy dissipation progressively decreasing with velocity.

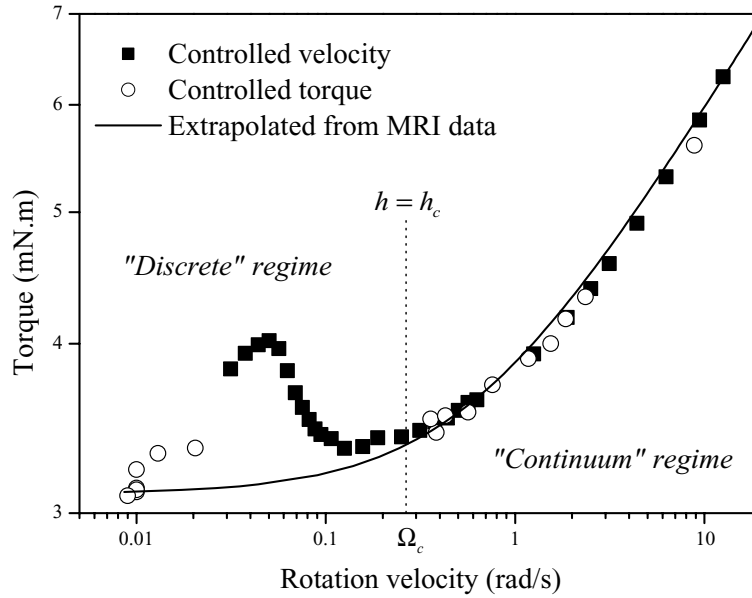


Fig. 9. Foam “flow curve” obtained under different conditions from experiments in a Couette geometry: from controlled torque experiments, controlled velocity or extrapolated from the model fitted to MRI data (from [41])

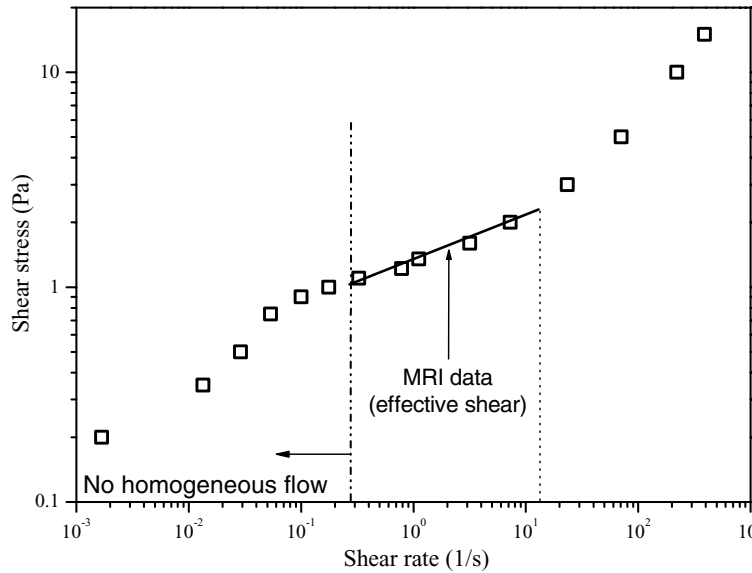


Fig. 10. Flow curve of a drilling emulsion obtained from MRI-rheometry and from conventional rheometry under controlled shear stress (pseudo steady state) (from [57])

More generally these different apparent behavior types result from complex interactions between the specific, local structure of the material (at the scale of the basic elements), the solid surface and the rest of the material (via osmotic pressure or migration effects). The apparent behavior of jammed materials under low (apparent) shear rates, in this “discontinuous” regime, remains a virgin field of research, which might nevertheless take advantage of existing knowledge in solid friction or lubrication of complex materials.

4 The Solid-liquid Transition in Jammed Systems: A Dynamic Phenomenon

4.1 Yielding and Thixotropy

Until now we focused on the steady state behavior of pasty materials, either in the solid or in the liquid regime. In fact the transition from the solid to the liquid regime, or from the liquid to the solid regime, appears to be dynamic phenomena. Let us first examine the solid-liquid transition, i.e. we consider the material at rest and observe under which conditions we can consider it has reached the liquid regime. Recent experiments [46] using a new technique for reconstructing the velocity or deformation profiles in time from creep tests with a laboratory rheometer showed that the material is viscoelastic in its solid regime and that the solid-liquid transition occurs, beyond a critical deformation, progressively in the gap (cf. Fig. 11).

This might in particular affect the physical interpretation of the variations of the apparent elastic and viscous moduli from dynamics tests. Locally there is an almost instantaneous transition from the solid to the liquid regime, so that we would expect a dramatic drop of G' for a critical stress or strain amplitude, associated to an increase of G'' if the stress distribution was homogeneous. Instead the G' and G'' curves progressively vary and their intersection is generally considered to reflect the solid-liquid transition of the material, and the yield stress associated to the stress amplitude at this intersection (cf. Fig. 12). From the above results we deduce that the progressive variations of these curves basically reflect the displacement of the solid-liquid interface in the fluid with stress amplitude increase.

Let us now assume a material in steady state in its liquid regime under a given stress. At a certain time we apply another stress level and observe the fluid flow. It appears that for an applied stress larger than a critical value the flow rate either increases or decreases progressively towards another shear rate value. For an applied stress smaller than this critical value the fluid progressively stops flowing (cf. Fig. 13) (“viscosity bifurcation” [47]). Finally, in steady state the fluid in general appears capable to flow only at a shear rate larger than a critical, finite value, which obviously corresponds to $\dot{\gamma}_c$ for sufficiently homogeneous stress distribution. These results are consistent with MRI data in steady state (cf. §3) along with MRI experiments in transient

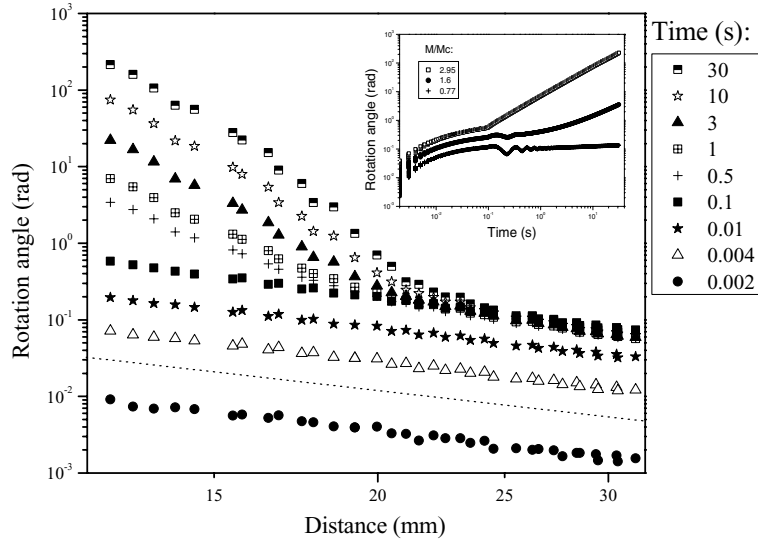


Fig. 11. Creep test with a carbopol gel: profiles of rotation angles within the gap at different times after the initial instant as reconstructed from systematic creep tests under smaller torques. The dashed line corresponds to a pure elastic behavior. The insert shows typical creep curves under different dimensionless torque values. Preparation: the materials were presheared at 20 rad/s during 30 s then left at rest during 20 s (from [46])

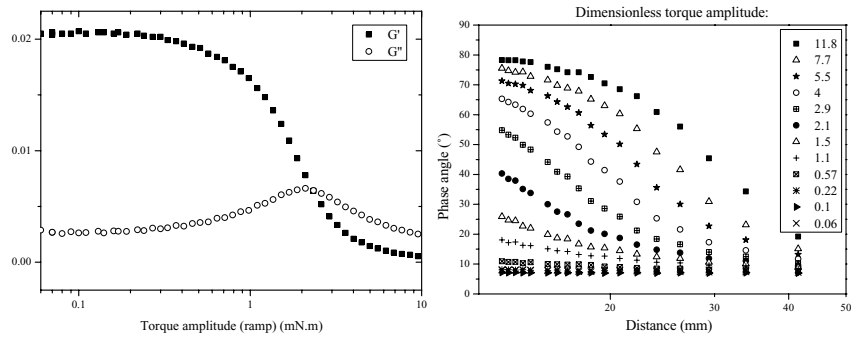


Fig. 12. Apparent G' and G'' curves (a) for a pasty material (carbopol gel of Fig. 11) as a function of stress amplitude. Reconstructed phase shift distribution in the gap for different torque amplitudes (b)

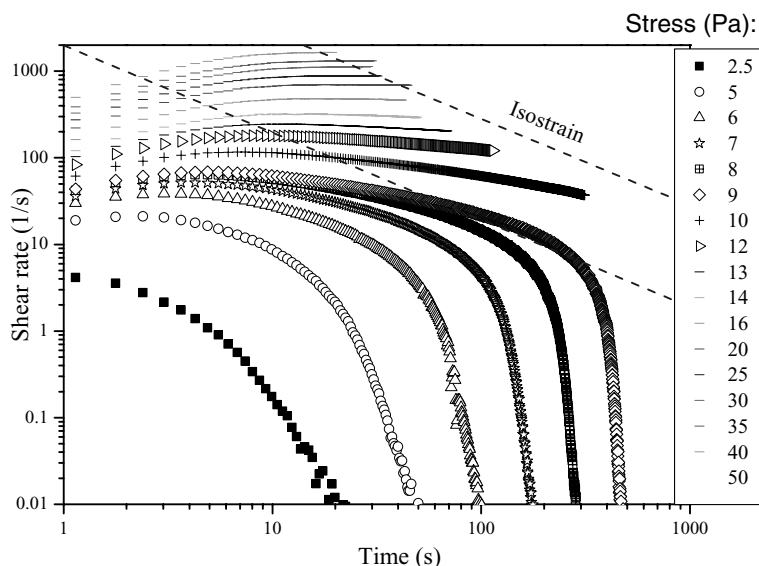


Fig. 13. Creep tests with a bentonite suspension under different shear stress after the same preparation of the material

flows: when an insufficient stress is suddenly applied to a flowing fluid the local velocity progressively tends to zero until complete stoppage (cf. Fig. 14). It is worth noting that this effect of viscosity bifurcation was also observed with granular systems [48] suggesting that it is a generic property of jammed systems.

A simple, phenomenological, thixotropy model makes it possible to reproduce these properties of the liquid-solid transition, and thus suggests a generic physical explanation of such phenomena. This model assumes a constant rate of restructuring, i.e. $g = 1/\theta$, and a simple function for the second factor, i.e. $h = \lambda$, in equation (3). Moreover the viscosity is given as: $\eta = \eta_o(1 + \lambda^n)$. This model appears capable to qualitatively predict the viscosity bifurcation effect [47] and the velocity bifurcation in the fall of an object through a less dense, thixotropic fluid either vibrated under different frequencies or after different times of rest [49]. This model also predicts rather well the delay before abrupt flow at the approach of some critical angle for a fluid layer over an inclined plane [50]. It finally appeared capable to predict quantitatively the flow characteristics observed by MRI after a sudden change of the rotation velocity of the inner cylinder (cf. Fig. 14) [51], and the evolution of the apparent yield stress after some time of rest [50]. Note that, in contrast with usual thixotropy models (see §2) this phenomenological model avoids assuming a priori a yield stress form for the constitutive equation. Here, in agreement with experimental observations, the fluid progressively evolves towards either the solid or the liquid regime depending on the stress applied and the initial state of structure (λ_o). It is thus mainly appropriate

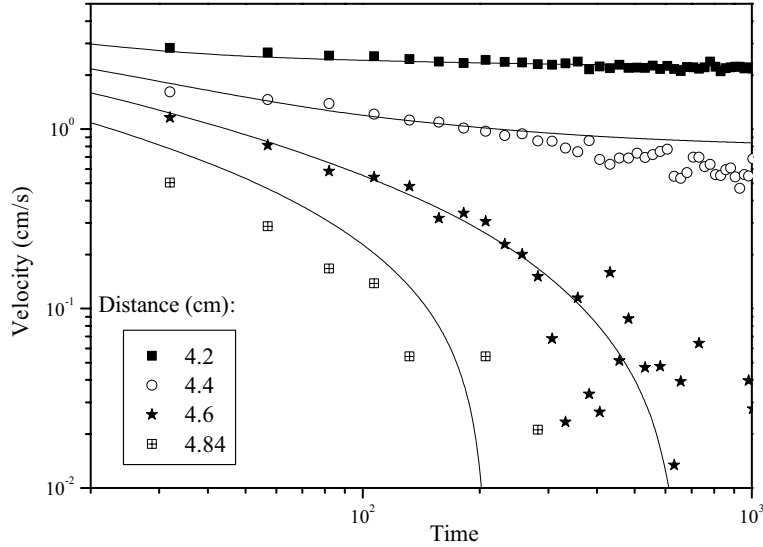


Fig. 14. Velocity as a function of time at different distances from the central axis as predicted by the model (*continuous lines*) and as measured by MRI in Fig. 4 (*symbols*) for a bentonite suspension in a Couette system after a sudden change of the rotation velocity of the inner cylinder (from 60 to 10 rpm) (from [51])

for describing the flow properties under flow, and less appropriate for describing the solid-liquid transition phenomena. In this context, according to this model, the fluid exhibits an apparent yield stress [51]

$$\tau_c(\lambda_o) = \frac{\mu_o(1 + \lambda_o^n)}{\alpha\theta\lambda_o}, \quad (15)$$

corresponding to the critical stress at which the regime bifurcation occurs. In agreement with existing data [52, 53] this apparent yield stress increases with the “degree of jamming” of the material, such as the fraction of elements in the liquid or its state of restructuration (which increases with the time of preliminary rest).

4.2 From Plasticity to Liquid Flow with Increase in Degree of Jamming

The critical shear rate appears to also increase with the degree of jamming of the material [47]. For example, under given velocity of rotation of the inner cylinder in a Couette flow, the thickness of the shear-band, which is roughly equal to $\Omega r_1 / \dot{\gamma}_c$ decreases with the degree of jamming of the material. This means that, as its degree of jamming increases, a material will turn from a simple liquid (extremely low $\dot{\gamma}_c$) to a pure plastic solid (high $\dot{\gamma}_c$). This property along with the dynamic aspects of the solid-liquid transition described

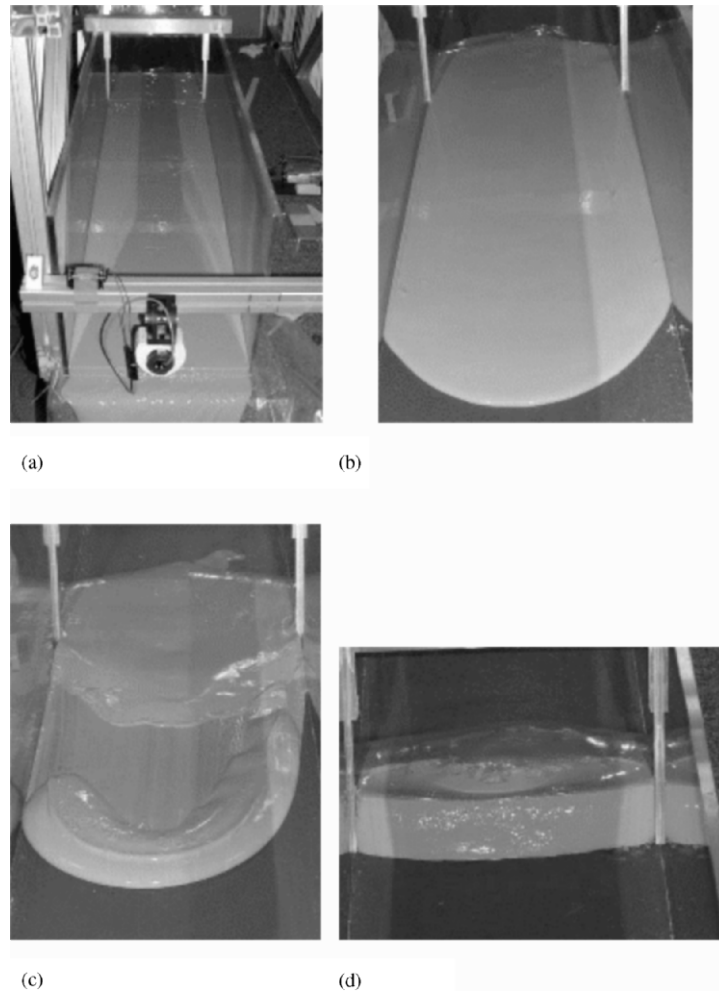


Fig. 15. Aspect of the main flow regimes following the dam-break of a bentonite suspension amount: **(a)** Type I, simple liquid wave ($\phi = 4.1$; $T = 5$ min.); **(b)** Type II, yield stress fluid layer (;); **(c)** Type III, landslide (;); **(d)** Type IV, solid at rest ($\phi = 16.4$; $T = 1$ min.); (c) Type III, landslide ($\phi = 6.4$; $T = 40$ min.); (d) Type IV, solid at rest ($\phi = 16.4$; $T = 1035$ min.)

above lead to a large variety of flow characteristics. Let us consider for example experiments of dam-break with a bentonite suspension (cf. Fig. 15): a certain amount of material (at a solid fraction ϕ) lying behind a dam at the top of an inclined plane is suddenly released by opening the reservoir gate, after some time of rest (T). As the degree of jamming (either T or ϕ) increases the resulting flow turns from an apparent simple liquid flow, to a yield stress fluid flow (forming a mouth stopped in the channel), a landslide

(abrupt flow in mass, after a certain time, of a part of the fluid), and a solid being only slightly deformed [54].

5 Conclusion

The solid-liquid transition in jammed systems is a dynamic phenomenon: the material evolves either towards a solid or a liquid regime depending on the relative values of the stress applied and a critical stress. In general this transition does not occur at the same time in different points so that a solid-liquid interface develops and displaces through the fluid. This in particular implies that rheometrical data with usual tools often reflect this coupled spatio-temporal evolution rather than the intrinsic properties of the material.

Recently it was also observed that in some systems, strong fluctuations of the velocity profiles occur either around the transition between two flowing phases [55] in micellar solutions or around the solid-liquid transition (likely in the “discontinuous” regime) in foams and granular materials [55–57]. This suggests that in some cases the solid-liquid transition might also depend on more complex spatio-temporal collective effects.

References

1. A.J. Liu, and S.R. Nagel, *Nature* **396**, 21 (1998).
2. R.B. Bird, G.C. Dai, and B.Y. Yarusso, *Rev. Chem. Eng.* **1**, 1-70 (1982).
3. P. Coussot, *Phys. Rev. Lett.*, **74**, 3971 (1995).
4. M. Cloitre, R. Borrega, L. Leibler, *Phys. Rev. Lett.* **75**, 2610 (1995).
5. A. Mujumdar, A. Beris, and A. Metzner, *J. Non-Newtonian Fluid Mech.* **2072**, 1 (2001).
6. J. Billingham and J.W.J. Ferguson, *J. Non-Newtonian Fluid Mech.*, **47**, 21 (1993).
7. P. Coussot, A.I. Leonov, and J.M. Piau, *J. Non-Newtonian Fluid Mech.* **46**, 179 (1993).
8. H.A. Barnes and K. Walters, *Rheol. Acta* **24**, 323 (1985).
9. H.A. Barnes, *J. Non-Newt. Fluid Mech.* **81**, 133–178, (1999).
10. J.P. Hartnett and R.Y.Z. Hu, *J. Rheol.* **33**, 671 (1989).
11. G. Astarita, *J. Rheol.* **34**, 275 (1990).
12. J. Schurz, *J. Rheol.* **36**, 1319 (1992).
13. I.D. Evans, *J. Rheol.* **36**, 1313 (1992).
14. R.D. Spaans and M.C. Williams, *J. Rheol.* **39**, 241 (1995).
15. D.C.-H. Cheng and F. Evans, *Brit. J. Appl. Phys.* **16**, 1599 (1965).
16. J. Mewis, *J. Non-Newtonian Fluid Mech.* **6**, 1–20 (1979).
17. F. Moore, *Trans. Brit. Ceramic Soc.* **58**, 470–494 (1959).
18. D.C.-H. Cheng, *Rheol. Acta* **42**, 372 (2003).
19. D. Quemada, *Eur. Phys. J. AP* **5**, 191 (1999).
20. P. Coussot, *Rheometry of pastes, suspensions and granular materials—Applications in industry and environment*, 312p. (Wiley, New York, 2005).

21. S.W. Sinton, and A.W. Chow, *J. Rheol.* **35**, 735 (1991).
22. J.R. Abbott, N. Tetlow, A.L. Graham, S.A. Altobelli, E. Fukushima, L.A. Mondy, and T.S. Stephens, *J. Rheol.* **35**, 773 (1991).
23. M. Nakagawa, S.A. Altobelli, A. Caprihan, E. Fukushima, E.K. Jeong, *Experiments in Fluids* **16**, 54 (1993).
24. C.J. Rofe, R.K. Lambert, and P.T. Callaghan, *J. Rheol.* **38**, 875 (1994).
25. A.W. Chow, S.W. Sinton, J.H. Iwamiya, and T.S. Stephens, *Phys. Fluids* **6**, 2561 (1994).
26. A.M. Corbett, R.J. Phillips, R.J. Kauten, and K.L. McCarthy, *J. Rheol.* **39**, 907 (1995).
27. S.J. Gibbs, K.L. James, L.D. Hall, D.E. Haycock, W.J. Frith, and S. Ablett, *J. Rheol.* **40**, 425 (1996).
28. D.F. Arola, G.A. Barrall, R.L. Powell, K.L. McCarthy and M.J. McCarthy, *Chem. Eng. Sci.* **52**, 2049 (1997).
29. K.L. McCarthy, and W.L. Kerr, *J. Food Eng.* **37**, 11 (1998).
30. A.D. Hanlon, S.J. Gibbs, L.D. Hall, D.E. Haycock, W.J. Frith and S. Ablett, *Magn. Reson. Imaging* **16**, 953 (1998).
31. P.T. Callaghan, *Rep. Prog. Phys.* **62**, 599 (1999).
32. S.I. Han, O. Marseille, C. Gehlen, and B. Blmich, *J. Magn. Res.* **152**, 87 (2001).
33. J. Gtz, W. Kreibich, M. Peciar, H. Buggisch, *J. Non-Newtonian Fluid Mech.* **98**, 117 (2001).
34. S. Jarny and P. Coussot, *Rhologie* **2**, 52 (2002) (in French).
35. V. Bertola, F. Bertrand, H. Tabuteau, D. Bonn, and P. Coussot, *Journal of Rheology* **47**, 1211 (2003).
36. J.S. Raynaud, P. Moucheront, J.C. Baudez, F. Bertrand, J.P. Guilbaud, P. Coussot, *Journal of Rheology* **46**, 709 (2002).
37. D. Bonn, P. Coussot, H.T. Huynh, F. Bertrand, G. Debregeas, *Europhysics Letters* **59**, 786 (2002).
38. P. Coussot, J.S. Raynaud, F. Bertrand, P. Moucheront, J.P. Guilbaud, H.T. Huynh, S. Jarny, and D. Lesueur, *Physical Review Letters* **88**, 218301 (2002).
39. J.C. Baudez, S. Rodts, X. Chateau, P. Coussot, *Journal of Rheology*, **48**, 69 (2004).
40. S. Jarny, N. Roussel, S. Rodts, R. Le Roy, P. Coussot, *Rheological behavior of cement pastes from MRI velocimetry*, in press in *Concrete Cement Research* (2004).
41. S. Rodts, J.C. Baudez, and P. Coussot, *From discrete to continuum flow in foams*, *Europhys. Lett.* **69**, 636 (2005).
42. H. Tabuteau, J.C. Baudez, F. Bertrand, and P. Coussot, *Rheologica Acta* **43**, 168 (2004).
43. F. Varnik, L. Bocquet, J.L. Barrat, and L. Berthier, *Phys. Rev. Lett.* **90**, 095702 (2003).
44. F. Pignon, A. Magnin, and J.M. Piau, *J. Rheol.* **40**, 573 (1996).
45. S. Meeker, R.T. Bonnecaze, and M. Cloitre, *Phys. Rev. Lett.* **92**, 198302 (2004).
46. J.C. Baudez and P. Coussot, *Physical Review Letters* **93**, 128302 (2004).
47. P. Coussot, Q.D. Nguyen, H.T. Huynh, and D. Bonn, *Phys. Rev. Lett.* **88**, 175501 (2002).
48. F. Da Cruz, F. Chevoir, D. Bonn, and P. Coussot, *Phys. Rev. E* **66**, 051305 (2002).
49. T. Ferroir, H.T. Huynh, X. Chateau, and P. Coussot, *Physics of Fluids* **16**, 594 (2004).

50. H.T. Huynh, N. Roussel, P. Coussot, *Physics of Fluids* **17**, 033101 (2005).
51. N. Roussel, R. Le Roy and P. Coussot, *J. Non-Newt. Fluid Mech.* **117**, 85 (2004).
52. N.J. Alderman, G.H. Meeten, and J.D. Sherwood, *J. Non-Newt. Fluid Mech.* **39**, 291 (1991).
53. P. Coussot, Q.D. Nguyen, H.T. Huynh, and D. Bonn, *J. Rheol.* **46**, 573 (2002).
54. H. Chanson, N. Roussel, S. Jarny, and P. Coussot, *Physics of Fluids* **17**, 011704 (2005).
55. J-B. Salmon, S. Manneville and A. Colin, *Phys. Rev. E* **68**, 051503 (2003).
56. J. Lauridsen, G. Chanan, and M. Dennin, *Phys. Rev. Lett.* **93**, 018303 (2004).
57. F. Da Cruz, *Flow of dry grains-Friction and jamming*, Ph.D. thesis (ENPC, Marne la Vallée, (2004) (in French).

Dynamics of Disordered Elastic Systems

T. Giamarchi¹, A.B. Kolton¹, and A. Rosso²

¹ DPMC, University of Geneva, 24 Quai Ernest Ansermet, 1211 Geneva
Switzerland

Thierry.Giamarchi@physics.unige.ch

Alejandro.Kolton@physics.unige.ch

² Laboratoire de Physique Théorique et Modèles Statistiques Bât. 100, Université
Paris-Sud, 91405 Orsay Cedex, France

rosso@lptms.u-psud.fr

In these notes we present a brief review of the dynamical properties of interfaces in a disordered environment. We focus in particular on the response of such systems to a very small external force, and the corresponding very slow motion it entails, so called creep. We discuss various general theoretical aspects of this problem and consider in detail the case of a one dimensional interface (domain wall).

1 Introduction

Understanding the statics and dynamics of elastic systems in a random environment is a longstanding problem with important applications for a host of experimental systems. Such problems can be split into two broad categories: (i) propagating interfaces such as magnetic [1–4] or ferroelectric [5, 6] domain walls, fluid invasion in porous media [7], contact line in wetting [8], epitaxial growth [9] or crack propagation [10]; (ii) periodic systems such as vortex lattices [11–13], charge density waves [14], or Wigner crystals of electrons [15, 16]. In all these systems the basic physical ingredients are identical: the elastic forces tend to keep the structure ordered (flat for an interface and periodic for lattices), whereas the impurities locally promote the wandering. From the competition between disorder and elasticity emerges a complicated energy landscape with many metastable states. This results in glassy properties such as hysteresis and history dependence of the static configuration.

To study the statics, the standard tools of statistical mechanics could be applied, leading to a good understanding of the physical properties. Scaling arguments and simplified models showed that even in the limit of weak disorder, the equilibrium large scale properties of disordered elastic systems are governed by the presence of impurities. In particular, below four (internal) dimensions, displacements grow unboundedly [17] with the distance, resulting in rough interfaces and loss of strict translational order in periodic structures. To go beyond simple scaling arguments and obtain a more detailed description of the system is rather difficult and requires sophisticated approaches such as replica theory [18] or functional renormalization group [19]. Much progress

was recently accomplished both due to analytical and numerical advances. For interfaces, the glassy nature of the system is confirmed (so called *random manifold*), and a coherent picture of the system is derived from the various methods. Periodic systems have also been shown to have glassy properties but to belong to a different universality class than interfaces, with quite different behavior for the long range nature of the correlation functions [12, 13, 20].

The competition between disorder and elasticity manifests also in the dynamics of such systems, and if any in a more dramatic manner. Among the dynamical properties, the response of the system to an external force F is specially crucial, both from a theoretical point of view, but also in connection with measurements. Indeed in most systems the velocity v versus force F characteristics is directly measurable and is simply linked to the transport properties (voltage-current for vortices, current-voltage for CDW and Wigner crystals, velocity-applied magnetic field for magnetic domain walls).

Some of the questions related to this issue are shown in Fig. 1. In the presence of disorder it is natural to expect that, at zero temperature, the system remains pinned and only polarizes under the action of a small applied force, i.e. moves until it locks on a local minimum of the tilted energy landscape. At larger drive, the system follows the force F and acquires a non-zero asymptotic velocity v . So a first set of questions is prompted by the zero temperature properties. What is F_c ? An estimate of F_c can be obtained via scaling arguments [21] or with a criterion for the breakdown of the large velocity expansion [22, 23] and related to static quantities such as the Larkin-Ovchinnikov length, or computed numerically by an exact algorithm [24]. The $v - F$ curve at $T = 0$ is reminiscent of the one of an order parameter in a second order phase transition [25]. Here the system is out of equilibrium so no direct analogy is possible but this suggests that one could

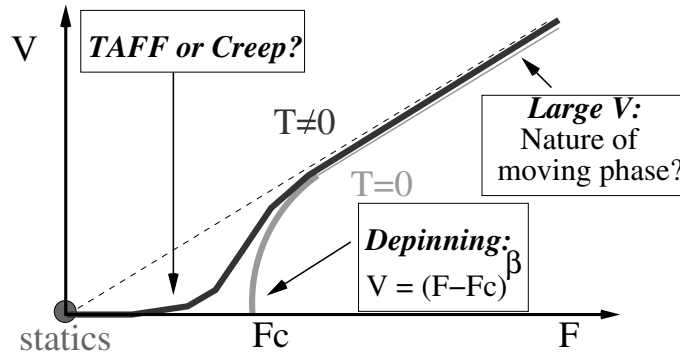


Fig. 1. The velocity v induced by an external force F of a disordered elastic system. At zero temperature $T = 0$ the system stays pinned until a critical force F_c is reached. At finite temperature a motion can occur even for forces below threshold $F < F_c$ since the barriers to motion can always be passed by thermal activation

expect $v \sim (F - F_c)^\beta$ with a dynamical critical exponent β [26]. Calculation of such exponents is of course an important question [27–30].

Another important set of questions pertain to the nature of the moving phase itself, and in particular to the behavior at large velocity: how much this moving system resembles or not the static one [31–33]? This concerns both the positional order properties and the fluctuations in velocity such as the ones measured in noise experiments.

Finally, one of the most important questions, and the one on which we will concentrate in these notes, is the response well below threshold $F \ll F_c$ at finite temperature. In this regime, the system is expected to move through thermal activation. What is the nature of this motion and what is the velocity? The simplest answer would be that the system can overcome barriers via thermal activation, [34] leading to a linear response at small force of the form $v \sim e^{-U_b/T} F$, where U_b is some typical barrier. However it was realized that such a typical barrier does not exist in a glassy system [35–38] and that the response of the system was more complicated. The motion is actually dominated by barriers which *diverge* as the drive F goes to zero, and thus the flow formula with finite barriers is incorrect. Well below F_c , the barriers are very high and thus the motion, usually called “creep” is extremely slow. Scaling arguments, relying on strong assumptions such as the scaling of energy barriers and the use of statics properties to describe an out of equilibrium system, were used to infer the small F response. This led to a non linear response, characteristic of the creep regime, of the form $v \sim \exp(-C F^{-\mu}/T)$.

Given the phenomenological aspect of these predictions and the uncontrolled nature of the assumptions made, many open questions remain to be answered, in particular whether such a behavior is indeed correct [39] and can be derived directly from microscopic equation of the motion [29, 40]. We will review these questions in these notes. The plan of the notes is as follows. In Sect. 2 we recall the basic concepts of interfaces in the presence of disorder. In Sect. 3, we recall the phenomenological derivation of the creep law. We present the microscopic derivation of the creep law from the equations of motion in Sect. 4, and discuss the similarities and differences with the phenomenological result. In Sect. 5 we focus on the situation of domain walls. Such a situation is a particularly important both for experimental realizations of the creep but also because one dimension is the extreme case for such systems. Conclusions can be found in Sect. 6.

2 Basic Concepts

Let us introduce in this section the basic ingredients of the systems under study. We will focus in these short notes to the case of interfaces, but similar concepts apply to periodic systems as well. The interface is a sheet of dimension d living in a space of dimensions D . For realistic interfaces $D = d + 1$

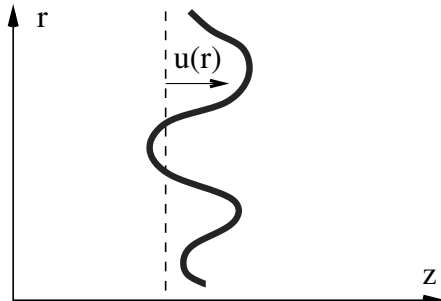


Fig. 2. A one dimensional interface (domain wall) living in a two dimensional space (film). The position of the interface is determined (provided there are no overhangs or bubbles) by the displacement u from a flat configuration

but generalization are of course possible (for example $D = d$ corresponds to periodic systems). We call r the internal coordinate of the interface and z all its transverse directions. The interface position is labelled by a displacement $u(r)$ from a flat configuration. This determines totally the shape of the interface provided that u is univalued, i.e. that there are no overhangs or bubbles. The case of a one dimensional interface ($d = 1$) in a two dimensional film is shown in Fig. 2. Since the interface distortions cost elastic energy, its zero temperature equilibrium configuration in the absence of disorder is the flat one. Deviation from this equilibrium position are described by an Hamiltonian $H[u]$ which is a function of the displacements u . For small displacements one can make the usual elastic approximation

$$H[u] = \frac{1}{2} \int \frac{d^d q}{(2\pi)^d} c(q) u_q^* u_q \quad (1)$$

where u_q is the Fourier transform of $u(r)$ and $c(q)$ are the so called elastic coefficients. If the elastic forces acting on the interface are short ranged then one has $c(q) = cq^2$ which corresponds to

$$H[u] = \frac{c}{2} \int d^d r (\nabla u(r))^2 \quad (2)$$

For some interfaces where long range interactions play a role different forms for the elasticity are possible. This is in particular the case when dipolar forces [41] are taken into account [6] or for the contact line in wetting [42] and crack propagation [43].

In addition to the elastic energy the interface gains some energy by coupling to the disorder. Two universality classes for the disorder exist (see Fig. 3). The so called random bond disorder corresponds to impurities that directly attract or repel the interface. On the contrary, for the so called random field disorder the pinning energy is affected by all the randomness that

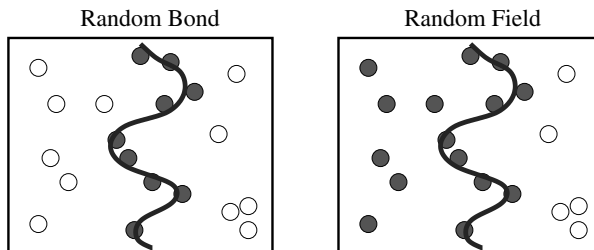


Fig. 3. The two types of disorder (the names are coming from the magnetic realization of such systems). The dark circles are the impurities that contribute to the pinning energy of the interface. In the random bond case only neighboring impurities contribute while in the random field case all the impurities on the left side of the the interface contribute. This makes the latter disorder effectively long ranged, even if the disorder potential $V(z, r)$ is short range

the interface has encountered in its previous motion. If $V(z, r)$ denotes the random potential generated by the impurities the pinning energy writes:

$$H_{\text{dis}}[u] = \int dr \begin{cases} V(u(r), r) & \text{random bond} \\ \int_0^{u(r)} dz V(z, r) & \text{random field} . \end{cases} \quad (3)$$

The competition between disorder and elasticity manifests itself in the static properties of the interface. The presence of disorder leads to the appearance of many metastable states and glassy properties. In particular, the interface deviates from the flat configuration and becomes rough. From the scaling of the relative displacements correlation function, a roughness exponent ζ can be defined by

$$B(r) = \overline{\langle [u(r) - u(0)]^2 \rangle} \propto r^{2\zeta} \quad (4)$$

where $\langle \rangle$ denotes thermodynamic average and $\overline{\dots}$ denotes disorder average. We will not enter in more details about the statics here and refer the reader to the literature on that point [9, 44].

Dynamics is much more complicated since the standard tools of statistical physics can not be used. One has to study the equation of motion of the system

$$\eta \frac{\partial}{\partial t} u(r, t) = - \frac{\delta H}{\delta u(r, t)} + F + \zeta(r, t) \quad (5)$$

This equation is written for overdamped dynamics, but can include inertia as well. η is the friction taking into account the dissipation, F the external applied force, and $\zeta(r, t)$ a thermal noise, needed to reproduce the effect of finite temperature. The correlation of the thermal noise is $\langle \zeta(r, t) \zeta(r', t') \rangle = 2\eta T \delta(r - r') \delta(t - t')$. Solving this equation of motion allows to extract all the dynamical properties of the system. The presence of disorder in the Hamiltonian H makes this a very complicated proposal. In the

absence of the external force $F = 0$, this Langevin equation allows to recover the static properties after the system has achieved its thermal equilibrium.

3 Creep, Phenomenology

Let us focus here on the response of the system to a very small external force. For usual systems we expect the response to be linear. Indeed earlier theories of such a motion found a linear response. The idea is to consider that a blob of pinned material has to move in an energy landscape with characteristic barriers U_b as shown in Fig. 4. The external force F tilts the energy landscape making forward motion possible. The barriers are overcome by thermal activation (hence the name: Thermally Assisted Flux Flow) with an Arrhenius law. If the minima are separated by a distance a the velocity is

$$v \propto e^{-\beta(U_b - Fa/2)} - e^{-\beta(U_b + Fa/2)} \simeq e^{-\beta U_b} F \quad (6)$$

The response is thus linear, but exponentially small.

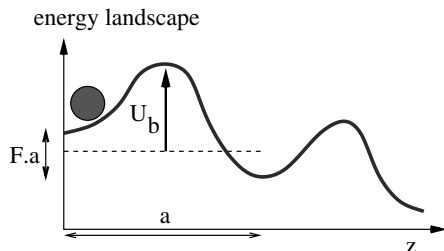


Fig. 4. In the Thermally Assisted Flux Flow (TAFF) [34] a region of pinned material is considered as a particle moving in an energy landscape characterized by characteristic barriers U_b . This leads to an exponentially small but linear response

However this argument is grossly inadequate for a glassy system. The reason is easy to understand if one remembers that the static system is in a vitreous state. In such states a characteristic barrier U_b does not exist, since barriers are expected to diverge as one gets closer to the ground state of the system. The TAFF formula is thus valid in systems where the glassy aspect is somehow killed and the barriers do saturate. This could be the case for example for a finite size interface. When the glassy nature of the system persists up to arbitrarily large length scales the theory should be accommodated to take into account the divergent barriers. This can be done quantitatively within the framework of the elastic description [35,36,38,45]. The basic idea rests on two quite strong but reasonable assumptions: (i) the motion is so slow that one can consider at each stage the interface as motionless and use its *static*

description; (ii) the scaling for barriers, which is quite difficult to determine, is the same as the scaling of the minimum of energy (metastable states) that can be extracted again from the static calculation. If the displacements scale as $u \sim L^\zeta$ then the energy of the metastable states (see (2)) scales as

$$E(L) \sim L^{d-2+2\zeta} \quad (7)$$

where we use that elastic and pinning energy scale the same way. Since the motion is very slow, the effect of the external force is just to tilt the energy landscape

$$E(L) - F \int d^d r u(r) \sim L^{d-2+2\zeta} - FL^{d+\zeta} \quad (8)$$

Thus, in order to make the motion to the next metastable state, one needs to move a piece of the pinned system of size

$$L_{\text{opt}} \sim \left(\frac{1}{F} \right)^{\frac{1}{2-\zeta}} \quad (9)$$

The size of the optimal nucleus able to move thus grows as the force decrease. Since the barriers to overcome grow with the size of the object, the minimum barrier to overcome (*assuming* that the scaling of the barriers is *also* given by (7))

$$U_b(F) \sim \left(\frac{1}{F} \right)^{\frac{d-2+2\zeta}{2-\zeta}} \quad (10)$$

leading to the well known *creep formula* for the velocity

$$v \propto \exp \left[-\beta U_c \left(\frac{F_c}{F} \right)^\mu \right] \quad (11)$$

where F_c is the depinning force and U_c a characteristic energy scale and the *creep exponent* μ is given by,

$$\mu = \frac{d-2+2\zeta}{2-\zeta} \quad (12)$$

Equations (11) and (12) are quite remarkable. They relate a dynamical property to *static* exponents, and shows clearly the glassy nature of the system. The corresponding motion has been called creep since it is a sub-linear response. Of course the derivation given here is phenomenological, and it will be important to check by other means whether the results here hold. This will be the goals of the two next sections, where first the creep law will be derived directly from the equation of motion in $d = 4 - \epsilon$ dimensions, and then the creep will be examined in the important case of $d = 1$ domain walls.

4 Around Four Dimensions

The previous phenomenological derivation of the creep formula rests on very strong hypothesis. In particular it is assumed that: (a) the motion is dominated by the typical barriers, and not by tails of distributions in the waiting times or barriers; (b) the motion is so slow that the line has the time to completely re-equilibrate between two hopping events so that one can take all exponents as the equilibrium ones. Given the phenomenological ground of these predictions and the uncontrolled nature of the assumptions made, both for the creep and for the depinning, it is important to derive this behavior in a systematic way, directly from the equation of motion.

In principle one has simply to solve the equation of motion (5). In practice this is of course quite complicated. A natural framework for computing perturbation theory in off-equilibrium systems is the dynamical formalism [46,47]. Integrating on all configurations u we can exponentiate the equation of motion by introducing an auxiliary field \hat{u} :

$$\int \mathcal{D}u \delta \left(\eta \frac{\partial u}{\partial t} + \frac{\delta H}{\delta u(r,t)} - F - \zeta(r,t) \right) = \int \mathcal{D}u \mathcal{D}\hat{u} \exp \left[i\hat{u} \left(\eta \frac{\partial u}{\partial t} + \frac{\delta H}{\delta u(r,t)} - F - \zeta(r,t) \right) \right] \quad (13)$$

the thermal and disorder average can easily be done, leading to a field theory with some action S

$$S(u, \hat{u}) = \int_{rt} i\hat{u}_{rt} (\eta \partial_t - c \nabla^2) u_{rt} - \eta T \int_{rt} i\hat{u}_{rt} i\hat{u}_{rt} - F \int_{rt} i\hat{u}_{rt} - \frac{1}{2} \int_{rtt'} i\hat{u}_{rt} i\hat{u}_{rt'} \Delta(u_{rt} - u_{rt'}) \quad (14)$$

where Δ is defined in the correlator of the pinning force $F_p = -\delta H_{\text{dis}}/\delta u$, as

$$\overline{F_p(u, r) F_p(u', r')} = \Delta(u - u') \delta(r - r') . \quad (15)$$

The functional form of this correlator depends on whether one has random bond or random field disorder (see e.g. [29] for more details). Essentially Δ is a function with a width of the order of the correlation of the disorder along the z direction. The advantages of this representation are many: disorder and thermal averages $\overline{\langle A[u] \rangle} = \langle A[u] \rangle_S$ of any observable $A[u]$ can be computed with the weight e^{-S} ; the response functions to an external perturbation h_{rt} are simply given by correlations with the response field: $\langle A[u] i\hat{u}_{rt} \rangle = \frac{\delta}{\delta h_{rt}} \langle A[u] \rangle$. In addition, since we are much more familiar with fields theories than with equations of motion, we have at our disposal a variety of tools to tackle the action S . Although it is impossible to solve the action exactly it is possible to look at its properties using a renormalization

group procedure. We will not detail the procedure but just recall here the resulting functional renormalization group (FRG) flow equations [29, 40] to give a flavor of their physics

$$\begin{aligned}
 \partial \tilde{\Delta}(u) &= (\epsilon - 2\zeta)\tilde{\Delta}(u) + \zeta u \tilde{\Delta}'(u) + \tilde{T} \tilde{\Delta}''(u) \\
 &+ \int_{s>0, s'>0} e^{-s-s'} \left[\tilde{\Delta}''(u) \left(\tilde{\Delta}((s' - s)\lambda) - \tilde{\Delta}(u + (s' - s)\lambda) \right) \right. \\
 &- \tilde{\Delta}'(u - s'\lambda) \tilde{\Delta}'(u + s\lambda) \\
 &\left. + \tilde{\Delta}'((s' + s)\lambda) \left(\tilde{\Delta}'(u - s'\lambda) - \tilde{\Delta}'(u + s\lambda) \right) \right] \\
 \partial \ln \lambda &= 2 - \zeta - \int_{s>0} e^{-s} s \tilde{\Delta}''(s\lambda) \\
 \partial \ln \tilde{T} &= \epsilon - 2 - 2\zeta + \int_{s>0} e^{-s} s \lambda \tilde{\Delta}'''(s\lambda) \\
 \partial \tilde{F} &= e^{-(2-\zeta)l} c \Lambda_0^2 \int_{s>0} e^{-s} \tilde{\Delta}'(s\lambda)
 \end{aligned} \tag{16}$$

where $\epsilon = 4 - d$, ∂ denotes $\frac{\partial}{\partial l}$ and $\lambda = \eta v$. The tilde denotes rescaled quantities (see [29] for the notations). Contrarily to the standard case of critical phenomena, where the potential Δ can be expanded in powers of the field and only the first terms are relevant, here all the powers of the expansion have the same dimension. It is thus necessary to renormalize the whole function [48] (in other words one has an infinite set of coupled renormalization equations). One of the most important consequences is shown in Fig. 5: the renormalized function Δ becomes nonanalytic beyond a certain length scale, and develop a cusp which signals pinning and the glassy properties of the system. This cusp appears at a finite length scale corresponding to the Larkin-Ovchinnikov length [23] and it is directly related to the existence of the finite critical force F_c [27, 28] at zero temperature. The FRG procedure has been push up to two loop expansion [49, 50].

The presence of a finite temperature and a finite velocity (proportional to λ) prevents the appearance of the cusp [29, 40]. For very small external force, the way the cusp is cut occurs in two steps, as shown in Fig. 6. At

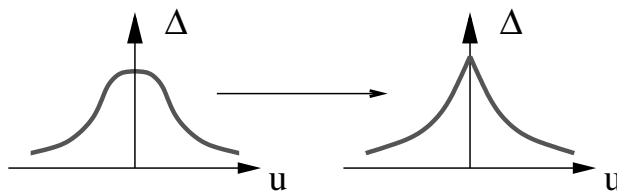


Fig. 5. Although the correlator of the disorder is initially an analytic function, a non analyticity (cusp) appears at a finite scale l_c . This length scale corresponds to the Larkin-Ovchinnikov length at which pinning and metastability occur

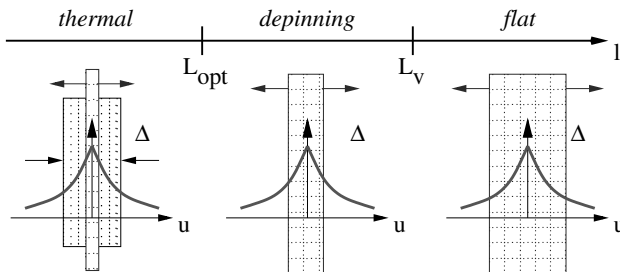


Fig. 6. The cusp is rounded by both the temperature and the finite velocity of the interface. In the thermal regime, the main source of rounding comes from the temperature and the role of velocity is negligible. Then the system enters a regime in which the main source of rounding is the velocity and the role of temperature is negligible. This regime is very similar to a depinning regime. Finally the velocity rounds the whole correlator of the disorder and thus disorder is washed out by the averaging due to motion. At this length scale one recovers a purely thermal interface

very low velocity the cusp is cut first by the temperature and the velocity can be forgotten. A physical way to interpret this regime is that the motion consists essentially in overcoming the barriers by thermal activation. This regime corresponds essentially to the one in the phenomenological derivation of the creep. Increasing the scale l the temperature renormalizes down and the velocity renormalizes up. For this reason, above a lengthscale that can be identified with L_{opt} , the cusp starts to be regularized by the velocity. The temperature can now be forgotten and a regime very similar to the standard depinning regime at $T = 0$ takes place. Then, finally, at a certain length scale L_v the whole u dependence of the correlator of the disorder $\Delta(u)$ is erased by the finite velocity. This corresponds to a regime where the motion of the interface has averaged over the disorder and thus, in the moving frame, the interface is now simply submitted to the thermal-like noise [27].

The FRG calculation of the velocity confirms the phenomenological arguments and finds the creep law (11). Moreover, at the first order in ϵ , the creep exponent μ agrees with the scaling (12). The velocity behavior is thus dominated by the first (thermal) regime. On the other hand because the second regime exists, we expect that the phenomenological derivation is incorrect as far as the characteristic lengthscales of the problem are concerned. Indeed, the phenomenological derivation would predict that the characteristic size of a moving domain is the optimal length scale L_{opt} , which coincides with the end of the thermal regime. However the FRG equations predict that the size of a moving domain corresponds to L_v , the scale of the end of the depinning regime. A physical way to understand this behavior is to say that the motion of the thermal nucleus, of size L_{opt} , triggers an avalanche of a larger size L_v . The FRG thus predicts much larger avalanche scales than what should

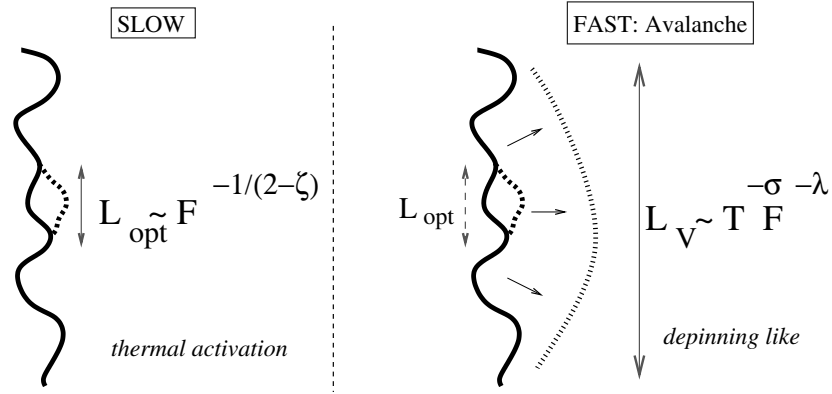


Fig. 7. The phenomenological theory of creep (*left*) would predict that the avalanche size corresponds to the size of the thermal nucleus L_{opt} . From the FRG a quite different size emerges corresponding to a larger avalanche of size L_v triggered by the thermal motion, in a way similar than for a depinning process. λ and σ are two characteristic exponents

be naively expected from the phenomenological theory, as shown in Fig. 7. Such large avalanches are in agreement with recent experiments in magnetic systems [3].

Confirming the stretched exponential behavior of the creep is of course an experimental challenge given the large span of velocities needed. The first unambiguous determination of the creep law with a precise determination of the exponent was made in magnetic films, for one dimensional domain walls [1], and confirmed with subsequent measurements [3,4]. Ferroelectric systems [5,6] have shown a creep exponent compatible with two dimensional domain walls in presence of dipolar forces. In periodic systems, such as vortices, it is more delicate to determine the precise value of the exponent, even when non linear behavior has been clearly observed. The experiment [51] shows a creep exponent in agreement with the theoretical predictions.

5 Low Dimensional Situation: Domain Walls

Around four dimensions the creep hypothesis gives a velocity dependence consistent with the one obtained from the microscopic derivation, at least up to the order ϵ at which the renormalization group analysis can be performed. Let us now focus at the other extreme limit, namely when the wall is one dimensional and moves in a two dimensional space. The interest in such a situation is twofold. First, as already mentioned, controlled experiments are performed on domain wall motion. Second, from the theoretical point of view the situations of a low dimensional domain wall is very interesting. Thermal effects are increasingly important as the dimension is lowered. For $d \leq 2$ they

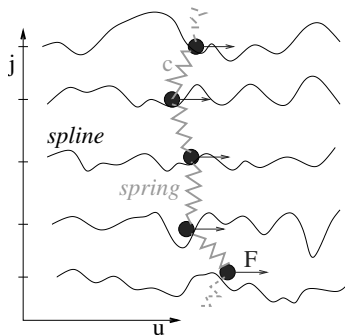


Fig. 8. Discretization scheme for the elastic line driven in a random potential

lead to a roughening of the domain wall, even in the absence of disorder (with an exponent $\zeta_T = (2-d)/2$). One can thus expect more intricate competition between temperature and disorder effects.

Numerical simulations are a valuable alternative theoretical tool to address this open issue. In this respect, Langevin dynamics simulations have been used to study both the velocity-force (v - F) characteristics and the dynamic roughness ζ of an elastic string in a random potential [39,52,53]. In [39] we have studied equation (5) with a short range elasticity:

$$\eta \frac{\partial}{\partial t} u(r, t) = c \partial_r^2 u(r, t) + F_p(u, r) + F + \zeta(r, t) \quad (17)$$

where $F_p(u, r) = -\partial_u V(u(r), r)$ is the pinning force derived from the random bond disorder $V(u, r)$.

To solve numerically (17) we discretize the string along the r direction, $r \rightarrow j = 0, \dots, L-1$, keeping $u_j(t)$ as a continuous variable. A second order stochastic Runge-Kutta method [54] is used to integrate the resulting equations. To model a continuous random potential we generate, for each j , a cubic spline $V(u_j, j)$ passing through regularly spaced uncorrelated Gaussian random points [24]. The geometry of our system is shown in Fig. 8. We are interested in the v - F characteristics. Typical curves, obtained in the simulations, are shown in Fig. 9. In the whole range of temperature and pinning strength analyzed we find that the v - F curve can be well fitted by the creep formula (11) with U_c and μ as fitting parameters. We thus confirm the predicted stretched exponential behavior. However, contrarily to the naive creep relation (12) we find that not only U_c , but also μ , depend on temperature. Since the phenomenological theory assumes that μ can be computed directly from the roughness exponent ζ it is important to study the geometrical properties of the driven string. For this reason we introduce the averaged structure factor,

$$S(q) \sim \left\langle \left| \int dr u(r, t) e^{-iqr} \right|^2 \right\rangle. \quad (18)$$

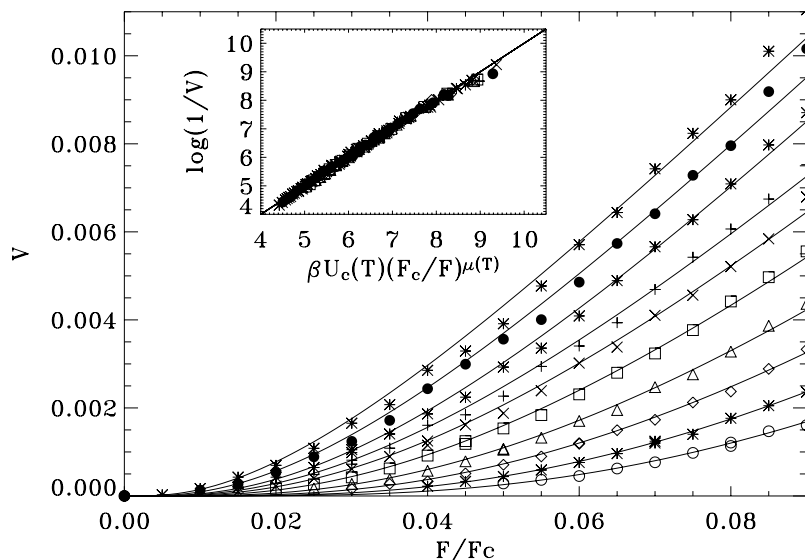


Fig. 9. After [39]. v - F characteristics for several temperatures, increasing from bottom to top. Solid lines are fits of the creep formula (11) with U_c and μ as fitting parameters. The inset assures the validity of the creep formula in the range of temperature and velocity analyzed

The dimensional analysis of this double integral allow us to compute ζ from $S(q) \sim q^{-(1+2\zeta)}$, valid for small q . In Fig. 10 we show the structure factor of an elastic string thermally equilibrated at $F = 0$. We can observe a crossover between a short distance regime where thermal fluctuations are dominant ($\zeta \sim \zeta_T = 1/2$) and a long distance disorder dominated regime where we find the well known roughness exponent $\zeta \sim \zeta_{eq} = 2/3$ [55]. For the dynamics (see Fig. 11), when $F \neq 0$ one can predict that the short distance behavior $L < L_T$ of the elastic string is still dominated by thermal fluctuations ($\zeta_T = 1/2$). Note that this thermally dominated regime has nothing to do with the regime derived in the previous section and valid up to the scale L_{opt} . In this regime disorder is already dominant and barriers are overcome by thermal activation. On the other hand, as already discussed, the finite velocity makes the quenched disorder to act as a thermal noise at the largest length scale $l > L_v$. Thus, in this case, the expected exponent is also $\zeta_v = 1/2$ [27]. Finally, at intermediate length scales, the physics is determined by the competition between disorder and elasticity and characterized by a non trivial random manifold roughness exponent.

A systematic analysis of the v - F characteristics and $S(q)$ show essentially two different regimes of creep motion. In Fig. 12(a) and (b) we show the structure factor for the two cases. As predicted, we get $\zeta \sim \zeta_T = 1/2$ for large q . At a certain scale we observe a crossover between the thermal and

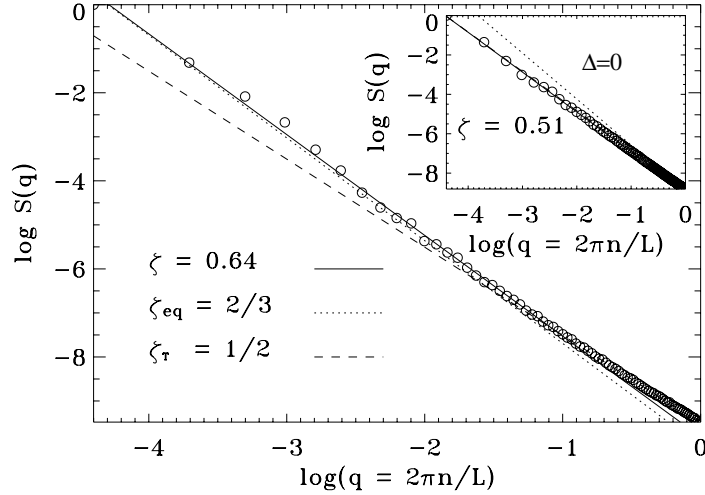


Fig. 10. Structure factor $S(q)$ of the elastic line for the statics. In the presence of disorder the long distance behavior is characterized by a roughness exponent $\zeta_{eq} = 2/3$, while in the absence of disorder (see inset) thermal fluctuation gives $\zeta_T = 1/2$

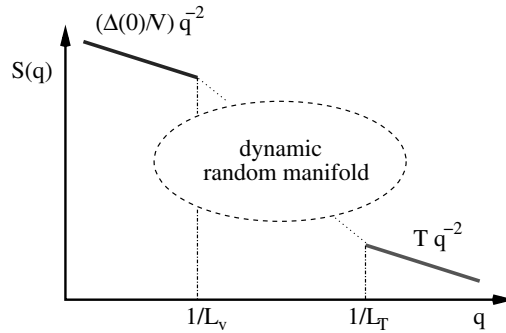


Fig. 11. Sketch of $S(q)$ expected for a driven elastic line

the random manifold scaling. The location of this crossover decreases as temperature (disorder) is increased (decreased). We can also observe that the second velocity-controlled crossover is not achieved in our finite-size simulation due to the very slow dynamics. Interestingly, for the small disorder case (Fig. 12(a)) the random manifold scaling gives $\zeta = 0.67 \pm 0.05$, in excellent agreement with the equilibrium value $\zeta_{eq} = 2/3$, while a much higher roughness exponent $\zeta = 0.9 \pm 0.05$ is found for the strong disorder case (Fig. 12(b)). The analysis of the v - F characteristics brings us to the same conclusion: the value of the exponent μ is close to the equilibrium value $\mu = 1/4$ for low disorder (high temperature) and departs from this value when the disorder

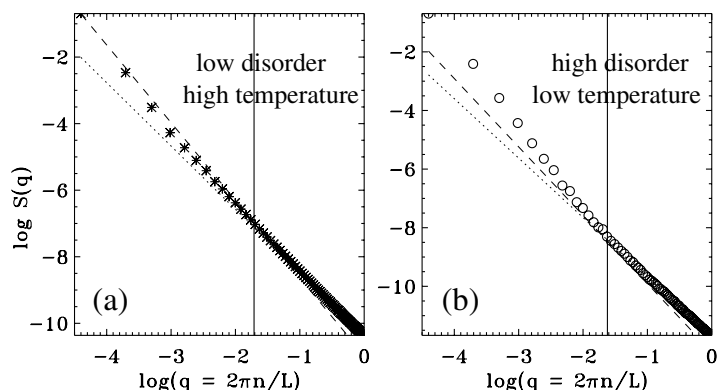


Fig. 12. After [39]. Structure factor $S(q)$ of the elastic line in the driven case. Two regimes are distinguished. (a) In the low disorder/high temperature regime the roughness exponent is consistent with $\zeta_{eq} = 2/3$. (b) In the high disorder/low temperature regime the roughness exponent is clearly bigger than ζ_{eq}

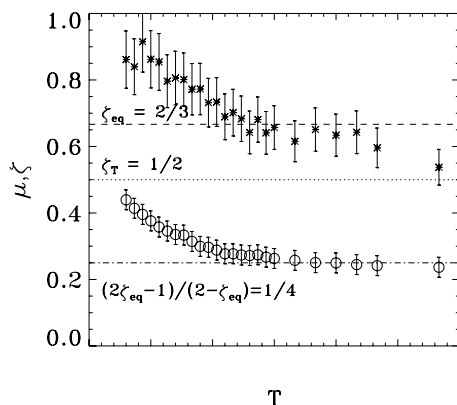


Fig. 13. After [39]. Roughness exponent, $\zeta(T)$, and creep exponent, $\mu(T)$, vs T . The *dashed line* gives the equilibrium roughness exponent $\zeta_{eq} = 2/3$, and the *dotted line* the purely thermal roughness $\zeta_T = 1/2$. The expected value for the creep exponent $\mu = 1/4$ is also indicated

(temperature) increases (decreases). In Fig. 13 we summarize all the results. We notice that although the values of ζ and μ depart from the equilibrium values, the relation (12) seems still to hold, within the error bars for the two exponents. This is highly non-trivial since equation (12) is derived from a calculation of the barriers in an equilibrium situation.

We thus have found two regimes of creep motion. The first one occurs when the temperature is larger than the strength of the disorder, giving $\mu \sim 1/4$ and $\zeta \sim 2/3$ as predicted by assuming a quasi-equilibrium nucleation picture of the creep motion. This implies that the domain wall has

time to re-equilibrate between hops, being the underlying assumption behind (12) essentially satisfied. The second regime occurs for temperatures smaller than the strength of the disorder, and is characterized by anomalously large values of both exponents. This clearly shows that in this regime the domain wall stays out of equilibrium, and that the naive creep hypothesis does not apply. Note that the measured roughness exponent is intermediate between the equilibrium value and the depinning value $\zeta_{dep} = 1.26 \pm 0.01$ [24]. The fact that the thermal nucleation which is the limiting process in the creep velocity, is in fact followed by depinning like avalanches was noted in the FRG study of the creep [29]. Whether such avalanches and the time it would take them to relax to equilibrium is at the root of the observed increase of the exponent, is clearly an interesting but quite complicated open question.

6 Conclusions and Open Questions

In these short notes we have presented a brief review of the dynamical properties of interfaces in a disordered environment. We have in particular focused on the response of such interfaces to a very small external force, and the corresponding very slow motion it entails (so called creep). Clearly many important questions remain to be understood for this problem. For large dimensions the microscopic derivation clearly supports the phenomenological one as far as the velocity is concerned, but also shows that different length scales enter to describe the dynamics. In particular, it predicts a much larger avalanche size than initially anticipated. For one dimensional walls the situation is even more complex, and the very hypothesis that the wall is constantly in equilibrium between two creep processes seems incorrect at least when the disorder is not weak enough or if the temperature becomes too low. The deviations such effect might entail on the creep exponent is of course important in connection with the experimental work.

Of course these questions are only the tip of the iceberg and more subtle questions such as how such a domain wall can age in the presence of the disorder are still largely not understood, and more analytical, numerical or experimental work is clearly needed to address these issues.

Acknowledgments

We have benefitted from invaluable discussions with many colleagues, too numerous to thank them all here. We would however like to specially thank D. Domínguez, J. Ferré, J. P. Jamet, W. Krauth, S. Lemerle, P. Paruch, V. Repain, J.M. Triscone. TG acknowledges the many fruitful and enjoyable collaborations with P. Le Doussal and P. Chauve. This work was supported in part by the Swiss National Science Foundation under Division II.

References

1. S. Lemerle, J. Ferré, C. Chappert, V. Mathet, T. Giamarchi, and P. Le Doussal, Phys. Rev. Lett. **80**, 849 (1998).
2. L. Krusin-Elbaum, T. Shibauchi, B. Argyle, L. Gignac, and D. Weller, Nature **410**, 444 (2001).
3. V. Repain, M. Bauer, J.-P. Jamet, J. Ferré, A. Mougin, C. Chappert, and H. Bernas, Europhys. Lett. **68**, 460 (2004).
4. F. Caysoll, D. Ravelosona, C. Chappert, J. Ferré, and J. P. Jamet, Phys. Rev. Lett. **92**, 107202 (2004).
5. T. Tybell, P. Paruch, T. Giamarchi, and J. M. Triscone, Phys. Rev. Lett. **89**, 097601 (2002).
6. P. Paruch, J. M. Triscone, and T. Giamarchi, Phys. Rev. Lett. **94** 197601 (2005).
7. D. Wilkinson and J. F. Willemsen, J. Phys. A **16**, 3365 (1983).
8. S. Moulinet, C. Guthmann, and E. Rolley, Eur. Phys. J. E **8**, 437 (2002).
9. A.-L. Barabasi and H. E. Stanley, in *Fractal Concepts in Surface Growth* (Cambridge University Press, Cambridge, 1995).
10. E. Bouchaud, J. P. Bouchaud, D. S. Fisher, S. Ramanathan, and J. R. Rice, Journal of the Mechanics and Physics of Solids **50**, 1703 (2002).
11. G. Blatter, M. V. Feigelman, V. B. Geshkenbein, A. I. Larkin, and V. M. Vinokur, Rev. Mod. Phys. **66**, 1125 (1994).
12. T. Nattermann and S. Scheidl, Adv. Phys. **49**, 607 (2000).
13. T. Giamarchi and S. Bhattacharya, in *High Magnetic Fields: Applications in Condensed Matter Physics and Spectroscopy*, edited by C. Berthier *et al.* (Springer-Verlag, Berlin, 2002), p. 314, cond-mat/0111052.
14. G. Grüner, Rev. Mod. Phys. **60**, 1129 (1988).
15. E. Y. Andrei, G. Deville, D. C. Glatli, F. I. B. Williams, E. Paris, B. Etienne, Phys. Rev. Lett. **60**, 2765 (1988).
16. T. Giamarchi, in *Quantum phenomena in mesoscopic systems*, edited by Italian Physical Society (IOS Press, Bologna, 2004), cond-mat/0403531.
17. A. I. Larkin, Sov. Phys. JETP **31**, 784 (1970).
18. M. Mézard and G. Parisi, J. Phys. I France **1**, 809 (1991).
19. D. S. Fisher, Phys. Rev. Lett. **56**, 1964 (1986).
20. T. Giamarchi and P. Le Doussal, in *Spin Glasses and Random fields*, edited by A. P. Young (World Scientific, Singapore, 1998), p. 321, cond-mat/9705096.
21. A. I. Larkin and Y. N. Ovchinnikov, J. Low Temp. Phys **34**, 409 (1979).
22. A. Schmidt and W. Hauger, J. Low Temp. Phys **11**, 667 (1973).
23. A. I. Larkin and Y. N. Ovchinnikov, Sov. Phys. JETP **38**, 854 (1974).
24. A. Rosso and W. Krauth, Phys. Rev. E **65**, 025101R (2002).
25. D. S. Fisher, Phys. Rev. B **31**, 1396 (1985).
26. O. Duemmer and W. Krauth, Phys. Rev. E **71**, 061601, (2005).
27. T. Nattermann, S. Stepanow, L. H. Tang, and H. Leschhorn, J. Phys. (Paris) **2**, 1483 (1992).
28. O. Narayan and D. Fisher, Phys. Rev. B **48**, 7030 (1993).
29. P. Chauve, T. Giamarchi, and P. Le Doussal, Phys. Rev. B **62**, 6241 (2000).
30. A. Rosso, A. K. Hartmann, and W. Krauth, Phys. Rev. E **67**, 021602 (2003).
31. A. E. Koshelev and V. M. Vinokur, Phys. Rev. Lett. **73**, 3580 (1994).
32. T. Giamarchi and P. Le Doussal, Phys. Rev. Lett. **76**, 3408 (1996).

33. A. B. Kolton and D. D. N. Grønbech-Jensen, *Phys. Rev. Lett.* **83**, 3061 (1999).
34. P. W. Anderson and Y. B. Kim, *Rev. Mod. Phys.* **36**, 39 (1964).
35. T. Nattermann, *Europhys. Lett.* **4**, 1241 (1987).
36. L. B. Ioffe and V. M. Vinokur, *J. Phys. C* **20**, 6149 (1987).
37. T. Nattermann, Y. Shapir, and I. Vilfan, *Phys. Rev. B* **42**, 8577 (1990).
38. M. Feigelman, V. B. Geshkenbein, A. I. Larkin, and V. Vinokur, *Phys. Rev. Lett.* **63**, 2303 (1989).
39. A. B. Kolton, A. Rosso, and T. Giamarchi, *Phys. Rev. Lett.* **94**, 047002 (2005).
40. P. Chauve, T. Giamarchi, and P. Le Doussal, *Europhys. Lett.* **44**, 110 (1998).
41. T. Nattermann, *J. Phys. C* **16**, 4125 (1983).
42. J. F. Joanny and P. G. de Gennes, *J. Chem. Phys.* **81**, 552 (1984).
43. H. Gao and J. R. Rice, *J. Appl. Mech.* **56**, 828 (1989).
44. M. Kardar, *Physica B* **221**, 60 (1996).
45. T. Nattermann, *Phys. Rev. Lett.* **64**, 2454 (1990).
46. H. K. Janssen, *Z. Phys. B* **23**, 377 (1976).
47. P. C. Martin, E. D. Siggia, and H. A. Rose, *Phys. Rev. A* **8**, 423 (1973).
48. D. S. Fisher, *Phys. Rev. B* **31**, 7233 (1985).
49. P. Le Doussal, K. J. Wiese, and P. Chauve, *Phys. Rev. B* **66**, 174201 (2002).
50. K. J. Wiese, *Acta Physica Slovaca* **52**, 341 (2002), cond-mat/0205116.
51. D. T. Fuchs, E. Zeldov, T. Tamegai, S. Ooi, M. Rappaport, and H. Shtrikman, *Phys. Rev. Lett.* **80**, 4971 (1998).
52. Hans G. Kaper, Gary K. Leaf, David M. Levine, and Valerii Vinokur, *Phys. Rev. Lett.* **71**, 3713 (1993).
53. L. W. Chen and M. C. Marchetti, *Phys. Rev. B* **51**, 6296 (1995).
54. H. S. Greenside and E. Helfand, *Bell Syst. Tech. J.* **60**, 1927 (1981).
55. M. Kardar, *Phys. Rev. Lett.* **55**, 2923 (1985).

Edge Contamination Effects in the Dynamics of Vortex Matter in Superconductors: Memory Effects and Excess Flux-flow Noise

G. Jung^{1,2}, Y. Paltiel^{2,3}, E. Zeldov², Y. Myasoedov², M.L. Rappaport², M.J. Higgins⁴, and S. Bhattacharya^{4,5}

¹ Ben Gurion University of the Negev, Department of Physics, Beer-Sheva 84105, Israel

² Weizmann Institute of Science, Department of Condensed Matter Physics, Rehovot 76100, Israel

³ Electro-Optics Division, Soreq NRC, Yavne 81800, Israel

⁴ NEC Research Institute, Princeton, New Jersey 08540, USA

⁵ Tata Institute of Fundamental Research, Mumbai-400005, India

The magnetic flux line lattice in type II superconductors serves as a useful system in which to study condensed matter flow, as its dynamic properties are tunable. Recent studies have shown a number of puzzling phenomena associated with vortex motion, including: low-frequency noise and slow voltage oscillations; a history-dependent dynamic response, and memory of the direction, amplitude duration and frequency of the previously applied current; high vortex mobility for alternating current, but no apparent vortex motion for direct currents; negative resistance and strong suppression of an a.c. response by small d.c. bias. A generic edge contamination mechanism that comprehensively accounts for these observations is based on a competition between the injection of a disordered vortex phase at the sample edges, and the dynamic annealing of this metastable disorder by the transport current. For an alternating current, only narrow regions near the edges are in the disordered phase, while for d.c. bias, most of the sample is in the disordered phase-preventing vortex motion because of more efficient pinning. The resulting spatial dependence of the disordered vortex system serves as an active memory of the previous history. Random injection of the strongly pinned metastable disordered vortex phase through the sample edges and its subsequent random annealing into the weakly pinned ordered phase in the bulk results in large critical current fluctuations causing strong vortex velocity fluctuations. The resulting excess low frequency flux-flow voltage noise displays pronounced reentrant behavior. In the Corbino geometry the injection of the metastable phase is prevented and, accordingly, the excess noise is absent.

1 Introduction: Vortex Matter

Type-I superconductors undergo a first-order transition from the superconducting state, with total magnetic flux expulsion (Meissner effect), to the normal state at a critical field H_c . In marked contrast, type-II superconductors above a lower critical field H_{c1} allow magnetic flux to penetrate in a regular array of quantum units of $\Phi_0 = h/2e$, each flux tube being confined by a circulating vortex of current. These materials remain superconducting until a second-order transition at an upper critical field H_{c2} . The magnetic flux vortices in type-II superconductors were predicted by A. Abrikosov in 1957 in his ground-breaking paper based on the Ginzburg-Landau theory. The achievements of V. Ginzburg and A. Abrikosov were honored by the Nobel committee only last year, some 30 years after granting the prize for the BCS theory, published in the same year as the Abrikosov paper, and almost two decades after awarding the Nobel prize for the 1986 break-through discovery of new classes of oxide-based high-temperature superconductors. This discovery extended the range of the phase diagram, within which the superconducting vortices exist, by orders of magnitude, making investigation of the vortex matter one of the most vigorous research areas in solid state physics [1–4].

When transport current flows through a superconducting specimen in a mixed state, i.e., the state containing magnetic flux vortices, a Lorentz force acts on the flux tubes causing them to move in a direction perpendicular to the current flow. Unless vortex motion is prevented by pinning (jamming) of the vortices on intrinsic and artificially introduced material imperfections, voltage appears across the specimen and energy is dissipated. However, even in the presence of pinning centers, the vortex system yields and starts to move at currents higher than the so-called critical depinning current.

The onset of motion is accompanied by significant low frequency noise. The fluctuations peak in close vicinity to the “peak effect”, where the critical current anomalously increases with increasing temperature. Excess low frequency noise at the peak effect is accompanied by a series of exotic and puzzling phenomena associated with vortex motion, such as slow voltage oscillations, history-dependent dynamic response, and memory of the direction, amplitude, duration and frequency of the previously applied current, high vortex mobility for alternating current, but no apparent vortex motion for direct currents, and strong suppression of an a.c. response by a small d.c. bias. Taken together, these phenomena can be comprehensively explained by a model that accounts for contamination of the ordered vortex phase by a disordered vortex phase created by vortices penetrating irregular sample edges [5]. In this paper we concentrate on how edges influence dynamic instabilities, memory, and noise in the vortex system.

2 Edge Contamination

Our current understanding of the peak effect (PE) is that it is due to a first order phase transition between a quasi-ordered weakly pinned Bragg glass-like vortex phase below the PE and a strongly pinned disordered phase (DP) of solid vortex matter within and above the PE. The order-disorder phase transition of the vortex lattice occurring between the two solid vortex matter phases allows for the existence of a supercooled metastable DP in the part of the phase diagram occupied by the equilibrium ordered phase (OP). At temperatures well below the PE the supercooled phase is very fragile and any small perturbation, such as transport current, will easily anneal it into the equilibrium OP. However, at temperatures only slightly below the PE the applied current will have two competing effects: on the one hand it will anneal the disorder, but on the other hand, it will contaminate the system by fresh penetration of DP resulting in dynamic coexistence of the two phases. The injection of the disordered vortex phase through the sample edges is the core of the edge contamination (EC) mechanism.

Current flow in a superconducting sample containing the equilibrium ordered vortex phase well below the phase transition results in uniform motion of the entire vortex lattice. The penetrating vortices enter at their proper lattice locations and the order of the lattice is preserved. The presence of surface barriers in real samples significantly changes the situation. The barrier height is sensitive to the surface quality; vortices penetrate predominantly at the weakest spots of the barrier, and locally destroy the ordered lattice. Far below the phase transition the disordered state is highly unfavorable energetically and anneals rapidly into OP. However, in the close vicinity below the order-disorder phase transition a metastable DP will be formed near the sample edge. Since the free energies of the two phases are comparable near the phase transition, the metastable DP becomes sufficiently stable on the relevant experimental time scales to gradually penetrate deep into the sample with the flow of the entire lattice [5–7]. The DP can be pinned more efficiently and is characterized by significantly larger critical current than the weakly pinned ordered vortex phase [8–11]. The contamination process thus causes an enhancement of the total integrated critical current of the sample. A strongly pinned metastable disordered vortex phase dynamically anneals in the bulk into an ordered phase with much smaller critical current. The applied current, therefore, has two effects: the current that flows at the edges causes “contamination” by injecting a disordered vortex phase, while the current that flows in the bulk acts as an annealing mechanism. The ensemble of puzzling phenomena observed in the vicinity of the peak effect and discussed in detail below arises because of the dynamic balance between these two competing processes.

2.1 Critical Current in the Edge Contamination Model

Let us characterize the DP by the local critical current density $J_c(x)$ at a distance x from the edge, which has a non-equilibrium excess value $\tilde{J}_c(x) = J_c(x) - J_c^{ord}$ relative to the critical current of the fully ordered phase. Since in low-temperature superconductors thermal activation is negligible, the sole annealing mechanism is current-driven displacement that promotes rearrangement of the vortices during their motion. The relative change of \tilde{J}_c upon displacement by a small Δx is therefore given by $\Delta x/L_r$, where L_r is a characteristic relaxation length over which the DP anneals into the OP. Since the lattice flows with velocity v , \tilde{J}_c at $x + \Delta x$ and at time $t + \Delta t = t + \Delta x/v$ is thus described by $\tilde{J}_c(x + \Delta x, t + \Delta x/v) = \tilde{J}_c(x, t)(1 - \Delta x/L_r)$, which leads to the partial differential equation for the annealing process [14]

$$\partial \tilde{J}_c(x, t) / \partial x + (1/v) \partial \tilde{J}_c(x, t) / \partial t = -\tilde{J}_c(x, t) / L_r(v), \quad (1)$$

The boundary condition at $x = 0$, where vortices penetrate into the sample, is $\tilde{J}_c(0, t) = J_c^{dis} - J_c^{ord}$, where J_c^{dis} is the critical current of the totally disordered phase. A key aspect of the annealing process is that the relaxation length L_r crucially depends on the displacement velocity v and on the proximity to the phase transition. Close to the phase transition the metastable DP is rather stable and L_r is large. Deeper into the OP region the metastable phase becomes more and more unstable, L_r is small and J_c is depressed. Theoretical considerations [15, 16] and fast transient measurements [9] show that L_r decreases with increasing vortex displacement velocity according to an empirical relation $L_r \simeq L_0(v_0/v)^\eta = L_0(V_0/V)^\eta$. Here η is typically in the range of 1 to 3, L_0 , v_0 , and V_0 are scaling parameters, $V = vBl$ is the measured voltage drop, B is the magnetic field, and l is the distance between the voltage contacts.

The d.c. solution of (1) is $J_c^{dc}(x) = (J_c^{dis} - J_c^{ord}) \exp(-x/L_r) + J_c^{ord}$ and the integrated d.c. critical current becomes:

$$I_c = d \int_0^W J_c^{dc}(x) dx = (J_c^{dis} - J_c^{ord}) [1 - e^{-\frac{W}{L_r(V)}}] L_r(V) d + I_c^{ord}, \quad (2)$$

where $I_c^{ord} = J_c^{ord} W d$, W is the sample width and d its thickness. Observe, that I_c depends on L_r , which in turn depends on the voltage V .

To evaluate the shape of the $V - I$ characteristics in the edge contamination model assume, for simplicity, that the flux-flow resistance R_f is the same for the DP and the OP and that the asymptotic $V - I$ characteristics for the DP and OP are $V = R_f(I - I_c^{dis})$ and $V = R_f(I - I_c^{ord})$, respectively. When the DP and OP coexist, $V = R_f(I - I_c)$ with the voltage dependent I_c given by 2. An example of the non-linear $V - I$ characteristic obtained by means of numerical simulations is shown in Fig. 1. At very low voltages, L_r is larger than the sample width, the entire sample is contaminated by the DP, and the $V - I$ curve initially follows the asymptotic dashed line of the DP

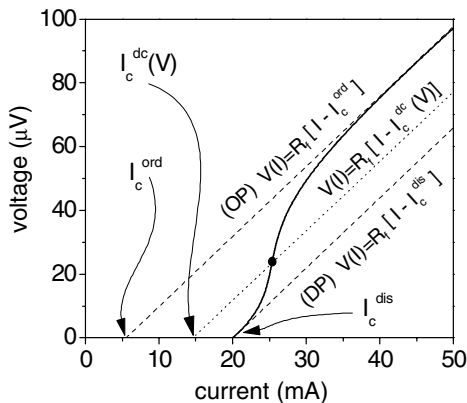


Fig. 1. Calculated $V-I$ characteristic (*solid line*) of coexisting vortex phases based on (2). The asymptotic characteristics of fully ordered and fully disordered vortex phases are shown with *dashed lines*

with $I_c = I_c^{dis}$, where $I_c^{dis} = J_c^{dis} W d$. At high vortex velocities, L_r becomes very short, most of the sample is in the OP, and the $V-I$ approaches the asymptotic line of the OP with $I_c = I_c^{ord}$. In the crossover region, due to a continuous decrease with current of the total I_c , a nonlinear $V-I$ characteristic is obtained. The curvature in the crossover region depends on the parameters η , L_0 , and V_0 . Our numerical simulations show that with rapidly decreasing L_r one may even obtain a negative slope resulting in S-shaped $V-I$ characteristics.

2.2 Strip and Corbino Configuration

In the Corbino disk geometry, the vortices circulate in the bulk without crossing the sample edges. In such an arrangement the contamination by DP is avoided and the true bulk properties of the vortex matter can be investigated [6,12,13]. In order to perform transport and noise measurements in both the Corbino and strip-like geometry on the same crystal we have prepared a special contact configuration, seen in the inset in Fig. 2b [6]. All experiments discussed in this paper were performed on Fe-doped (200 ppm) 2H-NbSe₂ single crystals with $T_c = 5.6$ K, which display a significantly broader PE as compared to pure crystals. However, additional experiments performed using samples with different doping showed the same general behavior as the one described here. This leads us to believe that the observed phenomena are common to all superconductors exhibiting PE and are not sample dependent.

Figure 2a shows the d.c. voltage response V vs. the magnetic field applied parallel to the crystal c -axis at 4.4 K in the strip and Corbino disk configuration. Since in the Corbino disk the current density varies across the sample, we have applied different driving currents in the two geometries in

order to have the same average current density between $+V$, $-V$ contacts in both arrangements. As a result, the measured V and the corresponding vortex velocity are identical at high fields. Upon decreasing the field from above $H_{c2}(T)$, the voltage decreases rapidly and vanishes in the PE region (4 to 8 kOe), where I_c of the sample is large due to the presence of the strongly pinned DP. The voltage appears again at intermediate fields between the phase transition fields H_{DT} . In this field range the voltage in the Corbino disk increases linearly with H , consistent with the well-known flux-flow behavior, indicating that the flowing lattice is in the ordered phase. The sharp drop of the voltage response at each H_{DT} is due to an abrupt disorder-driven transition of the equilibrium OP into a highly pinned equilibrium DP. The existence of two transition fields indicates the reentrant behavior of the equilibrium DP in Fe doped NbSe₂ [6, 17, 18]. The region of phase coexistence, seen in Fig. 2b, appears always on the Bragg glass side of the transition. Therefore at low fields we face a mirror-like image of high field behavior, see Fig. 2b.

The voltage response of the strip configuration is restricted to a narrower field range contained between high and low onset fields H_{on}^s . The strip voltage is strongly suppressed relative to the Corbino, indicating stronger effective pinning as a result of an intermixture of DP with OP due to the

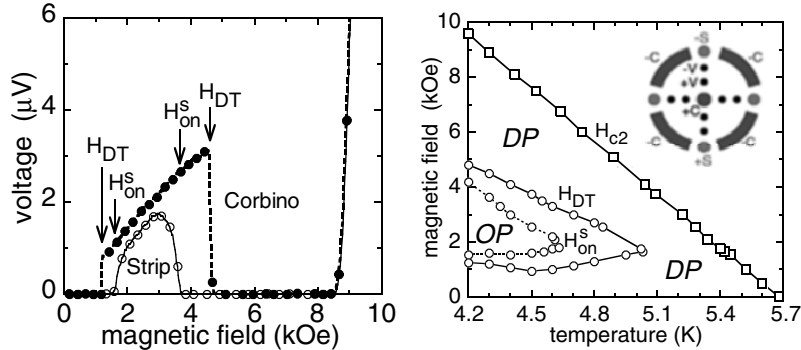


Fig. 2. (a) d.c. voltage seen in a Fe-doped NbSe₂ sample in Corbino and strip geometries. The currents in both geometries were adjusted to provide equal current densities in the vicinity of the voltage contacts. (b) Phase diagram of vortex matter in the same sample as in a). Dynamic coexistence of DP and OP occurs in the area contained between the H_{DT} and H_{on}^s lines. Inset: contact configuration enabling measurements in both Corbino and strip geometry. By applying the current to the $+S$, $-S$ contacts, the vortices penetrate through the edge and flow across the sample, similarly to the standard strip configuration. In contrast, by applying the current to the $+C$, $-C$ contacts, the vortices circulate in the bulk without crossing the edges, as in a Corbino disk. In both configurations the voltage and the corresponding noise are measured across the same contacts $+V$, $-V$. The distance between the voltage contacts is 0.15 mm and the Corbino disk diameter is 1.1 mm

EC mechanism. Figure 2b shows the phase diagram of the iron-doped NbSe₂ determined by transport measurements of the Corbino and strip geometries.

3 Memory Effects, Dynamical Instabilities and Edge Contamination

Many experiments performed in the past decade have demonstrated several surprising phenomena in the low frequency response of the vortex matter in conventional [8, 9, 19–22, 24, 25] and high- T_c superconductors [27–33]. These phenomena were particularly pronounced in 2H-NbSe₂ strips in the vicinity of the peak effect, where an ordered vortex lattice transforms into a highly disordered one. Among the most striking phenomena are the memory effects, in which the vortex system remembers the direction, amplitude, duration, and even the frequency of the previously applied current [24–26], and the history dependent dynamic response [8, 9, 21–23]. High vortex mobility is observed in the presence of a.c. transport current while the vortices appear to be immobile in the presence of d.c. current of the same or even substantially larger amplitude [24]. Moreover, the addition of a small d.c. current to a large a.c. current can fully suppress the a.c. response of the system [24]. Figure 3 shows a.c. resistance R_{ac} of a 2H-NbSe₂ sample recorded as a function of a superposed d.c. current I_{dc} . Note that the addition of only 10 to 20% of I_{dc} suppresses the a.c. response R_{ac} by orders of magnitude.

The edge contamination model can account for all the strange phenomena associated with the peak effect in terms of the competition between injection of a disordered vortex phase through the surface barriers at the sample edges, and annealing of the metastable disorder by the transport current [5]. The key

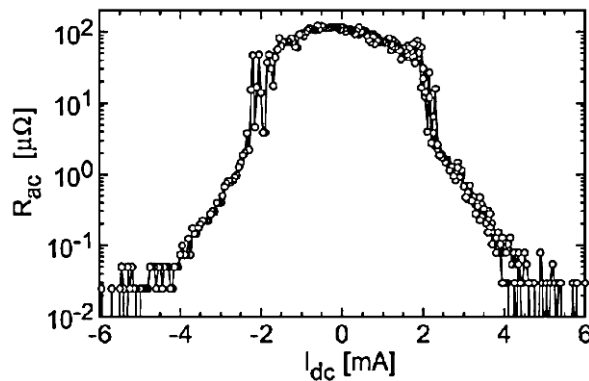


Fig. 3. a.c. resistance R_{ac} of a 2H-NbSe₂ as a function of the superposed d.c. bias in the vicinity of the peak effect. The experimental data were obtained for a.c. bias current $I_{ac} = 20$ mA, frequency $f = 181$ Hz, $B = 400$ mT, and $T = 5$ K

element of the edge contamination model is the spatial variation of the structural disorder in the vortex matter resulting in position dependent $J_c(x)$, as outlined in the Sect. 2.1. Correspondingly, transport current becomes nonuniform and follows the distribution $J_c(x)$. The EC model predicts that when a strip is biased with a d.c. current a significant part of the sample will be filled with the disordered phase injected through an edge. Strong pinning of the DP prevents vortex motion and one should expect a low response. If the d.c. bias is substituted by an a.c. current then only narrow regions near the edges will be contaminated by strongly pinned DP, leaving the remaining part of the sample with weakly pinned OP, and resulting in a large voltage response. With increasing frequency the time of injection of the DP decreases and the width of the contaminated areas close to the edges shrinks.

To verify the EC model predictions we have measured the self-induced field $B_{ac}(x)$ of the a.c. transport current using linear arrays of miniature Hall sensors and a lock-in detection technique [34, 35]. The Hall probes are based on the two-dimensional electron gas (2DEG) in AlGaAs/GaAs heterostructures grown on undoped semi-insulating GaAs substrates by means of molecular beam epitaxy [54]. The array comprises eleven $10 \times 10 \mu\text{m}^2$ Hall sensors, connected in series with a $30 \mu\text{m}$ separation between them. The 2DEG resides $0.1 \mu\text{m}$ below the surface. Their sensitivity to fields normal to the 2DEG is of the order of $100 \text{ m}\Omega/\text{gauss}$. These structures provide significantly better spatial resolution than SQUID sensors and operate better in a changing temperature environment. $B_{ac}(x)$ can be directly inverted into a current density distribution using the Biot-Savart law, as described elsewhere [34]. The resulting $J_{ac}(x)$ distributions are shown in Fig. 4. When a significant d.c. current $I_{dc} = 5.7 \text{ mA}$ is added to $I_{ac} = 20 \text{ mA}$, disordered vortices penetrate through the left edge of the sample and contaminate a significant part of the sample (Fig. 4a). Accordingly, as proven by the measured $J_{ac}(x)$ distribution, the majority of the current flows along the left edge occupied by DP with high critical current. Upon reversal of the direction of the d.c. current (see Fig. 4b), DP is injected through the right edge of the sample and the distribution looks like a mirror image of that from Fig. 4a. However, when the d.c. component is very weak compared to the a.c. current amplitude, as in the case illustrated in Fig. 4c for $I_{dc} = 1.7 \text{ mA}$, the contamination by the DP is restricted to two relatively narrow bands at the sample edges.

The frequency dependence of $J_{ac}(x)$ distributions is illustrated in Fig. 5. At high frequencies, the DP with enhanced J_c is present only in the narrow regions close to the edges (481 Hz data). At 181 Hz the DP areas grow and, correspondingly, the enhanced $J_{ac}(x)$ flows in wider regions near the edges. When the frequency is reduced to 22 Hz the disordered border regions overlap and the enhanced current flows through entire sample width. The actual measured $J_{ac}(x)$ is the magnitude of the local current density averaged over the cycle period. Close to the edges, the high J is present most of the time,

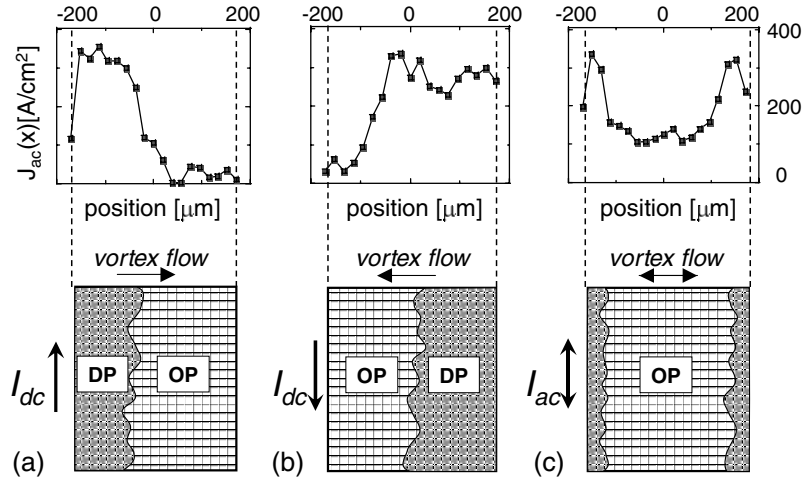


Fig. 4. a.c. current density distributions. (a) $I_{dc} = 5.7$ mA; DP is injected through the left edge, DP occupies a substantial part of the sample. (b) Reversed direction of current flow $I_{dc} = -5.7$ mA. (c) $I_{dc} = 1.7$ mA; at small d.c. bias $I_{dc} \ll I_{ac}$ the current distribution is similar to the zero d.c. bias case and peaks at the sample edges. The applied a.c. current has the same amplitude of 20 mA and frequency of 181 Hz in all cases

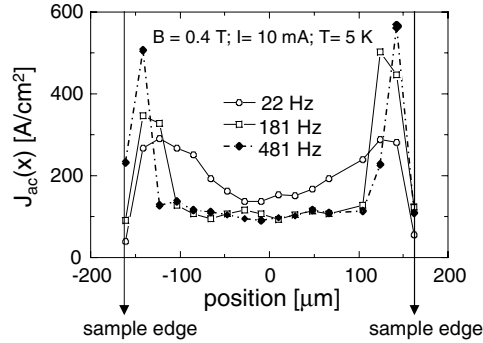


Fig. 5. Current density profiles $J_{ac}(x)$ obtained by inversion of the self-induced field measured by Hall sensors at frequencies $f = 22$ Hz (circles), 181 Hz (open squares), and 481 Hz (solid squares). The width of the disordered phase near the edges grows with decreasing frequency

while at the depth corresponding to the a.c. penetration depth of the DP, high current density persists only during a small fraction of the a.c. period since the DP continuously moves in and out of the sample. Therefore, the measured amplitude of the time-averaged $J_{ac}(x)$ decreases smoothly from the sample edge to the point determined by the a.c. penetration depth, (see Fig. 5).

The behavior of the a.c. response illustrated in Fig. 3 is a natural consequence of the EC mechanism. As follows from the profiles in Fig. 4, the addition of a small d.c. component to the a.c. current contaminates the sample very similarly to the pure d.c. case, except that the penetration depth of the DP is reduced. When $I_{dc} \ll I_{ac}$ the vortices move back and forth during the a.c. cycle, with a forward displacement being enhanced by about $2I_{dc}/I_{ac}$. Because the annealing process of the disordered vortex phase depends on the total displacement, regardless of the direction, the DP is thus annealed more efficiently. Therefore, at very small d.c. currents, the disordered phase is present only close to the edges where the DP exits and re-penetrates during every half-cycle. Vortices that drift deeper into the bulk are practically fully annealed. As a result, the initial decrease of R_{ac} for currents below 2mA in Fig. 4 is relatively small. With increasing d.c. current DP penetrates deeper into the sample leading to a marked drop in the a.c. response. The above mechanism accounts for the finite a.c. response and explains why the addition of a relatively small d.c. bias or asymmetry in the I_{ac} waveform dramatically suppresses the vortex motion.

The EC mechanism, by causing frequency, amplitude and direction-dependent distributions of current density, accounts also for the memory effects. The history of the previously applied current is encoded in the spatial profile of the lattice disorder, which in low temperature superconductors, such as NbSe₂, is preserved after the current is switched off owing to negligible thermal relaxation. On reapplying the current, the vortex system will display a memory of all the parameters of the previously applied current, including its direction, duration, amplitude and frequency.

4 Low Frequency Noise

The appearance of large, broadband, low frequency noise with the onset of motion of a condensate in the presence of a quenched random pinning potential (jamming), has been studied extensively in incommensurate charge density waves [36], Wigner crystals in two-dimensional electron gas [37], and most notably, in vortex matter in type-II superconductors [19,20,29–32,38–49,51–53]. In all cases, the noise is thought to represent spatio-temporal irregularities of the moving condensate due to its interaction with the underlying pinning potential, but its precise origin remains obscure and controversial. The voltage noise due to vortex motion in a current-biased superconductor is generally referred to as flux-flow noise for which various specific mechanisms have been considered (for a review of early results see [38]). They include vortex shot noise and the associated density fluctuations [30,32,38–41], velocity fluctuations resulting from vortex-pin interactions [38], or turbulent flow of surface currents [42], critical slowing down of vortex dynamics [44], and several suggestions [19,20,29,45–47] and numerical simulations [48,49,51] of various plastic vortex flow mechanisms. Each of

these mechanisms may make a substantial contribution to the total measured noise. Yet the puzzling observation, which has no satisfactory explanation, is that in a specific and narrow region of the $H - T$ phase diagram the noise is enhanced drastically. This unconventional noise, which we refer to as excess noise, exceeds the usual flux-flow noise level by orders of magnitude [19, 20, 29, 38, 45, 46]. In low- T_c superconductors the excess noise occurs in the vicinity of the peak effect (PE) below H_{c2} , where the critical current I_c anomalously increases with field [19, 20, 38, 45]. In high- T_c superconductors similar noise enhancement was found in the vicinity of the melting or order-disorder transitions [27–29, 46]. This low frequency excess noise is apparently inconsistent with the common flux-flow noise mechanisms due to its unusually high amplitude, strong field and current dependence, and frequently observed non-Gaussian character [19, 20, 29, 45].

4.1 Simplified Model of the Noise

The generation of the metastable DP is a random process due to the non-uniform penetration of vortices through the surface barrier. As a result, the degree of vortex-lattice disorder and the corresponding value of J_c^{dis} at the sample edge are random functions of time. Similarly, annealing of the flowing DP is a random process that can be taken into account by considering L_r to be a random variable. Since J_c^{dis} is typically an order of magnitude larger than J_c^{ord} [6], random variations δJ_c^{dis} and δL_r will result in large fluctuations of the integrated critical current of the sample, causing large voltage noise.

The $V(I)$ curve in the vicinity of the peak effect is described by $V(I) = R_f[I - I_c(V)]$, where I_c is given by 2. In the small signal approximation we separate voltage fluctuations into two terms:

$$\delta V(I) \approx \frac{\partial V(I)}{\partial I_c} \delta I_c + \frac{\partial V(I)}{\partial R_f} \delta R_f . \quad (3)$$

By defining the differential resistance as

$$R_d \equiv \frac{\partial V}{\partial I} = -\frac{\partial V}{\partial I_c} , \quad (4)$$

(3) becomes

$$\delta V(I) = -R_d \delta I_c + \frac{V(I)}{R_f} \delta R_f . \quad (5)$$

Since experimentally L_r is usually smaller than W we can approximate (2) by $I_c \simeq L_r d(J_c^{dis} - J_c^{ord}) + W dJ_c^{ord}$ [5]. In this approximation the fluctuation of the total critical current is

$$\delta I_c \approx d\tilde{J}_c(0)L_r + d\tilde{J}_c(0)\delta L_r . \quad (6)$$

From Eg. 5 we obtain that

$$\delta V(I) \approx -dR_d \tilde{J}_c(0) L_r \left[\frac{\delta \tilde{J}_c}{\tilde{J}_c} + \frac{\delta L_r}{L_r} \right] + V(I) \frac{\delta R_f}{R_f}. \quad (7)$$

We now write the power spectral density (PSD) of the voltage noise as

$$S_V \approx d^2 R_d^2 \tilde{J}_c^2(0) L_r^2 S_{in/ann} + V^2 S_{r_f}, \quad (8)$$

where $S_{r_f} = S_{R_f}/R_f^2$ is the normalized spectral density of the flux-flow resistance fluctuations and $S_{in/ann}$ is the normalized spectral density of the vortex injection and annealing noise. The most important conclusion that will enable us to understand the dependence of excess noise on applied magnetic field and current is that the noise intensity is proportional to $R_d^2 \tilde{J}_c^2(0) L_r^2$.

4.2 Experimental Results

The most direct test of the EC noise mechanism is the comparison of the Corbino disk noise with that of the strip, as shown in Fig. 6. In the Corbino the excess noise is almost entirely absent, indicating that the randomness in motion of the vortex lattice within the bulk of the sample does not, by itself, create excess noise. The absence of the noise in the Corbino clearly indicates the dominant role of edge contamination in the noise process. The residual small and narrow peaks in the Corbino noise in Fig. 6 can be ascribed to small deviations from a perfect Corbino disk configuration. Since L_r diverges at H_{DT} , any small non-radial part of the current may result in some injection of the metastable DP, giving rise to noise. Similarly, small inhomogeneities in the quenched disorder may result in a slightly position-dependent H_{DT} . In this case, in a narrow field region in the vicinity of the mean-field H_{DT} some parts of the sample are in the equilibrium DP, whereas others are in the OP. When the entire lattice is set in motion the DP drifts into regions of the OP, where it becomes metastable, and may cause noise in this narrow field region.

In contrast, the strip noise is very pronounced. The peak of the noise around 3.5 kOe in Fig. 6 is a result of the large L_r in the vicinity of the phase transition. The second noise peak at about 2 kOe marks the reentrant phase transition at which L_r becomes large again on approaching H_{DT} . This low-field peak was not previously observed since the noise studies were carried out on undoped NbSe₂ [19,20,45] which does not show a pronounced reentrant disorder-driven transition. The existence of two peaks demonstrates that the excess noise is not a mere result of the fact that I_c increases with H at the PE since at low fields the same excess noise is found in the region where I_c decreases with H . Furthermore, the same value of I_c is attained at three values of H : above the reentrant H_{DT} where I_c decreases with H , below the high field H_{DT} where I_c increases with H , and in the upper part of the PE, above the high field H_{DT} where I_c decreases again with H . The excess noise occurs only in the first two cases, where the metastable DP

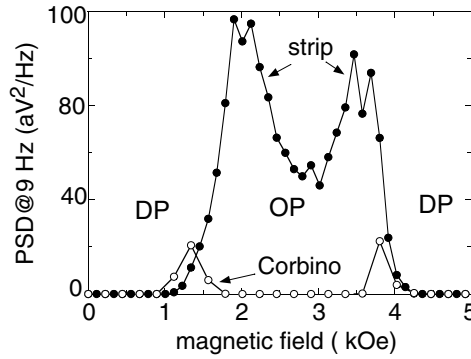


Fig. 6. Power spectral density of noise at 9 Hz and $T = 4.4$ K in Corbino (*open circles*) and strip (*solid circles*) geometries. The currents in the Corbino and strip geometries were adjusted to provide equal current densities in the vicinity of the voltage contacts for both geometries

contaminates the equilibrium OP. In the third case, above H_{DT} , the DP is the thermodynamically stable phase and therefore no “wrong” phase is generated at the edges.

Figure 7 shows the intensity of the strip noise $S_V^{1/2}$, seen at a selected frequency of 3 Hz, as a function of bias current, along with the $V - I$ characteristics for two different values of applied magnetic field. In each case, the onset of the noise coincides with the onset of d.c. current induced dissipation. With increasing current the $I - V$ curve shows an upturn and eventually approaches linear flux-flow behavior at elevated currents. The noise displays a large peak and then vanishes rapidly at higher currents. Assuming for simplicity that

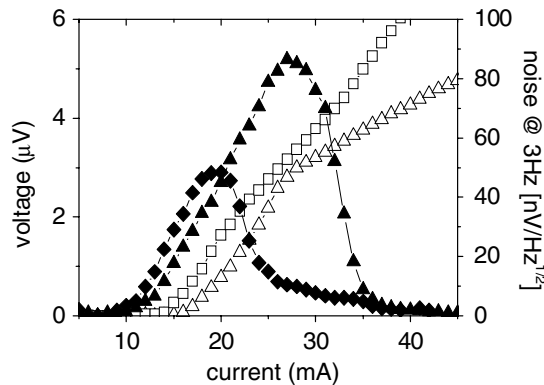


Fig. 7. $V - I$ characteristics (*open symbols*) and spectral intensity of the noise (*solid symbols*) at 3 Hz as a function of bias current at 4.2 K: triangles – 2 kOe, diamonds – 3 kOe

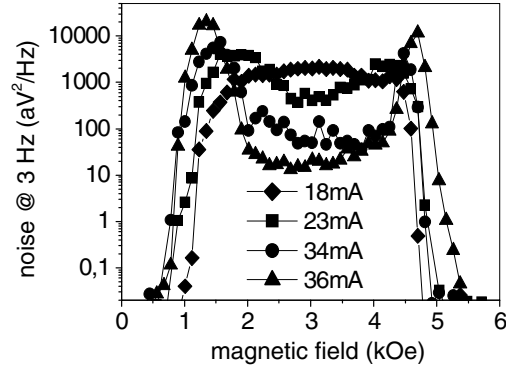


Fig. 8. Power spectral density of the strip noise at a fixed frequency of 3 Hz as a function of magnetic field at various bias currents. $T = 4.2$ K

δJ_c^{dis} is current independent, the dominant parameters affecting the noise intensity are the relaxation length L_r and the differential resistance R_d (see (8)).

The initial buildup of the noise with increasing current follows the initial growth of R_d . The subsequent decay of the noise is the result of a decrease of L_r with increasing vortex velocity. Indeed, above 28 mA the $V - I$ characteristic approaches the linear behavior of the OP, indicating that most of the sample volume is in the OP and that L_r is small. Since the ordered part of the sample does not contribute to the noise, the noise vanishes as the width of the DP near the edge shrinks to zero. The specific details of the above qualitative description are expected, however, to be significantly more complicated because of several factors, including the possible current dependence of δJ_c^{dis} and the fact that δV is often comparable to V , resulting in a highly nonlinear and apparently non-Gaussian response [19,20], for which the above oversimplified analysis is not valid.

The above considerations facilitate the analysis of the general behavior of the strip noise shown in Fig. 8. At low currents (< 18 mA), vortex motion occurs only in the central field region far away from H_{DT} . In the vicinity of the transition the integrated I_c of the strip is larger than the driving current due to the large L_r . As a result, the excess noise is present only in the central field range. At 23 mA, the range of fields, for which vortex motion and the corresponding noise are observable, expands and two noise peaks become readily apparent. In the central region the DP is less stable, L_r drops with I , and hence the noise decreases rapidly with current. Closer to the transition fields, however, the metastable DP is much more stable and therefore even at 23 mA L_r remains large and noise is still increasing with current. At 36 mA most of the sample is already in the OP and the noise in the central field range has accordingly dropped by two orders of magnitude. The strong excess

noise is restricted now only to the narrow regions adjacent to the transition fields where the metastable DP survives even at high vortex velocities.

4.3 Velocity vs. Density Fluctuations

The electric field due to magnetic flux motion with a velocity v , neglecting voltages induced by variations of the flux threading the loop enclosed by the voltage leads, can be written simply as $\mathbf{E} = -\mathbf{v} \times \mathbf{B}$. The voltage fluctuations $\delta V(t) = V(t) - \bar{V}$, where $\bar{V} = vBl$ is the d.c. voltage, can be due either to the fluctuations of magnetic field $\delta \mathbf{B} = \Phi_0 \delta n \mathbf{B} / B$, where δn are the fluctuations in the vortex density n , or to the fluctuations of the vortex velocity \mathbf{v} . In a small signal approximation

$$\delta V \approx l(v\delta B + B\delta v). \quad (9)$$

The first term contains density fluctuations $\delta n = n(t) - \bar{n}$, where $\bar{n} = B/\Phi_0 = N/Wl$ is the equilibrium vortex density and N is the total number of vortices. Vortex density fluctuations can be therefore directly evaluated by measuring the associated magnetic field noise. The second term describes velocity fluctuations $\delta v = v(t) - \bar{v}$, where the equilibrium vortex velocity $\bar{v} = \bar{V}/Bl$. Alternatively, the fluctuating component of the voltage due to current driven vortex motion is given by (3). Direct comparison of (9) with (5) suggests to associate vortex density fluctuations with the fluctuations of the flux-flow resistance δR_f and fluctuations of the vortex velocity with the fluctuations of the critical current $\delta I_c \propto \delta \tilde{J}_c(0)$.

In the experiments we have measured simultaneously the voltage and magnetic field noise associated with the current driven vortex motion. After sufficiently long thermalization at low temperatures the Hall sensor d.c. bias current level that causes onset of the excess shot noise was well above 200 μA enabling us to operate safely at high current bias, what significantly improves the signal to noise ratio of the sensor. The ultimate sensitivity of our flux detection system was typically better than $2 \times 10^{-7} \text{ T/Hz}^{1/2}$ at frequencies above 5 Hz.

To perform simultaneous conduction and magnetic noise measurements the NbSe₂ crystal with attached leads was placed directly on top of the Hall sensor array. The entire arrangement was immersed in a specially designed low noise variable temperature cryostat equipped with an external μ -metal shield and a superconducting magnet operating in persistent mode. In each experimental run the sample was zero-field cooled to the required temperature before application of the magnetic field and bias current. The sample voltage, measured in a four-point contact arrangement, and the Hall probe signal were brought to the top of the cryostat by twisted-pairs, amplified by home-made low noise voltage preamplifiers located within the cryostat head, and processed by a computer-assisted spectrum analyzer. The power spectra of the flux and voltage fluctuations were recorded simultaneously with the

time domain records and d.c. voltage response. Instrumental noise originating in the measurement circuit, was recorded at zero current through the NbSe₂ crystal and subsequently subtracted from the spectra measured in the presence of bias.

We have searched for flux noise manifestations in the entire range of currents, magnetic fields, and temperatures at which the excess voltage noise appears. Within the sensitivity of our Hall probe arrangement we could not detect any vortex density fluctuations. Even by biasing the sample at the very noise peak, where the voltage noise spectral intensity increases more than four orders of magnitude above the preamplifier background, we saw no difference in the magnetic noise detected with and without the application of the driving current causing the motion and annealing of the vortex lattice.

In the face of the negative result we carefully checked that the Hall probe was properly coupled to the sample by measuring the Meissner effect at low fields and the self-induced a.c. field of an a.c. transport current. All tests proved unambiguously that the Hall sensors were properly coupled.

The absence of density fluctuations, in fact, is not surprising and is consistent with the EC model predictions. Let us rewrite the total spectral density of the voltage noise (5) in terms of the normalized spectral density $S_v = S_V/V^2$:

$$S_v = \frac{1}{R_f^2} S_{R_f} + \frac{R_d^2}{V^2} S_{I_c} . \quad (10)$$

By plotting the normalized voltage noise spectral density as a function of the ratio R_d^2/V^2 one can separate contributions of the fluctuating vortex density and velocity to the total noise. The PSD value for $R_d^2/V^2 = 0$ corresponds to S_{R_f} , which in turn describes vortex density fluctuations, while the slope of the $S_v(R_d^2/V^2)$ plot gives the spectral density of the critical current fluctuations S_{I_c} .

The experimental data at 0.2 T from Fig. 1 are plotted in the above coordinate system in Fig. 9. The data fit very well to a straight line passing through the origin. It clearly demonstrates that the excess noise due to the contamination mechanism is entirely dominated by the critical current fluctuations causing large voltage noise by inducing strong fluctuations of the velocity of moving vortices. According to (10) any significant density fluctuations would offset the linear fit upward, such that it would cross the y-axis at the value corresponding to S_R . This is clearly not the case in Fig. 2.

We conclude that the excess flux-flow noise in the vicinity of the peak effect is entirely dominated by vortex velocity fluctuations resulting from the critical current fluctuations due to random injection and random annealing of the metastable disordered vortex phase. This result may seem surprising in view of the experimental evidence of local vortex density noise associated with current driven motion of vortices in high- T_c Bi₂Sr₂CaCu₂O_y (BSCCO) single crystals [30–32]. The flux noise in BSCCO system has been detected using a Hall probe with similar sensitivity. The major difference between

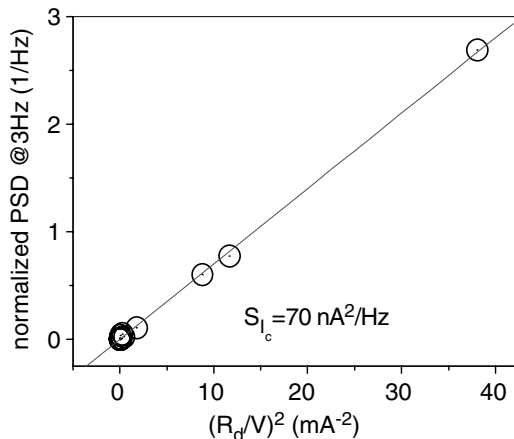


Fig. 9. Data points at 2 kOe from Fig. 7 plotted as a normalized power spectral density as a function of R_d^2/V^2 . Observe that the best linear fit to the data passes through the origin indicating that the voltage noise is due entirely to the critical current fluctuations (see text)

the two systems is the fact that in the low- T_c Nb_2Se the excess noise is associated with order-disorder transitions within the solid state of the vortex matter, whereas in high- T_c BSCCO the excess noise can be associated with the melting transition. Since the vortex liquid has higher density than the solid, local melting transitions may result in strong density fluctuations. Nevertheless, it has been shown that the order-disorder phase transition in the solid vortex phase is also associated with a magnetization jump which should result in similar density fluctuations [55, 56]. A possible reason for the lack of measurable density fluctuations at the solid-solid phase transition is the very slow dynamics with which the equilibrium magnetization is reached. In fact, to detect the magnetization step at the disorder-driven phase transition the special experimental technique of vortex dithering had to be applied [55]. For this reason density fluctuations, if any, may appear at very low frequencies, much lower than the frequencies at which the excess voltage noise has been observed and beyond the spectral range of the experiment. The exact reason for the different aspects of excess noise in low and high- T_c systems remains, however, an open question.

5 Conclusions

In summary, we have shown that the ordered Bragg glass phase becomes unstable with respect to disorder at both high and low fields, resulting in a reentrant disorder-driven transition. By using a Corbino geometry, and thus

avoiding the contamination from the sample edges, we have shown that this transition is very sharp and apparently of first order.

The injection of the disordered phase through the sample edges causes a nonuniform distribution of the pinning strength and, correspondingly, a nonuniform distribution of the current density. In the restricted areas of the phase diagram, in the vicinity of the peak effect, the disordered phase dynamically coexists with the ordered phase, giving rise to a plethora of exotic phenomena in the vortex matter dynamics. It follows from the proposed edge contamination model that the transport current has two antagonistic effects; injection of the disordered phase at the sample edge and its annealing in the bulk. The edge contamination model explains the memory effects in vortex matter by the history of the previously applied current being encoded in the spatial profile of the lattice disorder, which cannot be erased by negligible thermal fluctuations at low temperatures.

The excess flux-flow noise appearing in the vicinity of the peak effect has been associated with edge contamination and has been shown not to result from mere random motion of vortices in the bulk of the sample. The main conceptual difference is that in the conventional models only random vortex penetration or irregular vortex motion in the bulk is considered. We have considered randomness in the injection and annealing processes of the metastable disordered phase resulting in large fluctuations in the instantaneous critical current of the sample, leading to very large voltage noise. We have demonstrated that the excess noise can be eliminated by preventing the edge contamination in the Corbino disk geometry. Direct flux noise measurements and re-examination of the voltage noise data brought us to conclusion that the excess flux-flow noise is entirely dominated by vortex velocity fluctuations resulting from the critical current fluctuations. We believe that the new noise mechanism may be of importance for various condensed matter systems exhibiting similar noise associated with a fluctuating pinning force such as incommensurate charge density waves or Wigner crystals in two-dimensional electron gas.

Acknowledgments

This work was supported by the Israel Science Foundation - Center of Excellence Program, by the United States-Israel Binational Science Foundation (BSF), and by the German-Israeli Foundation for Scientific Research and Development (GIF).

References

1. G. Blatter, M. V. Feigelman, V. B. Geshkenbein, A. I. Larkin, V. M. Vinokur: *Rev. Mod. Phys.* **66**, 1125 (1994).

2. G. W. Crabtree and D. R. Nelson: *Phys. Today* **50**, 38 (1997).
3. S. Kuriki, S. Hirano, A. Maeda, T. Kiss: *Topics in Appl. Phys.* **91**, 5 (2003).
4. G. W. Crabtree: *Nature Mat.* **2**, 435 (2003).
5. Y. Paltiel, E. Zeldov, Y. N. Myasoedov, H. Shtrikman, S. Bhattacharya, M. J. Higgins, Z. L. Xiaok, E. Y. Andrei, P. L. Gammel and D. J. Bishop: *Nature* **403**, 398 (2000).
6. Y. Paltiel, E. Zeldov, Y. Myasoedov, M. L. Rappaport, G. Jung, S. Bhattacharya, M. J. Higgins, Z. L. Xiao, E. Y. Andrei, P. L. Gammel, and D. J. Bishop: *Phys. Rev. Lett.* **85**, 3712 (2000).
7. M. Marchevsky, M. J. Higgins, and S. Bhattacharya: *Phys. Rev. Lett.* **88**, 087002 (2002).
8. S. Bhattacharya and M. J. Higgins: *Phys. Rev. B* **52**, 64 (1995).
9. W. Henderson, E. Y. Andrei, M. J. Higgins, and S. Bhattacharya: *Phys. Rev. Lett.* **77**, 2077 (1996).
10. Song Yue, Bo Zhang, Shun Tan, Mingliang Tian and Yuheng Zhang: *Europhys. Lett.* **66**, 272 (2004).
11. M. Menghini, Y. Fasano and F. de la Cruz: *Phys. Rev. B* **65**, 064510 (2002).
12. P. Benetatos and M. C. Marchetti: *Phys. Rev. B* **65**, 134517 (2002).
13. S. Okuma and M. Kamada: *Phys. Rev. B* **70**, 014509 (2004).
14. Y. Paltiel, E. Zeldov, G. Jung, Y. Myasoedov, M. L. Rappaport, D. Feldman, M. J. Higgins, and S. Bhattacharya: *Phys. Rev. B* **66**, 060503R (2002).
15. M. Gitterman: *Phys. Rev. E* **70**, 036116 (2004).
16. B. Y. Shapiro, M. Gitterman, I. Shapiro: *Physica C* **388**, 681 (2003).
17. K. Ghosh, S. Ramakrishnan, A. K. Grover, Gautam I. Menon, Girish Chandra, T. V. Chandrasekhar Rao, G. Ravikumar, P. K. Mishra, V. C. Sahni, C. V. Tomy, G. Balakrishnan, D. Mck Paul, S. Bhattacharya: *Phys. Rev. Lett.* **76**, 4600 (1996).
18. S. S. Banerjee, N. G. Patil, S. Ramakrishnan, A. K. Grover, S. Bhattacharya, P. K. Mishra, G. Ravikumar, T. V. Chandrasekhar Rao, V. C. Sahni, M. J. Higgins, C. V. Tomy, G. Balakrishnan, and D. Mck. Paul: *Europhys. Lett.* **44**, 91 (1998).
19. A. C. Marley, M. J. Higgins, and S. Bhattacharya: *Phys. Rev. Lett.* **74**, 3029 (1995).
20. R. D. Merithew, M. W. Rabin, M. B. Weissman, M. J. Higgins and S. Bhattacharya: *Phys. Rev. Lett.* **77**, 3197 (1996).
21. S. S. Banerjee, N. G. Patil, S. Saha, S. Ramakrishnan, A. K. Grover, S. Bhattacharya, G. Ravikumar, P. K. Mishra, T. V. Chandrasekhar Rao, V. C. Sahni, M. J. Higgins, E. Yamamoto, Y. Haga, M. Hedo, Y. Inada, Y. Onuki: *Phys. Rev. B* **58**, 995 (1999).
22. S. S. Banerjee, N. G. Patil, S. Ramakrishnan, A. K. Grover, S. Bhattacharya, G. Ravikumar, P. K. Mishra, T. V. Chandrasekhar Rao, and V. C. Sahni, M. J. Higgins: *Appl. Phys. Lett.* **74**, 126 (1999).
23. Y. Liu, H. Luo, X. Leng, Z. H. Wang, L. Qiu, S. Y. Ding, and L. Z. Lin: *Phys. Rev. B* **66**, 144510 (2002).
24. W. Henderson, E. Y. Andrei and M. J. Higgins: *Phys. Rev. Lett.* **81**, 2352 (1998).
25. Z. L. Xiao, E. Y. Andrei and M. J. Higgins: *Phys. Rev. Lett.* **83**, 1664 (1999).
26. R. Schleser, P. J. E. M. van der Linden, P. Wyder, A. Gerber: *Phys. Rev. B* **67**, 134516 (2003).

27. S. N. Gordeev, P. A. J. deGroot, M. Oussena, A. V. Volkozub, S. Pinfeld, R. Langan, R. Gagnon, L. Taillefer: *Nature* **385**, 324 (1997).
28. W. K. Kwok, G. W. Crabtree, J. A. Fendrich, L. M. Paulius: *Physica C* **293**, 111 (1997).
29. G. D'Anna, P. L. Gammel, H. Safar, G. B. Alers, D. J. Bishop, J. Giapintzakis, D. M. Ginsberg: *Phys. Rev. Lett.* **75**, 3521 (1995).
30. T. Tsuboi, T. Hanaguri, and A. Maeda: *Phys. Rev. Lett.* **80**, 4550 (1998).
31. Y. Togawa, R. Abiru, K. Iwaya, H. Kitano, and A. Maeda: *Phys. Rev. Lett.* **85**, 3716 (2000).
32. A. Maeda, T. Tsuboi, R. Abiru, Y. Togawa, H. Kitano, K. Iwaya, T. Hanaguri: *Phys. Rev. B* **65**, 054506 (2002).
33. S. Kokkaliaris, P. A. J. de Groot, S. N. Gordeev, A. A. Zhukov, R. Gagnon and L. Taillefer: *Phys. Rev. Lett.* **82**, 5116 (1999).
34. Y. Paltiel, D. T. Fuchs, E. Zeldov, Y. N. Myasoedov, H. Shtrikman, M. L. Rappaport, E. Y. Andrei: *Phys. Rev. B* **58**, R14763 (1998).
35. D. T. Fuchs, E. Zeldov, M. Rappaport, T. Tamegai, S. Ooi, H. Shtrikman: *Nature* **391**, 373 (1998).
36. S. Bhattacharya, J. P. Stokes, Mark O. Robbins, and R. A. Klemm: *Phys. Rev. Lett.* **54**, 2453 (1985).
37. Yuan P. Li, T. Sajoto, L. W. Engel, D. C. Tsui, and M. Shayegan: *Phys. Rev. Lett.* **67**, 1630 (1991).
38. J. R. Clem: *Phys. Rep.* **75**, 1 (1981).
39. W. J. Yeh and Y. H. Kao: *Phys. Rev. B* **44**, 360 (1991).
40. V. D. Ashkenazy, G. Jung, and B. Ya. Shapiro: *Physica C* **254**, 77 (1995).
41. K. E. Gray: *Phys. Rev. B* **57**, 5524 (1998).
42. B. Placais, P. Mathieu, and Y. Simon: *Phys. Rev. Lett.* **70**, 1521 (1993)
43. B. Placais, P. Mathieu, and Y. Simon: *Phys. Rev. B* **49**, 15813 (1994).
44. P. J. M. Wöltgens, C. Dekker, S. W. A. Gielkens, and H. W. de Wijn: *Physica C* **247**, 67 (1995).
45. M. W. Rabin, R. D. Merithew, M. B. Weissman, M. J. Higgins and S. Bhattacharya: *Phys. Rev. B* **57**, R720 (1998).
46. H. Safar, P. L. Gammel, D. A. Huse, G. B. Alers, D. J. Bishop, W. C. Lee, J. Giapintzakis, and D. M. Ginsberg: *Phys. Rev. B* **52**, 6211 (1995).
47. S. Okuma and N. Kokubo: *Phys. Rev. B* **61**, 671 (2000).
48. I. Aranson and V. Vinokur: *Phys. Rev. Lett.* **77**, 3208 (1996).
49. C. J. Olson, C. Reichhardt, and F. Nori: *Phys. Rev. Lett.* **80**, 2197 (1998).
50. A. B. Kolton, D. Dominguez, and N. Gronbech-Jensen et al: *Phys. Rev. Lett.* **83**, 3061 (1999).
51. M. C. Marchetti, A. A. Middleton, and T. Prellberg: *Phys. Rev. Lett.* **85**, 1104 (2000).
52. Y. Paltiel, G. Jung, Y. Myasoedov, M. L. Rappaport, E. Zeldov, S. Bhattacharya, M. J. Higgins: *Europhys. Lett.* **58**, 112 (2002).
53. Y. Paltiel et al: *Europhys. Lett.* **66**, 412 (2004)
54. E. Zeldov, D. Majer, M. Konczykowski, V. B. Geshkenbein, V. M. Vinokur, H. Shtrikman: *Nature* **375**, 373 1995.
55. N. Avraham, B. Khaykovich, Y. Myasoedov, M. Rappaport, H. Shtrikman, D. E. Feldman, T. Tamegai, P. H. Kes, M. Li, M. Konczykowski, K. van der Beek, E. Zeldov: *Nature* **411**, 451 2001.
56. G. Ravikumar, P. K. Mishra, V. C. Sahni, S. S. Banerjee, S. Ramakrishnan, A. K. Grover, P. L. Gammel, D. J. Bishop, E. Bucher, M. J. Higgins and S. Bhattacharya: *Physica C* **332**, 145 (1999).

Out-of-equilibrium Relaxation of a Time-dependent Effective Temperature

A. Lemaître

¹ Department of physics, University of California, Santa Barbara, California
93106, U.S.A.

anael@physics.ucsb.edu

² L.M.D.H. - Université Paris VI, UMR 7603, 4 place Jussieu - case 86, 75005
Paris - France

The purpose of the present work is to introduce a limited set of kinetic equations which describe the out-of-equilibrium relaxation of a structural glass and its response to shear deformation. It was originally motivated by recent theories for the plasticity of amorphous solids, [4, 5] in an attempt to incorporate glassy relaxation at an elementary level. [8, 9] A quite simple picture emerges, which accounts for important properties of glassy materials, while its premises may hold for general classes of complex fluids; [7] it echoes early theories of structural relaxation [1, 10, 11, 14] in a much more systematic framework, and provides theoretical grounding for phenomenological rate-and-state equations. [2]

1 Assumptions and Constitutive Equations

We consider, in this study, a piece of material at pressure P , in contact with a thermal reservoir at temperature T . We sort the material into subsystems [1] (or zones) of, say, z molecules, and characterize structural disorder by the distribution ρ of volumes, $v_i \in [v_0, \infty]$, or enthalpies ($h_i = Pv_i$) of these molecular configurations. (v_0 is a lower bound imposed by excluded volume effects.) At low T , the distribution ρ evolves slowly, as opposed to the vibrations of the molecular structure which quickly equilibrate with the thermal bath. The evolution of ρ is expected to result from transitions between metastable basins in phase space, and these transitions are supposed to be triggered by conformational changes of molecular subsystems (rearrangements). The typical size of a rearranging zones fixes z , which is here supposed to be independent of T and P . At all times, molecular subsystems are in mechanical contact with neighboring subsystems, hence likely to exchange energy among themselves: very small displacements of the average positions of the molecules are sufficient to ensure these volume (or enthalpy) transfers. Mediated by acoustic modes (phonons), these transfers are thus expected to be fast, collective, processes, in contrast with rearrangements which, at low T , are expected to be rare, space-localized events.

This observation in the basis of the present work: it permits to separate these two thermodynamic processes (equilibration with the bath *v.s.* transfers between subsystems) and assume that *spatial* enthalpy fluctuations equilibrate on timescales at which the system is *not* in contact with the thermal reservoir. At all time, approximation is made that spatial fluctuations are in “adiabatic equilibrium”, characterized by a (P, H) -ensemble: the distribution ρ is determined *at every single moment* by statistical inference: it maximizes entropy under the single constraint that $H = \int dh \rho(h) h$ is known, whence $\rho(h) = \frac{1}{Z} \exp(-\lambda h)$, with the partition function $Z = \int_{h_0=Pv_0}^{\infty} dh \exp(-\lambda h) = (1/\lambda) \exp(-\lambda h_0)$, and where λ is the Lagrange multiplier that enforces adiabaticity. $\Theta = 1/(k\lambda)$ is an effective temperature, but differs from the temperature of the thermal reservoir, unless the system has reached thermal equilibrium. This effective temperature is a generalization of Edwards’: [3] I made no assumption here that the system is exploring all configurations of some ergodic component at any relevant timescale but, rather, that, by being very large, it samples, at any single time, all possible configurations allowed by macroscopic constraints. At all time, $k\Theta(t) = H(t) - Pv_0$.³

The previous Ansatz for ρ serves here as a basis to investigate the relaxation of the system towards equilibrium. At any time, H (or Θ) suffice to characterize the internal state of the material.⁴ Their dynamics is specified by energy conservation: it results from the balance between thermal exchanges with the reservoir (heat) and the work of external forces. Estimating the rate of thermal exchanges with the bath is a difficult task; it requires, in principle, to determine all probabilities $p(h \rightarrow h')$ for the reconformations of molecular subsystems, leading to:

$$\frac{dH}{dt} = \int dh dh' p(h \rightarrow h') \rho(h) (h' - h) + W^{\text{ext}} . \quad (1)$$

I argue that a generic form of this equation arises from the study of dominant contributions to the integral term. Then, I show that the resulting equation accounts for the emergence of slow relaxation and glassy behavior at low T , with a marked cooling rate dependence of the glass transition point. A study of the response to shear in various experimental set-up completes my presentation.

Rearrangements correspond to elementary contacts with the thermal reservoir: a fluctuation δh of enthalpy requires a transfer of heat $\delta q = -\delta h$

³ $k\Theta(t) = P(V - v_0)$ is proportional to a Van der Waals’ free-volume: [6] in light of the following discussion, free-volume activation [14] and effective temperature, [3] appear to be closely related concepts.

⁴The limit we consider is in some sense, “opposite” to the mean-field approximation, in which case every variable v_i is directly coupled with the average \bar{v} , whence the full distribution $\rho(v_i - \bar{v})$ becomes the dynamical variable. We see that the mechanical contacts between subsystems may (below some critical dimension) drastically reduce the dimensionality of the relevant dynamics.

from the thermal reservoir, hence occurs with probability $\exp(\delta S/k) = \exp(-\delta h/(kT))$. These thermally activated processes are very sensitive to the external constraints imposed on a molecular subsystem by its surroundings: for low v , the reformation of the molecules may require to deform their “cage” and pay a consequent price in elastic energy; for large v , molecules may move freely. Suppose, for the sake of simplicity, that the transitions $h \rightarrow h'$ are controlled by some energy barrier h_b which is a simple function of the volume v . Obviously, $h_b(v)$ must be non-increasing, hence there exist an *activation volume* v_a , such that $h_b(v_a) = Pv_a \equiv h_a$; beyond this point ($v > v_a$) the notion of barrier breaks down. Two different families of reaction pathways must be identified: when $h, h' < h_b$, transitions are activated, and transition state theory indicates that the rates must be written: $p(h \rightarrow h') = \nu \exp(-(h_b - h)/(kT))$; otherwise, there is no barrier *per se* and Monte-Carlo weights read: $p(h \rightarrow h') = \nu \min(1, \exp(-(h' - h)/(kT)))$. These transition probabilities verify detailed balance and are continuous functions of either h or h' when they cross h_a . ν is an update frequency, the temperature dependence of which might be neglected as it brings only minimal corrections. The calculation of the rhs of equation (1) is further simplified by allowing only transitions such that $h - h' = \pm \delta q$; the integral is separated into the sum I_1 over $h, h' \in [h_0, h_a]$, and I_2 over the complementary domain of integration. It appears that I_1 (resp. I_2) is of order $O((\Theta - T)^2)$ (resp. $O(\Theta - T)$) close to equilibrium, and is proportional to a factor of the form $\exp(-A/(kT))$ (resp. $\exp(-A/(k\Theta))$) when $\Theta \gg T$. In both these limits, I_1 is dominated by I_2 : the dynamics of Θ is controlled by the transition pathways (found with a frequency $\exp(-P(v_a - v_0)/(k\Theta))$) which do not involve the crossing of energy barriers. It is therefore sufficient to restrict our discussion to the situation in which $I_1 \rightarrow 0$. To fix ideas, I assume that $h_b(v) \rightarrow \infty$ below v_a and drops sharply at that point. (Such steep decay of h_b is expected, for example, in the case of hard-sphere materials.)

After integration one gets from equation (1):

$$k \dot{\Theta} = E_1 \exp \left[-\frac{\Delta h}{k \Theta} \right] \left(\exp \left(\frac{\delta q}{k \Theta} - \frac{\delta q}{k T} \right) - 1 \right) + \sigma \dot{\gamma}, \quad (2)$$

with $E_1 = \nu \delta q$ and $\Delta h = P(v_a - v_0)$. I anticipate here on the second part of this paper where the deformation of a material in a pure shear geometry will be considered: σ is the (deviatoric) shear stress, $\dot{\gamma}$ the plastic strain rate, whence $W^{\text{ext}} = \sigma \dot{\gamma}$. The results presented here do not depend qualitatively on further dependencies of E_1 on T or Θ , which may, however, bring logarithmic corrections.

2 Out-of-equilibrium Relaxation

In the absence of external stress ($\sigma = 0$), equation (2) admits thermodynamic equilibrium, $\Theta = T$, as its single fixed point. The timescale of the relaxation

towards equilibrium increases with decreasing T , and at low T the system may remain out-of-equilibrium on any observable timescale by the mere fact that Θ is small (or tries to). When $\Theta \gg T$, equation (2) is dominated by:

$$k \dot{\Theta} = -E_1 \exp \left[-\frac{\Delta h}{k \Theta} \right] + \sigma \dot{\gamma}. \quad (3)$$

In this limit, the long-time relaxation of the variable Θ is easily obtained by integrating (3) (with $\dot{\gamma}\sigma = 0$): $\int_{\Theta_0}^{\Theta(t)} \exp[\Delta h/k\Theta] k d\Theta = -E_1 t$, and keeping only the dominant contribution: $k\Theta(t) \simeq \frac{\Delta h}{\log(E_1 t/\Delta h)}$. For finite T , this process dominates so long as $t \ll \tau_T = \Delta h \exp[\Delta h/(kT)]/E_1$: τ_T diverges in the limit $T \rightarrow 0$.

An important property of the glass transition is that the observed transition point depends on the cooling rate. [7,10] Consider the following experiment: enthalpy is monitored during a steady cooling from an initial temperature T_{\max} ; after reaching T_{\min} , the temperature is increased at the same rate back to T_{\max} . This procedure is reproduced here by integrating equation (2) for different cooling/reheating rates. The resulting dynamics are portrayed Fig. 1 (left), where energy is shown as a function of T . Slowing down is seen as energy does not reach equilibrium at low temperature; upon reheating, energy does not go back along the same curve. As in the experiments, heat capacity is then extracted from this data according to the formula, $C_T = dH/dT$; the result is displayed Fig. 1 (right). The large increase of C_T observed upon reheating marks a fictive glass transition point, which clearly depends on the cooling rate.

The rest of this paper is devoted to the study of a material under shear. Like thermal equilibration, the deformation of a material under an applied

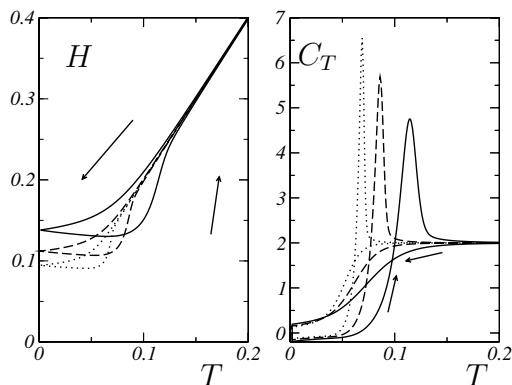


Fig. 1. Energy (*left*) and calorific capacity (*right*) as a function of temperature during cooling and reheating protocol, between $kT_{\max} = 0.5$ and $kT_{\min} = 0.001$, for cooling rates, $10^{-3}/k$ (*solid line*), $10^{-4}/k$ (*dashed line*), $10^{-5}/k$ (*dotted line*)

shear stress is expected to proceed by space-localized rearrangements. [4] However, the transition pathways that contribute respectively to elementary shear and elementary thermal equilibration processes, are not necessarily identical at the molecular level. Therefore they may, in general, display different activation enthalpies. Without more knowledge, we can expect the response to small shear stresses to be of the form:⁵

$$\dot{\gamma} = E_0 \exp \left[-\frac{\Delta h'}{k\Theta} \right] \sigma. \quad (4)$$

The update frequency E_0 normalizes the frequency of elementary vibrations, and incorporates corrections specific to this mode of deformation. Any dependency of E_0 on Θ or T is neglected. (E_0/E_1 and $\Delta h/\Delta h'$ are expected to be of order 1.)

With equations (4) and (2) in hand I now study three experimental protocols: aging in the stress-linear response to step strains, response to oscillatory forcing, and rheology of steady deformation.

Aging is characterized by monitoring the response of a material to a perturbation at various times after an initial quench from a high temperature equilibrium state. [7,13] The procedure is as follows: At time $t = 0$, the system is suddenly quenched from an equilibrium state ($\Theta_0 = T_0$) to low temperature. Relaxational dynamics take place from then on, and we study the situation when $\Theta \gg T$: equation (3) leads at long time to a time-logarithmic decay of enthalpy. At time t_w , a small strain $\delta\epsilon$ is applied; it provokes a quasi-instantaneous elastic response $\sigma = 2\mu\delta\epsilon$, followed by a slow occurrence of plastic deformations and stress release as: $\dot{\sigma} = -2\mu\dot{\gamma}$. For small $\delta\epsilon$, the term $\dot{\gamma}\sigma$ in equation (3) is negligible at all times.

At short times, stress decays exponentially, with a timescale, $\tau_\Theta = (1/(2\mu E_0)) \exp[\Delta h'/(k\Theta_w)]$, which depends only on $\Theta_w = \Theta(t_w)$. At long-times, stress release is controlled by the slow relaxation of Θ , and integrates as:

$$G(t, t_w) \equiv \frac{\sigma(t)}{\sigma(t_w)} \simeq \exp [A (t_w^\beta - t^\beta)]$$

with $\beta = 1 - \frac{\Delta h'}{\Delta h}$ and $A = \frac{2\mu E_0}{\beta} \left(\frac{E_1}{\Delta h} \right)^{\beta-1}$. If $\Delta h > \Delta h'$, $\beta > 0$ and stress undergoes KWW relaxation. The crossover between the short-time exponential relaxation and the long-time stretched exponential is illustrated Fig. 2. A plateau appears in the crossover region: this typical pattern emerges here solely from a change in the dynamical regime of Θ . Relaxation curves for different ages t_w are shown Fig. 3 (top). If fitted by $\exp(-t^\beta/\tau(t_w))$, it is easy to check that the apparent relaxation timescale $\tau(t_w)$ grows like, t_w^α , with $\alpha = 1 - \beta$; this phenomenon, usually referred as sub-aging is here a mere artifact of the lin-log representation: this type of scaling – which are very often used to treat experimental data – may be very misleading and

⁵I do not consider, in this work, dynamics of shear transformation zones. [4]

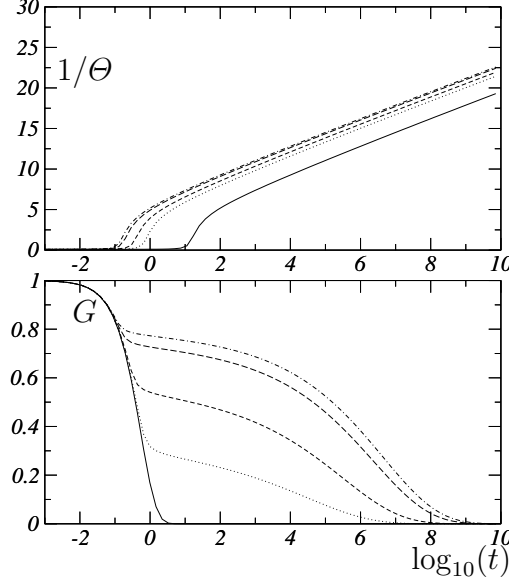


Fig. 2. Parameters are $E_0 = \mu = 1$, $\Delta h = 1.5$, $\Delta h' = 1$, $\Theta(0) = 10$, and $t_w = 0$. *Top:* $1/\Theta$ as a function of $\log_{10}(t)$ for $E_1 = 1, 20, 40, 80, 100$ from right to left. *Bottom:* relaxation spectra with E_1 increasing from left to right

hide, as it does here, the true aging behavior. If $\Delta h = \Delta h'$, $\beta = 0$, we find $G(t) \simeq 1/t$. If $\Delta h < \Delta h'$, $\beta < 0$ and stress assumes a non-vanishing asymptotic value after relaxation, which increases with the age of the sample: $G(t \rightarrow \infty) \simeq \exp[-|A| t_w^{-|\beta|}]$.

Another important experimental protocol consist in measuring the in-phase and out-of-phase moduli, G' and G'' , when the material is forced at time t_w by an oscillatory shear, $\gamma(t) = \gamma_0 \sin(\omega(t - t_w))$. In practice, the measurement is performed by integrating the response a fixed number of periods n , for each frequency ω . Since the material ages, every point on the spectrum depends on the whole history of the sample prior to its measurement. The resulting G' and G'' are shown Fig. 3 (bottom). They clearly show an α relaxation peak which, here is solely the signature of the slow evolution of Θ . This peak is obtained for large intervals of the parameters, under the conditions that μ is somewhat large (which, indeed, is reasonable, given the usual values of elastic constants); it weakens with the increasing age of the material.

To conclude this study, let me consider the regime of stationary deformation of the material, at temperature T , under a constant shear rate $\dot{\gamma}$. The steady state value of the variable Θ is the solution of:

$$\dot{\gamma}^2 = E_0 E_1 \exp\left[-\frac{\Delta h + \Delta h'}{k\Theta}\right] \left(1 - \exp\left(\frac{\delta q}{k\Theta} - \frac{\delta q}{kT}\right)\right) .$$

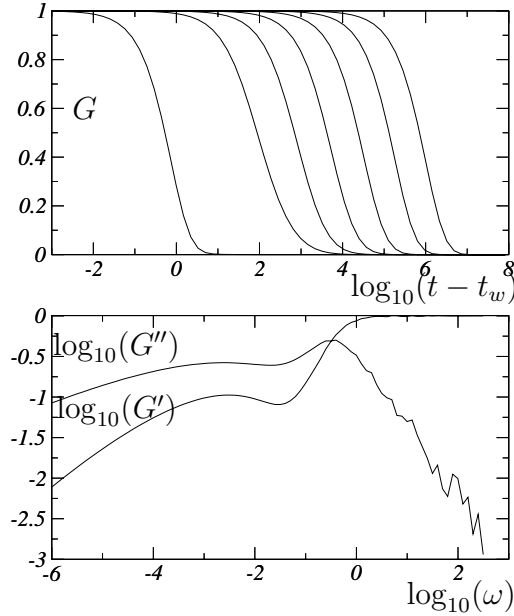


Fig. 3. *Top:* Relaxation modulus for $E_0 = E_1 = \mu = 1$, $\Delta h = 1.5$, $\Delta h' = 1$, $\Theta(0) = 10$, and $t_w = 10, 10^2, 10^3, 10^4, 10^5, 10^6, 10^7$. *Bottom:* Normalized frequency spectra for $\mu = 100$, $E_0 = E_1 = 0.01$, $\Delta h = 1.5$, $\Delta h' = 1$, $t_w = 10$, $\Theta(0) = 10$

For $\Delta h = \Delta h'$, one finds, $\eta \dot{\gamma} = \sigma(1 + \frac{E_0}{E_1} \sigma^2)^{-\frac{\Delta h}{\delta q}}$. For $\Delta h \neq \Delta h'$, and $k\Theta \gg \Delta h + \Delta h'$, this solution is dominated by the contribution, $\Theta = kT/(1 + (kT/\delta q) \log(1 - \dot{\gamma}^2/(E_1 E_0)))$ which, for small $\dot{\gamma}$, indicates that the system behaves as a Newtonian liquid with a viscosity, $\eta = \exp[\Delta h'/kT]/E_0$. For $kT \neq k\Theta \ll \Delta h + \Delta h'$, the solution is dominated by its $T \rightarrow 0$ value, which leads to a power relation between stress and strain rate: $\sigma \sim \dot{\gamma}^n$, with $n = \frac{\Delta h - \Delta h'}{\Delta h + \Delta h'}$.

3 Conclusion

This study suggest that, in the low temperature regime, there exists a direct relation between the exponent β (and α) of the KWW relaxation, and the power law rheology displayed in steady shear. It establishes a relation between two highly dissimilar experimental situations – linear response in the aging regime, and steady shear deformation – in direct relation to the ratio $\kappa = \Delta h/\Delta h'$ between activation barriers associated respectively to shear and energy relaxation processes. κ is expected to depend solely on geometrical aspect of the material: shape of the molecules or polydispersity of colloidal particles. The existence of such a relation can thus be tested experimentally

by considering families of closely related materials in order to allow some variation of the exponents.

The equations proposed here are exaggeratedly simple. Their interest lies in the possibility to account for a whole set of properties commonly associated with the glass transition, in a over-simplified framework, in comparison to other studies of rheology. [12] Various aspects of these questions certainly deserve further studies. In particular, a derivation of the transformation rates would bring out much needed information. One may, however, hope that out-of-equilibrium thermodynamics can be defined for structural glasses in terms of a few rate equations for the appropriate set of thermodynamic quantities.

I thank Jean Carlson and Eric Clément for their support and their interest in my research. I am especially grateful to Christiane Caroli and Jim Langer for their suggestions, and their helpful critiques. This work was sponsored by the W. M. Keck Foundation, and the NSF Grant No. DMR-9813752.

References

1. G. Adam and J. H. Gibbs. On the temperature dependence of cooperative relaxation properties in glass-forming liquids. *J. Chem. Phys.*, 43(1):139, 1965.
2. C. Derec, A. Ajdari, and F. Lequeux. Rheology and aging: A simple approach. *Eur. Phys. J. E*, 4:355–361, 2001.
3. S.F. Edwards. The role of entropy in the specification of a powder. In A. Mehta, editor, *Granular Matter: An Interdisciplinary Approach*, pp. 121–140. Springer-Verlag, New-York, 1994.
4. M. L. Falk and J. S. Langer. Dynamics of viscoplastic deformation in amorphous solids. *Phys. Rev. E*, 57(6):7192, 1998.
5. M. L. Falk and J. S. Langer. From simulation to theory in the physics of deformation and fracture. *M.R.S. Bulletin*, 25:40, 2000.
6. G. Gallavotti. *Statistical Mechanics: a short treatise*. Springer-Verlag, Berlin, Heidelberg, 1999.
7. R.G. Larson. *The structure and rheology of complex fluids*. Oxford University Press, New York, 1999.
8. Anaël Lemaître. A dynamical approach to glassy materials. cond-mat/0206417, unpublished, 2002.
9. Anaël Lemaître. Rearrangements and dilatancy for sheared dense materials. *Phys. Rev. Lett.*, 89:195503, 2002.
10. C. T. Moynihan, P. B. Macedo, C. J. Montrose, P. K. Gupta, M. A. DeBolt, J. F. Dill, B. E. Dom, P. W. Drake, A. J. Eastale, P. B. Elterman, R. P. Moeller, H. Sasabe, and J. A. Wilder. *Ann. NY Acad. Sci.*, 279:15, 1976.
11. O. S. Narayanaswamy. A model of structural relaxation in glass. *J. Amer. Ceram. Soc.*, 54:491, 1971.
12. Peter Sollich, François Lequeux, Pascal Hébraud, and Michael E. Cates. Rheology of soft glassy materials. *Phys. Rev. Lett.*, 78(10):2020, 1997.
13. L. C. E. Struik. ””. *Ann. NY Acad. Sci.*, 279:78, 1976.
14. D. Turnbull and M. H. Cohen. Free-volume model of the amorphous phase: Glass transition. *J. Chem. Phys.*, 34(1):120, 1961.

Depinning and Plasticity of Driven Disordered Lattices

M.C. Marchetti

Physics Department, Syracuse University, Syracuse, NY 13244, USA
mcm@phy.syr.edu

We review in these notes the dynamics of extended condensed matter systems, such as vortex lattices in type-II superconductors and charge density waves in anisotropic metals, driven over quenched disorder. We focus in particular on the case of strong disorder, where topological defects are generated in the driven lattice. In this case the response is plastic and the depinning transition may become discontinuous and hysteretic.

1 Introduction

Nonequilibrium transitions from stuck to flowing phases underlie the physics of a wide range of physical phenomena. In a first class of systems the onset of a stuck or frozen state occurs as a result of intrinsic dynamical constraints, due to interactions or crowding, and is usually referred to as *jamming* [1]. Familiar examples are supercooled liquids that become glasses upon lowering the temperature, colloidal suspensions that undergo a glass transition due to crowding upon increasing the density or the pressure, foams and granular materials that jam under shear, arrays of dislocations in solids that jam under an applied load. In a second class of systems the transition to a stuck state is due to external constraints, such as the coupling to quenched disorder (pinning centers from material defects in vortex lattices, optical traps in colloids, etc.), and is denoted as *pinning* [2]. Both classes of systems can be driven in and out of glassy states by tuning not only temperature, density or disorder strength, but also an applied external force. The external drive may be a shear stress in conventional glasses or simply a uniform applied force in systems with extrinsic quenched disorder, where even a uniform translation of the system relative to the fixed impurities represents a nontrivial perturbation. Vortex lattices in superconductors [3] and charge density waves (CDWs) in metals [4] can be driven in and out of stuck glassy states by a uniform external current or electric field, respectively. As recognized recently in the context of jamming, the external drive plays a role not unlike that of temperature in driving the system to explore metastable configurations and should be included as an axis in a complete phase diagram.

In this lectures I will focus on zero-temperature depinning transitions of interacting condensed matter systems that spontaneously order in periodic

structures and are driven over quenched disorder. The prototype examples are vortex lattices in type-II superconductors [5] and charge density waves in anisotropic metals [8]. Other examples include Wigner crystals of two dimensional electrons in a magnetic field moving under an applied voltage [6], lattices of magnetic bubbles moving under an applied magnetic field gradient [7], and many others. In general these systems form a lattice inside a solid matrix, provided by the superconducting or conducting material and are subject to pinning by random impurities. The statics of such disordered lattices have been studied extensively [5]. One crucial feature that distinguishes the problem from that of disordered interfaces is that the pinning force experienced by the periodic structure is itself periodic, although with random amplitude and phase [9]. As a result, although disorder always destroys true long-range translational order and yields glassy phases with many metastable states and diverging energy barriers between these states, the precise nature of the glassy state depends crucially on disorder strength. At weak disorder the system, although glassy, retains topological order (the resulting phase has been named Bragg glass in the context of vortex lattices) [9]. Topological defects proliferate only above some characteristic disorder strength, where a topologically disordered glass is formed.

The driven dynamics of disordered periodic structures have been studied extensively by modeling the system as an overdamped elastic medium that can be deformed by disorder, but is not allowed to tear, that is by neglecting the possible formation of topological defects due to the competition of elasticity, disorder and drive. This model, first studied in the context of charge density waves, exhibits a nonequilibrium phase transition from a pinned to a *unique* sliding state at a critical value F_T of the driving force. This nonequilibrium transition displays universal critical behavior as in equilibrium *continuous* transitions, with the medium's mean velocity v acting as an order parameter [2, 8, 10]. While the overdamped elastic medium model may seem adequate to describe the dynamics of driven Bragg glasses, many experiments and simulations of driven systems have shown clearly that topological defects proliferate in the driven medium even for moderate disorder strengths [11–14, 54]. The dynamics near depinning becomes spatially and temporally inhomogeneous, with coexisting moving and pinned degrees of freedom. This regime has been referred to as plastic flow and may be associated with memory effects and even hysteresis in the macroscopic response.

The goal of the present lectures is to describe coarse-grained models of driven extended systems that can lead to history-dependent dynamics. Such models can be grouped in two classes. In the first class the displacement of the driven medium from some undeformed reference configuration remains single-valued, as appropriate for systems without topological defects, but the interactions are modified to incorporate non-elastic restoring forces [15–20]. In the second class of models topological defects are explicitly allowed by removing the constraint of single-valued displacements [21–23]. Here we will

focus on the first class and specifically consider driven periodic media with a linear stress-strain relation, where the stress transfer between displacements of different parts of the medium is nonmonotonic in time and describes viscous-type slip of neighboring degrees of freedom. A general model of this type that encompasses many of the models discussed in the literature was proposed recently by us [18, 20, 24]. Here slips between neighboring degrees of freedom are described as viscous force, that allows a moving portion of the medium to overshoot a static configuration before relaxing back to it. It is shown below that such viscous coupling can be considered an effective way of incorporating the presence of topological defects in the driven medium. Related models have also been used to incorporate the effect of inertia or elastic stress overshoot in crack propagation in solids [19, 25]. The precise connection between the two classes of models has been discussed in [26].

In Sect. 2 we review the simplest example of depinning transition, obtained when non-interacting particles are driven through a periodic pinning potential. By contrasting the case of periodic and non-periodic pinning, we stress that care must be used in the definition of the mean velocity of the system. In Sect. 3, we first describe the generic coarse-grained model of a driven elastic medium that exhibits a *continuous* depinning transition as a function of the driving force from a static to a *unique* sliding state. Next we introduce an anisotropic visco-elastic model as a generic model of a periodic system driven through strong disorder. The model considers coarse-grained degrees of freedom that can slip relative to each other in the directions transverse to the mean motion, due to the presence of small scale defects (phase slips, dislocations, grain boundaries) at their boundaries, but remain elastically coupled in the longitudinal directions. The slip interactions are modeled as viscous couplings and a detailed physical motivation for this choice is given in Sect. 3.3. Most of our current results for these type of models are for the mean-field limit and are presented in Sect. 4. The studies carried out so far for finite-range interactions suggest that the mean-field theory described here may give the correct topology for the phase diagram, although there will of course be corrections to the critical behavior in finite dimensions [27]. Finally, we conclude in Sect. 5 by discussing the relation to other models described in the literature and the connection to experiments.

2 Depinning of Noninteracting Particles

It is instructive to begin with the problem of a single particle driven through a *periodic* pinning potential as the simplest illustration of driven depinning. Assuming overdamped dynamics, the equation of motion for the position x of the particle is

$$\zeta \frac{dx}{dt} = F + hY(x) , \quad (1)$$

where ζ is a friction coefficient (in the following we choose our units of time so that $\zeta = 1$), F is the external drive and $Y(x) = Y(x + n)$, with n an integer, is a periodic function of period 1. For simplicity we choose a piecewise linear pinning force, corresponding to $Y(x) = (1/2 - x)$, for $0 \leq x \leq 1$. In this case a periodic solution of (1) is obtained immediately in terms of the time T needed to traverse a potential well, or period. Introducing an arbitrary time t_J such that if $x(t_J) = n$, then $x(t_J + T) = n + 1$, the particle position for $t_J + nT \leq t \leq t_J + (n + 1)T$ is

$$x(t) = n + \frac{1 - e^{-h(t-t_J-nT)}}{1 - e^{-hT}}, \quad (2)$$

where T is given by

$$T(h) = \frac{1}{h} \ln \left(\frac{2F + h}{2F - h} \right), \quad (3)$$

for $F > h/2$ and diverges for $F < h/2$. In other words if $F < h/2$ the particle never leaves the initial well, i.e., it is pinned. The threshold force for depinning is then $F_c = h/2$. In the sliding state the mean velocity is defined as the average of the instantaneous velocity $v(t) = \frac{dx}{dt}$ over the arbitrary initial time t_J . This gives

$$\bar{v} \equiv \langle v \rangle_{t_J} = \int_{t-(n+1)T}^{t-nT} \frac{dt_J}{T} v(t) = \frac{1}{T}. \quad (4)$$

This definition naturally identifies the mean velocity of the particle with the inverse of the period. The logarithmic behavior of \bar{v} near threshold, $\bar{v} \sim -1/\ln(F_c - F)$, is peculiar to a discontinuous pinning force. For an arbitrary pinning force $Y(X)$ the period T is

$$T = \int_0^1 dx \frac{1}{F + hY(x)}, \quad (5)$$

and can be evaluated analytically for various forces. For instance, for a sinusoidal pinning force, $Y(x) = \sin(2\pi x)$, one finds $T = (F^2 - h^2)^{-1/2}$, which gives $\bar{v} \sim (F - F_c)^{1/2}$ near threshold, a generic behavior for continuous pinning forces.

The main focus of the remainder of this paper will be on the modeling of extended driven systems as collections of interacting degrees of freedom. It will then be important to distinguish two cases. For extended systems that are periodic, such as charge density waves and vortex lattices, the pinning potential is itself periodic as each degrees of freedom sees the same disorder after advancing one lattice constant. For non-periodic systems, such as interfaces, each degree of freedom moves through a random array of defects. When interactions are neglected, an extended *periodic* system moving through a periodic random pinning potential can be modeled as a collection

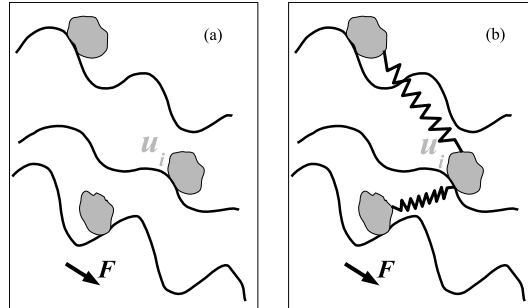


Fig. 1. (a) Sketch of noninteracting degrees of freedom driven over a random periodic pinning potential in one dimension. Spatial coordinates have been discretized so that degrees of freedom are labelled by an index i . In (b) the case where each degree of freedom interacts elastically with its neighbors is shown. This is a discretized one-dimensional realization of the elastic medium model described by (13) below

of N non-interacting particles, where each particle sees its own periodic pinning potential. The pinning potentials seen by different particles may differ in height and be randomly shifted relative to each other, as sketched in Fig. 1. The equation of motion for the i -th particle at position x_i is then

$$\frac{dx_i}{dt} = F + h_i Y(x_i + \gamma_i), \quad (6)$$

where γ_i are random phases uniformly distributed in $[0, 1)$ and the pinning strengths h_i are drawn independently from a distribution $\rho(h_i)$. Since the displacements x_i are decoupled, they can be indexed by their disorder parameters γ and h instead of their spatial label i , i.e., $x_i(t; \gamma_i, h_i) \rightarrow x(t; \gamma, h)$. The mean velocity of the many-particle system can then be written as an average over the random phases and pinning strengths,

$$\begin{aligned} \bar{v} &= \frac{1}{N} \sum_i v_i = \langle v(t; \gamma, h) \rangle_{\gamma, h} \\ &= \int dh \rho(h) \int_0^1 d\gamma v(t; \gamma, h), \end{aligned} \quad (7)$$

where $v(t; \gamma, h) = \frac{dx(t; \gamma, h)}{dt}$. The average over the random phase of each degree of freedom is equivalent to the average over the random time shift t_J described for the single-particle case and yields $\int_0^1 d\gamma v(t; \gamma, h) = 1/T(h)$, with $T(h)$ the period of each particle given in (3). The mean velocity is then

$$\bar{v} = \left\langle \frac{1}{T(h)} \right\rangle_h, \quad (8)$$

where $\langle \dots \rangle_h = \int dh \dots \rho(h)$ denotes the average over the barrier height distribution. For distributions $\rho(h)$ that have support at $h = 0$, a system of *noninteracting* particles with periodic pinning depins at $F = 0$, as there are always some particles experiencing zero pinning force.

A different single-particle problem that has been discussed in the literature is that of a particle moving through a *random (non-periodic)* array of defects [28]. The defects can be described as pinning potential wells centered at random positions and/or with random well heights. To make contact with the periodic case we consider a particle moving through a succession of evenly spaced pinning potential wells of random heights. The equation of motion is

$$\partial_t x = F + \sum_{p=0}^{N_p-1} h_p Y(x-p), \quad (9)$$

where N_p is the total number of pinning centers and the pinning strengths h_p are drawn independently from a distribution $\rho(h_p)$. Choosing again the piecewise-linear pinning force, the time to traverse the p -th well is simply $T(h_p)$, with T given by (3). The mean velocity of the particle is defined as the total distance travelled divided by the total time and is given by

$$\bar{v} = \frac{N_p}{\sum_p T(h_p)} \equiv \frac{1}{\langle T(h) \rangle_h}. \quad (10)$$

In this case, unless the distribution $\rho(h)$ is bounded from above, there is always a finite probability that the particle will encounter a sufficiently deep potential well to get pinned. Therefore for unbounded $\rho(h)$ the particle is always pinned in the thermodynamic limit. If $\rho(h)$ is bounded from above by a maximum pinning strength h_{\max} , this value also represents the depinning threshold. Finally, the case of many noninteracting particles driven through a random array of defects is equivalent to that of a single particle, as the mean velocity of each particle can be calculated independently. The mean velocity of the system is then again given by (10).

3 Depinning of an Extended Medium

We consider a d -dimensional periodic structure driven along one of its symmetry directions, chosen as the x direction. The continuum equations for such a driven lattice within the elastic approximation were derived by various authors by a rigorous coarse-graining procedure of the microscopic dynamics [29–31]. Assuming overdamped microscopic dynamics, the equation for the local deformation $\mathbf{u}(\mathbf{r}, t)$ of the medium (in the laboratory frame) from an undeformed reference state is written by balancing all the forces acting on each portion of the system as [32]

$$\partial_t u_i = \partial_j \sigma_{ij} + F \delta_{ix} + F_{pi}(\mathbf{r}, \mathbf{u}), \quad (11)$$

where σ_{ij} is the stress tensor due to interactions among neighboring degrees of freedom, F is the driving force and \mathbf{F}_p is the periodic pinning force. The periodicity of the pinning force, which contains Fourier components at all the reciprocal lattice vectors of the lattice, arises from the coupling to the density of the driven lattice.

3.1 Elastic Model

For conventional short-ranged elasticity the stress tensor is

$$\sigma_{ij}^{\text{el}} = 2c_{66}u_{ij} + \delta_{ij}(c_{11} - c_{66})u_{kk} , \quad (12)$$

where c_{11} and c_{66} are the compressional and shear moduli of the driven lattice, respectively, and $u_{ij} = \frac{1}{2}(\partial_i u_j + \partial_j u_i)$ is the strain tensor. It was shown in [29] that deformations of the driven lattice along the direction of the driving force grow without bound due to large transverse shear stresses that generate unbounded strains responsible for dislocation unbinding. For this reason, we focus here on the dynamics of a scalar field $u_x(x, \mathbf{y}, t) \equiv u(\mathbf{r}, t)$, with $\mathbf{r} = (x, \mathbf{y})$, describing deformations of the driven lattice along the direction of mean motion. The $d - 1$ -dimensional vector \mathbf{y} denotes the coordinates transverse to the direction of motion. Assuming $c_{11} \gg c_{66}$, we obtain a scalar model for the driven elastic medium, given by

$$\partial_t u = c_{11} \partial_x^2 u + c_{66} \nabla_{\mathbf{y}}^2 u + F + F_p(\mathbf{r}, u) , \quad (13)$$

where F_p denotes the x component of the pinning force. For simplicity we also consider a model that only retains the component of the pinning force at the smallest reciprocal lattice vector and choose our units of lengths so that the corresponding period is 1. The pinning force is then taken of the form

$$F_p(\mathbf{r}, u) = h(\mathbf{r})Y(u(\mathbf{r}, t) - \gamma(\mathbf{r})) , \quad (14)$$

where $Y(u) = Y(u + n)$ is a periodic function. The random pinning strengths h are drawn independently at every spatial point from a distribution with zero mean and short-ranged correlations to be prescribed below. The random phases γ are spatially uncorrelated and distributed uniformly in $[0, 1)$.

The model of a driven overdamped elastic medium embodied by (13) has been studied extensively both analytically and numerically [2, 8, 10, 33, 34]. It exhibits a depinning transition at a critical value F_T of the applied force from a static to a *unique* sliding state [35]. The depinning can be described as a continuous equilibrium transition, with the mean velocity $\bar{v} = \langle \partial_t u \rangle$ playing the role of the order parameter, and universal critical behavior. The velocity vanishes as F_T is approached from above as $\bar{v} \sim (F - F_T)^\beta$. The critical exponent β depends only on the system dimensionality and was found to be $\beta = 1 - \epsilon/6 + \mathcal{O}(\epsilon^2)$ using a functional RG expansion in $\epsilon = 4 - d$ [10, 36].

3.2 Viscoelastic Model

Strong disorder can yield topological defects in the driven lattice, making the elastic model inapplicable [37, 38]. In this case the dynamics becomes inhomogeneous, with coexisting pinned and moving regions [39, 40]. The depinning transition may be discontinuous (first order), possibly with macroscopic hysteresis. Several mean-field models of driven extended systems have been proposed [2, 16–19, 21, 22] to describe this inhomogeneous dynamics. Here we focus on a class of models that retains a single-valued displacement field and a linear stress-strain relation, but assumes that the presence of topological defects can be effectively incorporated at large scales by a non-instantaneous stress transfer that couples to gradients of the local velocity (rather than displacement). More precisely, we consider an anisotropic model of coarse-grained degrees of freedom that can slip relative to each other in at least one of the directions transverse to the mean motion, due to the presence of small scale defects (phase slips, dislocations, grain boundaries) at their boundaries, but remain elastically coupled in the longitudinal directions [20]. This model incorporates the anisotropy of the sliding state in the plastic flow region that results either from flow along coupled channels oriented in the direction of the drive (e.g., as in the moving smectic phase [41]) or in layered materials such as the high- T_c cuprate superconductors. It also encompasses several of the models discussed in the literature.

For generality, consider a $d = d_{\parallel} + d_{\perp}$ -dimensional medium composed of degrees of freedom that are coupled elastically in d_{\parallel} direction and can slip relative to each other in the remaining d_{\perp} directions. The axis x along which the driving force is applied is along one of the d_{\parallel} directions. The equation of motion for the displacement $u(\mathbf{r}_{\parallel}, \mathbf{r}_{\perp}, t)$ is given by

$$\partial_t u = K \nabla_{\parallel}^2 u + \eta \nabla_{\perp}^2 v + F + F_p(\mathbf{r}, u), \quad (15)$$

with $v = \partial_t u$ the local velocity. This model will be referred to as the viscoelastic (VE) model as it incorporates elastic couplings of strength K in d_{\parallel} directions and viscous couplings of strength controlled by a shear viscosity η in the remaining d_{\perp} directions. A two-dimensional cartoon of this anisotropic model is shown in Fig. 2.

For $\eta = 0$ (or $d_{\perp} = 0$) the VE model reduces to the elastic model (but with isotropic elasticity) of (13). Conversely, for $K = 0$ (or $d_{\parallel} = 0$) (15) reduces to the purely viscous model studied earlier by us [18, 24]. For any distribution of pinning strengths with support at $h = 0$, the purely viscous model has zero threshold for depinning, but it does exhibit a critical point separating regions of unique and multivalued solutions for the mean velocity. In the VE model ($\eta \neq 0$ and $K \neq 0$) even when fluid-like shear takes place, particle conservation gives a sharp depinning transition in flow along the channels. Furthermore, as shown below, the model has a sharp mean-field tricritical point separating a region of parameters where depinning is continuous, in

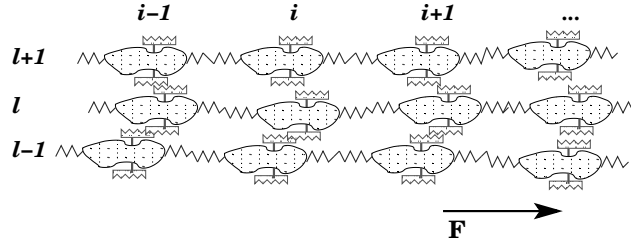


Fig. 2. A two-dimensional realization of the anisotropic driven medium described in the text. Spatial coordinates have been discretized in the figure so that degrees of freedom are labelled by indices ℓ and i , respectively transverse and longitudinal to the direction of the driving force, F . Each degree of freedom interacts with its neighbors via elastic couplings in the longitudinal direction and via viscous or similar slip couplings in the transverse direction

the universality class of elastic depinning, from one where depinning become discontinuous and hysteretic.

It is important to stress that the VE model still assumes *overdamped microscopic dynamics*. Velocity or viscous couplings can appear generically in the large-scale equations of motion upon coarse-graining the microscopic dynamics of a dissipative medium. In fact, next we show that viscous couplings indeed represent an effective way of incorporating the local dissipation due to the presence of topological defects.

3.3 Viscoelastic Coupling as an Effective Description of Topological Defects

The goal of this section is to provide some justification to the anisotropic VE model as an effective description of topological defects in a driven lattice. To this purpose we consider a two dimensional medium and take advantage of the continuum equations developed many years ago by Zippelius et al. [42] to describe the time-dependent properties of two-dimensional solids near melting. These authors combined the equations of free dislocation motion with solid hydrodynamics to construct a semimicroscopic dynamical model of a solid with free dislocations. They further showed that the dynamics of such of a “heavily dislocated solid” (an elastic medium with an equilibrium concentration of free dislocations) is identical to that of the hexatic phase obtained when a two-dimensional solid melts via the unbinding of dislocations [43]. More recently we [44] reconsidered the dynamical equations for the “heavily dislocated solid” of [42] and showed that they can be recast in the form of the phenomenological equations of a viscoelastic fluid (with hexatic order) introduced many years ago by Maxwell [45]. In the presence of free dislocations the local stresses in the medium have contributions from both elastic stresses and defect motion. The latter couple again to the the local strains which

control the defect dynamics. By eliminating the defect degrees of freedom, one obtains a linear, although nonlocal, relation between strain and stress, given by [46]

$$\begin{aligned} \sigma_{ij}^{\text{VE}}(\mathbf{r}, t) = & \delta_{ij} c_L u_{kk}(\mathbf{r}, t) + \delta_{ij}(c_{11} - c_L) \int_{-\infty}^t dt' e^{-(t-t')/\tau_b} v_{kk}(\mathbf{r}, t') \\ & + 2c_{66} \int_{-\infty}^t dt' e^{-(t-t')/\tau_s} \left[v_{ij}(\mathbf{r}, t') - \frac{1}{2} \delta_{ij} v_{kk}(\mathbf{r}, t') \right], \end{aligned} \quad (16)$$

where $v_{ij} = \frac{1}{2}(\partial_i v_j + \partial_j v_i)$ and the velocity \mathbf{v} is defined here in terms of the momentum density \mathbf{g} as $\mathbf{v} = \mathbf{g}/\rho_0$, with ρ_0 the equilibrium mass density of the medium. Also in (16) c_L is the compressional modulus of the liquid and $\tau_b \approx (c_{11}\mu_d^c n_f a_0^2)^{-1}$ and $\tau_s \approx (c_{66}\mu_d^g n_f a_0^2)^{-1}$ are the compressional and shear relaxation times, with μ_d^g the dislocation glide and climb mobility, respectively. Of course in the presence of dislocations the displacement u is no longer single-valued (although the strain u_{ij} remains single-valued and continuous) and $\partial_t u \neq v$ due to both the motion of vacancy/interstitial defects and of dislocations. The phenomenological Maxwell model of viscoelasticity is obtained by assuming that $\partial_t u = v$ even in the presence of dislocations. Then for $t \ll \tau_s, \tau_b$ the viscoelastic stress $\sigma^{\text{VE}}(\mathbf{r}, t)$ reduces to the familiar elastic stress tensor given in (12),

$$\sigma^{\text{VE}}(\mathbf{r}, t \ll \tau_s, \tau_b) \approx \sigma_{ij}^{\text{el}}. \quad (17)$$

Conversely for $t \gg \tau_s, \tau_b$ one obtains

$$\sigma_{ij}^{\text{VE}}(\mathbf{r}, t \gg \tau_s, \tau_b) \approx \delta_{ij} c_L u_{kk} + \delta_{ij}(\eta_b + \eta) v_{kk} + 2\eta v_{ij}, \quad (18)$$

which describes stresses in a viscous fluid of shear viscosity $\eta = c_{66}\tau_s$ and bulk viscosity $\eta_b = (c_{11} - c_L)\tau_b$. The first term on the right hand side of (18) is the pressure and incorporates the fact that even a liquid has a nonzero long-wavelength compressional elasticity, which is associated with density conservation. As we will see below this term plays a crucial role in controlling the physics of depinning of a viscoelastic medium. The Maxwell viscoelastic fluid has solid-like shear rigidity at high frequency, but flows like a fluid at low frequency. Since the relaxation times τ_s and τ_b are inversely proportional to the density n_f of free dislocations, the Maxwell model behaves as a continuum elastic medium on all time scales when $n_f \rightarrow 0$ and as a viscous fluid when $n_f a_0^2 \sim 1$.

Dislocation climb is much slower than dislocation glide ($\mu_d^c \ll \mu_d^g$), resulting in $\tau_b \gg \tau_s$. We therefore assume that the response to compressional deformations is instantaneous on all time scales, but retain a viscoelastic response to shear deformations. Letting $\tau_b \rightarrow \infty$, we find

$$\sigma_{ij}^{\text{VE}}(\mathbf{r}, t) \approx \delta_{ij} c_{11} u_{kk}(t) + 2c_{66} \int_{-\infty}^t dt' e^{-(t-t')/\tau_s} \left[v_{ij}(t') - \frac{\delta_{ij}}{2} v_{kk}(t') \right] \quad (19)$$

We now turn to the case of interest here, where topological defects are generated in an extended medium driven through quenched disorder. In this case the medium has no low frequency shear modulus, but particle conservation still requires long wavelength elastic restoring forces to *compressional* deformations. On the other hand, the number of topological defects is not fixed as dislocations are continuously generated and annihilated by the interplay of elasticity, disorder and drive [39, 40, 47]. Furthermore, unbound dislocations can be pinned by disorder and do not equilibrate with the lattice. In the plastic region near depinning the dynamics remains very inhomogeneous and fluid-like and the pinning of dislocations by quenched disorder is not sufficient to restore the long wavelength shear-stiffness of the medium. For this reason we propose to describe the effect of topological defects near depinning by replacing elastic *shear* stresses by viscoelastic ones, while retaining elastic *compressional* forces. Of course the resulting model that assumes a fixed density of dislocations becomes inapplicable at large driving forces where dislocations heal as the lattice reorders. For the case of interest here of a scalar model describing only deformations along the direction of motion, the viscoelastic model of a driven disordered medium is

$$\partial_t u = c_{11} \partial_x^2 u + c_{66} \int_{-\infty}^t dt' e^{-(t-t')/\tau_s} \partial_y^2 v(t') + F + h(\mathbf{r})Y(u - \gamma(\mathbf{r})), \quad (20)$$

with $v = \partial_t u$. This model naturally incorporates the anisotropy and channel-like structure of the driven medium, where *shear* deformations due to gradients in the displacement in the directions transverse to the mean motion ($\partial_y u \neq 0$) are most effective at generating the large stresses responsible for the unbinding of topological defects. It is instructive to note that due to the exponential form of stress relaxation the integro-differential equation (20) is equivalent to a second order differential equation for the displacement,

$$\tau_s \partial_t^2 u + \gamma_{\text{eff}} \partial_t u = c_{11} \partial_x^2 u + \eta \partial_y^2 v + F + h(\mathbf{r})Y(u - \gamma(\mathbf{r})), \quad (21)$$

with γ_{eff} an effective friction [18]. In other words the effect of a finite density of dislocations in the driven lattice yields “inertial effects” on a scale controlled by the time $\tau_s \sim 1/n_f$. The purely viscous model obtained from (21) with $c_{11} = 0$ was analyzed in detail in [24] where it was shown that if τ_s and $\eta = c_{66}\tau_s$ are tuned independently, then τ_s is a strongly irrelevant parameter in the RG sense. This allows us to consider a simplified form of the equation for the driven medium obtained from (21) with $\tau_s = 0$, but $\eta = c_{66}\tau_s$ finite, leading to the general anisotropic viscoelastic model introduced in (15).

4 Mean-field Solution

The mean-field approximation for the VE model is obtained in the limit of infinite-range elastic and viscous interactions. To set up the mean field theory,

it is convenient to discretize space in both the transverse and longitudinal directions, using integer vectors i for the d_{\parallel} -dimensional intra-layer index and ℓ for the d_{\perp} -dimensional layer index. The local displacement along the direction of motion is $u_{\ell}^i(t)$. Its dynamics is governed by the equation,

$$\partial_t u_{\ell}^i = \sum_{\langle j \rangle} K_{ij} (u_{\ell}^i - u_{\ell}^j) + \sum_{\langle m \rangle} \eta_{\ell m} [\dot{u}_{\ell}^i - \dot{u}_{\ell}^m] + F + h_{\ell}^i Y(u_{\ell}^i - \gamma_{\ell}^i), \quad (22)$$

where the dot denotes a time derivative and $\langle j \rangle$ ($\langle m \rangle$) ranges over sites j (m) that are nearest neighbor to i (ℓ). The random pinning strengths h_{ℓ}^i are chosen independently with probability distribution $\rho(h_{\ell}^i)$ and the γ_{ℓ}^i are distributed uniformly and independently in $[0, 1)$. For a system with $N = N_{\parallel} \times N_{\perp}$ sites, *one* mean field theory is obtained by assuming that all sites are coupled with uniform strength, both within a given channel and with other channels. Each discrete displacement then couples to all others only through the mean velocity, $\bar{v} = N^{-1} \sum \dot{u}_{\ell}^i$, and the mean displacement, $\bar{u} = N^{-1} \sum u_{\ell}^i$. We assume that the disorder is isotropic and the system is self averaging and look for solutions moving with stationary velocity: $\bar{u} = \bar{v}t$. Since all displacements u are coupled, they can now be indexed by their disorder parameters γ and h , rather than the spatial indices i and ℓ . The mean-field dynamics is governed by the equation

$$(1 + \eta)\dot{u}(\gamma, h) = K(\bar{v}t - u) + F + \eta\bar{v} + hY(u - \gamma). \quad (23)$$

The cases $K = 0$ and $K \neq 0$ need to be discussed separately.

4.1 Mean-field Theory for Viscous Model: $K = 0$, $\eta \neq 0$

When $K = 0$, the mean field equation becomes identical to that of a single particle discussed in Sect. 2 driven by an effective force $F + \eta\bar{v}$ (with friction $1 + \eta$). In this case different degrees of freedom move at different velocities even in the mean field limit. The mean field velocity is determined by the self-consistency condition $\bar{v} = \langle \dot{u} \rangle_{\gamma, h}$, where the average over the random phases is equivalent to the average over the random times shifts t_J given in (4). For the case of a piecewise linear pinning force using (8) we find

$$\bar{v} = \frac{1}{1 + \eta} \int dh \rho(h) \frac{1}{T(h, F + \eta\bar{v})}, \quad (24)$$

with $T(h, F)$ given by (3). The mean velocity obtained by self-consistent solution of (24) is shown in Figs. 3 and 4 for two distributions of pinning strengths.

For a narrow distribution, $\rho(h) = \delta(h - 1)$, there is a finite threshold $F_T = 1/2$, independent of η . The velocity is multivalued for any finite η . When the force is ramped up adiabatically from the static state the system depins at $F_{\uparrow} = F_T$. When the force is ramped down from the sliding state, the

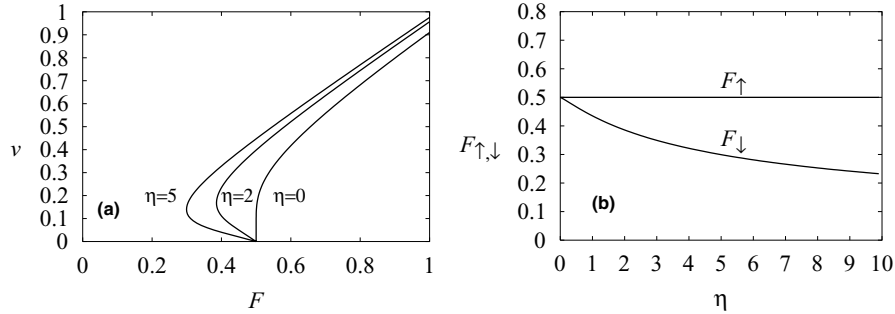


Fig. 3. (a) Velocity versus driving force for the purely viscous model ($K = 0$, $\eta \neq 0$) with a narrow distribution of pinning strength, $\rho(h) = \delta(h-1)$, for $\eta = 0, 2, 5$. There is a finite depinning threshold at $F_T = 1/2$. In (b) the depinning and repinning forces F_\uparrow and F_\downarrow are shown as functions of η

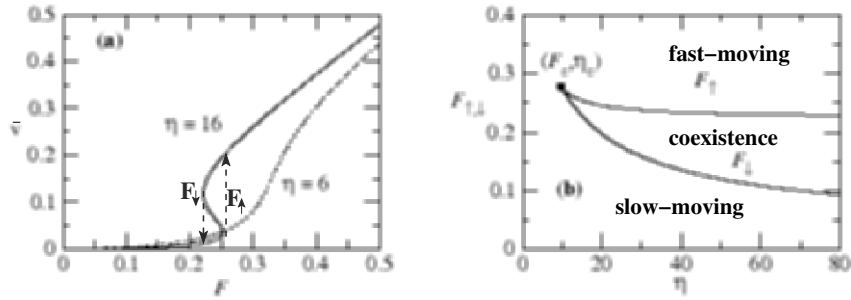


Fig. 4. (a) Velocity versus driving force for the purely viscous model ($K = 0$, $\eta \neq 0$) with a broad distribution of pinning strength, $\rho(h) = e^{-h}$ for $\eta = 6, 16$. In this case there are no stable static (pinned states). The velocity is single valued for $\eta < \eta_c$ and multi-valued for $\eta > \eta_c$. In this case when F is ramped up from zero, the velocity jumps discontinuously at F_\uparrow where the system goes from the “slow-moving” to the “fast-moving” state. Here and below “coexistence” refers to multistability of the solutions to the equations of motion. When F is then ramped down from within the fast-moving state the jump in \bar{v} occurs at the lower value F_\downarrow . The forces F_\downarrow and F_\uparrow become equal at the critical point, as shown in frame (b)

system repins at the lower value $F_\downarrow(\eta)$. The depinning and repinning forces are shown in Fig. 3(b). The region where unique and multivalued velocity solutions coexist extend to $\eta = 0$. For a broad distribution with support at $h = 0$, e.g., $\rho(h) = e^{-h}$, the threshold for depinning is zero as some of the degrees of freedom always experience zero pinning and start moving as soon as a force is applied. There is a critical point at (F_c, η_c) . For $\eta > \eta_c$ the analytical solution for $\bar{v}(F)$ is multivalued, as shown in Fig. 4. If the force is ramped up adiabatically from zero at a fixed $\eta > \eta_c$, the system depins discontinuously at $F_\uparrow(\eta)$, while when the force is ramped down it repins at

the lower value $F_{\downarrow}(\eta)$, as shown in Fig. 4. The viscous model has also been studied in finite dimensions by mapping it onto the nonequilibrium random field Ising model (RFIM) [24]. In the mapping, the local velocities correspond to spin degrees of freedom, the driving force is the applied magnetic field and the mean velocity maps onto the magnetization. The RFIM has a critical point separating a region where the magnetization versus applied field curve displays hysteresis with a discontinuous jump to a region where there is no jump in the hysteresis curve [48, 49]. In the viscous model the critical point separates a region where the velocity curve is smooth and continuous from the region where the “depinning” (from “slow-moving” to “fast-moving” states) is discontinuous and hysteretic. The critical point is in the Ising universality class, with an upper critical dimension $d_c = 6$.

4.2 Mean-field Theory for VE Model: $K \neq 0$ and $\eta \neq 0$

When $K \neq 0$, all degrees of freedom are coupled by a spring-like interaction (the first term on the right hand side of (23)) to the mean field $\bar{u} = \bar{v}t$ and cannot lag much behind each other. This forces all the periods to be the same, independent of h , and yields a nonvanishing threshold for depinning. In this case the mean field velocity is determined by imposing $\langle u(t; \gamma, h) - \bar{v}t \rangle_{\gamma, h} = 0$.

It is useful to first review the case where $K \neq 0$ and $\eta = 0$. In this limit, (23) reduces to the mean field theory of a driven elastic medium worked out by Fisher and collaborators [10]. No moving solution exists above a finite threshold force F_T . For the piecewise linear pinning force this is given by

$$F_T = \left\langle \frac{h^2}{2(K+h)} \right\rangle_h. \quad (25)$$

For $F > F_T$ there is a *unique* moving solution that has a universal dependence on F near F_T , where it vanishes as $\bar{v} \sim (F - F_T)^\beta$. In mean-field the critical exponent β depends on the shape of the pinning force: $\beta = 1$ for the discontinuous piecewise linear force and $\beta = 3/2$ for generic smooth forces. Using a functional RG expansion in $\epsilon = 4 - d$, Narayan and Fisher [10] showed that the discontinuous force captures a crucial intrinsic discontinuity of the large scale, low-frequency dynamics, giving the general result $\beta = 1 - \epsilon/6 + \mathcal{O}(\epsilon^2)$, in reasonable agreement with numerical simulations in two and three dimensions [33, 34]. For simplicity and to reflect the “jerkiness” of the motion in finite-dimensional systems at low velocities, we use piecewise linear pinning below.

When $\eta > 0$ the nature of the depinning differs qualitatively from the $\eta = 0$ case, in that hysteresis in the dynamics can take place. Again, no self-consistent moving solution exists for $F < F_T$, with F_T independent of η . Above threshold, both unique and multi-valued moving solutions exist, depending on the values of the parameters: η , K , and the shape of the disorder distribution, $\rho(h)$. To obtain the mean field solution in the sliding state, we

examine the motion during one period $T = 1/\bar{v}$ during which the displacement advances by 1. Equation (23) is easily solved for $0 \leq u \leq 1$ and $\gamma = 0$, with the result,

$$u(t; \gamma = 0, h) = \frac{K\bar{v}t + F + \eta\bar{v} + h/2}{(1 + \eta)\lambda} - \frac{K\bar{v}}{(1 + \eta)\lambda^2} + Ae^{-\lambda t}, \quad (26)$$

where $\lambda = (K + h)/(1 + \eta)$. At long times, regardless of the initial condition, $u(t)$ approaches a periodic function of period $T = 1/\bar{v}$ with jumps in its time derivative at times $t_J + nT$, with n an integer. The constant A is determined by requiring that if $u(t_J + nT) = n$, then $u(t_J + (n + 1)T) = n + 1$. Writing $u(t; \gamma, h) = \bar{v}t + \tilde{u}$, it is easy to see that for an arbitrary value of γ , the solution \tilde{u} will have the form $\tilde{u} = \tilde{u}(\bar{v}t - \gamma, h)$. The mean velocity is then obtained from $\langle \tilde{u}(\bar{v}t - \gamma, h) \rangle_{\gamma, h} = 0$. Averaging \tilde{u} over γ is equivalent to averaging \tilde{u} for a fixed γ over a time period, T , with the result,

$$\begin{aligned} \langle \tilde{u} \rangle_{\gamma} &= \int_{t_J + nT}^{t_J + (n+1)T} \frac{dt}{T} \tilde{u}(\bar{v}t - \gamma, h) \\ &= \frac{F + \eta\bar{v}}{K} - \frac{h^2}{2K(K + h)} - \frac{(K + 2h)\bar{v}}{\lambda(K + h)} - \frac{h^2}{K(K + h)} \frac{1}{e^{\lambda/\bar{v}} - 1}. \end{aligned} \quad (27)$$

Finally, averaging over h and using the consistency condition, we obtain

$$F - F_T = \bar{v}[1 - M(\eta, K)] + \left\langle \frac{h^2}{K(K + h)} \frac{1}{e^{(K+h)/(1+\eta)\bar{v}} - 1} \right\rangle_h, \quad (28)$$

with F_T the threshold force given in (25) and M given by

$$M(\eta, K) = (1 + \eta) \left\langle \frac{h^2}{(K + h)^2} \right\rangle_h. \quad (29)$$

As in the purely elastic case ($\eta = 0$) only static solutions exist for $F < F_T$. For $F > F_T$ there is a *unique* sliding solution, provided $M(\eta, K) < 1$, with mean velocity near threshold given by

$$\bar{v} \sim \frac{F - F_T}{1 - M(\eta, K)} \sim (1 + \eta_c) \frac{F - F_T}{\eta_c - \eta}, \quad (30)$$

giving $\beta = 1$, as in the purely elastic case. The critical line $\eta_c(K)$ separating unique from multivalued sliding solutions is determined by $M(\eta, K) = 1$,

$$\eta_c(K) = \left\langle \frac{h^2}{(K + h)^2} \right\rangle_h^{-1} - 1. \quad (31)$$

The velocity-force curves and a phase diagram are shown in Fig. 5 for $\rho(h) = e^{-h}$. There is a *tricritical point* at $(\eta_c, F_c = F_T)$. In contrast to the purely viscous model with $K = 0$, for finite long-time elasticity ($K > 0$) the behavior

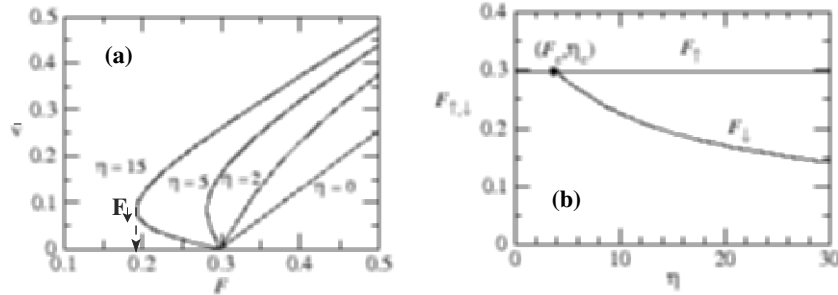


Fig. 5. (a) Velocity versus driving force for the VE model with $K = 1$ and a broad distribution of pinning strength, $\rho(h) = e^{-h}$. The velocity is continuous and single-valued for $\eta < \eta_c$ and becomes multivalued for $\eta > \eta_c$. The dashed line on the curve for $\eta = 15$ indicates the value F_{\perp} where the system repins when the drive is ramped down from the sliding state. Frame (b) shows the depinning and repinning forces F_{\uparrow} and F_{\perp} as functions of η . The tricritical point at (F_c, η_c) separates continuous from hysteretic depinning. Pinned and sliding states coexist in the region $F_{\perp} < F < F_{\uparrow}$.

is independent of the shape of the pinning force distribution, $\rho(h)$. For $\eta < \eta_c$, a continuous depinning transition at F_T separates a pinned state from a sliding state with *unique* velocity. In finite dimensions, this transition is likely to remain in the same universality class as the depinning of an elastic medium ($\eta = 0$). In our mean-field example, the linear response diverges at η_c , $v(\eta = \eta_c) \sim 1/\ln(F - F_T)$. For $\eta > \eta_c$ there is hysteresis with coexistence of stuck and sliding states.

Numerical simulations of the VE model in two dimensions ($d_{\parallel} = d_{\perp} = 1$) indicate a strong crossover (possibly a tricritical point) at a critical value of η_c from continuous to hysteretic depinning [27]. Although it is always difficult to establish conclusively on the basis of numerics that hysteresis survives in the limit of infinite systems, the size of the hysteresis loop evaluated numerically does appear to saturate to a finite value at large system sizes, indicating that the MF approximation may indeed capture the correct finite-dimensional physics.

5 Relationship to Other Models and to Experiments

Other models of driven systems with inertial-type couplings have been proposed in the literature. It is useful to discuss in some detail their relationship to the viscoelastic model considered here.

In the context of charge density waves, Littlewood [15] and Levy and collaborators [16, 17] modified the Fukuyama-Lee-Rice model [4] that describes the phase of the CDW electrons as an overdamped elastic manifold driven through quenched disorder by incorporating the coupling of the CDW

electrons to normal carriers. This was realized via a global coupling in the equation of motion for the phase to the mean velocity of the CDW, not unlike what obtained by a mean-field approximation of our viscous coupling. The model was argued to account for the switching and non-switching behavior observed in experiments.

Schwarz and Fisher [19, 25] recently considered a model of crack propagation in heterogeneous solids that incorporates stress overshoot, that is the fact that a moving segment of the crack can sometimes overshoot one or more potential static configurations before settling in a new one, inducing motion of neighboring segments. These effects may arise from elastic waves that can carry stress from one region to another of the driven medium. Stress overshoots, just like topological defects in a driven disordered lattice, have an effect similar to that of local inertia and were modeled by Fisher and Schwarz by adding couplings to gradients in the local crack velocity in the equation of motion for a driven elastic crack. These authors considered an automaton model where time is discrete. It is straightforward to define an automaton version of our VE model, where both the displacement u_i and time are discrete, as shown in [26]. It is then apparent that the automaton version of the viscoelastic model given in [26] is identical in its dynamics to the model of crack propagation with stress overshoot studied by Schwarz and Fisher, provided the strength M of the stress overshoot is identified with the combination $\eta/(1 + \eta)$. The two models differ in the type of pinning considered as the random force used in by Schwarz and Fisher is not periodic. We find, however, that the two models have identical mean-field behavior, with a mean-field tricritical point separating continuous from hysteretic dynamical transitions. The connection between the viscoelastic and the stress-overshoot model is important because it stresses that distinct physical mechanisms (inertia, nonlocal stress propagation, unbound topological defects) at play in different physical systems can be described generically by a coarse-grained model that includes a coupling to local velocities of the driven manifold. Finally, in a very recent paper, Maimon and Schwarz suggested that out of equilibrium a new type of generic hysteresis is possible even when the phase transition remains continuous [51]. Driven models with both elastic and dissipative velocity couplings may therefore belong to a novel universality class that exhibits features of both first and second order equilibrium phase transitions. They clearly deserve further study.

We now turn briefly to simulations and experiments. For comparison with experiments it is useful to point out that the tricritical point of the viscoelastic model can also be obtained by tuning the applied force and the disorder strength, rather than the applied force and the viscosity. Since the phase diagram does not depend on the form of the disorder distribution, $\rho(h)$, we choose for convenience a sharp distribution, $\rho(h) = \delta(h - h_0)$. The phase diagram in the (F, h_0) plane is shown in Fig. 6. For weak disorder the depinning is continuous, while for strong disorder it becomes hysteretic, with a region

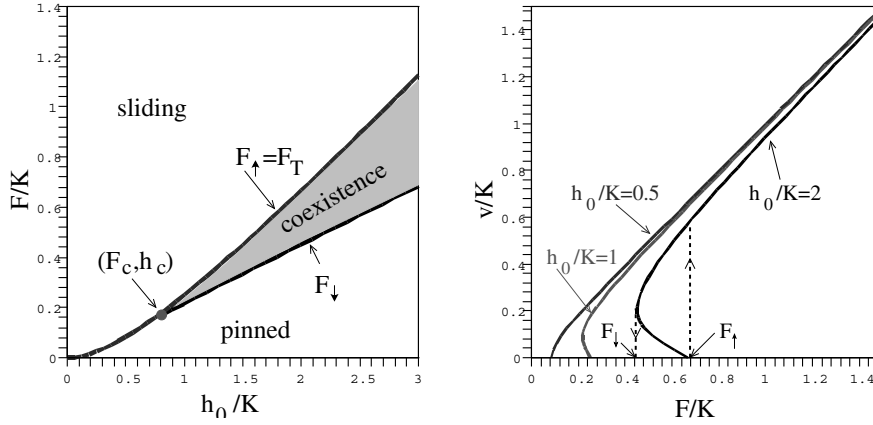


Fig. 6. Mean-field solution of the VE model with a piecewise parabolic pinning potential, $\rho(h) = \delta(h - h_0)$ and $\eta = 5$. *Left frame:* phase diagram. *Right frame:* velocity versus drive for $h_0/K = 0.5$, $h_0/K = 1$ and $h_0/K = 2$. Also shown for $h_0/K = 2$ are the discontinuous hysteretic jumps of the velocity obtained when F is ramped up and down adiabatically

of coexistence of pinned and moving degrees of freedom. The *tricritical point* is at $(h_c, F_c = F_T)$, with $h_c = K/(\sqrt{1 + \eta} - 1)$.

Simulations of two-dimensional driven vortex lattices clearly show a crossover as a function of disorder strength from an elastic regime to a regime where the dynamics near depinning is spatially inhomogeneous and plastic, with coexistence of pinned and moving degrees of freedom [39, 40, 52, 53]. In fact a bimodal distribution of local velocity was identified in [40] as the signature of plastic depinning. This local plasticity does not, however, lead to hysteresis in the macroscopic dc response in two dimension: the mean velocity remains continuous and single-valued, although it acquires a characteristic concave-up ward form near depinning that cannot be described by the exponent $\beta < 1$ predicted by elastic models in all dimensions. Hysteresis is, however, observed in simulations of three-dimensional layered vortex arrays where the couplings across layers are weaker than the in-layer ones [50]. In this case the phase diagram is qualitatively similar to that obtained for the viscoelastic model.

Recent experiments in $NbSe_2$ have argued that memory effects originally attributed in this system to “plasticity” of the driven vortex lattice [54] are actually due edge contamination effects [55–57]. In the experiments a metastable disordered vortex phase is injected in a stable ordered bulk vortex lattice. Memory effects may then arise in the macroscopic dynamics during the annealing of the injected disordered phase. Edge contamination does not, however, explain the plasticity seen in simulations, where periodic boundary conditions are used [40]. A possible scenario may be that while in

the experiments the vortex lattice in the bulk is always in the ordered phase, in the simulations the vortex lattice in the bulk of the sample may be strongly disordered even in the absence of drive. Such a disordered vortex lattice would then naturally respond plastically to an external drive. Finally, it is worth mentioning one experimental situation where hysteresis of the type obtained in our model is indeed observed in the macroscopic response. This occurs in the context of charge density waves, driven by both a dc and an ac field. In this case the dc response exhibits mode-locking steps. The “depinning” from such mode-locked steps was found to be hysteretic [58].

Several colleagues and students have contributed to various aspects of this work: Alan Middleton, Bety Rodriguez-Milla, Karl Saunders, and Jen Schwarz. I am also grateful to Jan Meinke for help with some of the figures. The work was supported by the National Science Foundation via grants DMR-0305407 and DMR-0219292.

References

1. A. J. Liu and S. R. Nagel, *Nature* **391**: 21 (1998); A. J. Liu, this proceedings.
2. D. S. Fisher, *Phys. Rep.* **301**: 113 (1998); and references therein.
3. G. Blatter, M. V. Feigel'man, V. B. Geshkenbein, A. I. Larkin, and V. M. Vinokur, *Rev. Mod. Phys.* **66**: 1125 (1994).
4. G. Grüner, *Rev. Mod. Phys.* **60**: 1129 (1988).
5. T. Giamarchi and S. Bhattacharya, in *High Magnetic Fields: Applications to condensed matter physics and spectroscopy*, C. Berthier, L. P. Lâevy, and G. Martinez, eds., p. 314 (Springer-Verlag, 2002).
6. E. Y. Andrei, *Phys. Rev. Lett.* **60**: 2765 (1988).
7. R. Seshadri and R. M. Westervelt, *Phys. Rev. B* **46**: 5142 & 5150 (1992).
8. D. S. Fisher, *Phys. Rev. B* **31**, 1396 (1985).
9. T. Giamarchi and P. Le Doussal, *Phys. Rev. Lett.* **72**: 1530 (1994); *Phys. Rev. B* **52**: 1242 (1995).
10. O. Narayan and D. S. Fisher, *Phys. Rev. B* **46**: 11520 (1992).
11. F. Nori, *Science* **271**: 1373 (1996).
12. A. Tonomura, *Micron* **30**: 479 (1999).
13. A. M. Troyanovski, J. Aarts and P. H. Kes, *Nature* **399**: 665 (1999).
14. A. Maeda, et al., *Phys. Rev. B* **65**: 054506 (2002).
15. P. B. Littlewood, *Solid State Commun.* **65**: 1347 (1988).
16. J. Levy, M. S. Sherwin, F. F. Abraham, and K. Wiesenfeld, *Phys. Rev. Lett.* **68**: 2968 (1992).
17. A. Montakhab, J. M. Carlson, and J. Levy, *Phys. Rev. B* **50**: 11227 (1994).
18. M. C. Marchetti, A. A. Middleton, and T. Prellberg, *Phys. Rev. Lett.* **85**: 1104 (2000).
19. J. M. Schwarz and D. S. Fisher, *Phys. Rev. Lett.* **87**: 096107 (2001).
20. M. C. Marchetti, A. A. Middleton, K. Saunders, and J. M. Schwarz, *Phys. Rev. Lett.* **91**: 107002 (2003).

21. S. H. Strogatz, C. M. Marcus, R. M. Westervelt, and R. E. Mirollo, *Phys. Rev. Lett.* **61**: 2380 (1988); *Physica D* **36**: 23 (1989).
22. V. M. Vinokur and T. Nattermann, *Phys. Rev. Lett.* **79**: 3471 (1997).
23. K. Saunders, J. M. Schwarz, M. C. Marchetti, and A. A. Middleton, *Phys. Rev. B* **69**: 37422 (2004).
24. M. C. Marchetti and K. A. Dahmen, *Phys. Rev. B* **66**: 214201 (2002).
25. J. M. Schwarz and D. S. Fisher, *Phys. Rev. E* **67**: 21603 (2003).
26. M. C. Marchetti, *Pramana*, **64**: 1097 (2005).
27. B. E. Rodriguez-Milla, M. C. Marchetti and A.A. Middleton, unpublished.
28. S. Zapperi, J. S. Andrade, Jr. and J. M. Filho, *Phys. Rev. B* **61**, 14791 (2000).
29. L. Balents, M. C. Marchetti and L. Radzihovsky, *Phys. Rev. B* **57**: 7705 (1998).
30. S. Scheidl, and V. M. Vinokur, *Phys. Rev. E* **57**: 2574 (1998).
31. T. Giamarchi and P. Le Doussal, *Phys. Rev. B* **57**: 11356 (1998).
32. Equation (11) should include a convective derivative that arises from the transformation to the laboratory frame [29]. This is negligible near a continuous depinning transition where the mean velocity is very small and it drops out in the mean field limit considered here. It will therefore be neglected, although it does play a crucial role on the dynamics well into the sliding state [29].
33. C. R. Myers and J. P. Sethna, *Phys. Rev. B* **47**: 11171 (1993).
34. A. A. Middleton, O. Biham, P. B. Littlewood, and P. Sibani: *Phys. Rev. Lett.* **68**, 1586 (1992).
35. A. A. Middleton, *Phys. Rev. Lett.* **68**: 670 (1992).
36. P. Le Doussal, K. J. Wiese, and P. Chauve, *Phys. Rev. E* **69**: 26112 (2004).
37. S. N. Coppersmith, *Phys. Rev. Lett.* **65**: 1044 (1990); *Phys. Rev. B* **44**: 2887 (1991).
38. S. N. Coppersmith and A. J. Millis, *Phys. Rev. B* **44**: 7799 (1991).
39. A.-C. Shi and A. J. Berlinsky, *Phys. Rev. Lett.* **67**: 1926 (1991).
40. M. C. Faleski, M. C. Marchetti and A. A. Middleton, *Phys. Rev. B* **54**: 12427 (1996).
41. L. Balents, M. C. Marchetti, and L. Radzihovsky, *Phys. Rev. Lett.* **78**: 751 (1997).
42. A. Zippelius, B. I. Halperin, and D. R. Nelson, *Phys. Rev. B* **22**: 2514 (1980).
43. See, for instance, D. R. Nelson in *Phase Transitions and Critical Phenomena*, C. Domb and J. Lebowitz eds. (Academic, London, 1983), Vol. 7, pp. 76–79.
44. M. C. Marchetti and K. Saunders, *Phys. Rev. B* **66**: 224113 (2002).
45. J. P. Boon and S. Yip, *Molecular Hydrodynamics* (McGraw-Hill, New York, 1980).
46. The strain-stress relation is nonlocal in both space and time. Only the nonlocality in time is retained here.
47. A. E. Koshelev and V. M. Vinokur, *Phys. Rev. Lett.* **73**, 3580 (1994).
48. K. Dahmen and J.P. Sethna, *Phys. Rev. Lett.* **71**: 3222 (1993); *Phys. Rev. B* **53**: 14872 (1996).
49. R. da Silveira and M. Kardar, *Phys. Rev. E* **59**: 1355 (1999).
50. C. J. Olson, C. Reichhardt and V. M. Vinokur, *Phys. Rev. B* **64**: 140502 (2001).
51. R. Maimon and J. M. Schwarz, *Phys. Rev. Lett.* **92**: 255502 (2004).
52. C. J. Olson, C. Reichhardt, and F. Nori, *Phys. Rev. Lett.* **81**: 3757 (1998).
53. N. Gronbech-Jensen, A. R. Bishop, and D. Dominguez, *Phys. Rev. Lett.* **76**: 2985 (1996).
54. S. Bhattacharya and M. J. Higgins, *Phys. Rev. Lett.* **70**: 2617 (1993); M. J. Higgins and S. Bhattacharya, *Physica C* **257**: 232 (1996).

55. Y. Paltiel, E. Zeldov, Y. N. Myasoedov, K. Shtrikman, S. Bhattacharya, M. J. Higgins, Z. L. Xiao, E. Andrei, P. L. Gammel, and D. J. Bishop, *Nature* **403**: 398 (2000).
56. Y. Paltiel, Y. Myasoedov, E. Zeldov, G. Jung, M.L. Rappaport, D. E. Feldman, M.J. Higgins, and S. Bhattacharya, *Phys. Rev. B* **66**: 60503 (2002).
57. M. Marchevsky, M. J. Higgins, and S. Bhattacharya, *Phys. Rev. Lett.* **88**: 87002 (2002).
58. M. J. Higgins, A. A. Middleton, and S. Bhattacharya *Phys. Rev. Lett.* **70**: 3784–3787 (1993).

Mixing, Ergodicity and the Fluctuation-Dissipation Theorem in Complex Systems

M.H. Vainstein, I.V.L. Costa, and F.A. Oliveira

Institute of Physics and International Center of Condensed Matter Physics,
University of Brasília, CP 04513, 70919-970, Brasília-DF, Brazil
fao@fis.unb.br

Complex systems such as glasses, gels, granular materials, and systems far from equilibrium exhibit violation of the ergodic hypothesis (EH) and of the fluctuation-dissipation theorem (FDT). Recent investigations in systems with memory [1] have established a hierarchical connection between mixing, the EH and the FDT. They have shown that a failure of the mixing condition (MC) will lead to the subsequent failures of the EH and of the FDT. Another important point is that such violations are not limited to complex systems: simple systems may also display this feature. Results from such systems are analytical and obviously easier to understand than those obtained in complex structures, where a large number of competing phenomena are present. In this work, we review some important requirements for the validity of the FDT and its connection with mixing, the EH and anomalous diffusion in one-dimensional systems. We show that when the FDT fails, an out-of-equilibrium system relaxes to an effective temperature different from that of the heat reservoir. This effective temperature is a signature of metastability found in many complex systems such as spin-glasses and granular materials.

1 Introduction

Since its formulation by Boltzmann [2], the EH has called the attention of mathematical physicists and chemists. In the last century, a branch of the mathematics dedicated to its study has been developed. However, most of its results are accessible only to the specialist. On the other hand, the FDT has played a central role [3,4] in nonequilibrium statistical mechanics in the linear response regime (NESML). It gained such importance that Kubo proposed a complete formulation of the NESML based on it [4]. Since the FDT is directly related to relaxation processes, its more empirical character has caught the attention of experimentalists and most of the discussion about its validity has remained in the hands of theoretical physicists and chemists, instead of mathematicians.

A necessary requirement for the validity of the FDT is that the time-dependent dynamical variables be well defined at equilibrium. The presence

of nonlinear effects or far from equilibrium dynamics may lead to situations where the FDT does not hold [1, 5], the aging process in spin-glass systems being a good example [6–11].

Most of experimental situations in which the EH and the FDT are violated happen in complex structures. Nevertheless, we show here simple situations where those violations appear. Their explicit condition and simplicity allows the judgment of non-specialists in the subject. This is important because it opens the possibility that more complex structures can be investigated on a solid basis.

This work is organized as follows: In this section, we shall define the EH, the MC, and other main concepts and ideas to be discussed throughout this work. In Sect. 2, we outline some historical achievements in the study of diffusion and introduce the FDT. We discuss reaction rates in Sect. 3, before introducing, in Sect. 4, the concept of memory, i.e., we discuss a system governed by a Generalized Langevin's Equation (GLE) and we show how to obtain anomalous diffusion. Next, we discuss random walks, fractional derivatives and their connection to the GLE in Sect. 5. We then continue by defining in a clear manner the noise in Sect. 6, and its connection with memory and correlation functions. After that, we discuss reversibility in Sect. 7. In Sect. 8, we discuss the main issue of this review, which is the interconnection between the MC, the EH, and the FDT, and we show under what conditions they fail. Examples of such violations are given in Sect. 9, where we study ballistic motion. In Sect. 10, we introduce some speculative topics on the forefront of physical research; the “skeptical reader” can skip it. Finally, we introduce a conjecture in Sect. 11 and conclude the paper in Sect. 12.

Let us start by considering the evolution of a dynamical stochastic variable $A(t)$ see Fig. 1. The variable could be either at equilibrium, Fig. 1(a), or approaching it, Fig. 1(b). The ensemble average $\langle G(A) \rangle$ of any function $G(A)$ is defined as

$$\langle G(A) \rangle = \int_{\Omega} \exp(-\beta E(A)) G(A) d\Omega, \quad (1)$$

where $\beta^{-1} = k_B T$ is the inverse temperature, $E(A)$ are the energies, and the integration is performed over all the accessible states of the phase space Ω . From that, it is possible to define a correlation function as

$$C_A(t) = \langle A(t)A(0) \rangle. \quad (2)$$

For an exponential decay of the correlation function, it is possible to associate a relaxation time τ , which is larger than the typical time for a fluctuation Δt . One can also define a time average as

$$\overline{A(t)} = \frac{1}{T} \int_{-T/2}^{T/2} A(t+t') dt' \quad (3)$$

For $\Delta t \ll T \ll \tau$, the average will produce the continuous line in Fig. 1, i.e., it will wash out the fluctuations which we measure with a sensitive probe.

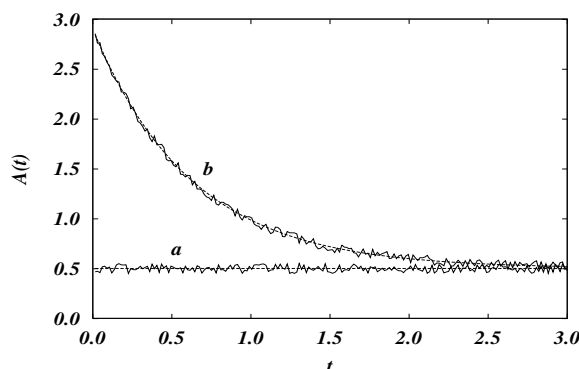


Fig. 1. Evolution of a dynamical stochastic variable

For times $T \gg \tau$, the EH reads

$$\overline{A(t)} = \langle A(t) \rangle . \quad (4)$$

In simple words: *given enough time, the system will reach every accessible state*, and a time average will be equal to an ensemble average. The proof of the EH has been the Holy Grail of statistical mechanics. One expects it will hold for macroscopic systems at equilibrium, Fig. 1(a), and for small deviations from equilibrium; on the other hand, it will not hold for curve (b), although it is expected that the system in situation (b) will be driven to equilibrium for longer times. However, a general proof of the EH is still missing. The concept of “far from equilibrium” is itself sometimes misleading, since it depends not only on the initial conditions, but also on the possible trajectories the system may follow [1, 12, 13]. The way a system approaches an equilibrium is crucial for these definitions.

The “mixing property of a physical system” or mixing condition (MC) can be stated as

$$\lim_{t \rightarrow \infty} R(t) = 0 , \quad (5)$$

where we have defined the normalized quantity $R(t) = C_A(t)/C_A(0)$. The MC tells us that after a long time $t \gg \tau$, we do not expect that $A(t)$ will remember its initial value $A(0)$.

2 Diffusion

Diffusion is one of the most fundamental mechanisms for transport of energy, mass and information; it is a main process for a system to reach uniformity and equilibrium, and has therefore been the focus of extensive research in many different disciplines of natural science. For almost two hundred years,

it has caught the attention of the scientific community. The famous observations by Robert Brown [14, 15] of the erratic trajectories of pollen opened a new world for experimental and theoretical studies in what was named Brownian motion. As a biologist, Brown first assumed he had discovered the basic essence of life, an idea to be expected from a man dedicated to biology. Nevertheless, he reproduced the experiments with non-organic material and observed the same erratic motion. Brown then concluded that this was due to the motion of matter. Considering his aim, the second conclusion is not only more difficult; it is a highly advanced and honest conclusion. Unfortunately, most books are unfair with Brown, in not mentioning his subsequent experiments.

At the centennial celebration of the Einstein miraculous year, one could be easily driven to the conclusion that most of the diffusive phenomena are well understood today. However, if we ask simple questions such as “How do spin waves diffuse in a Heisenberg system with correlated disorder?”, “How do electrons behave in an irregular lattice?”, or “How does a ratchet device work?”, it takes a short time to realize that these unanswered problems are related to diffusion.

For instance, when we flip a spin in the ground state of a ferromagnetic chain, the principle of equal a priori probability for the accessible states tells us that somehow the energy due to this disturbance will not remain localized in a single state. However, it does not say whether or not the system will support a spin wave, whether the wave propagates, and how it propagates in the affirmative case. To answer this kind of question, we usually need to go on into specific calculations. Our aim is to try to understand the general character of diffusion and, hopefully, to classify it prior to extensive calculations.

At the beginning of the twentieth century, much important research was dedicated to the irregular motion of microscopic particles dispersed in a fluid, namely Brownian motion. Despite being irregular, the motion reveals some regularity when analyzed statistically. The main observed quantity was the mean square displacement $\langle x^2(t) \rangle$ of the particles, which evolves linearly with time.

Einstein’s basic idea was to explain the Brownian motion by going beyond thermodynamics and into kinetic theory. He considered single spherical particles of mass m and radius a suspended in a liquid of viscosity η , and obtained [16]

$$\lim_{t \rightarrow \infty} \langle x^2(t) \rangle = 2Dt . \quad (6)$$

As usual, by infinite time, we mean a time larger than the maximum relaxation time of the process. The diffusion constant D was given by

$$D = \frac{RT}{6\pi N_a a \eta} = \frac{RT}{m N_a \gamma} = \frac{RT \mu}{N_a} , \quad (7)$$

where R is the gas constant, N_a the Avogadro number, μ the mobility, and γ the friction the particle feels in the fluid. The last equation is known as the Einstein relation [16]. However, considering that Sutherland [17] obtained it almost simultaneously [18], it would be fair to name it the Einstein-Sutherland relation.

Equation (6) was a major achievement; the linear relation with time was confirmed and an expression for the diffusion constant was obtained. The last form for D in (7) establishes a connection to the mobility, which is fundamental for the study of conductivity and transport. It was then possible to check the theory with the data available at the time. If one knows D , it is possible to make an estimation of the Avogadro number N_a . Future works helped establish the Boltzmann constant, $k_B = R/N_a$, as a new fundamental constant. Moreover, estimation of the size of sugar molecules dissolved in water became possible. Besides that, the frequency-dependent diffusion constant $\tilde{D}(\omega)$ can be directly associated with the conductivity by the relation [19, 20]

$$\tilde{\sigma}(\omega) = \frac{ne^2}{k_B T} \tilde{D}(\omega), \quad (8)$$

where e is the carrier charge and n the carrier density.

The series of Einstein articles about diffusion [16] together with the work of Smoluchowski [21] paved the way for the modern theory of Brownian motion.

The next step forward was taken by Langevin. In order to describe the motion of a particle immersed in a fluid, in 1908, Langevin [22] proposed the equation

$$m \frac{dv(t)}{dt} = -m\gamma v(t) + f(t). \quad (9)$$

where $f(t)$ is a stochastic force subject to the conditions $\langle f(t)v(0) \rangle = 0$, $\langle f(t) \rangle = 0$ and $\langle f(t)f(t') \rangle = A\delta(t-t')$. If we solve (9) and by using the equipartition theorem we impose $\langle v^2(t \rightarrow \infty) \rangle = k_B T/m$, we obtain the proportionality constant $A = 2mk_B T\gamma$ and write

$$\langle f(t)f(t') \rangle = 2mk_B T\gamma\delta(t-t'). \quad (10)$$

This last relation is known as the fluctuation-dissipation theorem (FDT). Although the Einstein-Sutherland diffusion constant contains implicitly the relation between fluctuation and dissipation, in Langevin's formulation, it acquires the importance of a basic theorem.

From (9) and the above conditions, one obtains the velocity-velocity correlation function

$$C_v(t) = \langle v(t+t')v(t') \rangle = (k_B T/m) \exp(-\gamma t). \quad (11)$$

The correlation function $C_v(t)$, or $R(t) = \exp(-\gamma t)$, will satisfy (5), the MC, with a relaxation time $\tau = \gamma^{-1}$. This exponential decay from the initial

conditions is the expected form for the MC. Now, it is possible to obtain the mean square displacement as

$$\langle x^2(t \gg \tau) \rangle = \int_0^t dt' \int_0^{t'} dt'' \langle v(t')v(t'') \rangle = 2Dt, \quad (12)$$

where, in the last step, we used the Kubo formula

$$D = \int_0^\infty C_v(t) dt. \quad (13)$$

The Kubo formula, together with (11), reproduces Einstein-Sutherland's results.

There are many reasons why one should always look back to Langevin's work, the first one being that it focuses attention on the motion of a particle, which is very intuitive for any physicist. Second, it combines the old Newtonian deterministic approach with the new "uncertainty" of the stochastic force $f(t)$. The breaking of the atomic forces in two parts: a fast changing force $f(t)$ with time scale Δt , and the slow friction force with time scale τ , introduces a large simplification which facilitates understanding and computer simulation. Consequently, the use of the Langevin equation, and of its generalization (Sect. 4), is still very active, having been applied successfully to the study of many different systems such as the dynamics of dipolar [23] and polymeric chains [24–28], metallic liquids [29], Lennard Jones liquids [30], diffusion in periodic potentials [31–33], ratchet devices [34, 35], and synchronization [36], only to name a few. Finally, it established explicitly for the first time the connection between fluctuation and dissipation, the FDT, which remains a major theorem of statistical mechanics.

The Langevin equation, however, presents some limitations: (a) It is a classical formalism; (b) It has uncorrelated noise with only two time scales Δt and τ , whereas a complex system has in general many time scales; (c) We cannot make any predictions for times shorter than Δt ; (d) It predicts only normal diffusion.

A quantum formulation of the FDT has been put forward by Callen and Welton [37]. Following their work, much research has been done in the field, with many attempts at generalization [6, 38]. We shall focus our attention on the Kubo FDT [4, 39–44], or the so-called second FDT, since it is more useful to the study of diffusion; see Sect. 4.

3 Reaction Rates

Diffusion may be considered the simplest problem of nonequilibrium statistical mechanics; however, if one considers a particle moving in an irregular media, it is quite probable that the particle will be affected by some potential and, in moving from point A to point C , will have to cross a potential barrier

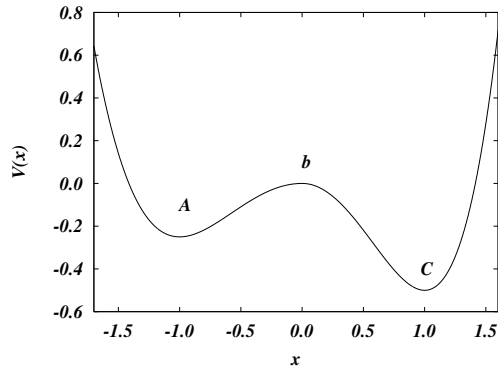


Fig. 2. Potential with two minima

at point b , see Fig. 2. This is one of the oldest problem in statistical mechanics and was first mentioned by Arrhenius [45]. Arrhenius proposed that the rate of particles crossing the potential barrier will be given by

$$k = \nu_0 \exp(-\beta E_b) , \quad (14)$$

where ν_0 is the attempt frequency and E_b is the barrier height. Arrhenius associated the attempt frequency to the vibration frequency at the well bottom.

The issue stood still until Kramers [46] re-addressed it with a more accurate analysis, in such way that the problem is known today as the Kramers problem. He gave an expression for the attempt frequency, which depends on the curvature at the top of the potential barrier and on the friction. The Kramers theory of reaction rates has many applications in biology, chemistry and physics.

Recent works [31–33] address the diffusion of particles in a periodic potential. They simulated the diffusion using Langevin's equation and used Kramers reaction rate to analyze the jumping between successive wells. A good agreement between theory and the simulation was obtained. This is a nice exhibition of the relation between transport processes and reaction rates.

For systems with memory a first attempt for a consistent reaction rate theory was given by Hänggi and Mojtabai [47]. In the 80's some interesting works appeared [48, 49]; for a review, see [50]. However, for some complex situations, such as polymer breaking [24–27] or long-range memory [51], it is possible to show that the reaction rate has an anomalous behavior. Another point is the dependence of the reaction process on the dimensionality of the system [52].

4 Complex Systems have Memory

If one asks “What makes a system complex?”, a few concepts will come to mind: a large number of degrees of freedom, nonlinearity and memory. However, if we ask for a definition of memory, only a few answers will be precise. We shall use here the concept of memory introduced by Mori in his seminal paper [53], where he used a method of projection operators which has many advantages: it allows the treatment of quantum systems, it is not empirical, it has time correlation, and it is a non-Markovian formulation with an explicit definition of memory.

Forty years after Mori’s work, many fundamental concepts and methods have been developed [3, 4, 53–60], which allowed a generalization of the Langevin formalism and the elimination of most of its limitations (see items (a) to (d) at the end of Sect. 2). The new formalism gives origin to a Generalized Langevin Equation (GLE) of the form

$$\frac{dA(t)}{dt} = - \int_0^t \Pi(t-t')A(t')dt' + F(t) , \quad (15)$$

where $F(t)$ is a stochastic noise subject to the conditions $\langle F(t) \rangle = 0$, $\langle F(t)A(0) \rangle = 0$ and

$$C_F(t) = \langle F(t)F(0) \rangle = \langle A^2 \rangle_{eq} \Pi(t) . \quad (16)$$

Equation (16) is the Kubo FDT [4, 39, 40], being a generalization of (10). The memory, $\Pi(t)$, arises here explicitly and, in principle, it allows us to study a large number of correlated processes. Notice that now many time scales are possible within $\Pi(t)$; this is a natural condition for complexity. An equation for $C_A(t)$, or for the renormalized correlation function $R(t)$ is given by

$$\frac{dR(t)}{dt} = - \int_0^t \Pi(t-t')R(t')dt' , \quad (17)$$

where we have used the conditions $\langle A(0)F(t) \rangle = 0$. The Laplace transform of this equation yields

$$\tilde{R}(z) = \frac{1}{z + \tilde{\Pi}(z)} . \quad (18)$$

From here on, we shall use the tilde to indicate Laplace transforms.

Let us now define the variable $y(t)$ as

$$y(t) = \int_0^t A(t')dt' , \quad (19)$$

with asymptotic behavior

$$\lim_{t \rightarrow \infty} \langle y^2(t) \rangle \sim t^\alpha . \quad (20)$$

For normal diffusion, $\alpha = 1$; we have subdiffusion for $\alpha < 1$, and superdiffusion for $\alpha > 1$. Notice that if $A(t)$ is the momentum of a particle, then $y(t)/m$ is its position.

It is very simple to show that this new formalism allows both normal and anomalous diffusion. Consider two examples: first, take

$$H(t) = 2\gamma\delta(t) . \quad (21)$$

With this short range memory, we return to the normal Langevin's equation, (9), and obtain $\alpha = 1$, i.e., normal diffusion. Second, consider an extremely long memory

$$H(t) = \omega_0^2 , \quad (22)$$

which gives a force of the form $-m\omega_0^2 y$, i.e., an harmonic oscillator which does not exhibit diffusion at all, $\alpha = 0$. Those are artificial but simple examples of how the memory determines diffusion.

Recently, Morgado et al. [61] obtained a general classification for anomalous diffusion. They considered that

$$\tilde{H}(z \rightarrow 0) \sim z^\nu , \quad (23)$$

with $\nu < 1$, and used the time-dependent diffusion function

$$D(t) = \int_0^t C_v(t') dt' , \quad (24)$$

$$\lim_{t \rightarrow \infty} D(t) = \lim_{z \rightarrow 0} z \tilde{D}(z) = \lim_{z \rightarrow 0} \tilde{H}^{-1}(z) = \lim_{t \rightarrow \infty} \frac{1}{\tilde{H}(1/t)} \quad (25)$$

to obtain, with $t \sim z^{-1}$,

$$\alpha = \nu + 1 . \quad (26)$$

Here, we have used the final value theorem [62], and (18). Note that the long range time behavior, i.e. the dynamics, is dominated by the small frequencies.

This result is fundamental for the classification of diffusion. Let us take the previous examples: first, $H(t) = 2\gamma\delta(t)$ with Laplace transform $\tilde{H}(z) = \gamma$; here $\nu = 0$, $\alpha = 1$, and the diffusion is normal as expected. Second, from (22), we get $\tilde{H}(z) = \omega_0^2/z$, $\nu = -1$, and $\alpha = 0$.

We are now in condition to discuss mixing. Consider a system governed by a GLE. The asymptotic behavior

$$\lim_{t \rightarrow \infty} H(t) = \lim_{z \rightarrow 0} z \tilde{H}(z) , \quad (27)$$

$$\lim_{t \rightarrow \infty} R(t) = \lim_{z \rightarrow 0} z \tilde{R}(z) = \lim_{z \rightarrow 0} \frac{z}{z + \tilde{H}(z)} , \quad (28)$$

and condition (23) show that mixing exists only for $-1 < \nu < 1$. In other words, the mixing condition is fulfilled between the limits of ballistic motion and harmonic oscillator motion. Close to the limits, one can expect problems.

Notice that for the memory given in (22), we have the exact solution

$$R(t) = \cos(\omega_0 t) , \quad (29)$$

which obviously does not fulfil the MC, (5). Notice also that if (13) converges, then it is always possible to have an associated “friction constant” γ , even for correlated systems

$$\gamma^{-1} = \int_0^\infty R(t) dt . \quad (30)$$

This definition can be plugged into the diffusion formula (7). This explains why normal diffusion is so widely found in nature, even for processes we clearly know are strongly correlated [61]. For a long time, the only evidence of anomalous diffusion had been for subdiffusion processes due to trapping mechanisms [19] and hierarchical lattices [63]. However, superdiffusive motion has recently been studied both theoretically [64,65] and experimentally [66–71] (see Sect. 9). We also expect that research in the new nanoclay technology will produce anomalous diffusion [72]. Recent works on chain dynamics [23, 26,73] show that the system dynamics may build up a memory. This “casual” result is explored in the conjecture described in Sect. 11.

5 Random Walk

The study of random walks is somehow older than statistical mechanics and it has produced many alternative ways to describe diffusive processes. Even before Einstein, the mathematical works of Bernoulli opened up the possibility of understanding fluctuations; for example one can arrive at (6) by considering the famous drunk man problem, a starting point in many undergraduate texts [74]. Besides that, the famous law of large numbers, or $N^{-1/2}$, for the relative standard deviation of a variable suggested that if atoms exist they must be very small, with N being very big, otherwise thermodynamics would not make sense. However, the basic expression for diffusion (7) was not obtained before 1905; it has the basic information one needs to know about the nature of the process. That is a main difference between mathematics and physics. In this sense, the Einstein-Sutherland diffusion constant was a stunning achievement. We shall call the attention to the famous Chandrasekhar review on stochastic process [75], which was an up-to-date article until the origin of the Mori formalism. It still remains as a clear and concise review.

By the end of the nineteenth century, the works of Lord Rayleigh [76] on random flights allowed to understand scattering in random directions, one of the most famous application of which was to explain the blue color of the sky, due to light scattering by impurities in the atmosphere. A modern

formulation shows the latter approach is incorrect and that light scattering is associated with fluctuations in the dielectric constant [77]. After the creation of the laser, light scattering became itself a large field of research. [78, 79]

Let us consider here a simple random walk analogy to Langevin's work. Consider a set of N_0 particles with initial velocities equal to zero. The particles are subject to a random force $\pm f_0$ at each time interval Δt with equal probability. After N time steps, the average velocity will be $\langle v(t) \rangle = 0$ and the average squared velocity

$$\langle v^2(t) \rangle = N f_0^2 \Delta t^2 / m^2 . \quad (31)$$

We can see from the previous expression that the kinetic energy grows linearly with time, $t = N\Delta t$, i.e., the random force acts as a pump of energy. Such a simple model does not represent a physical process, since it contradicts the kinetic theory, $\langle v^2(t \rightarrow \infty) \rangle = k_B T / m$. To make it more realistic, we add a dissipative force $-m\gamma v(t)$, and impose the balance of energy to obtain $f_0^2 = 2mk_B T \gamma / \Delta t$. Notice that if we define the Dirac delta function as the limit $\Delta t \rightarrow 0$ of $\delta(t) = 1/\Delta t$ for $-\Delta t/2 \leq t \leq \Delta t/2$, and 0, otherwise, we recover the FDT, (10). The FDT is nothing more than a detailed balance condition; it is a guarantee that the dispersed particles will reach thermal equilibrium after a reasonable time.

In the same way, there are alternative ways to describe anomalous diffusion besides the GLE. One proposal is to use the continuous random walk, which can be mathematically described by fractional derivatives [80–82]. The fractional derivative of a function $f(x, t)$ can be defined as

$${}_0 D_t^{1-\alpha} f(x, t) = \frac{1}{\Gamma(\alpha)} \frac{\partial}{\partial t} \int_0^t dt' \frac{f(x, t')}{(t-t')^{1-\alpha}} , \quad (32)$$

where $\Gamma(x)$ is the Gamma function. Equation (32) is a natural generalization of the derivative of a complex variable using the residue theorem. The nonlocal character of the fractional derivative is the same as that of the memory. Therefore, it is quite natural that they yield the same results as the GLE. Indeed, it is possible to obtain a fractional Fokker-Planck equation (FFPE) of the form

$$\frac{\partial f}{\partial t} = {}_0 D_t^{1-\alpha} \left[\frac{\partial}{\partial x} \frac{V'(x)}{m\eta_\alpha} + K_\alpha \frac{\partial^2}{\partial x^2} \right] f(x, t) , \quad (33)$$

to address the problem of subdiffusion [81] and to obtain a relation similar to (26).

The generalization for superdiffusion was recently discussed in a few articles ([82], and references therein). Fractional derivatives are a very compact way to obtain results; however, there are some points one should bear in mind.

First, we assume a priori a fractional geometry and as a result we obtain fractional diffusion; that appears to be a circular argument. From the GLE, that comes naturally from the memory, or from the noise; see (36).

Second, if $x(t)$ gives the time evolution for a particle position, we know precisely what ${}_0D_t^\mu x(t)$ means only for $\mu = 1, 2, \dots$. However, no one has an idea of what it means for $\mu = 0.51$, or for any non-integer value.

Finally, natural solutions for the fractional derivatives are the Lévy functions. Unfortunately, these yield an infinite mean square displacement, which is not a good physical result. The Lévy distributions, $\phi_\mu(x)$, are very popular because they fulfill the generalized central limit theorem (GCLT) [83]

$$\phi_\mu(x) = \int \phi_\mu(x - x')\phi_\mu(x')dx' . \quad (34)$$

Moreover, recently [84, 85], it has been shown that the GCLT represents the first uncorrelated term in a renormalization process. Correlations, such as those one expects to find in anomalous diffusion, will cause the deviation of the studied variables from the GCLT. Recently, Figueiredo et al. [86–89], have proposed some theorems on the limit sum of stochastic variables without making the classical assumptions of the GCLT. They developed a general formalism to explain the non-convergence (or the slow convergence) to the Gaussian distribution. With this, they have explained the origin of the self-similar property that appears in real economics time series data. They have also explained how autocorrelations (linear and nonlinear) can be considered as a source of truncated Lévy flights. The asymmetry they have found in their distributions are similar to those found in relaxation in supercooled liquids and in the height distributions in the etching of a crystalline solid [90–92]. The experiments of Monte et al. [93, 94] show both asymmetric and superdiffusive behavior.

6 Noise

A fundamental aspect of stochastic processes is the noise. A stochastic generalized force $F(t)$ can be decomposed into a set of harmonic oscillators of the form

$$F(t) = \langle A^2 \rangle_{eq}^{1/2} \int \rho(\omega)^{1/2} \cos(\omega t + \phi(\omega))d\omega \quad (35)$$

Here, $0 < \phi(\omega) < 2\pi$ is the random phase. From the FDT, it follows that

$$\Pi(t) = \int \rho(\omega) \cos(\omega t)d\omega , \quad (36)$$

where $\rho(\omega)$ is the noise density of states (NDS). Now, we take the Laplace transform of (36) to obtain

$$\gamma = \lim_{z \rightarrow 0} \tilde{\Pi}(z) = \frac{\pi}{2} \rho(0) . \quad (37)$$

This is another relevant result. The friction is equal to the noise density of states at the origin. This shows how the lower modes determine the type

of diffusion. A system which has a finite friction presents normal diffusion, since its NDS is finite at the origin. Subdiffusion will have an infinite friction and an infinite NDS. Finally, superdiffusion has a null friction. To obtain superdiffusion for a null friction is a very intuitive and appealing concept. A null NDS tells us that the lower modes do not relax and the process has “less interference”, or, in Langevin’s language, “weak collisions”.

Consider now the colored noise

$$\rho(\omega) = \begin{cases} \frac{2\gamma_0}{\pi} \left(\frac{\omega}{\omega_D}\right)^\beta & , \text{ if } \omega < \omega_D \\ 0 & , \text{ otherwise .} \end{cases} \quad (38)$$

Here, ω_D is a Debye cutoff frequency. This kind of noise has been used by Caldeira and Leggett in quantum dissipative systems [95]. If we plug this noise into (36), take its Laplace transform, and then the limit of small z , we obtain the exponent [96] from (23)

$$\nu = \begin{cases} \beta & , \text{ if } \beta < 1 \\ 1 & , \text{ otherwise .} \end{cases} \quad (39)$$

For most of the cases, the exponent of the NDS for low frequencies will be the same as that of the Laplace transform of the memory for small z . Equation (39) shows that $\alpha \leq 2$ and, consequently, the motion is limited by the ballistic motion. Ballistic motion appears to be a limit of this kind of GLE, see Sect. 8. Notice as well that for $\nu = 0$, we get $\gamma = \gamma_0$, from (37).

We shall consider here another possibility. Let the noise be

$$\rho(\omega) = \begin{cases} \frac{2\gamma_0}{\pi} & , \text{ if } \omega_1 < \omega < \omega_2 \\ 0 & , \text{ otherwise.} \end{cases} \quad (40)$$

For $\omega_1 = 0$, we have the Debye density of states for a thermal noise composed of acoustic phonons. Thus, for $\omega_1 = 0$ we have normal diffusion and for any $\omega_1 \neq 0$ we have superdiffusion. This NDS is the difference between two Ornstein-Uhlenbeck processes and is a simple way to produce ballistic diffusion [1, 61]. Since there is a window, $0 < \omega < \omega_1$, where there is no fluctuation of the modes, this introduces a very practical mechanism to control simulations. This kind of noise seems more appropriate to describe real ballistic propagation [97] than (38), see Sect. 9.

7 Reversibility and Correlation Functions

As early as 1876, Loschmidt called attention to the reversibility paradox [98]. His paradox states that all molecular processes must be reversible, since there is a symmetry between past and future $t \rightarrow -t$ in the laws of physics. Consequently, statistical mechanics must be reversible, in apparent contradiction

with thermodynamics, where certain processes are irreversible. At that time, reversible physics was composed of classical mechanics and electrodynamics. This paradox, together with the dynamical problems of Liouville, Zermello, and Poincaré are central in the work of Boltzmann. Those lead to the Boltzmann equation, to the H theorem [99], and to the studies of the Poincaré recurrence theorems.

Again, our aim here is not to go into extensive mathematical proof; rather we focus on the correlation function. In the definition of the correlation function we have used

$$R(t_1 - t_2) = \frac{\langle A(t_1)A(t_2) \rangle}{\langle A^2 \rangle} \quad (41)$$

and

$$R(-t) = R(t) . \quad (42)$$

The first relation relies on our basic knowledge of the temporal invariance of physical laws. However, if the evaluation is made far from equilibrium, the correlation function R may depend both on t_1 and t_2 , and not on their difference.

The second relation is time reversal, which can be easily understood for a classical variable where $A(t)$ and $A(0)$ commute. Given a string of values $A(t_i)$ $i = 1, 2, \dots, N_{int}$, for large N_{int} , one can obtain the relations given by (41) and (42). For quantum systems, the reader is recommended the review of Balucani et al. [100]

A great achievement in the discussion of time reversal symmetry for macroscopic systems was made by Onsager. He considered a solid subject to a general field E . In the linear regime, the field induces a generalized current density J of the form

$$J_i = \sigma_{i,k} E_k . \quad (43)$$

The susceptibility σ satisfies

$$\sigma_{i,k} = \mu_{i,k} \sigma_{k,i} . \quad (44)$$

Here, $\mu_{i,i} = 1$ for the diagonal terms. The off-diagonal terms are $\mu_{i,k} = 1$ for variables which do not change sign under time reversal, such as the electric field, and $\mu_{i,j} = -1$ for variables which do change, such as the magnetic field. Equation (44) is the Onsager reciprocal relation.

A natural generalization of susceptibility is the correlation function or the response function, sometimes called a Green function. Consider, for example, that one applies a perturbation $P(x_1)$ at the position x_1 and wants to know the disturbance $S(x_2)$ at x_2 . In the linear regime, we get

$$S_i(x_2) = \int G_{i,k}(x_2, x_1) P_k(x_1) dx_1 . \quad (45)$$

For systems with translational invariance, we expect that

$$G(x_1, x_2) = G(x_1 - x_2) . \quad (46)$$

When the translational invariance is broken, due to the existence of surfaces such as in a film [101,102], defects, or topological disorder [103], the response becomes a function of both variables x_1 and x_2 . However, Oliveira [101] has given a proof based on time reversal symmetry that

$$G_{i,k}(x_1, x_2) = \mu_{k,i} G_{k,i}(x_2, x_1) \quad (47)$$

The tensor $\mu_{i,j}$ here is the same as the one in (44), i.e., we lose the space invariance, but, on the other hand, we gain a useful space exchange symmetry. This result is general and has many applications. For example, it was used to explain certain asymmetries found in light scattering [101].

The usual Onsager reciprocal relations are actually limited to systems asymptotically close to equilibrium. For example, they apply at the level of the Navier-Stokes equations for a simple fluid, but fail for the higher-order corrections to those equations, as pointed out by McLeannan [104,105]. Dufty and Rubí [105] generalized McLeannan's work to nonequilibrium stationary states.

Many correlation functions of the form $\langle A(x_1, t_1)A(x_2, t_2) \rangle$ have properties similar to (46). Notice that even in nonlinear systems, sometimes it is possible to make some general statements. For example, in the growth process, the height of a surface $h(x, t)$ is a function of the position x and of the time t . The main studied quantity is the roughness [106], defined by the mean square fluctuation

$$\Delta h^2(x, t) = \langle (h(x, t) - \langle h(x, t) \rangle)^2 \rangle . \quad (48)$$

The roughness satisfies the scaling laws

$$b\Delta h^2(bx, b^z t) = \Delta h^2(x, t) . \quad (49)$$

where b is a number and z is the growth exponent. Notice that this relation holds only statistically. Many symmetries or scaling in the correlation function hold in situations where nothing can be said for a single process.

We now return to the correlation functions of the GLE. Note that the memory is an even function of t , independent of the NDS (see (36)). The analytical extension of the Laplace transform of an even function is an odd function, $\tilde{H}(-z) = -\tilde{H}(z)$. Consequently from (18), $\tilde{R}(-z) = -\tilde{R}(z)$, and, by a converse argument, $R(t)$ is an even function [96]. This is in agreement with the results by Lee for Hamiltonian systems [107]. Notice also that (17) requires the derivative of $R(t)$ to be null at the origin. Since both memory and $R(t)$ are even, they can be written as

$$H(t) = \sum_{n=0}^{\infty} b_n t^{2n} , \quad (50)$$

and

$$R(t) = \sum_{n=0}^{\infty} a_n t^{2n} . \quad (51)$$

Unfortunately, a large number of works has been presented in the literature where the correlation function does not satisfy these requirements. We shall not comment further on these works here: some may be useful approximations, others represent artificial solutions. The reader should be cautious in identifying them.

Exponentials, stretched exponentials, and power laws are examples of asymptotic behavior that can be obtained from more complex even functions [96], but obviously they do not fulfil (17).

Determination of the coefficients in (50) and (51) can be done for every specific noise. For short times, those equations yield $R(t) = \cos(\omega_0 t)$, where $\omega_0 = \sqrt{H(0)}$. For broadband noise, the asymptotic times yield exponential decay for normal diffusion. For anomalous diffusion, the behavior is of a stretched exponential followed by inverse power-law. For short band noise a very rich oscillatory behavior may be found [96].

A large and growing literature in which non-exponential behavior has been observed for correlation functions can be found in the following articles: in glasses and supercooled liquids [108], frustrated lattice gases [109], liquid crystals [110–112], plasmas [66], hydrated proteins [113], growth [114], disordered vortex lattice in superconductors [115], and in aging in dissipative systems [116].

8 Mixing, Ergodicity, and the Fluctuation-Dissipation Theorem

In this section, we arrive at the central point of this work by showing that the EH, (4), the MC, (5), and the second FDT, (16) are strongly connected in the GLE. Consequently, one could expect that the violation of one of these conditions could lead to the violation of the others. However, we will show that there is a hierarchy among the three concepts, in such a way that some may be violated, while others are not. Most of the systems that present violation of the FDT are complex, such as supercooled organic liquids, some algebraic maps, evolutionary models, and the eternal spin-glass problem. We try to show here a minimal condition for violation of that hierarchy.

We may expect from (15) and (16) that a system will be driven to an equilibrium state, i.e.

$$\lim_{t \rightarrow \infty} \overline{A^2(t)} = \langle A^2 \rangle_{eq} , \quad (52)$$

which can be identified with the EH. We shall see, however, that this is not always the case for superdiffusive dynamics.

Note that the Laplace transform of (15) suggests a solution of the form

$$A(t) = A(0)R(t) + \int_0^t R(t-t')F(t')dt', \quad (53)$$

where we have an ensemble of initial $A(0)$. Squaring (53) and taking the ensemble average, we obtain for the asymptotic behavior [1]

$$\langle A^2(t \rightarrow \infty) \rangle = \langle A^2 \rangle_{eq} + R^2(t \rightarrow \infty)[\langle A^2(0) \rangle - \langle A^2 \rangle_{eq}]. \quad (54)$$

This simple result leads to very important consequences. First, the system will reach full equilibrium only if the MC, (5), holds. Second, the EH holds if the MC holds. Finally, the FDT will hold only if the EH holds. Consequently, the FDT is the end validation of the sequence: Mixing \Rightarrow Ergodic Hypothesis \Rightarrow Fluctuation-Dissipation Theorem. Observe that if the MC is violated, then the final value of (54) will depend on the initial conditions. That is just the essence of the MC.

At this point, we shall call again the attention to Lee's work in ergodicity [58]. Unlike any other previous attempt at establishing the validity of the Boltzmann EH, his work approaches the time average directly and explicitly, which was made possible by his recurrence relation method [56]. Moreover, it has been demonstrated in several exact solvable models when the hypothesis is valid. When it is not valid, it is shown the reason why the hypothesis fails.

If the mean square value of A can be associated with a given temperature by the equipartition theorem, we have $\langle A^2(0) \rangle \sim T_0$ for the initial temperature, T for the reservoir temperature, and T_{eff} for the final effective temperature. Equation (54) becomes

$$T_{eff} = T + R^2(t \rightarrow \infty)[T_0 - T]. \quad (55)$$

From (28), we see that the MC is satisfied for $0 < \alpha < 2$. For the ballistic motion, $\lim_{z \rightarrow 0} \Pi(z) = az$, $\nu = 1$, $\alpha = 2$, and $R(t \rightarrow \infty) = (1+a)^{-1}$. This system never thermalizes to the reservoir temperature, unless it already starts at equilibrium. The system acquires an effective temperature different from that of the reservoir. This effective temperature is a signature of metastability found in glasses, where the FDT does not hold [1, 7–9, 13].

The first observation of such phenomena was reported by Kauzmann [7]. He noticed that when the entropy of a supercooled liquid is extrapolated below the glass temperature T_g , it can become smaller than the entropy of the crystalline solid. To avoid this paradox, he suggested the existence of an effective spinodal temperature T_{sp} in the supercooled liquid phase. Ricci-Tersenghi et al. [9] and Cavagna et al. [117] performed single-spin-flip Monte Carlo simulations in square lattices with frustration, in which they obtained effective temperatures $T_{eff} \neq T$. Methods for measuring those effective temperature [5, 10], and many attempts to get a form of FDT for inhomogeneous systems have been discussed in the literature [38, 118, 119].

It has been shown that a drastic elimination of the fast degrees of freedom in the dynamics of a system may lead to a violation of the fluctuation-dissipation theorem [120]. This is due to the fact that equilibration in the

coarsened description does not necessarily imply full equilibration of the system; therefore a fluctuation-dissipation relation, whose validity is limited to equilibrium or local equilibrium states [121–123], may not exist. The theorem is valid when there is a great disparity between slow and fast scales in such a way that faster scales relax practically immediately. This feature has been found in very different situations as in the diffusion of a Brownian particle in a shear flow [8, 27, 124], in the anomalous diffusion problem [1, 13, 61], in systems undergoing activated dynamics [125, 126], and in slow relaxation of supercooled colloidal systems [127]. This common scenario may suggest that the violation of the fluctuation-dissipation theorem could originate from the lack of ergodicity inherent to a coarsened description, which is related to the tacit reduction of the dimensionality of the system phase space.

9 Ballistic Motion

As discussed earlier in Sect. 4, most of the anomalous diffusion is subdiffusive, what can also be observed in most conductors [19]. However, very recently in the history of conductivity investigations, superdiffusive and even ballistic motion have been produced in laboratories. Indeed, we can find reliable reports on ballistic conductivity in carbon nanotubes [67, 70], in semiconductors [128], and in semiconductor superlattices with intentional correlated disorder [68, 69].

For a simple description of ballistic diffusion, we use (36) and (38) and obtain

$$\Pi(t) = \frac{2\gamma_0}{\pi} \left[\frac{\sin(\omega_2 t)}{t} - \frac{\sin(\omega_1 t)}{t} \right]. \quad (56)$$

The Laplace transform of (56) gives, as $z \rightarrow 0$, $\tilde{\Pi}(z) \sim z$. Consequently, $\nu = 1$ and $\alpha = 2$, which is the ballistic limit. If we set $\gamma_0 = \pi\omega_2/4$, the initial temperature $T_0 = 0$, in (55), we get the effective temperature as T_{eff} as

$$\lambda^* = \frac{T_{eff}}{T} = 1 - \left(\frac{2\omega_1}{\omega_1 + \omega_2} \right)^2. \quad (57)$$

Equation (57) has a control parameter ω_1 , which measures the “hole” in the density of states, and how far we are from the result predicted by the FDT.

Now, we examine the case when $A(t) = v(t)$, the particle’s velocity, so that we obtain $\langle v^2(t) \rangle = \langle v^2 \rangle_{eq} \lambda(t)$. We simulate the GLE for a set of 10000 particles starting at rest at the origin, using the memory in (56) with $\omega_2 = 0.5$ and different values of ω_1 . The results of these simulations are shown in Fig. 3, where we plot $\langle v^2(t) \rangle$. We used the normalization $\langle v^2 \rangle_{eq} = 1$, so that $\langle v^2(t) \rangle = \lambda(t)$. Notice that $\lambda(t)$ does not reach a stationary value; rather, it oscillates around a final average value λ_s . This value of λ_s should be compared with λ^* obtained from (57).

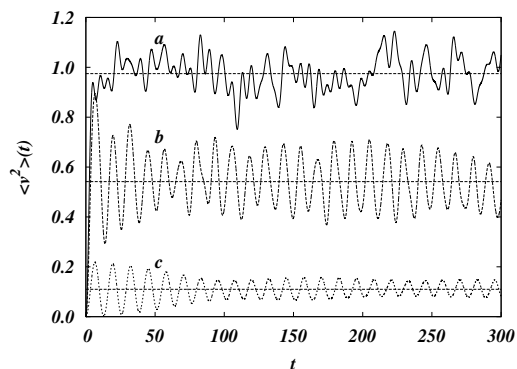


Fig. 3. Normalized mean square velocity as a function of time for the memory given by (56). Here $\beta = \omega_2/2$ and $\omega_2 = 0.5$. Each curve corresponds to a different value of ω_1 . (a) $\omega_1 = 0$; (b) $\omega_1 = 0.25$; (c) $\omega_1 = 0.45$. The *horizontal lines* correspond to the final average value λ_s . In agreement with the theoretical prediction, λ_s decreases as ω_1 grows

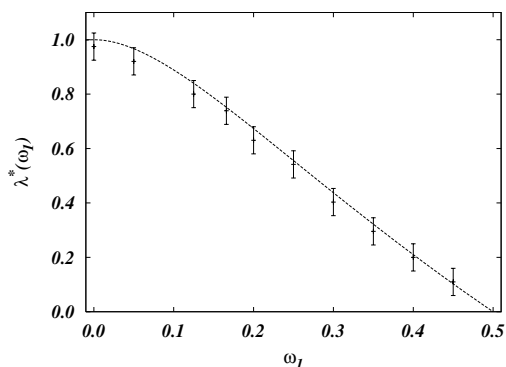


Fig. 4. λ^* as a function of the parameter w_1 . The line corresponds to the theoretical prediction given by (57). Each point corresponds to a value of λ_s obtained from simulations like those described in Fig. 3

In Fig. 4, we plot λ^* as a function of ω_1 as in (57) with a fixed value of $\omega_2 = 0.5$. We also plot the average values λ_s obtained from simulations for different values of ω_1 . Notice that as ω_1 increases, λ^* decreases as expected. The agreement between simulations and (57) shows that we can predict the average value λ_s , even when the FDT does not hold.

10 Shape of Things to Come

After the description of some “well-established physics”, we shall take this section to discuss some less conventional ideas about irreversibility, diffusion, fluctuations, and the approach to equilibrium.

Blasone et al. [129] have shown that a quantum harmonic oscillator can emerge from a couple of classical harmonic oscillators. Every classical oscillator will obey the laws of classical physics, however, together their behavior will follow quantum mechanics. Biró et al. [130], studying the quantization of classical fields, demonstrated that a classical system that operates in 5 dimensions can transmute into a quantum system in 4 dimensions.

In the same context, the method of Lie symmetry applied to differential equations has been often invoked as a mechanism to derive, not only solutions, but also classes of Fokker-Planck equations with non-trivial drift and diffusion terms [131–139]. The study of Lie-group representations in space-time has been recently developed, following similar procedures as those of field theories [140]. As a result, the usual Fokker-Planck equation has been derived from a $U(1)$ gauge invariant Lagrangian, and the generalization of such a formalism for the $SU(2)$ symmetry has provided a new class of Fokker-Planck dynamics, which is non-abelian gauge invariant. The drift and the diffusion terms, in this situation, are associated with a tensor metric in a Riemannian manifold. This manifold is based on a Galilean metric space-time, introduced (via the light-cone of a (4+1) Minkowski-like space) to derive the non-relativistic physics in a covariant fashion [141–143].

The apparent contradiction between the irreversibility of the macroscopic phenomena and the time-reversal symmetry of the fundamental laws has driven passionate discussion since Boltzmann times. This paradox of irreversibility, discussed in Sect. 7, finds its place both in classrooms and in highly specialized conferences. According to Zwanzig [54], there is no paradox. According to Chaves et al. [144], the paradox still remains as a problem far from being solved. Though some people believe that the only mystery related to irreversibility is the fact that the universe started in a very special initial state, the question is in fact much subtler and deep. The point is that the laws of quantum mechanics warrant that time evolution of an isolated system is described by a unitary operator that keeps constant the value of the entropy. The only escape from that fate could be quantum gravity, a theory still to be constructed. The point is that the gravitational interaction has infinite quantities that have not been renormalized. Thus, we cannot assure that the zero-point quantum fluctuations of the gravitational field – which in fact are fluctuations of space-time itself! – result only in the renormalization of the physically observed quantities.

Those fluctuations can in fact create a non-unitary contribution to the quantum mechanics evolution operator and thus be a fundamental source of irreversibility. Chaves et al. [144] suggested that this in fact occurs. On the basis of the quantum fluctuations of the metric tensor, they proposed an

extra term in the Schrödinger equation which makes time evolution operator non-unitary. Their calculations demonstrated that the coherence time of the microscopic system would be too long to be observed, but macroscopic systems would decohere very quickly. Acebal et al. [145] demonstrated that those metric fluctuations could also remove the infinities that plague quantum field theories.

These unconventional analyses may prove useful for other derivations. They require a deeper understanding of time and space in the field of statistical mechanics.

11 Spatio-temporal Conjecture for Disordered System

Up to now, we have discussed stochastic systems, i.e., systems with noise that we shall name *temporal disorder*. For those, given the NDS, $\rho(\omega)$, it is possible to obtain the memory and then, by using (26), the diffusive exponent α .

A second class of systems is composed by those which present *spatial disorder*. They have been thoroughly investigated in the last half century [146], nevertheless, some questions concerning localization or diffusion still remain open. Let us consider, as an example, the Heisenberg chain [147, 148]

$$H = - \sum_{l=1}^N J_l \mathbf{S}_l \cdot \mathbf{S}_{l+1} , \quad (58)$$

where $S = 1/2$. Here, J_l is the exchange integral at the site l . Equivalently, we could consider the disordered harmonic chain [149] or even the Anderson model [150].

Can we predict the properties of those systems in the same way we do for the GLE? The answer is partially yes, partially no. The conjecture [97], being valid, will help to answer those questions.

Consider a system which presents fluctuations in its energy density of states $D(E)$; let us call $\rho_F(E)$ the fluctuation density, then

$$\rho_F(E) = \rho(E) . \quad (59)$$

If this is true, then ρ_F can be introduced in (36) to obtain the diffusive exponent α . This is the spatio-temporal conjecture [97]. This conjecture has been verified for the quantum disordered Heisenberg chain [151] and is under consideration for many similar systems.

12 Conclusion

In this review we discussed some old and permanent problems of statistical mechanics. The way a system approaches equilibrium is connected with some

basic questions in physics such as the reversibility paradox, the mixing condition, the ergodic hypothesis and the fluctuation-dissipation theorem. We have drawn a line between them and, in particular, we have discussed the hierarchy $MC \Rightarrow EH \Rightarrow FDT$, established by Costa et al. [1].

We have approached the problem taking diffusion as a main phenomena in physics, since most processes are related with transport of matter, energy, or information. In this context, the validity of the FDT is exhibited for ballistic motion. Ballistic motion is presented here as the frontier between a stochastic process described by a GLE and other processes such as hydrodynamical ones.

We discussed relaxation processes and the conditions that the correlation functions must fulfill. We presented, in Sect. 10, discussions on the frontier of physics with particular consequence to statistical physics. We revive the reversibility paradox as an unclosed subject, as well as the MC, EH and FDT. We discussed a conjecture that, if valid, will make an important connection between stochastic and Hamiltonian descriptions.

Nonlinear dynamics is a field which deserves much attention; in particular, the coalescence of trajectories has been intensively studied in the last few years [152, 153]. There, the restriction of the degrees of freedom may confirm as well the hierarchy exposed here.

We have not focused deeper on real complex systems; we chose to follow easy-to-understand concepts where limits could be analytically obtained. This gave us a good framework for analyzing more complex structures.

We also tried to show that a given result may be obtained through many different formalisms. Feynman once said: “A physicist must know at least five different ways to obtain a result” [154]. If we consider the FPE, the FFPE, and the GLE as alternative approaches, we are close to fulfilling Feynman’s requirement. It is nice to know that those approaches agree in the main results; however, the full picture has not yet been drawn, particularly for anomalous diffusion.

Although anomalous diffusion remains as a surprising phenomenon, we hope that this work will help in the centennial effort to understand diffusion and the relation between fluctuation and dissipation. A generalization of the FDT to include nonlinearities and ballistic motion is necessary, what will require a deeper understanding of systems far from equilibrium.

Acknowledgements

One of us (FAO) would like to thank the hospitality and enlightening discussions with professors Alaor Chaves (Belo Horizonte), Alex Hansen (Trondheim), Fernando Moraes (João Pessoa), Howard Lee (Athenas-USA), João Florencio (Niterói), Jon Otto Fossum (Trondheim), Lech Longa (Krakow), Miguel Rubí (Barcelona), Nitant Kenkre (New Mexico), Robin Stinchcombe (Oxford), Sam Edwards (Cambridge), and Silvio Salinas (São Paulo). In Brasília, we would like to thank Ademir Santana, Adriano Batista, Annibal

Figueiredo, Geraldo Magela, Geraldo Silva, Hugo Nazareno, Rafael Morgado, and Sebastião Silva. This work was supported by CAPES, CNPq, FINEP, and FINATEC.

References

1. I. V. L. Costa, R. Morgado, M. V. B. T. Lima, and F. A. Oliveira. The Fluctuation-Dissipation Theorem fails for fast superdiffusion. *Europhys. Lett.*, 63:173, 2003.
2. L. Boltzmann. On the Development of the Methods of Theoretical Physics in Recent Times. In *Theoretical Physics and Philosophical Problems: Selected Writings*. Kluwer Academic Publishers, 1974.
3. R. Kubo. Fluctuation-Dissipation theorem. *Rep. Prog. Phys.*, 29:255, 1966.
4. R. Kubo, M. Toda, and N. Hashitsume. *Statistical Physics II*. Springer, Berlin, 1991.
5. L. Bellon, L. Buisson, M. Ciccotti, S. Ciliberto, and F. Douarche. Thermal noise properties of two aging materials. cond-mat/0501324, 2005.
6. G. Parisi. Off-Equilibrium Fluctuation-Dissipation Relation in Fragile Glasses. *Phys. Rev. Lett.*, 79:3660, 1997.
7. W. Kauzmann. The nature of the glassy state and the behavior of liquids at low temperatures. *Chem. Rev.*, 43:219, 1948.
8. I. Santamaría-Holek, D. Reguera, and J. M. Rubí. Diffusion in stationary flow from mesoscopic nonequilibrium thermodynamics. *Phys. Rev. E*, 63:051106, 2001.
9. F. Ricci-Tersenghi, D. A. Stariolo, and J. J. Arenzon. Two Time Scales and Violation of the Fluctuation-Dissipation Theorem in a Finite Dimensional Model for Structural Glasses. *Phys. Rev. Lett.*, 84:4473, 2000.
10. R. Exartier and L. Peliti. Measuring effective temperatures in out-of-equilibrium driven systems. *Eur. Phys. J. B*, 16:119, 2000.
11. T. S. Grigera and N. E. Israeloff. Observation of Fluctuation-Dissipation-Theorem Violations in a Structural Glass. *Phys. Rev. Lett.*, 83:5038, 1999.
12. J. D. Bao. Comment on “The Fluctuation-Dissipation Theorem fails for fast superdiffusion” by IVL Costa et al. *Europhys. Lett.*, 67:1050–1051, 2004.
13. I. V. L. Costa, R. Morgado, M. V. B. T. Lima, and F. A. Oliveira. Comment on “The Fluctuation-Dissipation Theorem fails for fast superdiffusion” - Reply. *Europhys. Lett.*, 67:1052, 2004.
14. R. Brown. A brief account of microscopical observations made in the months on june, july, and august, 1827, on the particles contained in the pollen of plants; and on the general existence of active molecules in organic and inorganic bodies. *Phil. Mag.*, 4:161, 1828.
15. R. Brown. *Ann. Phys. Chem. B*, 14:294, 1828.
16. A. Einstein. *Investigation on the theory of the Brownian Movement*. Dover, New York, 1956.
17. W. Sutherland. A dynamical theory of diffusion for non-electrolytes and the molecular mass of albumin. *Phil. Mag.*, 9:781–785, 1905.
18. A. Pais. *Subtle Is the Lord: The Science and the Life of Albert Einstein*. Oxford University Press University Press, Oxford, 1983.

19. J. C. Dyre and T. B. Schroder. Universality of AC conduction in disordered solids. *Rev. Mod. Phys.*, 72:873, 2000.
20. F. A. Oliveira, R. Morgado, A. Hansen, and J. M. Rubi. Superdiffusive conduction: Ac conductivity with correlated noise. *Physica A*, 357:115–121, 2005.
21. M. von Smoluchowski. Zur kinetischen Theorie der Brownschen Molekularbewegung und der Suspensionen. *Ann. Phys.*, 21:756, 1906.
22. P. Langevin. Sur la theorie du mouvement brownien. *Comptes Rendus*, 146:530, 1908.
23. R. Toussaint, G. Helgesen, and E. G. Flekkøy. Dynamic Roughening and Fluctuations of Dipolar Chains. *Phys. Rev. Lett.*, 93:108304, 2004.
24. F. A. Oliveira and P. L. Taylor. Breaking in polymer-chains .2. The Lennard-Jones chain. *J. Chem. Phys.*, 101:10118, 1994.
25. F. A. Oliveira and J. A. Gonzalez. Bond-stability criterion in chain dynamics. *Phys. Rev. B*, 54:3954, 1996.
26. F. A. Oliveira. Transition-state analysis for fracture nucleation in polymers: The Lennard-Jones chain. *Phys. Rev. B*, 57:10576, 1998.
27. A. M. Maroja, F. A. Oliveira, M. Ciesla, and L. Longa. Polymer fragmentation in extensional flow. *Phys. Rev. E*, 63:061801, 2001.
28. C. L. Dias, M. Dube, F. A. Oliveira, and M. Grant. Scaling in force spectroscopy of macromolecules. *Phys. Rev. E*, 72:011918, 2005.
29. A. Rahman, K. S. Singwi, and A. Sjölander. Stochastic model of a liquid and cold neutron scattering. ii. *Phys. Rev.*, 126:997, 1962.
30. R. M. Yulmetyev, A. V. Mokshin, and P. Hänggi. Diffusion time-scale invariance, randomization processes and memory effects in Lennard-Jones liquid. *Phys. Rev. E*, 68:051201, 2003.
31. J. M. Sancho, A. M. Lacasta, K. Lindenberg, I. M. Sokolov, and A. H. Romero. Diffusion on a Solid Surface: Anomalous is Normal. *Phys. Rev. Lett.*, 92:250601, 2004.
32. J. D. Bao and Y. Zhuo. Comment on “Diffusion on a solid surface: Anomalous is normal”. *Phys. Rev. Lett.*, 94:188901, 2005.
33. J. M. Sancho, A. M. Lacasta, K. Lindenberg, and A. H. Romero. Comment on “Diffusion on a solid surface: Anomalous is normal” - Reply. *Phys. Rev. Lett.*, 94:188902, 2005.
34. J. D. Bao and Y. Z. Zhuo. Ballistic diffusion induced by a thermal broadband noise. *Phys. Rev. Lett.*, 91:138104, 2003.
35. J. D. Bao. Transport in a flashing ratchet in the presence of anomalous diffusion. *Phys. Lett. A*, 314:203, 2003.
36. M. Ciesla, S. P. Dias, L. Longa, and F. A. Oliveira. Synchronization induced by Langevin dynamics. *Phys. Rev. E*, 63:065202(R), 2001.
37. H. B. Callen and T. A. Welton. Irreversibility and generalized noise. *Phys. Rev.*, 83:34, 1951.
38. V. V. Belyi. Fluctuation-dissipation-dispersion relation and quality factor for slow processes. *Phys. Rev. E*, 69:017104, 2004.
39. R. Kubo, M. Yokota, and S. Nakajima. Statistical-Mechanical Theory of Irreversible Processes .1. General Theory and Simple Applications to Magnetic and Conduction Problems. *J. Phys. Soc. Jpn.*, 12:570–586, 1957.
40. R. Kubo, M. Yokota, and S. Nakajima. Statistical-Mechanical Theory of Irreversible Processes .2. Response to Thermal Disturbance. *J. Phys. Soc. Jpn.*, 12:1203–1211, 1957.

41. P. Hänggi and H. Thomas. Stochastic processes: Time evolution, symmetries and linear response. *Phys. Rep.*, 88:207, 1982.
42. P. Hänggi and H. Thomas. Time evolution, correlations, and linear response of non-markov processes. *Z. Physik B*, 26:85, 1977.
43. P. Hänggi. Stochastic-processes .2. response theory and fluctuation theorems. *Helvetica Physica Acta*, 51:202, 1978.
44. G. N. Bochkov and Yu. E. Kuzovlev. Nonlinear fluctuation-dissipation relations and stochastic models in nonequilibrium thermodynamics : I. generalized fluctuation-dissipation theorem. *Physica A*, 106:443–479, 1981.
45. S. Arrhenius. Über die Reaktionsgeschwindigkeit bei der Inversion von Rohrzucker durch Säuren. *Zeit. Phys. Chem.*, 4:226, 1889.
46. H. A. Kramers. Brownian motion in a field of force and the diffusion model of chemical reactions. *Physica*, 7:284, 1940.
47. P. Hänggi and F. Mojitabai. Thermally activated escape rate in presence of long-time memory. *Phys. Rev. A*, 26:1168, 1982.
48. R. F. Grote and J. T. Hynes. The stable states picture of chemical-reactions .2. Rate constants for condensed and gas-phase reaction models. *J. Chem. Phys.*, 73:2715, 1980.
49. E. Pollak, S. C. Tucker, and B. J. Berne. Variational transition state theory for reaction-rates in dissipative systems. *Phys. Rev. Lett.*, 65:1399, 1990.
50. P. Hänggi, P. Talkner, and M. Borkovec. Reaction-rate theory - 50 years after Kramers. *Rev. Mod. Phys.*, 62:251, 1990.
51. F. A. Oliveira. Reaction rate theory for non-Markovian systems. *Physica A*, 257:128, 1998.
52. J. A. Gonzalez and F. A. Oliveira. Nucleation theory, the escaping processes, and nonlinear stability. *Phys. Rev. B*, 59:6100, 1999.
53. H. Mori. Transport, Collective Motion, and Brownian Motion. *Prog. Theor. Phys.*, 33:423, 1965.
54. R. Zwanzig. *Nonequilibrium Statistical Mechanics*. Oxford University Press, New York, 2001.
55. D. J. Evans and G. P. Morris. *Statistical Mechanics of Nonequilibrium Liquids*. Academic Press, London, 1990.
56. M. H. Lee. Derivation of the generalized Langevin equation by a method of recurrence relations. *J. Math. Phys.*, 24:2512, 1983.
57. M. H. Lee. Fick's Law, Green-Kubo Formula, and Heisenberg's Equation of Motion. *Phys. Rev. Lett.*, 85:2422, 2000.
58. M. H. Lee. Ergodic Theory, Infinite Products, and Long Time Behavior in Hermitian Models. *Phys. Rev. Lett.*, 87:250601, 2001.
59. R. A. Marcus. Theory of oxidation-reduction reactions involving electron transfer .4. A statistical-mechanical basis for treating contributions from solvent, ligands, and inert salt. *Discuss. Faraday Soc.*, 29:21, 1960.
60. S. Nakajima. On quantum theory of transport phenomena steady diffusion. *Prog. Theor. Phys.*, 20:948, 1958.
61. R. Morgado, F. A. Oliveira, G. G. Batrouni, and A. Hansen. Relation between Anomalous and Normal Diffusion in Systems with Memory. *Phys. Rev. Lett.*, 89:100601, 2002.
62. M. R. Spiegel. *Theory and Problems of Laplace Transforms*. McGraw-Hill, New York, 1965.
63. S. Alexander and R. Orbach. Density of states on fractals - fractons. *J. Phys. (france) Lett.*, 43:L625, 1982.

64. E. Baskin and A. Iomin. Superdiffusion on a Comb Structure. *Phys. Rev. Lett.*, 93:120603, 2004.
65. A. A. Budini and M. Caceres. Functional characterization of generalized Langevin equations. *J. Phys. A: Math. Gen.*, 37:5959–5981, 2004.
66. J. L. Ferreira, G. O. Ludwig, and A. Montes. Experimental investigations of ion-acoustic double-layers in the electron flow across multidipole magnetic fields. *Plasma Phys. Controlled Fusion*, 33:297–311, 1991.
67. S. Frank, P. Poncharal, Z. L. Wang, and W. A. de Heer. Carbon nanotube quantum resistors. *Science*, 280:1744, 1998.
68. V. Bellani, E. Diez, R. Hey, L. Toni, L. Tarricone, G. B. Parravicini, F. Domínguez-Adame, and R. Gómez-Alcalá. Experimental Evidence of Delocalized States in Random Dimer Superlattices. *Phys. Rev. Lett.*, 82:2159, 1999.
69. V. Bellani, E. Diez, A. Parisini, L. Tarricone, R. Hey, G. B. Parravicini, and F. Domínguez-Adame. Experimental evidence of delocalization in correlated disorder superlattices. *Physica E*, 7:823, 2000.
70. P. Poncharal, C. Berger, Y. Yi, Z. L. Wang, and W. A. de Heer. Room temperature ballistic conduction in carbon nanotubes. *J. Phys. Chem. B*, 106:12104, 2002.
71. A. F. G. Monte, S. W. da Silva, J. M. R. Cruz, P. C. Morais, and A. S. Chaves. Asymmetric carrier transport in InGaAs quantum wells and wires grown on tilted InP substrates. *Physica E*, 17:169, 2003.
72. A. Bakk, J. O. Fossum, G. J. da Silva, H. M. Adland, A. Mikkelsen, and A. Elgsaeter. Viscosity and transient electric birefringence study of clay colloidal aggregation. *Phys. Rev. E*, 65:021407, 2002.
73. F. A. Oliveira. Dynamical renormalization of anharmonic lattices at the onset of fracture: Analytical results for scaling, noise, and memory. *Phys. Rev. B*, 52:1009, 1995.
74. S. R. A. Salinas. *Introduction to Statistical Physics*. Springer, 2001.
75. S. Chandrasekhar. Stochastic Problems in Physics and Astronomy. *Rev. Mod. Phys.*, 15:1–89, 1943.
76. L. Rayleigh. *Scientific papers of Lord Rayleigh*. Dover, New York, 1964.
77. R. Loudon. *The Quantum Theory of Light*. Oxford University Press, New York, 2000.
78. A. Scalabrin, A. S. Chaves, D. S. Shin, and S. P. S. Porto. Temperature-dependence of A1 and E optical phonons in Batio3. *Phys. Status Solidi B*, 79:731–742, 1977.
79. D. L. Rousseau, R. P. Bauman, and S. P. S. Porto. Normal mode determination in crystals. *J Raman Spectrosc*, 10:253–290, 1981.
80. A. S. Chaves. A fractional diffusion equation to describe Lévy flights. *Phys. Lett. A*, 239:13, 1998.
81. R. Metzler and J. Klafter. The random walk’s guide to anomalous diffusion: a fractional dynamics approach. *Phys. Rep.*, 339:1, 2000.
82. R. Metzler and J. Klafter. The restaurant at the end of the random walk: recent developments in the description of anomalous transport by fractional dynamics. *J. Phys. A: Math. Gen.*, 37:161, 2004.
83. P. Lévy. *Théorie de l’Addition des Variables Aléatoires*. Guthier-Villars, Paris, 1954.
84. F. A. Oliveira, B. A. Mello, and I. M. Xavier. Scaling transformation of random walk distributions in a lattice. *Phys. Rev. E*, 61:7200, 2000.

85. F. A. Oliveira, J. A. Cordeiro, A. S. Chaves, B. A. Mello, and I. M. Xavier. Scaling transformation of random walk and generalized statistics. *Physica A*, 295:201, 2001.
86. A. Figueiredo, I. Gleria, R. Matsushita, and S. da Silva. On the origins of truncated Lévy flights. *Phys. Lett. A*, 315:51, 2003.
87. A. Figueiredo, I. Gleria, R. Matsushita, and S. da Silva. Autocorrelation as a source of truncated Lévy flights in foreign exchange rates. *Physica A*, 323:601, 2003.
88. A. Figueiredo, I. Gleria, R. Matsushita, and S. da Silva. Autocorrelation and the sum of stochastic variables. *Phys. Lett. A*, 326:166, 2004.
89. A. Figueiredo, I. Gleria, R. Matsushita, and S. da Silva. Lévy flights, auto-correlation, and slow convergence. *Physica A*, 337:369, 2004.
90. B. A. Mello, A. S. Chaves, and F. A. Oliveira. Discrete atomistic model to simulate etching of a crystalline solid. *Phys. Rev. E*, 63:041113, 2001.
91. F. D. A. A. Reis. Dynamic transition in etching with poisoning. *Phys. Rev. E.*, 68:041602, 2003.
92. F. D. A. A. Reis. Universality in two-dimensional Kardar-Parisi-Zhang growth. *Phys. Rev. E.*, 69:021610, 2004.
93. A. F. G. Monte, S. W. da Silva, J. M. R. Cruz, P. C. Morais, A. S. Chaves, and H. M. Cox. Symmetric and asymmetric fractal diffusion of electron-hole plasmas in semiconductor quantum wells. *Phys. Lett. A*, 268:430–435, 2000.
94. A. F. G. Monte, S. W. da Silva, J. M. R. Cruz, P. C. Morais, and A. S. Chaves. Experimental evidence of asymmetric carrier transport in InGaAs quantum wells and wires grown on tilted InP substrates. *Appl. Phys. Lett.*, 81:2460–2462, 2002.
95. A. O. Caldeira and A. J. Leggett. Quantum tunnelling in a dissipative system. *Ann. phys.*, 149:374–456, 1983.
96. M. H. Vainstein, I. V. L. Costa, R. Morgado, and F. A. Oliveira. Non-exponential relaxation for anomalous diffusion. to be published., 2006.
97. M. H. Vainstein, R. Morgado, and F. A. Oliveira. Spatio-temporal conjecture for diffusion. *Physica A*, 357:109–114, 2005.
98. J. Loschmidt. Über den Zustand des Wärmegleichgewichtes eines Systems von Körpern mit Rücksicht auf die Schwerkraft. *Wien. Ber.*, 73:139, 1876.
99. K. Huang. *Statistical Mechanics*. John Wiley & Sons, New York, 1987.
100. U. Balucani, M. H. Lee, and V. Tognetti. Dynamical Correlations. *Phys. Rep.*, 373:409, 2003.
101. F. A. Oliveira. Time-reversal symmetry in light scattering by excitations in a film. *Sol. Stat. Comm.*, 40:859–861, 1981.
102. F. A. Oliveira. How to build the Green-function for the elementary excitations in a film once we know those for a single interface. *Sol. Stat. Comm.*, 85:1051, 1993.
103. F. Moraes, A. M. de M. Carvalho, I. V. L. Costa, F. A. Oliveira, and C. Furtado. Topological interactions in spacetimes with thick line defects. *Phys. Rev. D*, 68:043512, 2003.
104. J. A. McLennan. Onsager's theorem and higher-order hydrodynamic equations. *Phys. Rev. A*, 10:1272–1276, 1974.
105. J. W. Dufty and J. M. Rubí. Generalized Onsager symmetry. *Phys. Rev. A*, 36:222–225, 1987.
106. A. L. Barabási and H. E. Stanley. *Fractal Concepts in Surface Growth*. Cambridge University Press, Cambridge, 1995.

107. M. H. Lee. Can the velocity autocorrelation function decay exponentially? *Phys. Rev. Lett.*, 51:1227–1230, 1983.
108. X. Xia and P. G. Wolynes. Microscopic Theory of Heterogeneity and Non-exponential Relaxations in Supercooled Liquids. *Phys. Rev. Lett.*, 86:5526, 2001.
109. M. H. Vainstein, D. A. Stariolo, and J. J. Arenzon. Heterogeneities in systems with quenched disorder. *J. Phys. A: Math. Gen.*, 36:10907–10919, 2003.
110. F. Benmouna, B. Peng, J. Gapinski, A. Patkowski, J. Ruhe, and D. Johannsmann. Dynamic light scattering from liquid crystal polymer brushes swollen in a nematic solvent. *Liq. Cryst.*, 28:1353, 2001.
111. M. B. L. Santos, E. A. Oliveira, and A. M. F. Neto. Rayleigh scattering of a new lyotropic nematic liquid crystal system: crossover of propagative and diffusive behavior. *Liq. Cryst.*, 27:1485, 2000.
112. P. Licinio and M. B. L. Santos. Pretransitional scaling close to a double critical point in a potassium laurate, 1-decanol, and heavy water lyotropic liquid crystal. *Phys. Rev. E.*, 65:031714, 2002.
113. M. Peyrard. Glass transition in protein hydration water. *Phys. Rev. E*, 64:011109, 2001.
114. F. Colaiori and M. A. Moore. Stretched exponential relaxation in the mode-coupling theory for the Kardar-Parisi-Zhang equation. *Phys. Rev. E*, 63:057103, 2001.
115. J. P. Bouchaud, M. Mézard, and J. S. Yedidia. Variational theory for disordered vortex lattices. *Phys. Rev. Lett.*, 67:3840, 1991.
116. A. Pérez-Madrid. A model for nonexponential behavior and aging in dissipative systems. *J. Chem. Phys.*, 122:214914, 2005.
117. A. Cavagna, I. Giardina, and T. S. Grigera. Glassy dynamics, metastability limit and crystal growth in a lattice spin model. *Europhys. Lett.*, 61:74, 2003.
118. V. V. Belyi. Fluctuation-dissipation dispersion relation for a Nonlocal Plasma. *Phys. Rev. Lett.*, 88:255001, 2002.
119. V. V. Belyi. Fluctuation-dissipation-dispersion relations for a time and space nonlocal Plasma. *Int. J. Quantum Chem.*, 98:183–190, 2004.
120. J. M. G. Vilar and J. M. Rubí. Thermodynamics “beyond” local equilibrium. *Proc. Nat. Acad. Sci.*, 98:11081–11084, 2001.
121. H. B. Callen and R. F. Greene. On a Theorem of Irreversible Thermodynamics. *Phys. Rev.*, 86:702, 1952.
122. R. F. Greene and H. B. Callen. On a Theorem of Irreversible Thermodynamics. II. *Phys. Rev.*, 88:1387, 1952.
123. S. R. deGroot and P. Mazur. *Non-Equilibrium Thermodynamics*. Dover, New York, 1984.
124. J. M. Rubí and D. Bedeaux. Brownian-motion in a fluid in elongational flow. *J. Stat. Phys.*, 53:125, 1988.
125. J. M. Rubí A. Pérez-Madrid, D. Reguera. Origin of the Violation of the Fluctuation-Dissipation Theorem in Systems with Activated Dynamics. *Physica A*, 329:357, 2003.
126. M. Naspredra, D. Reguera, A. Pérez-Madrid, and J. M. Rubí. Glassy dynamics: effective temperatures and intermencencies from a two-state model. *Physica A*, 351:14–21, 2005.
127. A. Perez-Madrid J. M. Rubí, I. Santamaría-Holek. Slow dynamics and local quasi-equilibrium - relaxation in supercooled colloidal systems. *J. Phys - Condens. mat.*, 16:2047, 2004.

128. B. B. Hu, E. A. de Souza, W. H. Knox, J. E. Cunningham, M. C. Nuss, A. V. Kuznetsov, and S. L. Chuang. Identifying the Distinct Phases of Carrier Transport in Semiconductors with 10 fs Resolution. *Phys. Rev. Lett.*, 74:1689–1692, 1995.
129. M. Blasone, P. Jizba, and G. Vitiello. Dissipation and quantization. *Phys. Lett. A*, 287:205–210, 2001.
130. T. S. Biró, S. G. Matinyan, and B. Müller. Chaotic quantization of classical gauge fields. *Found. Phys. Lett.*, 14:471–485, 2001.
131. M. Suzuki. New unified formulation of transient phenomena near the instability point on the basis of the Fokker-Planck equation. *Physica A*, 117:103, 1983.
132. I. An, S. Chen, and H. Guo. Search for the symmetry of the Fokker-Planck equation. *Physica A*, 128:520, 1984.
133. G. Cicogna and D. Vitali. Generalised symmetries of Fokker-Planck-type equations. *J. Phys. A: Math. Gen.*, 22:L453, 1989.
134. W. M. Shtelen and V. I. Stogny. Symmetry properties of one-dimensional and two-dimensional Fokker-Planck equations. *J. Phys. A: Math. Gen.*, 22:L539, 1989.
135. P. Rudra. Symmetry classes of the Fokker-Planck type equations. *J. Phys. A: Math. Gen.*, 22:L539, 1990.
136. G. Cicogna and D. Vitali. Classification of the extended symmetries of Fokker-Planck equations. *J. Phys. A: Math. Gen.*, 23:L85, 1990.
137. S. Spichak and V. Stognii. Symmetry classification and exact solution of the one-dimensional Fokker-Planck equations with arbitrary coefficients of drift and diffusion. *J. Phys. A: Math. Gen.*, 32:8341, 1999.
138. V. Cherkasenko. Galilei invariance of the Fokker-Planck equations with non-linearity. *Nonlinear Math. Phys.*, 2:416, 1995.
139. J. A. Cardeal, A. E. Santana, and T. M. Rocha. Symmetry and Classes of transport equations. *Physica A*, 308:292–300, 2002.
140. M. de Montigny, F. C. Khanna, and A. E. Santana. Gauge symmetry in Fokker-Planck dynamics. *Physica A*, 323:327, 2003.
141. C. Duval, G. Burdet, H. P. Künzle, and M. Perrin. Bargmann Structures and Newton-Cartan Theory. *Phys. Rev. D*, 31:1841–1853, 1985.
142. Y. Takahashi. Towards the Many-Body theory with the Galilei invariance as a guide I. *Fortschr. Phys.*, 36:63, 1988.
143. M. de Montigny, F. C. Khanna, and A. E. Santana. On Galilei-Covariant Lagrangian Models of fluids. *J. Phys. A: Math. Gen.*, 34:10921, 2001.
144. A. S. Chaves, J. M. Figueiredo, and M. C. Nemes. Metric fluctuations, thermodynamics, and classical physics - A proposed connection. *Ann. Phys.*, 231:174–184, 1994.
145. J. L. Acebal, A. S. Chaves, J. M. Figueiredo, A. L. Mota, and M. C. Menes. Statistical approach for quantum gravity fluctuations in QFT. *Phys. Lett. B*, 445:94, 1998.
146. P. W. Anderson. Absence of diffusion in certain random lattices. *Phys. Rev.*, 109:1492–1505, 1958.
147. S. N. Evangelou and D. E. Katsanos. Super-Diffusion in random chains with correlated disorder. *Phys Lett. A.*, 164:456–464, 1992.
148. F. A. B. F. de Moura, M. D. Coutinho-Filho, E. P. Raposo, and M. L. Lyra. Delocalization and spin-wave dynamics in ferromagnetic chains with long-range correlated random exchange. *Phys. Rev. B*, 66:014418, 2002.

149. F. A. B. F. de Moura, M. D. Coutinho-Filho, E. P. Raposo, and M. L. Lyra. Delocalization in harmonic chains with long-range correlated random masses. *Phys. Rev. B.*, 68:012202, 2003.
150. F. A. B. F. de Moura and M. L. Lyra. Delocalization in the 1D Anderson model with long-range correlated disorder. *Phys. Rev. Lett.*, 81:3735–3738, 1998.
151. M. H. Vainstein, R. Morgado, F. A. Oliveira, F. A. B. F. de Moura, and M. D. Coutinho-Filho. Stochastic description of the dynamics of the random-exchange Heisenberg chain. *Phys. Lett. A*, 339:33–38, 2003.
152. L. Longa, E. M. F. Curado, and F. A. Oliveira. Roundoff-induced coalescence of chaotic trajectories. *Phys. Rev. E*, 54:R2201, 1996.
153. S. Boccaletti, J. Kurths, G. Osipov, D. L. Valladares, and C. S. Zhou. The synchronization of chaotic systems. *Phys. Rep.*, 366:1–101, 2002.
154. R. P. Feynman. *The character of physical law*. The Random House Publishing Group, New York, 1994.

Jamming and Yielding of Dislocations: from Crystal Plasticity to Superconducting Vortex Flow

Stefano Zapperi¹, M. Carmen Miguel², Paolo Moretti³, and Micheal Zaiser³

¹ INFN UdR Roma 1 and SMC, Dipartimento di Fisica, Università “La Sapienza”, P.le A. Moro 2, 00185 Roma, Italy
zapperi@pil.phys.uniroma1.it

² Departament de Física Fonamental, Facultat de Física, Universitat de Barcelona, Diagonal 647, 08028, Barcelona, Spain

³ Center for Materials Science and Engineering, University of Edinburgh, King’s Buildings, Sanderson Building, Edinburgh EH93JL, UK

We discuss the statistical properties of interacting dislocations in plastically deformed crystals. Due to their long-range mutual interactions, dislocations arrange into jammed configurations, that can be set into motion under the action of an external stress. Disorder provides an additional source of pinning which we study by scaling theories, considering the case of parallel arrays of dislocations in a pileup or a low angle grain boundaries. As an application of these ideas, we discuss the plastic yielding of a vortex lattice in the Corbino disk and the growth of a vortex polycrystal in a field cooling experiment.

1 Introduction

Plastic deformation is a multi-scale problem of immense complexity. Relevant processes range from the atomistic scale where the atomic arrangement and defect properties of a material are of crucial importance for its deformation properties, up to the geological scale where deformation instabilities manifest themselves in the form of earthquakes, avalanches and so on.

In the past, the problem of plastic deformation has been addressed by two quite distinct communities, using different methods and distinct conceptual frameworks. The mechanics community has developed the powerful mathematical framework of continuum mechanics into a tool for handling complex deformation processes. Finite element modeling has become a standard method for describing deformation processes in engineering applications. Due to the very nature of the continuum framework, in the absence of ‘pathological’ cases (plastic instabilities) it is assumed that the state of the material can be characterized by smooth and differentiable displacement fields, and plastic deformation is envisaged as a smooth, quasi laminar flow process. The microscopic properties of materials are reflected by constitutive laws which serve as an input to the mathematical formalism. The plasticity view of the

materials science community, on the other hand, starts from the observation that, on the microscopic scale, plastic deformation is brought about by the generation, motion and interactions of discrete defects, in the case of crystalline materials: dislocations [1–4]. A huge amount of experimental and theoretical work has been devoted to modeling and understanding the properties of these defects and their links to the atomic structure. However, the crucial question how defect and microstructure properties link to the macroscopic constitutive equations of continuum mechanics has only recently been put into the focus of attention. Only too often it has been assumed that the transition from discrete defects and microstructural features to continuum mechanics can be accomplished by simple homogenization procedures – as soon as one is well above the scale of the relevant defects, straightforward averaging of their dynamics should lead to the smooth plastic flow envisaged by continuum mechanics.

A recent experiment has shown that plastic deformation in ice single crystals occurs in a jump-like, spatially heterogeneous and temporally intermittent manner not only on the scale of the individual dislocations whose motions are responsible for the deformation (where spatial heterogeneity and jump-like motions might be considered trivial) but also on scales where deformation jumps literally involve millions of these defects [5]. Hence plastic deformation results to be a complex process which cannot be understood without explicitly considering the collective dynamics of huge dislocation ensembles. The dynamics has scale-free features both in the spatial and temporal domain. This finding poses intriguing questions about the possibility of homogenization, and hence about the applicability of continuum descriptions in general. Of course there must be some scale above which averaging is feasible and continuum mechanics takes over – but what defines this scale? Only by combining concepts from mechanics, materials science, and complementing them with the conceptual tools provided by the statistical physics of complex systems we will be able to develop tools to a world where multiscale modeling and scale transition problems may become part and parcel of the everyday work of a design engineer.

The relevance of dislocations dynamics and fluctuations in materials plasticity goes beyond the conventional case of atomic crystals. A wide class of novel materials ranging from synthetic nanocrystals, magnetic colloids, charged particles in Coulomb crystals, proteins and surfactants, or vortices in type II superconductors and in Bose-Einstein condensates, form ordered self-assembled structures. The response of these structures to external forces of various kinds (optical, magnetic, mechanical) is of particular importance [6–8] and can in many cases be interpreted in terms of dislocation dynamics. A vast experimental and theoretical effort has been recently devoted to characterize the phase diagram of flux lines in type II superconductors [9–11]. Depending on the value of the temperature T , H , and sample preparation, magnetic vortices can either form a crystal [12], which at higher temperatures melts into

a liquid [13], or due to quenched disorder, they may exhibit more complex glassy phases [11]. Of special importance is the non-equilibrium response of vortex matter to the flow of an external current, since the dissipative motion of the vortices induces an undesirable macroscopic resistance. The moving phase can be as simple as the collective motion of an elastically deforming vortex crystal or more complex, such as in plastic vortex flow [14]. Clearly vortex lattice dislocations play an important role in this plastic flow phase and one can use similar concepts to describe crystal plasticity and superconducting vortex flow. In the following we present an overview of the statistical properties of interacting dislocations in both contexts.

2 Dislocations

2.1 Crystal Dislocations

Crystal dislocations are topological defects characterized by a Burgers vector \mathbf{b} [3]. While in a three dimensional crystal dislocations are deformable lines, one often treats them in the *rigid approximation*, obtaining an effective two dimensional particle model, which becomes exact for thin samples. Dislocations produce long-range stress and strain fields in the host crystal, and experience a Peach-Koehler force due to the overall local stress. This induces an interaction force between dislocations that depends on their character (edge or screw, when \mathbf{b} is perpendicular or parallel to the corresponding dislocation axis, respectively [3]), but that is generally long-range, decaying as $1/r$, and anisotropic. For instance, the force between two edge dislocations at a distance $\mathbf{r} = (x, y)$, and with Burgers vectors b_1 and b_2 in the x direction is given by

$$f_x(x, y) = \frac{\mu b_1 b_2}{2\pi(1-\nu)} \frac{x(x^2 - y^2)}{(x^2 + y^2)^2}, \quad (1)$$

where μ is the shear modulus, and ν is the Poisson ratio of the host crystal. We have only considered the x component since, differently from other particles, dislocations move mainly by gliding along preferential directions, namely the direction of the Burgers vector. This fact, together with the anisotropic character of the interaction, gives rise to metastable structures that act as geometric constraints for their own dynamics.

2.2 Vortex Lattice

Superconducting vortices can be schematized as interacting flexible lines. Nevertheless, as in the case of dislocations, one can consider flux-lines in the rigid approximation and obtain their mutual force from the London theory

$$\mathbf{f}(\mathbf{r}) = \Phi_0^2 / (8\pi^2 \lambda^3) K_1(|\mathbf{r}|/\lambda) \hat{\mathbf{r}}, \quad (2)$$

where Φ_0 is the quantized flux carried by the vortices, K_1 is a Bessel function and λ is the London penetration length [9, 10]. Notice that this is a short-range (since $K_1(x) \sim \exp(-x)$ for large x) repulsive central force, with a divergence of the form x^{-1} at short distances which is cut off by the vortex core.

As first discussed by Abrikosov, vortices due their mutual repulsion tend to form a crystal. A simplified but rather effective description of the vortex lattice is provided by its representation as an elastic crystal of flux lines. At large enough distances, the elastic energy of the vortex lattice can be expressed in terms of the vortex displacement field \mathbf{u} as follows

$$\mathcal{H} = \frac{1}{2} \int d^3r [c_{66}(\nabla\mathbf{u})^2 + (c_{11} - c_{66})(\nabla \cdot \mathbf{u})^2 + c_{44}(\partial_z\mathbf{u})^2] , \quad (3)$$

where c_{11} , c_{44} , c_{66} are the local elastic moduli, and the magnetic induction \mathbf{B} is parallel to the z direction. As in conventional atomic crystals one can characterize vortex lattice dislocations from the theory of elasticity. In particular, one can compute vortex dislocations mutual interactions as we discussed in Sect. 2.1.

3 Experimental Background

3.1 Acoustic Emission and Dislocation Avalanches

Experimentally, the complex character of collective dislocation dynamics can be revealed by acoustic emission (AE) measurements [5, 15]. The acoustic waves recorded in a piezoelectric transducer disclose the pulse-like changes of the local displacements undergoing in the material during plastic deformation, whereas a smooth plastic flow would not be detected. Thus this method is particularly useful to inspect possible fluctuations in the dislocation velocities and densities.

Ice single crystals can be considered as a model material to study glide dislocation dynamics due to the following reasons: (i) Transparency allows direct verification that AE activity is not related to microcracking. (ii) Within the range of temperature and stress corresponding to our experimental conditions, diffusional creep is not a significant mechanism of inelastic deformation which, in hexagonal ice single crystals, occurs essentially by dislocation glide on the basal planes along a preferred slip direction. (iii) An excellent coupling between sample and transducer can be obtained by fusion/freezing.

Uniaxial compression creep experiments were performed on artificial ice single crystals, employing several steps of constant applied stress. One observes an intense acoustic activity, exhibiting strong intermittent signal that can be analyzed using statistical methods. In particular, the probability distribution of energy burst intensities exhibits a power law behavior spanning

several decades [5]. The complex dislocation dynamics is reflected by a corresponding fractal geometrical patterning, which has been revealed by a triangulation analysis of the AE signals recorded from different transducers [16].

Multiscale properties and pattern formation are ubiquitous in plastic materials and we expect that the large dynamical fluctuations observed in ice single crystals are also a significant and rather prevalent feature of plastic deformation micromechanics. For instance, similar acoustic activity has also been recorded in ice polycrystals [17]. It is important to notice that a strongly fluctuating avalanche activity of the kind discussed in [5] is typically associated to more dramatic instabilities, such as fracture and earthquakes. The most remarkable feature of the present result is that it appears in plastic deformation, which is conventionally believed to be a smoother process.

3.2 Andrade Creep

At the beginning of last century, Andrade observed the creep deformation of soft metals at constant temperature and stress and reported that the global plastic strain γ grows in time according to a power law with exponent $1/3$, (i.e. $\gamma \sim t^{1/3}$) [18]. It was later shown in more generality that the creep deformation curve usually follows the relation $\gamma = \gamma_0 + \beta t^{1/3} + \kappa t$, where γ_0 is the instantaneous plastic strain, $\beta t^{1/3}$ is Andrade creep, and κt is referred to as linear creep [1, 2]. This behavior has subsequently been observed in many materials with different structures implying that this should be a process determined by quite general principles, independent of most material specific properties. In crystalline materials, the microscopic origin of this phenomenon lies in the dynamics of dislocations. Plastic flow only occurs when the externally applied stress overcomes a threshold value, the yield stress of the material, such that large-scale dislocation motion may take place. Despite various arguments proposed in the past literature [1, 2, 19–21], there is no general consensus on the basic mechanism to explain Andrade’s law. Mott [19] attributed the power law to an athermal cooperative process taking place close to the yield stress, but his idea was not worked out. Later explanations have always focused on thermally activated processes [20, 21].

3.3 Solid Solution Hardening

Solid solution hardening is the increase of the yield stress value when solute atoms are present in a crystal [22, 23]. The presence of solute atoms changes the local properties of the host material, resulting in a pinning force on nearby dislocations [22, 23]. This is not the only source of pinning, which can also be provided by particle inclusions or by immobile dislocations in other inactive slip systems. Several approximate calculations have been performed in the past to obtain the depinning stress from a statistical summation of individual pinning forces [1, 24–26]. In general terms, this problem falls in the class of

depinning transitions of elastic manifolds. We will discuss in Sect. 6 how the dislocation arrangements and the associated long-range stresses affect the process.

3.4 Plasticity in Vortex Matter

Transport experiments in superconductors provide an indirect measure of vortex dynamics, since vortex motion induces an electric field proportional to the vortex velocities. The interplay between the driving current and local pinning forces often results in a breakdown of the crystalline structure through the formation of dislocations. A clean example of plastic flow is observed in the Corbino disk geometry [27–30], where the current is applied at the disk center and flows radially towards the boundary. Vortices tend to move in concentric circles without crossing the sample boundaries. This inevitably produce shear stresses in the vortex lattice and as the current is raised one expect to observe yielding. López et al. [30] have evaluated the vortex velocity profiles measuring the voltage drop across a series of contacts placed radially on a $\text{YBa}_2\text{Cu}_3\text{O}_{7-\delta}$ disk. For low currents and temperatures all the vortices move as a rigid solid, giving rise to a linear velocity profile $v(r) = \omega r$. Above a threshold current I_0 , the vortex crystal cannot sustain the shear stress induced by the resulting inhomogeneous Lorentz force and the response becomes plastic. Vortex lattice dislocations are expected to play a relevant role in this process as confirmed by numerical simulations.

4 Jamming and Yielding in Crystal Plasticity

4.1 Two Dimensional Model of Interacting Dislocations

In order to investigate the creep behavior of a set of interacting dislocations we consider a two-dimensional model representing a cross section of a single-slip oriented crystal where N point-like edge dislocations glide in the xy plane along directions parallel to the x axis (the effect of the dislocation line tension will be discussed in Sect. 6). Dislocations with positive and negative Burgers vectors $\mathbf{b}_n = \pm b\hat{x}$ are assumed to be present in equal numbers, and the initial number of dislocations is the same in every realization. An edge dislocation with Burgers vector $b\hat{x}$ located at the origin gives rise to a force at a point $\mathbf{r} = (x, y)$ given by (1). We further assume an overdamped dynamics in which the dislocation velocities are linearly proportional to the local forces. Accordingly, the velocity of the n th dislocation along the glide direction, if an external shear stress σ is also applied, is given by

$$\frac{\chi_d^{-1} v_n}{b} = \sum_{m \neq n} f_x(\mathbf{r}_{nm}) + b_n \sigma, \quad (4)$$

where χ_d is the effective mobility of the dislocations and $\mathbf{r}_{nm} \equiv \mathbf{r}_n - \mathbf{r}_m$ the relative position vector of dislocations n and m . Periodic boundary conditions are imposed in the direction of motion (i.e. the x axis). In order to take correctly into account the long range nature of the elastic interactions, the stress has to be summed over an infinite number of images. When the distance between two dislocations is of the order of a few Burgers vectors, linear elasticity theory (i.e. (1)) breaks down. In these instances, phenomenological nonlinear reactions, such as the annihilation of a pair of dislocations, describe more accurately the real behavior of dislocations in a crystal. In our model, we *annihilate* a pair of dislocations with opposite Burgers vectors when the distance between them is shorter than a cutoff y_e [5,31]. In addition, we have included in the model dislocation multiplication introducing a pair creation rate r .

4.2 Dislocation Jamming and Andrade Creep

In [32], we studied the temporal relaxation of a simple dislocation dynamics model discussed above. We recovered Andrade creep law without invoking thermally activated processes, considering an ideal situation where thermal fluctuations are irrelevant for the process. The strain rate, which is proportional to the density of mobile dislocations $d\gamma/dt = \sum_i b_i v_i$ with v_i the velocity of each dislocation, decays as a power law with an exponent close to $2/3$ in agreement with Andrade's observations. At larger times, the strain-rate was observed to cross over to a linear creep regime (i.e. to a plateau signaling a steady rate of plastic deformation) whenever the applied stress is larger than a critical threshold σ_c , or, otherwise, to decay exponentially to zero (see Fig. 1).

These results suggest that a possible interpretation of dislocation motion and the corresponding creep laws of crystalline materials could also be found within the general "jamming" framework proposed to encompass a wide variety of non-equilibrium soft and glassy materials [33,34]. Most of these physical systems consist of various types of soft particles closely packed into an amorphous state. At such high concentrations, the relative motion of these particles is drastically constrained and, as a consequence, soft and concentrated materials usually respond like elastic solids upon the application of low stresses. One then says that the system is jammed, since it is unable to explore all the available configuration space. On the other hand, they flow like viscous fluids above the so-called yield stress value σ_y , exhibiting a common rheology. Recent light scattering experiments [35,36] allow, for instance, to detect the intermittent dynamics of a gel formed from attractive colloids suggesting that intermittent behavior seems to be a fundamental ingredient for the slow relaxation of jammed materials. Moreover, this unjamming transition can be induced by changing either the external stress applied, the density, or the temperature of the system. The analogies of dislocation motion and these so-called jammed systems are further explored by considering the

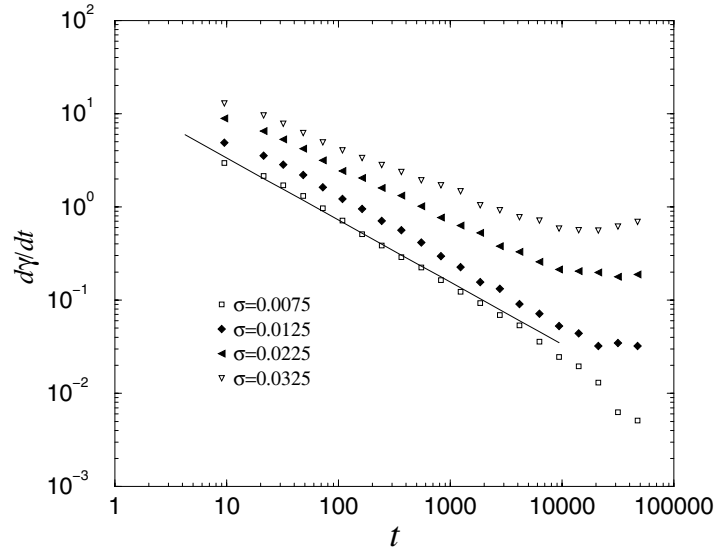


Fig. 1. The strain rate relaxation for different stress values. The system size is $L = 300b$ and the initial density of edge dislocations is around 1%. The solid line is the Andrade law $d\gamma/dt \sim t^{-2/3}$

influences of dislocation multiplication, and thermal-like fluctuations on the dynamics. Dislocation multiplication favors the rearrangements of the system and induces a linear creep regime (flowing phase) at lower stress values, but it does not affect the initial power-law creep. The introduction of a finite effective temperature T has a similar effect [32].

4.3 Dislocation Avalanches

While the average creep relaxation of the model is well described by the smooth Andrade law, the velocity signal is in general strongly fluctuating. In presence of a dislocation multiplication rate r , the model displays an intermittent steady-state characterized by dislocation avalanches with a power law distribution of energies that is in close agreement with the experiments [5]. Due to their complicated mutual interactions, dislocations are most of the time jammed into metastable configurations, formed by walls, dipoles, and far more complex dislocation structures. The formation of metastable configurations is responsible for the quiescent intervals in the acoustic activity, followed by bursty events that occur when the accumulated shear stress and/or the multiplication and annihilation processes may eventually favor the partial destruction and/or rearrangement of the dislocation structures. Thus the complex features of AE can be explained by the jamming of dislocations and their subsequent slip, giving rise to avalanche-like events.

5 Plastic Yielding in the Vortex Lattice

Transport experiments in the Corbino disk geometry indicate that the vortex lattice undergoes plastic yielding. This process can be studied by molecular dynamics (MD) simulations of interacting vortices [37]. One considers a set of N rigid vortices confined in a disk of radius D . The equation of motion for each vortex i at position \mathbf{r}_i

$$\Gamma \frac{d\mathbf{r}_i}{dt} = \sum_j \mathbf{f}_{vv}(\mathbf{r}_i - \mathbf{r}_j) + \mathbf{f}_L(\mathbf{r}_i), \quad (5)$$

where Γ is an effective viscosity for vortex flow. The first term on the right hand side of this equation follows from the fact that a pair of vortices interact with each other via a long-range force $\mathbf{f}_{vv}(\mathbf{r}) = AK_1(|\mathbf{r}|/\lambda)\hat{r}$, where $A = \Phi_0^2/(8\pi^2\lambda^3)$, λ is the London penetration length, and K_1 is a first order modified Bessel function. Distances are always measured in units of λ . The last term corresponds to the current induced Lorentz-like force acting on the vortices. The N vortices are confined inside the disk by the external magnetic field and the sample edge barrier, that we model by imposing an extra normal force on the vortices of the form $\mathbf{f}_B = -g \exp[-(D-r)/r_0]/r_0\hat{r}$, with $r_0 = 0.1\lambda$ and $g/A = 1$. The coupled (5) are integrated numerically with an adaptive step size fifth-order Runge-Kutta method. We do not truncate the range of the vortex-vortex interaction since this leads to spurious fluctuations caused by the force discontinuities. We study the response of the system as a function of the applied current for different values of N , ranging from $N = 332$ to $N = 2064$, and D ($D = 18\lambda, 36\lambda, 72\lambda$).

As in the experiments, for low currents we find a linear velocity profile that corresponds to the rigid rotation of the vortex lattice. Above a threshold current I_0 , the profile ceases to be linear, indicating the onset of plastic flow. For higher currents $I > I_1$, we observe that vortices end up moving in uncorrelated annular channels, displaying a laminar $1/r$ velocity profile.

To better identify the transitions in the system rheology, we measure the variations of the flow resistance $R \equiv \sum_i v_i/I$ with I . After an initial transient, the resistance reaches a steady state which fluctuates strongly in the plastic regime and is much smoother in the solid and laminar phases (see Fig. 2). As the current is increased, the steady-state resistance show a first sharp jump around I_0 corresponding to the breakdown of the linear velocity profile, and a smaller jump at I_1 indicating the onset of the hyperbolic profile. The final plateau scales with the number of moving vortices N . Indeed in this laminar regime, a scaling factor of N/D follows from a simple continuum approximation with a constant density of vortices.

The Delaunay triangulation of the vortex positions in the disk allow to characterize their topology. A pair of five-fold and seven-fold neighboring vortices identify an edge dislocation in the vortex lattice. For $I < I_0$, all vortices within the bulk of the disk are six-fold as in a perfect triangular

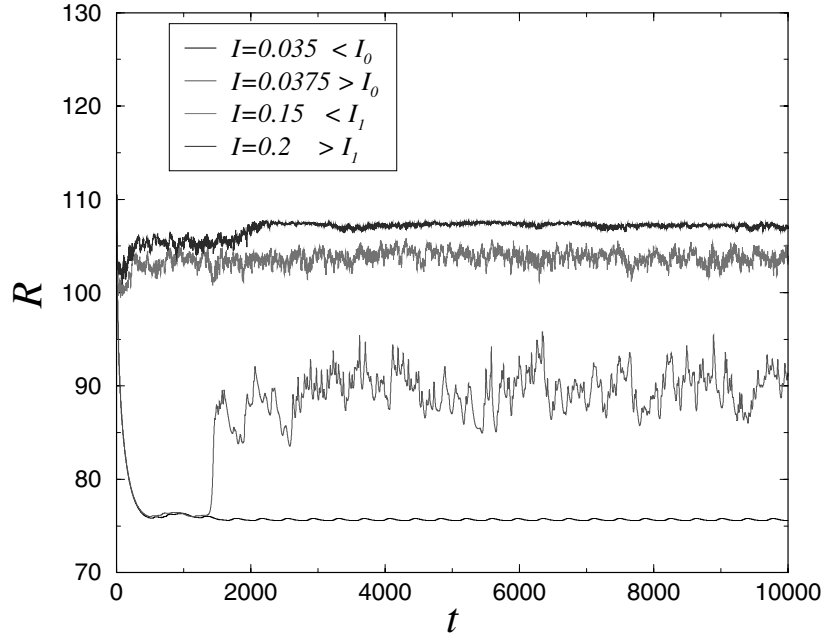


Fig. 2. The resistance noise observed in the Corbino disk for different values of the injected current I . The strongest noise is observed for $I \simeq I_0$

lattice, whereas a large number of five-fold and seven-fold coordinated vortices are only observed along the boundary. These are geometrically necessary dislocations and disclinations which need to be present in order to adjust a triangular lattice into a circular geometry. As the resistance, the number of five/seven-fold coordinated vortices reaches a fluctuating steady value after an initial transient. As the current overcomes I_0 , new dislocation pairs are nucleated, mainly within the highly strained central region. Typically we observe the reiterative formation of new dipoles that readily unbind and glide along the direction of their Burgers vector, in most cases towards the disk boundary. To accommodate the shear stress generated by the external current, the crystal should nucleate dislocations that are able to glide either radially or tangentially. Nevertheless, in the undistorted triangular lattice (or when the concentration of free dislocations is low), the dislocations that are nucleated are the most elementary (with Burgers vectors along the three basic crystalline directions), and only those with \mathbf{b} almost parallel to the radial direction can easily glide over long distances due to the Peach-Koehler forces involved.

6 Depinning of Dislocation Systems

6.1 Isolated Dislocations

A dislocation interacting with a pinning center such as a solute atom, a particle, or a forest dislocation, typically does not remain straight. Bending a dislocation has an energy cost, which can be used to balance the pinning energy due to the collective effect of a random collection of defects. In the simplest picture, the dislocation can be treated as an elastic string with a line tension Γ , but this can only be considered as an approximation for the long-range self-stress of the dislocation. As an illustration, consider a prevalently edge dislocation lying on the xy plane, with Burgers vector in the y direction, and denote by $(x(s), y(s), 0)$ its position as a function of the line coordinate s . The relevant component of the self-stress of the dislocation is given by

$$\sigma_{yz}(x_0, y_0) = \frac{\mu b}{4\pi} \int ds \left[\left(\frac{dy}{ds} \right) \frac{x_0 - x(s)}{(1-\nu)(r_0 - r(s))^3} - \left(\frac{dx}{ds} \right) \frac{y_0 - y(s)}{(r_0 - r(s))^3} \right]. \quad (6)$$

From this expression it is possible to compute the restoring force associated with a deformation of the dislocation and estimate the related line tension. (6) can be generalized to dislocations of any character and the result is reported in [38].

If we consider only small deformations of an edge dislocation in the xy plane with Burgers vector along y , the line can be parametrized by a single valued function $y = u(x)$. The restoring force on the deformed dislocation is given by

$$f_y(x) = \frac{\mu b^2}{4\pi} \int dx' \left[\left(\frac{du}{dx} \right) \frac{x - x'}{(1-\nu)|x' - x|^3} - \frac{u(x) - u(x')}{(x - x')^3} \right], \quad (7)$$

which is in the form of a linear interaction kernel of the type used in conventional models of the depinning transition. It is convenient to express the stress in Fourier space, and expand to lowest order in q

$$\tilde{f}_y(q) \propto q^2 \log(|q|a) \tilde{u}(q), \quad (8)$$

where a is a low scale cutoff, of the order of b . From this result, we see that the line tension approximation is correct up to a logarithmic factor and we can directly apply the critical exponents expected for the depinning transition of a linear interface [39–43]. In particular, the average dislocation velocity reaches a steady state value v , playing the role of the order parameter of the transition, that scales with the distance from the depinning stress σ_c as

$$v \sim (\sigma - \sigma_c)^\beta, \quad (9)$$

where β is a critical exponent and $v = 0$ for $\sigma < \sigma_c$. The roughness exponent ζ is usually defined from the displacement correlation function

$$\langle (u(x) - u(0))^2 \rangle \sim |x|^{2\zeta}. \quad (10)$$

The expected numerical values are $\beta \simeq 0.25$ and $\zeta \simeq 1$ [39–41] as it is confirmed by numerical simulations [44].

6.2 Pileup and Low Angle Grain Boundaries

Dislocation pileups and low angle grain boundaries (LAGB) display a quite similar geometrical structure; they are both one-dimensional arrangements of N dislocation lines with the same Burgers vector \mathbf{b} and average line direction \hat{e} (for edge dislocations $\hat{e} \perp \mathbf{b}$) along a given direction of space \hat{d} , but they differ in the relative orientation of the Burgers vector and the arrangement direction \hat{d} . In particular, in a pileup a set of edge dislocations lies in the slip plane, defined by the dislocations axis \hat{e} and the Burgers vector, so that $\hat{d} \parallel \hat{b}$, while in the LAGB the edge dislocations lie in the perpendicular plane such that $\hat{d} \perp \hat{b}$. Neglecting climb, i.e. the motion of a dislocation perpendicular to its slip plane, deformations of the structure occur solely within the slip plane both for the pileup and for the LAGB.

As in the case of isolated dislocations, the elastic stress associated with small deformations of these dislocation assemblies is needed in order to derive the yield stress from statistical pinning theories and to determine the critical behavior. In the rigid dislocation approximation, we do not consider the deformations along the z axis so that each dislocation is described by a set of coordinates (x_n, y_n) , where $y_n = nD$, D is the grain boundary spacing, and where x_n is a small displacement from the $x = 0$ plane. A direct calculations of the self-stress using isotropic elasticity yields a Peach-Koehler force on the dislocation in (x_m, y_m)

$$f_x(x_m, y_m) = -\frac{\mu b^2}{2\pi(1-\nu)} \sum_{n=-\infty}^{+\infty} \frac{x_m - x_n}{(y_m - y_n)^2}. \quad (11)$$

In Fourier space the associated elastic energy reads as

$$E = \frac{\mu b^2}{8\pi(1-\nu)D^2} \int_{BZ} \frac{dk}{2\pi} (2\pi|k| - Dk^2) \tilde{x}(k)\tilde{x}(-k). \quad (12)$$

From this expression, one can see that the elastic interaction kernel $(2\pi|k| - Dk^2)$ is not quadratic in the wavevector, as it would be the case for a local elastic manifold with a constant tension or stiffness, but grows roughly as $|k|$ for long wavelength deformations. This is a consequence of long range interactions between dislocations in the LAGB which render a much stiffer structure. A similar result is found for a pileup and even beyond the rigid line

approximation, when three dimensional deformations are explicitly included [45].

The morphology and dynamics of a pileup or a LAGB result from a complicated interplay between elasticity and disorder. Pileup and LAGB are another examples of the general problem of the depinning of elastic manifolds in random media [39–43]. In the elastic approximation, the dynamics of the pileup or the LAGB follows

$$\chi \frac{\partial u}{\partial t} = \int d^d x' K(x - x')(u(x') - u(x)) + b\sigma + \eta(x, u), \quad (13)$$

where χ is a damping constant, σ is the applied stress, $\eta(x, u)$ describes the effect of the pinning centers and the elastic interaction kernel scales as $|k|$ in Fourier space. This is similar to the problems of contact line [46], and planar crack depinning [47, 48]. We can thus directly apply to our case the results obtained for a manifold with long-range elastic energy [49]. The renormalization group analysis predicts that $d_c = 3$ is the upper critical dimension, above which fluctuations are suppressed. Thus for $d > d_c$ there is no roughening (i.e. $\zeta = 0$) and the other exponents can be computed in the mean-field approximation. These results are valid in the physically interesting dimension $d = 3$ apart from additional logarithmic corrections.

6.3 Zener Pinning in Grain Growth

From an experimental viewpoint, grain boundary pinning is important since the mobility of grain boundaries may be a limiting factor in grain growth [50]. Grain growth is driven by a reduction in energy: For an average grain size R and straight grain boundaries, the characteristic energy stored per unit volume in the form of GB dislocations is of the order of Γ_0/R and, hence, the energy gain achieved by increasing the grain size by dR is $(\Gamma_0/R^2) dR$.

Physically, the removal of GB dislocations occurs through the motion of junction points in the GB network. As junction points must drag the connecting GB with them, which may be pinned by disorder, motion can only occur if the energy gain at least matches the dissipative work which has to be done against the pinning forces. The dissipative work per unit volume expended in moving all GB by dR is $\sigma_c b/(DR)dR$, and balancing against the energy gain yields the limit grain size

$$R_l \approx \frac{\Gamma_0 D}{\sigma_c b} \approx \frac{\mu b}{\sigma_c}. \quad (14)$$

According to this relation, the grain size is inversely proportional to the pinning stress. This gives a possibility to experimentally assess the nature of the pinning by “tuning” the pinning stress and measuring the grain size as a function of the tuning parameters.

An obvious method to tune the pinning stress is to modify the concentration of the pinning centers and to measure the impact that this has on grain

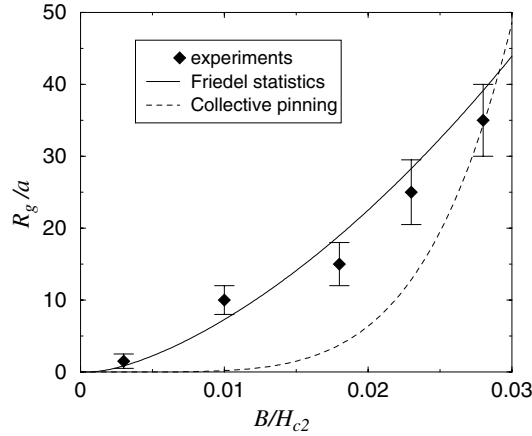


Fig. 3. The average grain size of a vortex polycrystal as a function of the magnetic induction on a sample of NbMo (data from [55]). In this case b is the lattice spacing and H_{c2} the second critical field of the type II superconductor. The full line is obtained assuming strong pinning and non-local elasticity, while the dotted line is derived under the hypothesis of local elasticity, that is, neglecting the long range nature of the LAGB self-stress. The dashed line was first derived in [55] assuming that the average grain size could be approximated by the Larkin length of the vortex lattice.

size. However, this requires the comparison of results from different samples and experimental results reported in the literature are inconclusive [51, 52]. We therefore refer to a quite different and unusual type of grain growth experiment where the configuration of the pinning obstacles is kept constant but the properties of the lattice are changed.

This type of grain growth experiment may be carried out on vortex lattices of type-II superconductors in which quasi two-dimensional grain structures are observed in *vortex polycrystals*. In such a system an external magnetic field penetrates the sample in the form of flux lines that are disposed in a triangular lattice. Its elastic properties (namely the lattice spacing b and the elastic moduli) depend on the magnetic field itself. Details on the theory of grain growth in vortex polycrystals are given elsewhere [53, 54]. Here we report the result obtained in the presence of strong pinning due to columnar defects (screw dislocations of the underlying crystalline lattice). As seen from Fig. 3 the agreement with Bitter decoration data from [55] is quite satisfactory, especially if compared to the estimate obtained from a local elasticity assumption.

7 Conclusions

The plastic flow in crystalline solids display complex features that are well captured by dislocation dynamics models. Simulations suggest a possible interpretation of dislocation motion within the general *jamming* scenario that is currently being investigated to ascertain the non-equilibrium behavior of this wide class of materials. In presence of solute atoms, dislocation flow and plastic yielding represent instead a vivid example of the depinning transition of elastic manifolds.

Dislocation dynamics models appear to be particularly well suited to describe plastic flow and dislocation-induced phase transitions in vortex lattices in type II superconductors. We have shown that, in response to an injected current in the superconductor, the resistance exhibits sharp jumps indicating the onset of two different regimes of plastic flow in the superconducting Corbino disk. The first is mediated by dislocation motion, mainly along the radial direction, whereas the second is mediated by the coherent glide motion of radial grain-boundaries. We have also described the formation of grain boundaries and vortex polycrystals in thin superconducting films with quenched disorder. In this case, we can apply concepts and ideas borrowed from the theory of interface depinning.

Acknowledgements

M.C.M. acknowledges financial support from the Ministerio de Educación y Ciencia (Spain), and from the Departament d'Universitats, Recerca i Societat de la Informació, Generalitat de Catalunya. This work has also been partly supported by the Spanish Ministerio de Educación y Ciencia (FEDER), Project No. FIS2004-05923-CO2-02.

References

1. J. Friedel, *Dislocations* (Pergamon Press, Oxford, 1967).
2. A. H. Cottrell, *Dislocations and Plastic Flow in Crystals* (Oxford University Press, London, 1953).
3. J. P. Hirth and J. Lothe, *Theory of Dislocations* (Krieger Publishing Company, 1992).
4. F. R. N. Nabarro, *Theory of Crystal Dislocations* (Dover, New York, 1992).
5. M.-C. Miguel, A. Vespignani, S. Zapperi, J. Weiss and J. R. Grasso, *Nature* **410**, 667 (2001).
6. C. Murray, C. Kagan, and M. Bawendi, *Ann. Rev. Mat. Sci.* **30**, 545 (2000).
7. T. B. Mitchell et al., J. J. Bollinger, W. M. Itano and D. H. E. Dubin, *Phys. Rev. Lett.* **87** 183001 (2001).
8. Pertsinidis A. and Ling X. S., *Nature* **413**, 47 (2001).
9. G. Blatter et al., *Rev. Mod. Phys.* **66**, 1125 (1994).

10. E. H. Brandt, Rep. Prog. Phys. **58**, 1465 (1995).
11. T. Giamarchi and S. Bhattacharya, in “High Magnetic Fields: Applications in Condensed Matter Physics and Spectroscopy”, p. 314, C. Berthier et al. eds., (Springer-Verlag, Berlin, 2002).
12. A. A. Abrikosov, Zh. Eksp. Teor. Fiz. **32**, 1442 (1957).
13. H. Safar, P. L. Gammel, D. A. Huse, D. J. Bishop, J. P. Rice, and D. Ginsberg, Phys. Rev. Lett. **69**, 824 (1992).
14. S. Bhattacharya and M. J. Higgins, Phys. Rev. Lett. **70**, 2617 (1993).
15. J. Weiss, J. R. Grasso, M. C. Miguel, A. Vespignani and S. Zapperi, Mat. Sci. and Eng. A **309-310**, 321 (2001).
16. J. Weiss and D. Marsan, Science **299**, 89 (2003).
17. J. Weiss, F. Lahaie and J. R. Grasso, J. Geophys. Res. **105**, 433 (2000).
18. E. N. da C. Andrade, Proc. R. Soc. London A **84**, 1 (1910); **90**, 329 (1914).
19. N. F. Mott, Phil. Mag. **44**, 741 (1953).
20. A. H. Cottrell, Phil. Mag. Lett. **73**, 35 (1996); **74**, 375 (1996); **75**, 301 (1997).
21. F. R. N. Nabarro, Phil. Mag. Lett. **75**, 227 (1997).
22. M. Z. Butt and P. Feltham, J. Mat. Sci. **28**, 2557 (1993).
23. H. Neuhäuser, Phys. Scr. **T49** 412 (1993).
24. R. Labusch, Phys. Status Solidi **41**, 659 (1970); Acta Metall. **20**, 917 (1972).
25. R. Labusch, Cryst. Lattice Defects **1**, 1 (1969).
26. A. I. Lar’kin and Yu. N. Ovchinnikov, J. Low Temp. Phys. **34**, 409 (1979).
27. Y. Paltiel, E. Zeldov, Y. N. Myasoedov, H. Shtrikman, S. Bhattacharya, M. J. Higgins, Z. L. Xiao, E. Y. Andrei, P. L. Gammel, D. J. Bishop, Nature **403**, 398 (2000); Y. Paltiel, E. Zeldov, Y. Myasoedov, M. L. Rappaport, G. Jung, S. Bhattacharya, M. J. Higgins, Z. L. Xiao, E. Y. Andrei, P. L. Gammel, and D. J. Bishop, Phys. Rev. Lett. **85**, 3712 (2000).
28. G. W. Crabtree, D. Lopez, W. K. Kwok, H. Safar, L. M. Paulius, J. Low. Temp. Phys. **117**, 1313 (1999).
29. G. D’Anna, P. L. Gammel, A. P. Ramirez, U. Yaron, C. S. Oglesby, E. Bucher, and D. J. Bishop, Phys. Rev. B **54**, 6583 (1996).
30. D. López, W. K. Kwok, H. Safar, R. J. Olsson, A. M. Petrean, L. Paulius, and G. W. Crabtree, Phys. Rev. Lett. **82**, 1277 (1999).
31. M. C. Miguel, A. Vespignani, S. Zapperi, J. Weiss and J. R. Grasso, Mat. Sci. and Eng. A **309-310**, 324 (2001).
32. M. C. Miguel, A. Vespignani, M. Zaiser and S. Zapperi, Phys. Rev. Lett. **89**, 165501 (2002).
33. A. J. Liu and S. R. Nagel, Nature **396**, 21 (1998).
34. A. J. Liu and S. R. Nagel (Eds.), *Jamming and Rheology*, (Taylor and Francis, London, 2001).
35. W. K. Kegel and A. van Blaaderen, Science **287**, 290 (2000).
36. E. Weeks et al., Science **287**, 627 (2000).
37. M.-C. Miguel and S. Zapperi, Nat. Mater. **2**, 477 (2003).
38. A. J. E. Foreman, Phil. Mag. **15** (1967) 1011.
39. T. Nattermann, S. Stepanow, L. H. Tang, and H. Leschhorn J. Phys. II (France) **2**, 1483 (1992).
40. H. Leschhorn, T. Nattermann, S. Stepanow, and L. H. Tang, Ann. Physik **6**, 1 (1997).
41. O. Narayan and D. S. Fisher, Phys. Rev. B **48**, 7030 (1993).
42. P. Chauve, T. Giamarchi, and P. Le Doussal Phys. Rev. B **62**, 6241 (2000).

43. P. Le Doussal, K. J. Wiese, and P. Chauve Phys. Rev. B **66**, 174201 (2002).
44. S. Zapperi and M. Zaiser, Mat. Sci. and Eng. A **309-310**, 348 (2001).
45. P. Moretti, M.-C. Miguel, M. Zaiser and S. Zapperi, Phys. Rev. B **69**, 214103 (2004).
46. D. Ertas and M. Kardar, Phys. Rev. E **49**, R2532 (1994).
47. J. Schmittbuhl, S. Roux, J. P. Villotte, and K. J. Maloy, Phys. Rev. Lett. **74**, 1787 (1995).
48. S. Ramanathan and D. Fisher, Phys. Rev. Lett. **79**, 877 (1997); Phys. Rev. B **58**, 6026 (1998).
49. M. Kardar, Phys. Rep. **301** 85(1998).
50. P. M. Hazzledine and R. D. J. Oldershaw, Phil. Mag. A **61**, 579 (1990).
51. D. L. Olgaard and B. Evans, J. Am. Ceram. Soc. **69**, C-272 (1986).
52. M. Miodownik M, E. A. Holm and G. M. Hassold, Scripta Mater. **42**, 1173 (2000).
53. P. Moretti, M.-C. Miguel, M. Zaiser and S. Zapperi, Phys. Rev. Lett. **92**, 257004 (2004).
54. P. Moretti, M.-C. Miguel, and S. Zapperi, Phys. Rev. B **72**, 014505 (2005).
55. I. V. Grigor'eva, Sov. Phys. JETP **69**, 194 (1989)
56. E. Schneider, J. Low. Temp. Phys. **31**, **375 (1978)**.

Index

- acoustic 38
 - activity 192, 193, 196
 - emission 192
 - phonons 129, 171
 - waves 192
- aging 16, 19, 23–27, 30, 32, 33, 35, 38, 40–42, 46, 47, 72, 133–135, 160, 174
 - dynamics 24, 33, 34, 47–49
 - effects 3, 32
 - materials 23–25, 27, 29, 31, 33, 35, 37, 39, 41, 43, 45, 47, 49, 51
 - systems 24, 40, 46–48
 - time 23, 27, 29, 41, 42
- arrest 4, 5, 9, 10, 19
 - collective 5, 15
 - state 4, 15
 - structural 53
 - transition 6, 9, 15
- avalanche 100, 101, 106, 189, 192, 193, 196
- chaos 17–19
 - rheochaos 3, 17, 18
- colloids 3, 4, 6, 9, 11, 15, 17–19, 48, 53, 72, 135, 137, 176, 190, 195
 - colloidal fluid 4
 - colloidal gel 4, 5, 25, 46
 - colloidal glass 4, 5, 8, 15, 18, 19, 23–25, 40, 46, 48, 53
 - colloidal suspension 4, 6, 14, 17, 42, 46, 53, 69, 137
- Corbino 109, 113–115, 120, 125, 126, 189, 194, 197, 198, 203
- creep 83–85, 91, 93, 96–98, 100–103, 106, 192–196
 - Andrade 193, 195
 - exponent 97, 100, 101, 105, 106
 - law 93, 97, 100, 101, 195
- motion 103, 105
- critical 69, 70, 118, 202
 - behavior 99, 138, 139, 143, 200
 - current 109–112, 116, 119, 123–126
 - deformation 71, 72, 78, 83, 86
 - dimension 130, 150, 201
 - distance 73, 74
 - exponent 93, 143, 150, 199, 200
 - force 92, 99, 138, 143
 - point 144, 149–154
 - stress 9, 13, 69, 70, 78, 83, 86, 88, 195
- dislocation 137, 139, 143–147, 189–196, 199, 203
 - assemblies 194, 200
 - Burgers vector 191, 194, 198–200
 - edge 191, 194, 197, 199, 200
 - interaction 189, 191, 200
 - motion 145–147, 190–193, 195, 203
 - pair 195, 198
 - Peach-Koehler force 191, 198, 200
 - pileup 189, 200, 201
 - screw 191, 202
- disorder 91–95, 106, 109, 111, 118, 125, 129, 137–139, 141, 143, 145, 147–149, 151, 153, 155, 157, 162, 173, 179, 189, 201
- correlated 176
- disordered phase 109–112, 115, 117, 118, 124, 126
- disordered system 91–93, 95, 97, 99, 101, 103, 105, 107, 138, 147, 153, 179
- quenched 103, 120, 137, 138, 147, 152, 191, 203
- random bond 94, 98, 102
- random field 94, 98

- strength 91, 104, 105, 137–139, 144, 153–155
- domain wall 91–93, 97, 101, 105, 106
- edge contamination 109, 111, 112, 115, 120, 126, 154
- effective temperature 24–26, 29, 34, 129, 130, 159, 175, 176, 196
- electrical
 - mechanical 46
- fluctuation-dissipation 24, 58, 176
 - theorem 6, 23, 24, 56, 159, 163, 174–176, 180
- gel 5, 17, 23, 25, 40, 43, 49, 69, 78, 159, 195
 - sol-gel transition 23, 40, 48
- glass transition 6, 11, 13, 15, 16, 18, 19, 53, 54, 61, 63, 66, 130, 132, 136
- grain boundary 189, 200, 201, 203
- granular 54, 85
 - material 53–55, 58, 88, 137, 159
 - media 53–57, 59, 61, 63, 65–67
- hard sphere 4, 7–10, 15, 55, 56, 58, 62
- hardening 193
- hysteresis 27, 91, 137, 138, 144, 145, 150, 152–155
 - cycle 11, 150, 152
- instability 3, 17, 193
 - dynamic 110, 115
 - flow 80
 - plastic 189
- interface 14, 17, 41, 69, 78, 91–96, 100, 106, 138, 140, 199, 203
 - solid-liquid 76, 78, 83, 88
- intermittent 23, 31, 33, 34, 43, 45, 46, 190, 192, 195, 196
 - dynamics 23, 32, 34, 46, 47, 195
 - intermittency 23–25, 32, 33, 40, 41, 45–49
- jamming 3, 5, 7, 9, 11–13, 15, 17, 19, 21, 53, 55, 57, 59, 61, 63, 65, 67, 86, 87, 137, 189, 194–196, 203
 - full 11, 13–15
 - jammed systems 69, 76, 80, 83, 85, 88, 195
- transition 13, 15, 18, 53, 54, 63, 66, 195
- manifold 153, 201
 - elastic 152, 194, 200, 201, 203
 - random 92, 103, 104
 - Riemannian 178
- mode coupling theory 3–8, 10, 12, 14–19, 64, 65
- noise 5, 24–26, 31, 32, 38, 39, 41, 46–48, 93, 109, 113, 118–123, 160, 164, 166, 170, 171, 174, 179, 198
 - electrical 23, 25, 26, 32, 34, 41
 - excess 109, 110, 119, 120, 122, 124–126
 - mechanical 23, 25, 38, 45, 46, 48, 49
 - signal-to-noise ratio 38, 41, 123
 - thermal 23–25, 27, 29, 31, 33, 35, 37–41, 43, 45, 47, 49, 51, 95, 100, 103
 - voltage 42, 43, 45, 109, 114, 118–120, 123–126
- pinning 94, 97, 99, 102, 109, 110, 114, 116, 118, 137–139, 141, 142, 189, 193, 199, 200, 202
 - depinning 97, 98, 100, 106, 110, 137–140, 142–144, 146, 147, 149, 150, 152–155, 193, 199, 201, 203
 - force 98, 102, 126, 138, 140–143, 148, 150, 193, 194, 201
 - Zenner 201
- plastic 70, 79, 86, 118, 131, 133, 137, 147, 154, 189, 193, 194, 197, 203
 - deformation 189, 190, 192, 193, 195
 - flow 138, 144, 190–194, 197, 203
 - plasticity 86, 129, 137, 139, 141, 143, 145, 147, 149, 151, 153–155, 157, 189–191, 194
 - viscoplastic 70
- polymer 23–26, 33, 36, 38, 46, 48, 69, 164, 165
 - glass 25, 45, 46
- renormalization group 99, 101, 201
 - functional 91, 99–101, 106
- shear 6, 7, 10, 69, 70, 74, 83, 129–132, 134, 135, 137, 144, 146, 147, 176

- banding 3, 11, 16, 17, 19, 76, 79, 80, 86
- localization 80
- modulus 10, 143, 147, 191
- stress 3, 8, 9, 53, 69–76, 79, 131, 133, 137, 143, 147, 194, 196, 198
- thickening 3, 11–13, 15, 17, 18
- thinning 3, 6, 8, 9, 18
- thixotropy 72, 83, 85
- viscosity 3, 8, 11, 15, 37, 69, 71, 72, 135, 144, 146, 153, 162, 197
 - bifurcation 16, 17, 19, 69, 83, 85
 - viscoelastic 36–38, 70, 71, 83, 144–147, 152–154
- vortices 92, 101, 110–116, 118, 119, 123, 124, 126, 190–192, 194, 197, 198
- vortex crystal 191, 194
- vortex flow 189, 191, 197
- vortex lattice 91, 111, 115, 120, 124, 137, 138, 140, 154, 155, 174, 189, 191, 192, 194, 197, 202, 203
- vortex matter 109–111, 113–116, 125, 126, 191, 194
- vortex polycrystal 189, 202, 203
- yield 6, 110
 - stress 3, 4, 8–11, 15–17, 19, 69–73, 75, 76, 78, 79, 83, 85–87, 193, 195, 200
 - yielding 3, 5, 7, 9, 11, 13, 15–17, 19, 21, 70, 72, 80, 81, 83, 189, 194, 197, 203

Lecture Notes in Physics

For information about earlier volumes
please contact your bookseller or Springer
LNP Online archive: springerlink.com

- Vol.639: G. Ripka, Dual Superconductor Models of Color Confinement
- Vol.640: M. Karttunen, I. Vattulainen, A. Lukkarinen (Eds.), Novel Methods in Soft Matter Simulations
- Vol.641: A. Lalazissis, P. Ring, D. Vretenar (Eds.), Extended Density Functionals in Nuclear Structure Physics
- Vol.642: W. Hergert, A. Ernst, M. Däne (Eds.), Computational Materials Science
- Vol.643: F. Strocchi, Symmetry Breaking
- Vol.644: B. Grammaticos, Y. Kosmann-Schwarzbach, T. Tamizhmani (Eds.) Discrete Integrable Systems
- Vol.645: U. Schollwöck, J. Richter, D. J. J. Farnell, R. F. Bishop (Eds.), Quantum Magnetism
- Vol.646: N. Bretón, J. L. Cervantes-Cota, M. Salgado (Eds.), The Early Universe and Observational Cosmology
- Vol.647: D. Blaschke, M. A. Ivanov, T. Mannel (Eds.), Heavy Quark Physics
- Vol.648: S. G. Karshenboim, E. Peik (Eds.), Astrophysics, Clocks and Fundamental Constants
- Vol.649: M. Paris, J. Rehacek (Eds.), Quantum State Estimation
- Vol.650: E. Ben-Naim, H. Frauenfelder, Z. Toroczkai (Eds.), Complex Networks
- Vol.651: J. S. Al-Khalili, E. Roeckl (Eds.), The Euroschool Lectures of Physics with Exotic Beams, Vol.I
- Vol.652: J. Arias, M. Lozano (Eds.), Exotic Nuclear Physics
- Vol.653: E. Papantonopoulos (Ed.), The Physics of the Early Universe
- Vol.654: G. Cassinelli, A. Levrero, E. de Vito, P. J. Lahti (Eds.), Theory and Application to the Galileo Group
- Vol.655: M. Shillor, M. Sofonea, J. J. Telega, Models and Analysis of Quasistatic Contact
- Vol.656: K. Scherer, H. Fichtner, B. Heber, U. Mall (Eds.), Space Weather
- Vol.657: J. Gemmer, M. Michel, G. Mahler (Eds.), Quantum Thermodynamics
- Vol.658: K. Busch, A. Powell, C. Röthig, G. Schön, J. Weissmüller (Eds.), Functional Nanostructures
- Vol.659: E. Bick, F. D. Steffen (Eds.), Topology and Geometry in Physics
- Vol.660: A. N. Gorban, I. V. Karlin, Invariant Manifolds for Physical and Chemical Kinetics
- Vol.661: N. Akhmediev, A. Ankiewicz (Eds.) Dissipative Solitons
- Vol.662: U. Carow-Watamura, Y. Maeda, S. Watamura (Eds.), Quantum Field Theory and Noncommutative Geometry
- Vol.663: A. Kalloniatis, D. Leinweber, A. Williams (Eds.), Lattice Hadron Physics
- Vol.664: R. Wielebinski, R. Beck (Eds.), Cosmic Magnetic Fields
- Vol.665: V. Martinez (Ed.), Data Analysis in Cosmology
- Vol.666: D. Britz, Digital Simulation in Electrochemistry
- Vol.667: W. D. Heiss (Ed.), Quantum Dots: a Doorway to Nanoscale Physics
- Vol.668: H. Ocampo, S. Paycha, A. Vargas (Eds.), Geometric and Topological Methods for Quantum Field Theory
- Vol.669: G. Amelino-Camelia, J. Kowalski-Glikman (Eds.), Planck Scale Effects in Astrophysics and Cosmology
- Vol.670: A. Dinklage, G. Marx, T. Klinger, L. Schweikhard (Eds.), Plasma Physics
- Vol.671: J.-R. Chazottes, B. Fernandez (Eds.), Dynamics of Coupled Map Lattices and of Related Spatially Extended Systems
- Vol.672: R. Kh. Zeytounian, Topics in Hypersonic Flow Theory
- Vol.673: C. Bona, C. Palenzuela-Luque, Elements of Numerical Relativity
- Vol.674: A. G. Hunt, Percolation Theory for Flow in Porous Media
- Vol.675: M. Kröger, Models for Polymeric and Anisotropic Liquids
- Vol.676: I. Galanakis, P. H. Dederichs (Eds.), Half-metallic Alloys
- Vol.678: M. Donath, W. Nolting (Eds.), Local-Moment Ferromagnets
- Vol.679: A. Das, B. K. Chakrabarti (Eds.), Quantum Annealing and Related Optimization Methods
- Vol.680: G. Cuniberti, G. Fagas, K. Richter (Eds.), Introducing Molecular Electronics
- Vol.681: A. Llor, Statistical Hydrodynamic Models for Developed Mixing Instability Flows
- Vol.682: J. Souchay (Ed.), Dynamics of Extended Celestial Bodies and Rings
- Vol.683: R. Dvorak, F. Freistetter, J. Kurths (Eds.), Chaos and Stability in Planetary Systems
- Vol.685: C. Klein, O. Richter, Ernst Equation and Riemann Surfaces
- Vol.686: A. D. Yaghjian, Relativistic Dynamics of a Charged Sphere
- Vol.687: J. W. LaBelle, R. A. Treumann (Eds.), Geospace Electromagnetic Waves and Radiation
- Vol.688: M. C. Miguel, M. Rubi (Eds.), Jamming, Yielding, and Irreversible Deformation in Condensed Matter